An Integrated Geoscientific Study of Sulfate Dissolution Related

Sinkhole Occurrence

Aksara Mayamae

A Thesis Submitted in Partial Fulfillment of the Requirements for the

Degree of Master of Science in Geophysics

Prince of Songkla University

2011

Thesis Title   An Integrated Geoscientific Study of Sulfate Dissolution Related Sinkhole Occurrence

Author   Miss Aksara Mayamae

Major Program   Geophysics

_____

Major Advisor

…………………………………..…
(Dr.Helmut Dürrast)

Co-advisor

…………………………………..…
(Dr.Sawasdee Yordkayhun)

Examining Committee:

……….…………………Chairperson
(Assoc. Prof. Dr.Sumpun Wongnawa)

……………………………………………
(Prof.John Warren)

……………………………………………
(Dr.Sawasdee Yordkayhun)

……………………………………………
(Dr.Helmut Dürrast)

The Graduate School, Prince of Songkla University, has approved this thesis as partial fulfillment of the requirements for the Master of Science Degree in Geophysics

……………………………………………
(Prof. Dr.Amornrat Phongdara)
Dean of Graduate School

ชื่อวิทยานิพนธ์	การประยุกต์การศึกษาธรณีศาสตร์การละลายชั้นหินซัลเฟตที่เกี่ยวข้อง กับการเกิดหลุมยุบ
ผู้เขียน	นางสาวอักษรา มะยาแม
สาขาวิชา	ธรณีฟิสิกส์
ปีการศึกษา	2554

บทคัดย่อ

สาเหตุที่ทำให้เกิดการก่อตัวของหลุมยุบ ในบริเวณใกล้เหมืองยิปซัมที่ตำบลท่า ยาง อำเภอทุ่งใหญ่ จังหวัดนครศรีธรรมราช ได้สืบสวนด้วยการประยุกต์การศึกษาทางธรณีศาสตร์ ผลของการศึกษาระบุโครงสร้างทางธรณีวิทยาที่มีอิทธิพลทำให้เกิดการก่อตัวของโพรงใต้ดินเมื่อ การไหลของน้ำใต้ดินและเกิดการกัดเซาะของชั้นหินซัลเฟต ลักษณะของชั้นหินซัลเฟตน่าจะเป็น โครงสร้างที่มีการเทเอียงหรือรอยเลื่อนแนวดิ่งในทิศเหนือใต้ วิธีการทางธรณีฟิสิกส์หลายวิธีได้ใช้ ในการศึกษานี้ ผลจากระเบียบวิธีการหยั่งไฟฟ้าในแนวดิ่งแสดงความต่อเนื่องของโครงสร้างใต้ดิน ตั้งแต่ผนังเหมืองถึงพื้นที่เกิดหลุมยุบ ชั้นหินซัลเฟตผุที่มีค่าความต้านทานไฟฟ้า อยู่ในช่วง 80 ถึง 150 โอห์ม-เมตร ที่ระดับความลึก 25 ถึง 30 เมตร และบริเวณที่มีหลุมยุบเกิดขึ้น โครงสร้างมี ลักษณะเทเอียงหรืออาจจะเป็นรอยเลื่อนแนวดิ่ง ระดับความลึกนี้ตรงกับความลึกจากผลการ ตีความของระเบียบวิธีคลื่นไหวสะเทือนสะท้อนและความหนา ชั้นซัลเฟตผุประมาณ 15 ถึง 25 เมตร ด้วยความเร็ว 1,800 ถึง 1,850 เมตรต่อวินาที ค่าความต้านทานไฟฟ้าของการละลายของ ชั้นหินซัลเฟตนี้ซึ่งทำให้เกิดหลุมยุบ ได้เปรียบเทียบด้วยปริมาณของซัลเฟตที่พบในน้ำในหลุมยุบที่ สอง (23มิลลิกรัมต่อลิตร; 151 โอห์ม-เมตร) แผนที่เส้นศักย์ธรรมชาติระบุว่ายังมีโพรงอยู่ใต้ดินซึ่ง อยู่ใกล้กับหลุมยุบหลุมแรก และแสดงบริเวณที่มีการละลายของชั้นหินซัลเฟตผุระหว่างหลุมยุบ หลุมแรกและหลุมที่สอง บริเวณนี้ตรงกับโครงสร้างที่มีการเทเอียงของชั้นดินหรือรอยเลื่อน ใน บริเวณนี้ได้สมมติฐานว่ายังคงมีการละลายต่อไป ดังพบจากน้ำใต้ดินอยู่ในสถานะไม่อิ่มตัวด้วยค่า ดัชนีการอิ่มตัว -3.84 ของตัวอย่างน้ำในหลุมยุบที่สอง การเข้าใจกลไกและเงื่อนไขสามารถใช้ใน การประเมินความอันตราย สุดท้ายประชาชนในหมู่บ้านควรได้รู้ถึงเหตุการณ์นี้

Thesis Title   An integrated geoscientific study of sulfate dissolution related sinkhole occurrence

Author   Miss Aksara Mayamae

Major Program   Geophysics

Academic Year   2011

ABSTRACT

The causes of sinkhole formation in the area near a gypsum mine in Tha Yang Subdistrict, Thung Yai District, Nakhon Si Thammarat Province were investigated by an integrated geoscientific study. The results indicate a potential geological structure, which causing the formation of voids in the subsurface when the groundwater is flowing and dissolving the sulfate formation. It is likely a west dipping structure or a N–S striking vertical fault. Several geophysical methods were applied in this study. VES results provided a continuous profile over the structure in the subsurface, from the mine wall to the area of sinkholes occurrence. The weathered sulfate layer was in the range 80 to 150 ohm-m at the depth 25 to 30 meters and at the area of the sinkhole occurrence the structure either consists of dipping layers or a vertical fault. The depth conforms to the seismic reflection interpretation and the thickness of the weathered sulfate layer is about 15 to 30 meters with as velocity of 1,800 to 1,850 m/s. This resistivity of the dissolved sulfate layer, which caused the sinkhole occurrence, was comparable to a sulfate concentration found in the water of the second sinkhole (23 mg/l sulfate; 151 ohm-m). The self-potential contour map indicates the existence of voids in the subsurface in close proximity to the first sinkhole and reveals a dissolution zone of weathered sulfate layer between the first and the second sinkhole. This zone coincides with the dipping structure or fault zone. Continuing dissolution can be assumed as seen from the undersaturated state of groundwater with a saturation index of -3.84 for the water sample from the second sinkhole. The understanding of these mechanisms and conditions can be used in a hazard assessment. Finally, it is recommended that local villagers should be made aware of the situation.

ACKNOWLEDGEMENTS

CONTENTS

CONTENTS (CONTINUED)

APPENDIX

LIST OF TABLES

LIST OF FIGURES (CONTINUED)

Page

LIST OF FIGURES (CONTINUED)

CHAPTER 1

INTRODUCTION

Sinkholes are one type of geological natural hazards, and their occurrence is directly related to the occurrence of soluble subsurface formations, like limestone, rock salt, and other evaporates, for example gypsum and anhydrite (e.g. Appelo and Postma, 2005). The development of a sinkhole in an urban area is a direct threat to people, housing, and infrastructure, because the area above a subsurface hole stays intact until suddenly the sinkhole develops. The size of a sinkhole can vary from less than a meter to tens of meters in diameter and depth. However, it is also known that land use practices, with groundwater pumping and construction, can trigger or even cause the development of sinkholes (e.g. Kresic, 2006).

In the Tayang Sub-district, Tungyai District, Nakhon Si Tammarat Province, two larger sinkholes occurred. The first one, with 15 meters in diameter and 10 meters depth, occurred in January 2005, and the second has formed in August 2009, with 5 meters in diameter and 19 meters depth. Both sinkholes were about 100 m apart from each other, and about half a kilometer away from an active gypsum mine. Local people claimed that sinkholes were not a common feature in their village area until early 2005; besides the existence of the subsurface evaporate formation.

1.1 Gypsum and anhydrite

The characteristic of sulfate rocks are summarized in table 1.1. Gypsum is a common mineral, know also by its chemical name of hydrated calcium sulfate $CaSO_4 \cdot 2H_2O$. Chemically pure gypsum contains CaO 32.5%, SO_3 46.5% and H_2O 20.9%. The mineral has a hardness of 2 on the Mohs' scale and its density varies from 2.2 to 2.4 g/cm^3. Gypsum may form as granular, laminated, powdered, fibrous and radiate-fibrous aggregates. In crystals gypsum is normally colorless and transparent, but it sometimes has brownish colors. Compact masses of gypsum may be white, gray, pink, red, brown, pale yellow or pale blue. Massive varieties of

gypsum are known as alabaster; fibrous varieties are referred to as satin spar and large tabular monocrystals can be defined as selenite (Klimchouk and Andrejchuk, 1996).

Anhydrite is the anhydrous form of calcium sulfate, $CaSO_4$. Chemically pure anhydrite is CaO 41.2%, SO_3 58.8%. Anhydrite crystals are rhombic with perfect cleavage along three orthogonal directions producing rectangular crystals. The hardness is 3.0 to 3.5 on the Mohs' scale and its density varies from 2.86 to 3.10 g/cm^3. Anhydrite commonly forms very compact fine-grained masses, but it also occurs as tabular, prismatic and fibrous aggregates. Common colors are white or pale shades of gray, blue, green, yellow and red-brown (Klimchouk and Andrejchuk, 1996).

Table 1.1   Physical and chemical characteristic of gypsum and anhydrite (from Cooper and Calow, 1998).

	Gypsum	Anhydrite
Chemical name	calcium sulphate dihydrate	calcium sulphate
Chemical formula	$CaSO_4.2H_2O$	$CaSO_4$
Specific gravity	2.3-2.37	2.9-3
Hardness, Mohs' scale	1.5-2	3-3.5
Main varieties	fibrous, alabastrine, crystalline	crystalline and nodular
Colour	white, pale grey, pink, yellow-brown	grey and pale bluish grey
Porosity	typically fairly low around 4-7%	typically low around 3%
Compressive strength	moderately strong, unconfined compressive strength, 24-35 MPa	strong to very strong, unconfined compressive strength, 66-123 MPa
Tensile strength	2.2-3.6 MPa (Brazilian tensile strength)	7.1-8.2 MPa (Brazilian tensile strength)
Schmidt hammer hardness	8-23	35-37

Calcium sulfate rocks can be represented by gypsum, anhydrite or varying proportions of both minerals. Mixed rocks are called gypsiferous if the content of minor mineral is considerable. Sulfate rocks may contain, admixtures of clayey materials, carbonates and grains of sand; however, their purity is commonly high with the content of $CaSO_4$ (or $CaSO_4 \cdot 2H_2O$) varying between 95.0 and 99.5 %.

Gypsum rocks can be formed in different environments. The genetic classification differentiates between primary and secondary deposits. Primary deposits are lagoon deposits, which formed due to evaporation of marine brines, and continental deposits, which formed by evaporation in inland basins or formed at the surface. Secondary deposits (all continental) are redeposited, metasomatic, which formed by gypsum replacement of carbonates due to reactions with sulfuric acid

groundwater, or formed by the action on limestone of sulfuric springs or volcanic agents, caprock deposits in salt diapirs and weathering deposits formed by the hydration of anhydrite. The most common are primary gypsum deposits and weathering deposits where anhydrite has rehydrated to gypsum (Klimchouk and Andrejchuk, 1996).

Sulphates and halides precipitate from oversaturated water under arid climatic conditions (evaporite facies). The former consist of the sulphate anion (SO_4^{2-}) and different cations. Gypsum ($CaSO_4 \cdot 2H_2O$) and anhydrite ($CaSO_4$) are the most relevant sulphates. Gypsum often transforms into anhydrite during diagenesis under increasing pressure and temperature. Anhydrite retransforms into gypsum when it comes in contact with groundwater, which results in an increased volume.

Most gypsum and anhydrite rocks have originate as evaporite formations in marine (lagoon) and epicontinental (basins on a continent or a continental shelf) sea environments. However, in some evaporate formations potassium or sodium salts are dominant, within evaporite marine basins, gypsum commonly precipitate on shoals and shelves, with halite in the deeps; highly soluble K-Mg or Ca-Mg-chlorides preferentially on the flanks. Gypsum and/or anhydrite sequences are commonly associated with beds and formations composed of carbonate and terrigenous sedimentary rocks (shallow marine sedimentary deposits composed of eroded terrestrial material from the land). Evaporate formations occur both in marine and continental sedimentary sequences. Marine evaporite sequences are commonly associated with carbonates, but clays, siltstones and sandstones are also common. In continental sequences the most common associations are sand, sandstone, clay, shale, evaporite dolomites and limestone (Klimchouk and Andrejchuk, 1996).

Based on evaporite surrounding sediment associations four types of sequences can be distinguished, first are alternating marine and lagoon sedimentary sequences where evaporate are associated mainly with carbonates, second are evaporate accumulations suppressed by large inputs of continental terrigenous material, the third type begins with a continental sedimentary environment and continue through lagoon to marine environments, and fourth are evaporate formations within continental sequences. Gypsum and anhydrite can occur as single beds, but they more typically occur as a series of bed intercalated with other sedimentary rocks.

Sulfate can also comprise some isolated miner beds, or formations, that have distinct lithological boundaries with the over and underlying sediments, which can form continuous spreads through quite extensive areas. The abrupt termination of sulfate beds commonly signifies either truncation by tectonic faults or dissolution removal, either recent or ancient (Klimchouk and Andrejchuk, 1996).

The conversions between gypsum and anhydrite are considerably affected by changes in the physical and chemical parameters occurring within common geological environments. Gypsum is the most common primary marine sulfate and the first precipitate in evaporite basins. However, anhydrite can form as a primary deposit in evaporating basins when the temperature exceeds 25 °C. Primary anhydrite is rare and most anhydrite is believed to originate from dehydration of gypsum which occurs at pressures of $18\text{-}75\times10^{-5}$ Pa and high temperatures during burial resulting in a volume reduction of approximately 38% (Ford and Williams, 2005). Subsequent uplift of anhydrite formed during burial causes its rehydration and conversion to secondary gypsum (Figure 1.1). These can vary considerably from these generalities depending on the geothermal gradient, the supply of rehydrating water, and its chemical composition (Klimchouk and Andrejchuk, 1996).

Other mechanisms and factors that affect the dehydration of gypsum occurring at shallow depths are mainly during early diagenesis stages, where the gypsum to anhydrite conversion is due to its interaction with hygroscopic sodium, magnesium or calcium chlorides brines. Other parameters are the tectonic regime, permeability and properties of surrounding formations such as the flow regime. Most gypsum has passed through the dehydration cycle. In the upper zone of active groundwater circulation, sulfates are represented predominantly by gypsum. This situation is further complicated by the considerable age range of the formations, their complex geological histories and different tectonic regimes (Klimchouk and Andrejchuk, 1996).
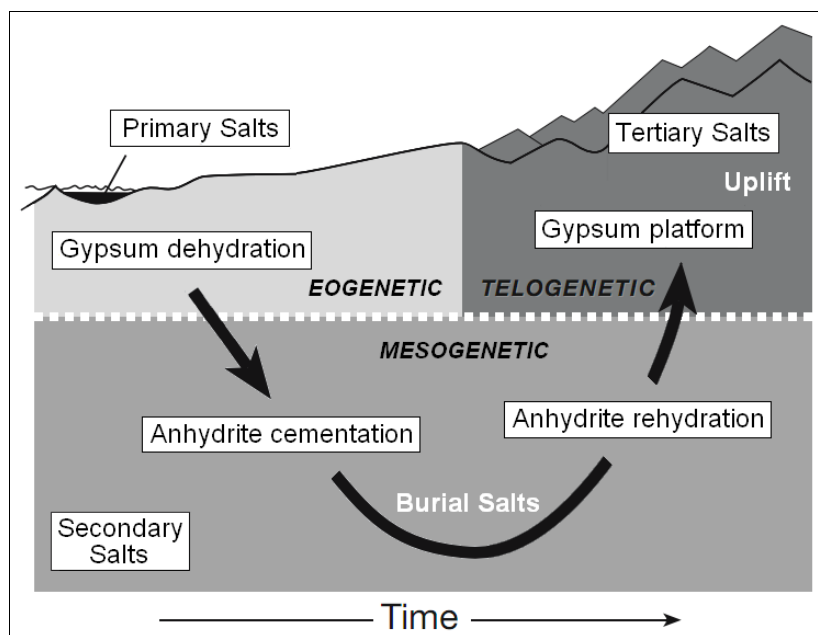
Figure1.1   Calcium sulfate rocks conversion associated with complex diagenetic history as units pass through the primary stages of burial diagenesis, which are eogenetic (rocks have not been buried beyond the range of meteoric diagenesis), mesogenetic (rocks have undergone compaction and cementation associated with burial diagenesis) and telogenetic (rocks have undergone burial diagenesis and re-exposed to meteoric diagenesis near the earth surface through uplift and/or surface denudation) (from Warren, 2006).

The distribution of evaporate formations (Table 1.2) began to appear at the end of the Proterozoic (Figure 1.2). There are some epochs when almost no evaporate rocks were formed and other epochs when evaporate generation was extremely intense. During Halogenic epochs of the Palaeozoic, a few very large evaporate rocks were formed. In contrast, through the Mesozoic to the Cenozoic the number of deposits formed was large, but they were of limited area and mass. In general the Halogenic epochs show some affinity to the epochs of orogenesis (mountain building) and regression, although the actual distribution is quite complex. Continental formations represented by gypsum are known in the Carboniferous and the Neogene. Formations of lagoon type can be traced from the Cambrian to the present, but formations in large gulfs are known mainly from the Cretaceous and

Paleogene. Formation marginal to the vast epicontinental sewes formed in the Devonian, and formations deposited in large internal salt-generating seas were common in the Permian. The most extensive and thick sulfate formations have formed during the Palaeozoic shows superimposed areas of gypsum and anhydrite accumulation around the globe for different epochs from the pre-Cambrian through to the Permian. During the Mesozoic and Cenozoic, sulfate had formed in numerous relatively small basins, which surrounded young tectonically active areas, particularly the Paratethis (Alps, Carpathians, Caucasus, and mountains of central and southern Asia). Gypsum and anhydrite are wide-spread throughout the Cenozoic, they are particularly developed in the Miocene formations of the Mediterranean region (in the Pyrenees and Apennines, Sicily and North), along both sides of the Carpathian arch. Neogene gypsum is known in the epiplatform environment of the Ustjurt Plateau and mountainous regions of Central Asia (Pamir-Alaj, Bajsuntau, Kugitangtau), as well as in some regions of Turkey. Sulfate rocks and/or salts were estimated underlie 25% of the continental surface of the world, an area of more than 60 million km^2. The area of gypsum/anhydrite calculated on the continents was seven million km^2 (Klimchouk and Andrejchuk, 1996).

Table 1.2   Representative examples of basinwide evaporates (also called saline giants and basin center evaporite). In some the former evaporate beds are now represented by laterally extensive solution breccia horizons (Warren, 2006).

Sequence of interest	Basin/setting and Location	Age	Basin style	Tectonic event	References
Messinean Evaporites	Lago Mare ("lake sea"), Mediterranean	Miocene, Upper	Flexure	Convergent foreland Alpine	Krijgsman et al., 1999
Belayim and Gharib formations	Gulf of Suez - Red Sea, Middle East	Miocene, Middle - Upper	Extension	Red Sea Breakup and the formation of the Red Sea/Suez Rift	Rouchy et al., 1995; Meshref, 1990
Gachsaran Formation	Mesopotamian Basin, Middle East	Miocene, Middle	Flexure	Convergant foreland Zagros-Taurus	Tucker, 1999
Maha Sarakham Formation	Khorat Basin, Thailand	Cretaceous, Upper	Flexure	Convergant foreland Cretaceous inversion and thrust loading	Utha-Aroon, 1993; Booth and Sattayarak, 2000
Todilto Formation	Todilto Basin, New Mexico, USA	Jurassic, Middle	Flexure	Convergant foreland Ancestral Rockies	Benan and Kocurek, 2000
Louann Salt	Gulf of Mexico Basin, Gulf Coast	Jurassic, Middle	Extension	Incipient Gulf of Mexico- Atlantic rift	Land et al., 1988, 1995; Salvador, 1987
Argo Formation & Osprey Evaporites	Scotian Basin, and Grand Banks, Canada	Upper Triassic-Lower Jurassic	Extension	Incipient Atlantic rifting	Holser et al., 1988
Northwich Halite	Cheshire Basin, United Kingdom	Triassic	Extension	Incipient Atlantic rifting	Pegrum and Mounterey, 1978
Halite (S1-S4, Las and Dogger Anhydrite units)	Oued Mya Basin, Algeria, Northern Sahara	Upper Triassic-Lower Jurassic (Liassic)	Extension	Intraplate sag basin atop grabens created by incipient Atlantic and Tehyan rifting	Yahi et al., 2001; Turner et al., 2001
Saliferous units	Ghadames (Berkine) Basin, Algeria	Triassic, Upper Jurassic, Lower	Extension	Intraplate sag basin atop grabens created by incipient Atlantic and Tehyan rifting	Yahi et al., 2001; Turner et al., 2001
Argiles d'Argana	Essaouria Basin, Morocco	Triassic, Upper	Flexure	Intraplate sag basin atop grabens created by incipient Atlantic and Tehyan rifting	Hafid, 2000; Evans 1978
Formation Salifere	Saharan Atlas, Algeria	Triassic, Upper	Flexure	Intraplate sag basin; incipient Atlantic and Tehyan rifting	Hardie, 1990; Merabet and Popov, 1971
Salina d'Ourgla	Northern Sahara Salt Basin, Algeria	Triassic, Upper	Flexure	Intraplate sag basin; incipient Atlantic and Tehyan rifting	Hardie, 1990; Merabet and Popov, 1971
Nikitov, Slavyan, and Kramatov Formations	Dnieper-Denets Basin, Ukraine and Russia	Permian, Lower (Kungurian salt)	Flexure	Post-rift sag reactivated by Uralian Orogeny (Hercynian)	Ulmishek, 2001a; Chekunov et al., 1992
Rotliegende	Dniepr-Donets Basin, Eastern Europe	Permian, Lower	Flexure	Foreland Variscan Orogeny	Kabyshev et al., 1998
Zechstein Basin, NW Europe	NW European Basin, NW Europe	Permian, Upper	Flexure	Post Variscan Orogeny collapse	Hardie 1990

Table 1.2 (continued) Representative examples of basinwide evaporates (also called saline giants and basin center evaporite). In some the former evaporate beds are now represented by laterally extensive solution breccia horizons (Warren, 2006).

Sequence of interest	Basin/setting and Location	Age	Basin style	Tectonic event	References
Castille Formation	Delaware Basin, west Texas	Permian, Upper	Flexure	Marathon-Ouchita	Kirkland et al., 2000
Iren Horizon Kungurian evaporites	North Caspian Basin (aka Pri- or Peri-Caspian), Khazakhstan and Russia	Permian, Lower	Flexure	Foreland, Uralian Orogeny. Collision of Russian Platform with the Siberia/Ka-zakhstan block	Ulmishek, 2001b
Otto Fiord Formation	Sverdrup Basin, Canadian Arctic Islands	Carboniferous	Extension	Synrift stage of post-Caledonian intracontinental rifting	Balkwill, 1978; Stephenson et al., 1992
Paradox Formation	Paradox Basin, Colorado-Utah USA	Carboniferous, Upper	Flexure	Ancestral Rockies	Barbeau, 1999
Caurauri Formation	Amazonas Basin, South America	Carboniferous, Upper	Flexure	Distal effect of Marathon-Ouchita orogeny	Hardie, 1990; Szatmari et al., 1979;
Windsor Group	Magdalen Basin, Eastern Canada	Carboniferous, Lower	Extension	Cabot fault-Belle Isle transtensional system	Langdon and Hall, 1994; Lynch and Keller, 1998
Liven Horizon	Dnieper-Denets Basin, Ukraine and Russia	Devonian, Upper Frasnian and Fammenian	Extension	Synrift via crustal stretching (passive margin)	Ulmishek, 2001a; Ulmishek et al., 1994
Prairie Evaporite	Elk Point Basin, Western Canada Plains	Devonian, Middle	Flexure	Intracratonic sag; a distal effect of thrust-loaded compression of the western Laurasian plate	Pysklywec and Mitrovica, 2000
Salina Group	Michigan Basin, USA	Silurian, Middle-Upper	Flexure	Intracratonic sag during Taconian thrust loading, sits atop Mesoproterozoic Midcontinent rift basin	Howell and Van der Pluijm, 1999
Mallowa Salt (Carribuddy Formation)	Canning Basin, Northwest Australia	Ord.-Silurian	Extension	Pre-rift to Synrift stage of intracratonic sag	Cathro et al., 1992
Chandler Formation	Amadeus Basin, Central Australia	Cambrian, Lower	Flexure	Petermann Range Orogeny	Bradshaw, 1991
Lower and upper Usolye Group	Turukhan - Irkutsk - Olekmin salt basin, SE Siberian Craton	Cambrian, Lower	Flexure		Ulmishek, 2001b
Bitter Springs Formation	Amadeus Basin, Central Australia	Neoproterozoic	Extension	Rift - Rodinia breakup	Lindsay, 1987; Southgate, 1991
Callana Formation	Adelaide Geosyncline, South Australia	Neoproterozoic	Extension	Rift - Rodinia breakup	Powell et al., 1994
Hormuz Formation	Arabian Basin, Middle East	Neoproterozoic	Extension	Rift Basin	Edgell, 1991; Husseini, 1989
Ara Salt, Oman	Fahud, Gaba and South Oman Salt Basins, Oman	Neoproterozoic	Extension or transtension	Rifts driven by Najd transfrom fault system	Schröder et al., 2000a; Sharland et al., 2001
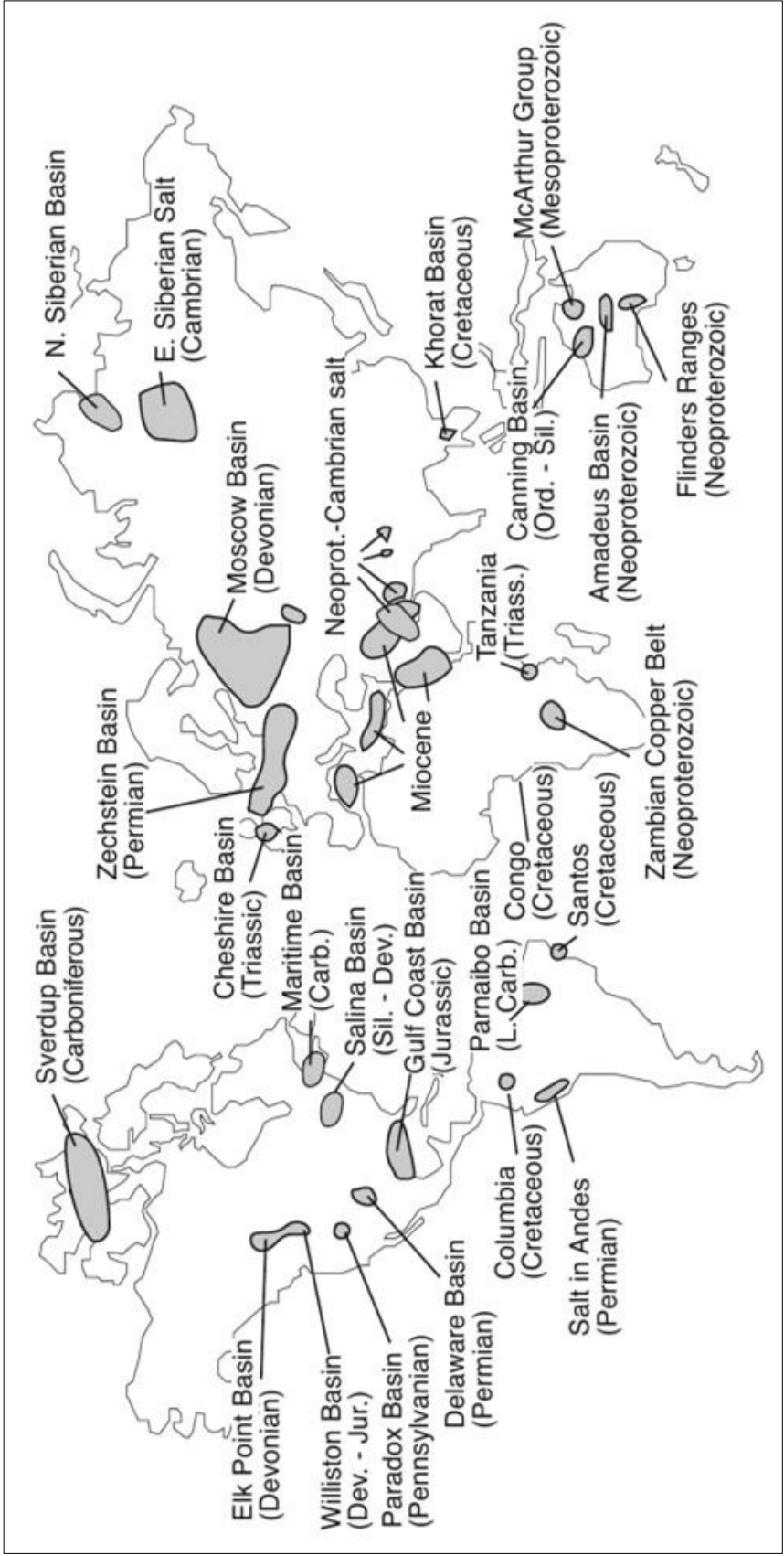
Figure 1.2 Major basinwide evaporite deposit locations during Proterozoic Eon to Mesozoic Era (from Warren, 2006).

1.2 Dissolution of gypsum and anhydrite

The dissolution of gypsum and anhydrite in the groundwater through groundwater flow both in jointed rock and porous granular material depends primarily upon two mineral properties. The first is the solubility of the mineral (Table 1.3), which is the amount which can be dissolved in a given quantity of solvent at equilibrium, and the second is the rate of solution of mineral, which is the speed at which it reaches the equilibrium concentration (Fell et al., 2005).

Table 1.3   Solubility in freshwater of various evaporate salts in comparison to the limestone (Warren 2006).

Mineral Name	Composition	Solubility in fresh water (moles/liter)	Solubility with respect to limestone
Calcite	$CaCO_3$	0.00014	1
Magnesite	$MgCO_3$	0.001	7.1
Gypsum	$CaSO_4 \cdot 2H_2O$	0.014	100
Nahcolite	$NaHCO_3$	1.22	8.7×10^3
Mirabilite	$Na_2SO_4 \cdot 10H_2O$	1.96	14.0×10^3
Natron	$Na_2CO_3 \cdot 10H_2O$	2.77	19.8×10^3
Epsomite	$MgSO_4 \cdot 7H_2O$	3.07	21.9×10^3
Thenardite	$NaSO_4$	3.45	24.6×10^3
Hexahydrite	$MgSO_4 \cdot 6H_2O$	4.15	29.6×10^3
Bischofite	$MgCl_4 \cdot 6H_2O$	5.84	41.7×10^3
Halite	$NaCl$	6.15	43.9×10^3
Antarcticite	$CaCl_2 \cdot 6H_2O$	7.38	52.7×10^3

From the solubility of each evaporite shown in Table 1.3 it can be seen that limestone dissolves slower than gypsum or halite, with a saturation concentration that varies according to pH and CO_2 levels, but typically in the range 50-400 ppm. Thus, when exposed to meteoric crossflows, gypsum is one to two orders of magnitude as soluble as limestone (Warren, 2006).

All natural water contains some dissolved salts and this can affect the solubility of other minerals. Saline and common ions strongly influence the solubility of gypsum. Salinity produces an increase in the solubility of gypsum such as the presence of NaCl in the solution may substantially enhance the solubility of gypsum.

However, if the dissolved ions in water contain more Ca^{2+} and/or SO_4^{2-} (the common ions) the solubility of gypsum decreases (Klimchouk, 1996; Elorza and Santolalla, 1998).

The rate of the dissolution processes depends on a chemical component and a hydrodynamic component. The chemical component relates to the equilibrium and kinetics of the dissolution reaction. The hydrodynamic component relates to the aqueous phase as a static or a moving medium, which influences the procedure and the rate of mass transfer from the solid phase to the liquid phase. If the water is static (not moving), the solute flux takes place by diffusion. If the water is moving, mass transfer in the moving water, termed convection, is added to the diffusion and increases the dissolution rate. From this, two types of dissolution systems can be differentiated. The first is the surface-reaction controlled system; this applies to low solubility compounds, in which the dissolution rate is essentially controlled by the dissolution reaction (the chemical component). The second is the transport-controlled system, which applies to high solubility compounds, in which the dissolution rate depends largely on the flow velocity and regime (the hydrodynamic component).

The gypsum dissolution rate is assumed to be controlled by diffusion transport (transport-controlled system) across a boundary layer (Klimchouk, 1996; Birk et al., 2005; Fell et al., 2005) and the dissolution rate follows a first order relationship:

$$\frac{dC}{dt} = KA(C_S - C) \qquad (1.1)$$

From this it can be seen that the rate of gypsum dissolution over time dC/dt is a function of, first, the degree of saturation of the solution C_S-C (C_S is the solubility of the material, C is the concentration of material in solution), second, the area A exposed to solution, and third the solution rate constant K for a unit area. This coefficient K is inversely proportional to the thickness of the diffusion layer and depends on the diffusion coefficient of gypsum in the diffusion layer (Elorza and Santolalla, 1998; Fell et al., 2005). The solution rate of anhydrite follows the second order (Klimchouk, 1996; Fell et al., 2005) with

$$\frac{dC}{dt} = KA(C_S - C)^2 \tag{1.2}$$

So, the rate of gypsum dissolution and the intensity of the karstification processes depend greatly on the flow velocity and the flow regime, whether it is laminar or turbulent (James and Lupton, 1978; White, 1988).

In the development of gypsum formations, the physical–chemical factors that control the dissolution process are directly related to a complex of interacting geological and environmental factors (Elorza and Santolalla, 1998). Geological factors are: lithological (texture, size and geometry of the crystals and/or particles, internal structure, porosity, presence of non soluble components), stratigraphical (thickness of the gypsum formations, intercalations of non soluble bodies, existence of halite beds, presence of adjacent aquifers), structural (structure of the gypsum formations, discontinuity planes joints, faults, stratification planes and their geometrical characteristics width, extension, density, orientation, tectonics), geomorphological (relief configuration, time of development) and hydrogeological cross flow rate in different environments (Figure 1.3), fissure flow, interstitial flow, flow in an adjacent aquifer, flow velocity, flow regime laminar or turbulent, residence time of the water in the karstic system, chemical composition of water, and water table fluctuations (Elorza and Santolalla, 1998).

The environmental factors mainly relate to climate, especially rainfall and temperature. The karstic systems developed in gypsum are very sensitive to climatic variations. The rapid evolution of gypsum karst also means that recent human activity can considerably influence the genesis of some gypsum karst features such as sinkhole formation (Elorza and Santolalla, 1998).
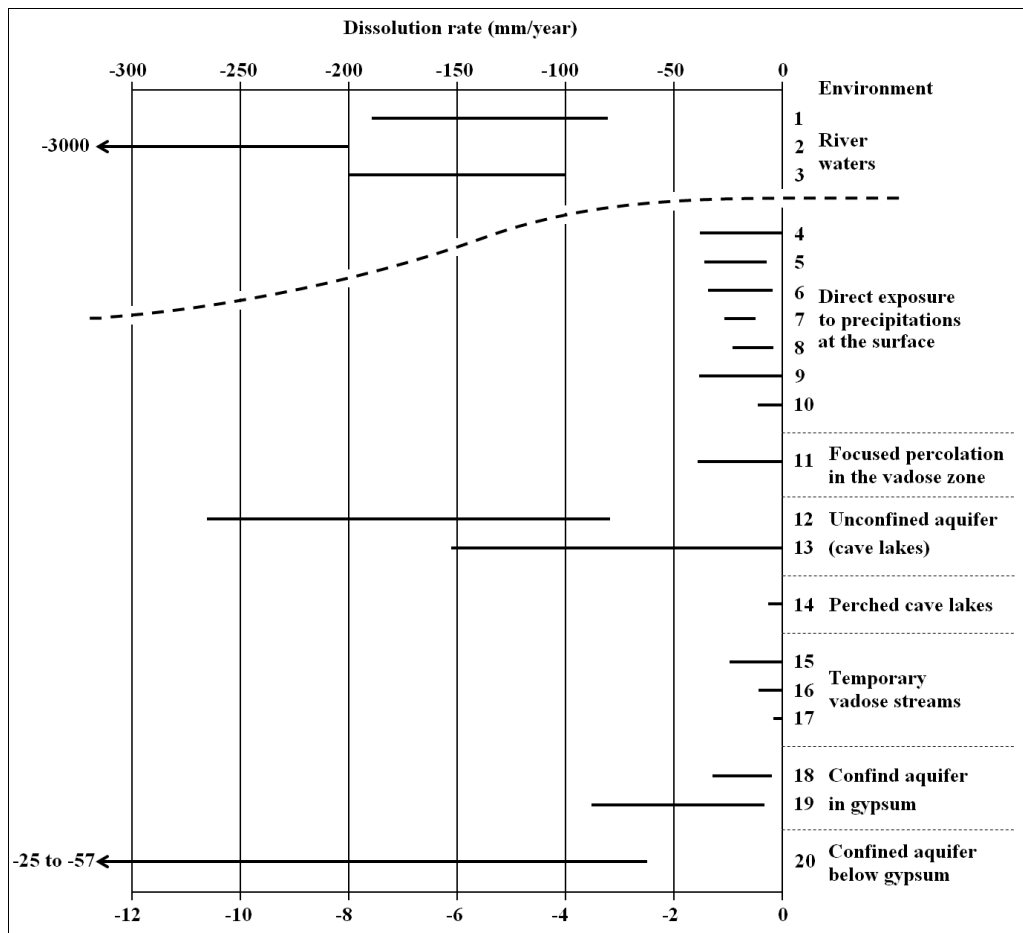
Figure 1.3 Solution rate of minerals depends on the flow velocity of each different natural environment (Klimchouk et al., 1996).

The main factors that control evaporite dissolution processes are discussed by Gutiérrez and Gutiérrez (1998), Klimchouk (2000), and Jeschke et al. (2001) There are five; first, the composition of the evaporites and any adjacent aquifers (lithology and mineralogy), second, the structure and texture of the soluble rocks and any adjacent aquifers, third, the amount of water flow in contact with the evaporites and its physico-chemical properties (including saturation index and temperature), forth, the flow regime and groundwater conditions (laminar or turbulent, phreatic or vadose), and fifth, the variations in the water table (or piezometric level).

Due to the fact that gypsum is easy to dissolve, it creates holes in the subsurface. This leads to a downward movement of the overlying material due to a lack of basal support (gravitational deformation). Finally it results in sinkhole formation. Two main sinkholes genetic classifications are presented by Gutierrez et

al. (2008) (Figure 1.4); first, sinkholes generated by the differential dissolutional lowering of the ground in areas where the evaporites are exposed at the surface, and the different types of sinkholes resulting from both subsurface dissolution and downward gravitational movement (internal erosion and deformation) of the overlying material. Second, the sinkholes generated over dissolutional voids by the upward propagation caused by collapse of the rock cavity roofs are designated as bedrock collapse or caprock collapse sinkholes (Gutierrez et al., 2008).
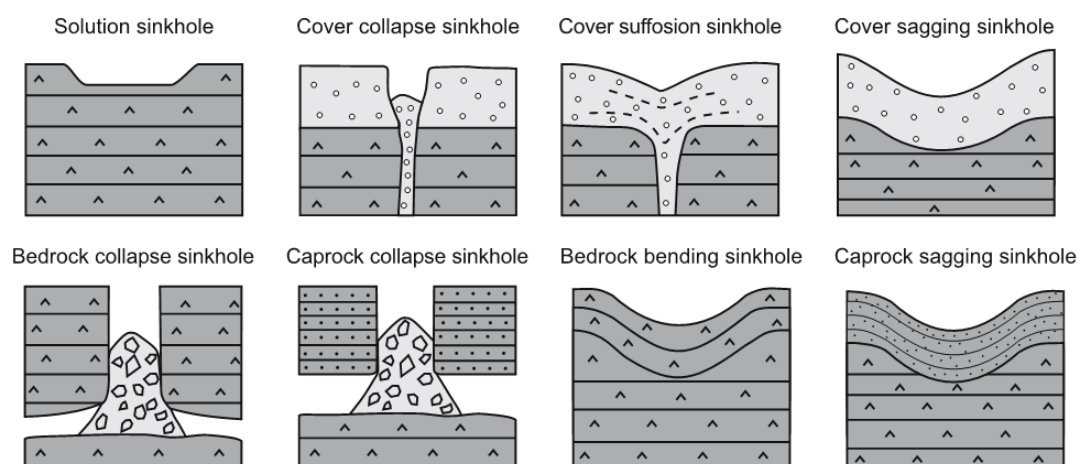
Figure 1.4   Genetic classification of sinkholes developed in evaporite karst areas (from Gutierrez et al., 2008).

In areas where the evaporitic bedrock is covered by an allogenic sediments or residual soils, sinkholes genesis can be separated into three groups (Figure 1.4); first, cover sagging sinkholes are caused by the differential lowering of the rockhead, which may lead to the gradual sagging of the overlying mantle. These are commonly shallow depressions that may reach several hundred meters in length. In this case, a thick karstic residue may form between the cover and the ''unweathered'' evaporitic bedrock. Second, cover suffosion sinkholes result from the downward migration of the cover through dissolutional voids (raveling) and its ductile settlement. A wide range of processes may be involved in the downward transport of the particles, including downwashing and viscous or cohesionless granular sediment gravity flow. These are commonly bowl shaped hollows, and their diameter can range from a few meters to tens of meters. Third cover collapse sinkholes form by the

collapse of soil arches resulting from the upward propagation of breakdown cavities developed through a cohesive and brittle cover above dissolutional voids (Gutierrez et al., 2008).

Cover collapse and cover suffusion sinkholes are the types with higher probabilities of occurrence. In most cases, human activities (see Table 1.4) increase in the sinkhole formation, which is related to change in the hydrology, such as in Ukraine, where dewatering of gypsum karst for sulfur mining has increased substantially the rate of gypsum dissolution and has favored the occurrence of sinkholes within the area affected by the cones of depression (Sprynskyy et al., 2009).

Table 1.4   Main changes in the evaporite karst environment that may trigger or accelerate the development of sinkholes (Gutierrez et al., 2008).

Type of change	effects	(1) Natural process (2) Human activities	
Increased water input to the ground (cover and bedrock)	Favors dissolution	(1)	Rainfall events, floods, snow melting, permafrost thawing
	Increases percolation accelerating suffusion Increases the weight of the sediments May reduce the mechanical strength of the sediments	(2)	Irrigation, leakages from utilities (pipes, canals, and ditches), impoundment of water, runoff concentration (urbanization, soakaways) or diversion, vegetation removal, unsealed wells, injection of fluids
Water table decline	Increase the effective of the sediments (lost of buoyant support)	(1)	Climate change, sea-level decline, entrenchment of drainage network
	Slow phreatic flow replaced by more rapid downward percolation favoring suffusion, especially when the water table is lowered below the rockhead May reduce the mechanical strength by desiccation	(2)	Water abstraction or de-watering for mining operations, decline of the water level in lakes (Dead Sea)
Impoundment of water	May create very high hydraulic gradients favoring dissolution and internal erosion processes	(1)	Natural lakes
	Imposes a load	(2)	Reservoirs, lagoon
Permafrost thawing	Favors dissolution	(1)	Climate change
	Significant reduction in the strength of the sediments	(2)	Development, deforestation
Static loads	Favors the failure of cavity roofs and compaction processes	(1) (2)	Aggradation processes Engineered structures, dumping, heavy vehicles
Dynamic loads	Favors the failure of cavity roofs and may cause liquefaction-fluidization processes involving a sharp reduction in the strength of soils.	(1) (2)	Earthquakes, explosive volcanic eruptions Artificial vibrations (blasting, explosions)
Thinning of the sediments over voids	Reduces the mechanical strength of cavity roofs	(1)	Erosion processes
	May concentrate runoff and created a local base level of groundwater flows	(2)	Excavations
Underground excavation	Disturb groundwater flows	(1)	Biogenic pipes
	May weaken sediments over voids	(2)	Mining, tunneling

Gravitational deformation of the ground during sinkhole development may cause severe damage to buildings and other man-made structures including roads, railways and dams even nuclear power stations. Subsidence phenomena caused by evaporite dissolution have a substantial detrimental effect on development in numerous regions of the world. The Spanish cities of Oviedo and Calatayud, which are situated on cavernous gypsum, have seen direct economic losses caused by single collapse events by affecting buildings in 1998 and 2003. Sinkholes may also cause the loss of human lives when they occur in a disastrous way. Thirty-four people have been killed by sudden collapses in the dolomite karst of the Far West Rand of South Africa. Several people have been swallowed and injured by sinkholes resulting from halite dissolution on the Dead Sea coast of Israel. Other sinkhole problems are related to hydrogeology and hydraulic structures. Sinkholes can act as water-inlets connected to high-transmissivity karstic aquifers and cave systems, making the impoundment of water in reservoirs difficult. They can facilitate the rapid pollution of groundwater, and in some places it might affect the safety of sensitive structures such as the radioactive waste repository in New Mexico. Moreover, these topographic depressions are frequently prone to flooding, either by the concentration of surface runoff or by groundwater flooding, when the water table rises above their ground level (Gutierrez et al., 2008).

1.3. Sinkhole investigations

The selection and application of mitigation measures aimed at reducing the sinkhole risk generally require the recognition of existing sinkholes (identification) and the delineation of the areas where future new sinkholes are likely to occur (prediction). It is also important to gather information on the size and frequency of the sinkhole events, and on the subsidence mechanisms and rates. Following main methods are used.

1.3.1 Airborne investigations

Aerial photographs are a very useful tool for identifying sinkholes. Their main limitation is that, depending on the scale and definition of the images, it may not be possible to pinpoint small or shallow sinkholes. The interpretations help to obtain minimum estimates of the probability of sinkhole occurrence and allow the analysis of distribution patterns of the subsidence phenomena. Low sun-angle photographs with conspicuous shadows can emphasize subtle topographic features and may be practical for the detection of sinkholes with poor geomorphic expression. Airborne laser scanning (Figure 1.5) is another useful application which also using for surface data to characterize sinkholes geometric detail in terms of size, shape, and depth (Filin et al., 2011).
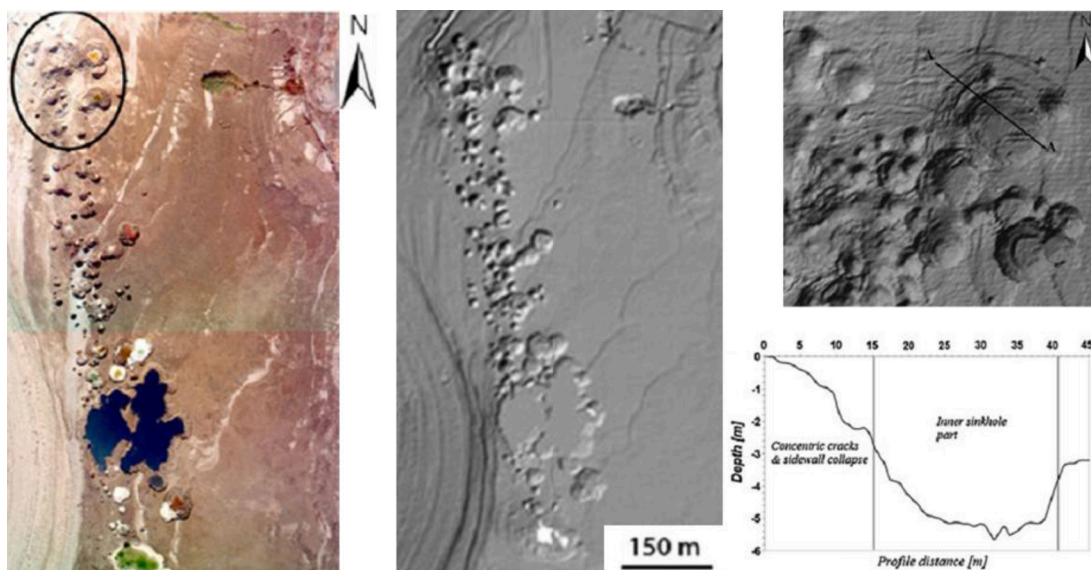
Figure 1.5   Sinkholes along Mineral Beach, Red Sea, with diverse characteristics in terms of size, shape, and depth which taken from low altitude aerial images (left) and airborne laser scanning data with a shaded relief map (middle) and extracted profiles showing height variations of these phenomena (right) (from Filin et al., 2011).

The contour lines of detailed topographic maps may depict subsidence depressions not detectable by means of field surveys and aerial photograph interpretations. Several geodetic techniques, like in SAR, GPS, photogrammetry, and

high-resolution digital elevation models (DEMs) may be applied to locate sinkholes and estimate subsidence rates accurate to a few millimeters per year (Gutiérrez, 2008).

Trenching provides an opportunity for detailed study of the stratigraphy and structure of the deposits, and when complemented with the application of absolute dating techniques, it is a very useful methodology for sinkhole investigation in mantled karst settings. This methodology may provide extensive practical information about several aspects, including; first, the nature of geophysical anomalies and topographic depressions that have an uncertain origin, second, the precise limits of filled and poorly defined sinkholes, third, the structure of the deposits (synclines, failure planes, and raveling zones) and an insight into the subsidence mechanisms and magnitude (cumulative displacement), forth, a retro-formation analysis of the deposits by means of the progressive restoration of the sedimentary bodies may allow the interpretation of multiple subsidence episodes, and fifth, absolute dating techniques, primarily radiocarbon and luminescence (OSL and TL) methods may be used to obtain mean subsidence rates and constrain the timing of the subsidence episodes. The inferred evolution of particular sinkholes from trenching may be used to forecast their future behavior. Closely allied with trenching, the stripping of topsoil or overburden can show the positions of subsidence features on a site during construction (Gutiérrez, 2008).

1.3.2 Geophysical investigations

Geophysical techniques can be used to identify the feature geometries by contrasts in the physical properties (Table 1.5), such as density, magnetic susceptibility, electrical resistivity and conductivity, which vary between the media in the subsurface such as limestone, gypsum, siltstone, clay, sand, air, water, etc. In the area where there are soluble rocks (gypsum, salt, limestone etc.) wash out by the groundwater flow might occur. This dissolution process cause changes in the properties and structure (forming cavities with air, water, or sediment refilled) of the subsurface material and tend to develop sinkholes.

Table 1.5   Main advantages and disadvantages of the most commonly used geophysical methods for the detection of cavities, subsidence structures, and buried sinkholes (Gutierrez et al., 2008).

Geophysical method (output)	Advantages	Disadvantages
Electrical resistivity (profiles showing the resistance of the ground to the passage of an electric current; the technique can also be used to construct maps and 3D tomographic surveys)	Not affected by vibrations and irregular topography	Interferences from utilities like buried electric lines and wire fences
	Can provide full 3D tomographic surveys, but depth of resolution decreases around the margins; depth of penetration up to about 40 m	Does not work on man-made surfaces like tarmac and concrete
		The soil moisture reduces the quality of the results
	Fast acquisition if done with automated computerized equipment	Slow acquisition of data if done manually
		Anomalies must be checked with intrusive methods
Electromagnetic conductivity—EM (maps showing the conductivity of the ground in plan view)	Rapid acquisition of data	Interferences from utilities, buildings, and metallic structures
	Not affected by vibrations and irregular topography	Limited depth of penetration
	Does not require sensors to be placed on the ground	Anomalies must be checked with intrusive methods
Ground penetrating radar—GPR (profiles showing reflectors that represent variations in the ground's electrical impedance)	Rapid acquisition of data	Limited depth of penetration
	Allows one to identify the geometry of dissolution and subsidence features	Penetration reduced by conductive materials (clay and water)
		Interferences from external electromagnetic fields
Microgravimetry (profiles or maps showing minute changes in the Earth's gravitational field)	May be used satisfactorily on man-made surfaces, near or within buildings and next to electrical sources	Slow and requires accurate surface leveling plus complex correction calculations
		Difficult in areas with significant topographic relief
		Anomalies must be checked with intrusive methods
		Small dissolution and subsidence features need to be at shallow depth
Cross-hole tomography (profiles or 3D images showing changes in the ground's seismic transparency or electrical resistivity)	May be used satisfactorily in developed areas	Requires pairs of boreholes
	May provide 3D images	Expensive when boreholes need to be drilled

To locate the hazardous areas of dissolution processes, subsidence structures are investigated by geophysical methods. Microgravity, magnetic and ground penetrating radar (GPR) surveys (Figure 1.6 and 1.7) (Batayneh et al., 2002; Tallini et al., 2006; Crespo and Ortiz, 2007) were applied for mapping the location and determining the size of cavities below the surface (Mochales et al., 2008). High-resolution seismic reflections have been used to characteristic sinkholes formed from the dissolution of a bedded salt (Figure 1.8, Miller et al., 2009). Seismic refraction was used to delineate the salt layer that is an essential condition for sinkhole occurrence (Ezersky, 2006). An electrical resistivity tomography (ERT) study was carried out to understand the subsurface geoelectrical structure at a sinkhole development area (Ezersky, 2008).
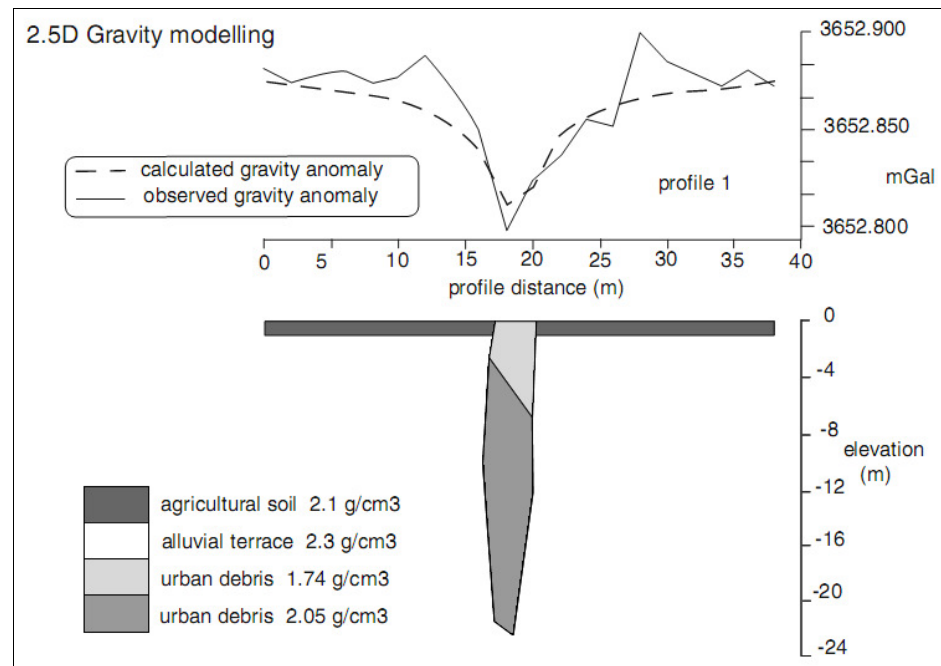
Figure 1.6   An example of a gravimetric modeling cross section of the gravity anomalies of the funnel-shaped sinkhole which filled with two difference densities (Mochales et al., 2008).
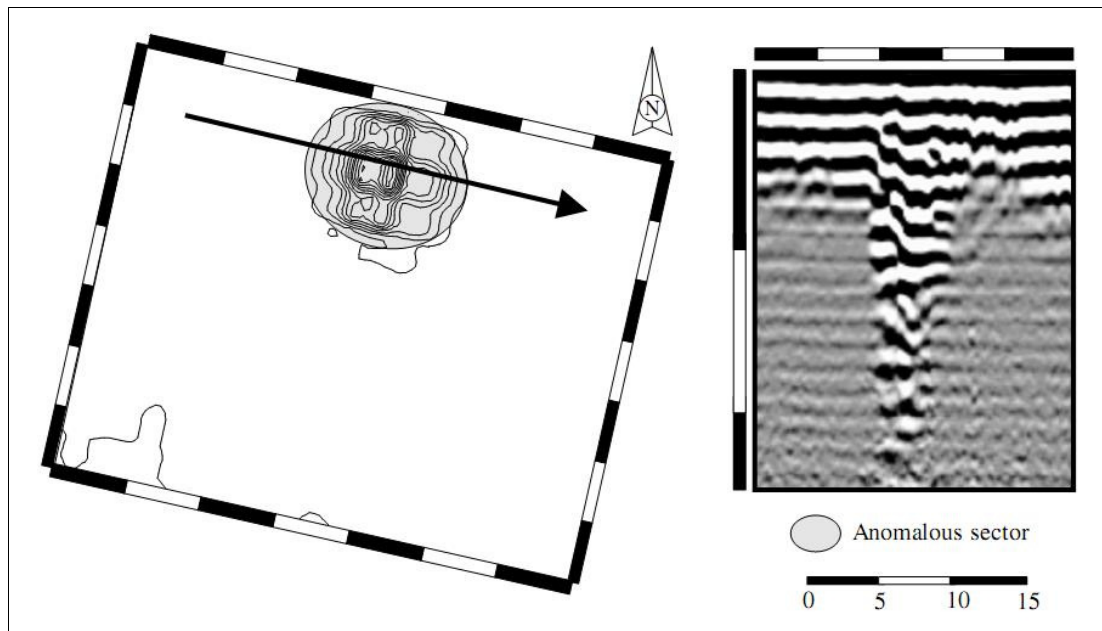
Figure 1.7   An example of a GPR-profile showing homogeneous wave behavior on the main collapse, which is characterized by the presence of high conductivity elements (Mochales et al., 2008).
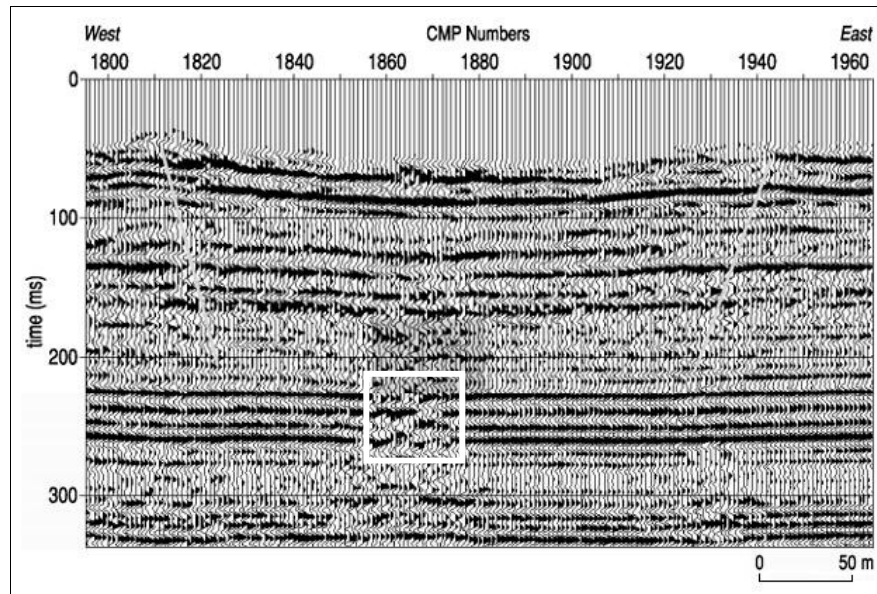
Figure 1.8 An example of seismic reflection interpretation of the dissolution feature in the subsurface (white box) with discontinuing reflectors (Miller et al., 2009).

1.3.3 Hydrogeophysical investigations

Hydrogeology is another importance aspect of sinkhole hazard analysis. The groundwater flow is the geological agent responsible for the karstification of evaporite rocks and commonly one of the most important conditioning and triggering factors involved in the generation of sinkholes (Gutierrez et al., 2008). A relevant factor that may significantly influence sinkhole development is the position of the water table (or piezometric level) with respect to the rock head. The groundwater flow velocity and flow path are also important. Self-potential method is very useful technique in hydrological investigation which has been use to study groundwater movement and flow path (Fournier, 1989) to map sinkholes and evaluate the risk of potential collapses (Figure 1.9) in karst areas (Wanfang et al., 1999). An efficient techniques for characterizing the aquifer in the sinkhole development area (Figure 1.10) is the magnetic resonance sounding (MRS) method and transient electromagnetic (TEM) method was used to locate the interface of difference bulk resistivity (fresh water and contaminated water or saline water) (Figure 1.11) of the studied medium, especially in the range of low resistivity (Ezersky et al., 2009). The high-resolution seismic method and 2-D electrical imaging

were used also to mapping a hydrogeological model in karst areas environments (Sumanovac and Weisser, 2001).
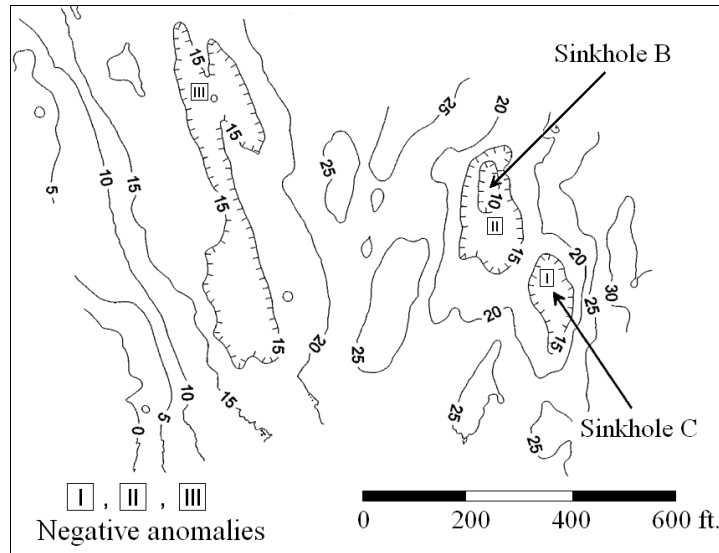
Figure 1.9   An example of streaming potential anomalies map related to sinkhole investigation using self-potential method (Wanfang et al., 1999).
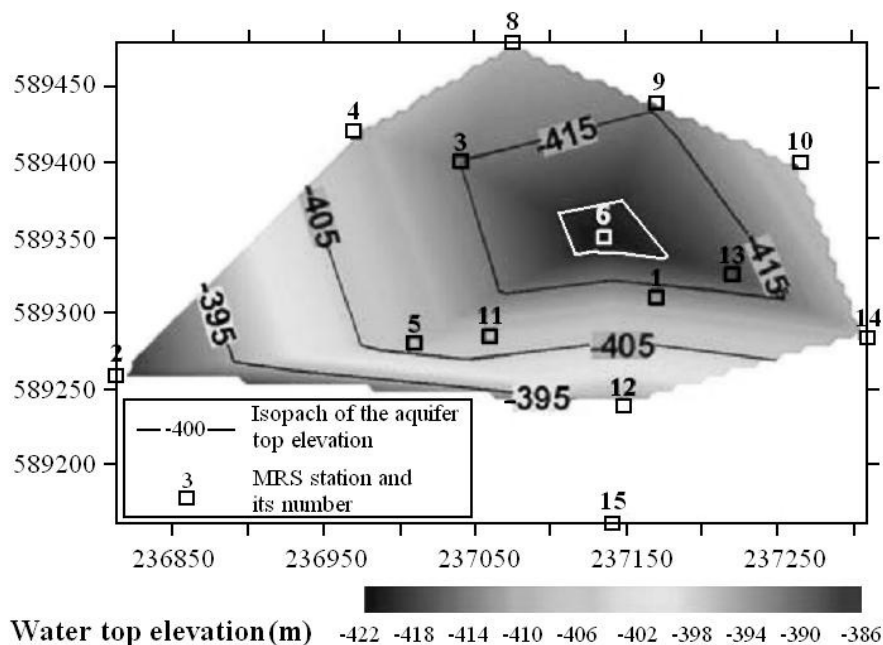
Figure 1.10   An example of the 2D map of MRS results characterizing the topography of the top of the water table which can indicate that water flow into the main cavern (at MRS6 station) (Ezersky et al., 2009).
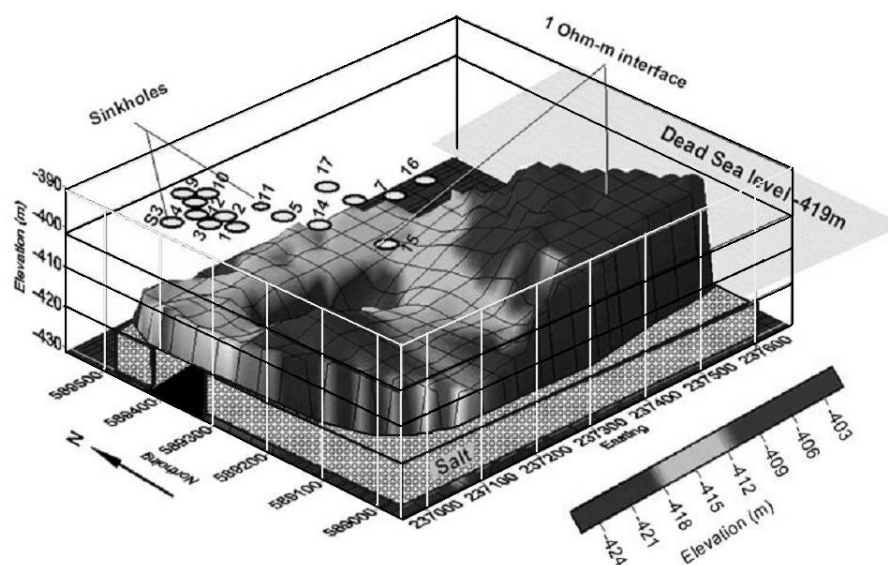
Figure 1.11   An example of the 3D topography based on TEM results. The lower 1 Ω-m interface in the subsurface showing the large funnel-shaped hole with approximately 200 m in diameter and most of sinkholes are located in the vicinity of this hole (Ezersky et al., 2009).

The hydrochemistry of groundwater and the saturation index with respect to the main gypsum minerals, sulfate ions in the groundwater, can be used as an indicator of hydraulic communication between flow system components, flow direction and intensity, in order to understand flowing patterns and groundwater behavior (Klimchouk and Aksem, 2005) that by this is how aggressive and how fast dissolution will proceed (Table 1.6).

Table 1.6   Gypsum solution rate data in difference situation of the Western Ukraine study site for the purposes of calibration, adjustment and verification of speleogenetic and karst development models (Klimchouk and Aksem, 2005).

Settings and situations of the gypsum aquifer	Relative general circulation intensity	Characteristic range of SO_4 contents (g/dm^3)	Approximate SR (mm/year) (order of magnitude)
Unconfined settings, bulk water body	Sluggish		
Confined settings, undisturbed situation	Sluggish	1.1–1.4	0.1
Unconfined settings, the upper layer of water body	Moderate		
Confined settings, disturbed situation	Moderate	0.8–1.2	1.0
Unconfined settings, the upper layer of water body	Active		
Confined settings, the water entering the gypsum from the lower aquifer (buoyant currents within the bulk water body, rising from the feeding channels)	Active	0.4–0.8	10.0

1.3.4 Sinkhole hazard analysis

Several strategies may be applied to address the spatial prediction of sinkholes. A commonly used approach is the delineation of the a priori more susceptible areas to sinkhole events by an expert, based on geological criteria and the known information on the spatial and temporal distribution of previous sinkholes. Some aspects related to the spatial distribution and geometry of the sinkholes may be used to produce or refine the susceptibility maps.
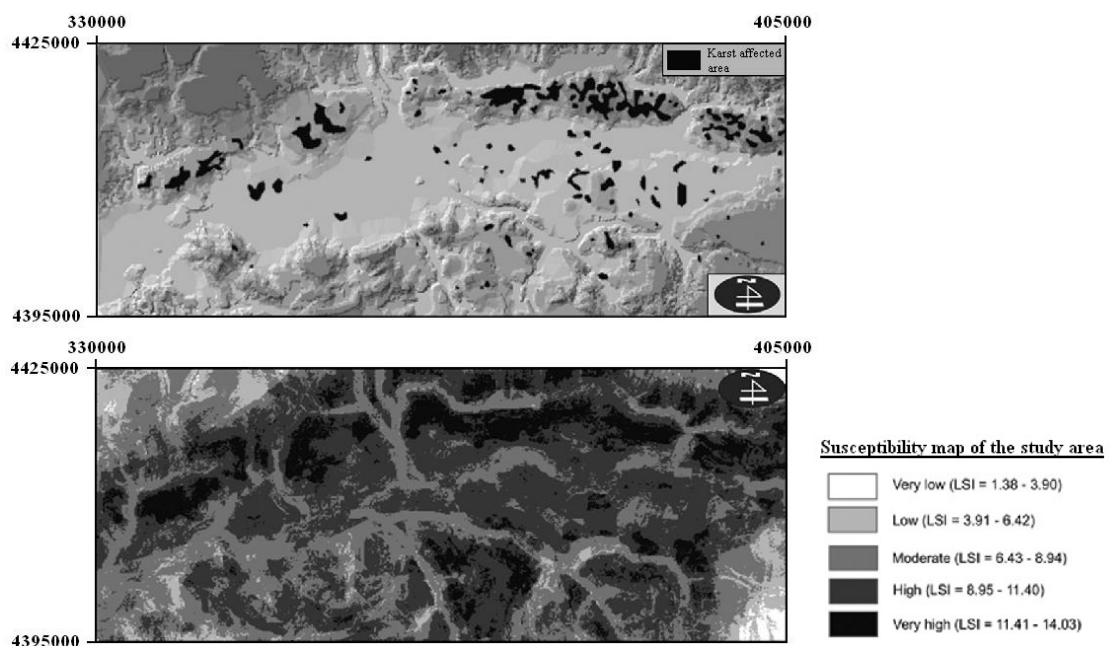
Figure 1.12   Collapse susceptibility map using GIS. The database of distribution of the collapse, lithology, drainage system, structural lineaments (such as faults and folds), morphology (slopes, elevation), springs and vegetation cover was compiled by field, air photo and satellite image studies and digitized (Yilmaz, 2007).

A geographic information system (GIS) was used to prepare of collapse susceptibility maps (Figure 1.12) will serve to successful urban planning in karst terrains. Susceptibility of collapses and the effects of collapse-related factors, such as geological and hydrological (lithology, tectonic activity, drainage systems, springs), topographical (slope angle, slope aspect, elevation), land-use (distance from roads and settlement areas) and vegetation cover were evaluated (Yilmaz, 2007).

1.4 Objective

Unexpected sinkholes occurred in a rubber tree plantation area in Tayang Subdistrict, Tungyai District, Nakhon Si Tammarat Province in 2005 and 2009. The depth and size of the subsidences made villagers worry about the cause of their development. The geology in the area where the sinkhole occurred showed the occurrence of gypsum and anhydrite. Because of their easier and higher solubility than limestone in groundwater, the primary hypothesis was the cavities were formed by gypsum/anhydrite dissolution through groundwater flow in the subsurface and then subsequently caused the sinkhole development. Despite the general understanding of sinkhole development the real processes leading to the sinkhole development in this area were not clear and fully understood. Therefore further investigations were needed to understand the scope of the sinkhole risk in the area.

Geophysical techniques consisting of resistivity, seismic refraction and reflection and self-potential method as well as geological approaches were applied in the sinkhole area to reveal the geological structures, the groundwater flow and its behavior, and the dissolution mechanisms of the local gypsum/anhydrite formation. Additionally, a hydrogeology and geochemistry study was carried out in the area. These integrated investigations applying different methods aimed to understand the actual mechanisms of the sinkholes development. Results of this study then might be used to delineate potential hazardous areas and by this mitigate any further impact of future sinkhole developments.

CHAPTER 2

RESEARCH METHODOLOGY

2.1. Study area

Geophysical methods were applied to understand geological, hydrological, and chemical property of the groundwater correlating to sinkhole occurrence in the area of Tha Yang Subdistrict, Tung Yai District, Nakhon Si Thammarat Province, the southern part of Thailand (Figure 2.1). The study area was in the area where sinkholes happened and close to the gypsum mine which its trend is along north to south with uncontinuities (Figure 2.2).
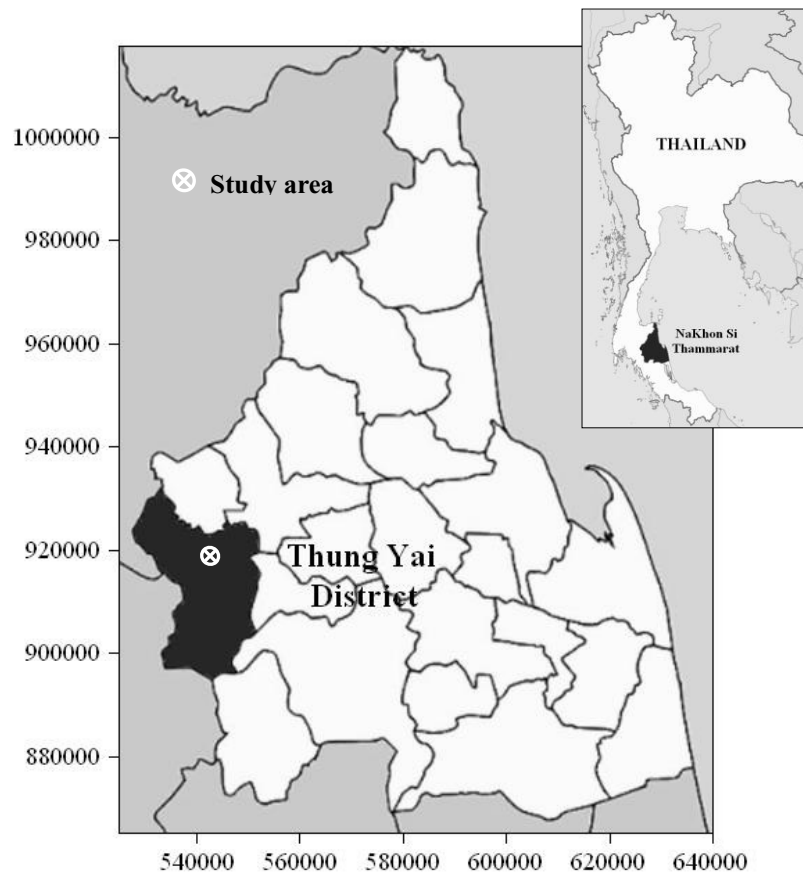
Figure 2.1   Map of Nakhon Si Thammarat Province with the location of study area in Thung Yai District (from Wikipedia, 2011).
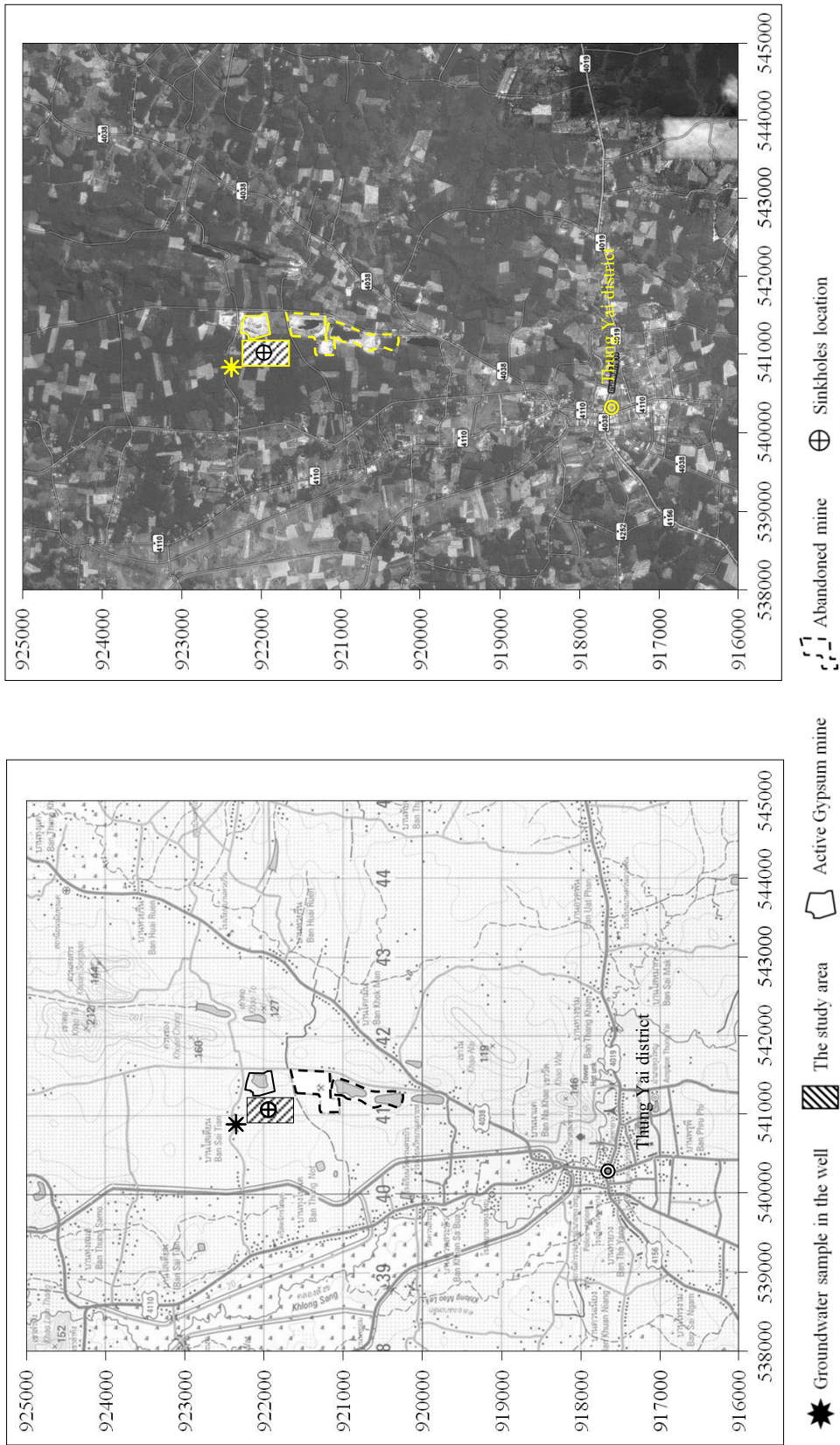
Figure 2.2   Location of study area where sinkholes occurrence near the area of the gypsum mine in Tha Yang Subdistrict, Thung Yai District (from maps.google).

2.2   Geological survey

Before geophysical investigations were carried out in the study area, it was important to understand the geological structure, lithology and hydrogeology around the study area in order to appropriately applying the geophysical methods. An initial survey was done in early January 2005 shortly after the main, first sinkhole was reported, however, it was not part of this study. On 20 June 2009, a second field trip and part of this study was carried out in order to see the general geology in the surrounding area and to collect samples, including anhydrite and gypsum with different textural features, from the mining and surrounding area for further geological characterization and determination of the physical properties.

2.3   Density determination of rock samples

In general, densities of crustal rocks vary from 1.2 to 3.5 g/cm^3 (see Table 2.1), with the principal factors that affect rock density are the mineralogical composition of the rock (chemical composition of the principal rock forming minerals), the structure and texture of the rock (mainly porosity), the degree of its diagenesis and metamorphism. Age and geological position also have a considerable influence on the density of the rock. The same rock may display difference densities, deviating by 5 to 20% from the average value, at difference locations (Mares, 1984).

The nature of the porosity of porous media (sediments and all rocks in general) is that it is the single most important factor to determining the storage and movement of groundwater in the subsurface. It is also the important parameter that has an effect on the interpretation of geophysical data (Wyllie et al., 1958; Bachrach and Mukerji, 2004). To estimate the porosity of a rock sample, the measurement of its density is the most straightforward approach with linear relation between density ρ and porosity ϕ as shown below.

$$\phi = \left(1 - \frac{\rho_b}{\rho_s}\right) \times 100\% \tag{2.1}$$

where ρ_b is the bulk density and ρ_s is the matrix density of the rock. Rock density is basically the ratio of the mass of rock sample to its volume. Rock usually consists of two phases that is solid (mineral particle/grain), fluid or gaseous phase (pore filling). Therefore, the rock density ρ is the ratio of the mass m of the whole phase under natural conditions of its volume V as

$$\rho = \frac{m}{V} \qquad (2.2)$$

while the bulk density ρ_b considering of dry-rock condition which is defined as the ratio of the mass of the solid phase m_s to the volume of the whole body V

$$\rho_b = \frac{m_s}{V} \qquad (2.3)$$

and the matrix density (density of the solid phase) of the rock ρ_s is determined by the ratio of the mass of solid phase m_s to its volume V_s

$$\rho_s = \frac{m_s}{V_s} \qquad (2.4)$$

The porosity of the rock ϕ can also defined by the ratio of the volume of its pores V_p to the total volume of the body

$$\phi = \frac{V_p}{V} \times 100\% \qquad (2.5)$$

The matrix density of the rock depends only on the mineralogical composition of the solid phase. As in non-porous (porosity less then 1%) rocks the bulk and matrix density are the same the rock density can be inferred from the volume density by introducing a correction for the water content in the rock pores.

Table 2.1   Porosities and densities for different geological materials (Bell, 1998).

	Matrix density (g/cm^3)	Bulk density (g/cm^3)	Porosity (%)
Granite	2.67		
Basalt	2.91		
Fell sandstone	2.69	2.25	9.8
Sherwood sandstone	2.68	1.87	25.7
Carboniferous	2.71	2.58	2.9
Anhydrite	2.93	2.82	2.9
Gypsum	2.36	2.19	4.6

For this study, eight rock samples were collected from the gypsum mine for a rock description and determining the density by applying the Archimedes Principle. According to it, an object immersed in a fluid is buoyed up by a force equal to the weight of the fluid displaced by the object (McCormick, 1969). This causes the object weight in the water less than it weight in air. Then the weight difference is equal to the buoyed force, which is related to object volume as shown in Equation 2.6 below.

$$F = \rho_w V g = m_{air} - m_{water}$$
(2.6)

where F is the buoyant force in Newton, ρ_w is density of fluid, here 0.996 g/cm^3, V is the object volume in cm^3, m_{air} is the object weight in air in grams and m_{water} is the object weighing in water in grams.

Therefore, the bulk density was known from Equation 2.7 when the object volume was determined.

$$\rho = \frac{m_{air}}{V}$$
(2.7)

where ρ is the object density and m_{air} is the object weight in air.

The density of the rock sample was determined as following: First, measuring the weight of dry-cleaned rock samples in the air. For some weathered rock sample acrylic polymer glue was used to cover the rock's surface (covered-rock)

before measuring in the water for preventing water-erosion and the infiltration of water in the dried pores. Then, measuring the weight of covered-rock in the water and then peeling off the glue which was measured it weight in the water, too. After that, subtract the weight of the glue in the water from the weight of the covered-rock in the water (m_{water}). Finally, the density rock was calculated according to Equation 2.8:

$$\rho = \frac{m_{air}}{\left(m_{air} - m_{water}\right)} \times \rho_w \qquad (2.8)$$

where ρ is density of rock sample in g/cm^3, ρ_w is density of fresh water, w_{air} is a rock sample weight in air in grams and w_w is a rock sample weight in water in grams.

2.4 Powder X-ray diffraction technique.

Rocks, sediments, and precipitates are examples of geologic materials that are composed of minerals. Powder X-ray diffraction is one of the most powerful technique to identify minerals, as well as other crystalline compounds. As the name suggests, the sample is usually in a powdery form, consisting of fine grains of single crystalline material to be studied. The information obtained includes types and nature of crystalline phases present, structural make-up of phases, degree of crystallinity, amount of amorphous content, microstrain and size and orientation of crystallites. By these, it can determine the proportion of the different minerals present, possible deviations of the minerals from their ideal compositions, the structural state of the minerals and the degree of hydration for minerals that contain water in their structure (Pecharsky and Zavalij, 2009).

X-rays are electromagnetic waves with a wavelength in the range of interatomic distances (0.1-10 Å). This match of length scales makes them suitable for the study of crystalline materials. For single-phase materials the atomic structure of crystalline substances can be obtained directly using X-Ray diffraction (XRD). With the help of a database of known structures XRD can be used for phase identification. (He, 2011)

The example of three-dimensional structure of non amorphous materials, such as minerals, is defined by regular, repeating planes of atoms that form a crystal lattice (see Figure 2.3). When a focused X-ray beam interacts with these planes of atoms, part of the beam is transmitted, part is absorbed by the sample, part is refracted and scattered, and part is diffracted (see Figure 2.3). X-rays are diffracted by each mineral differently, depending on what atoms make up the crystal lattice and how these atoms are arranged. (Ulery and Drees, 2008)
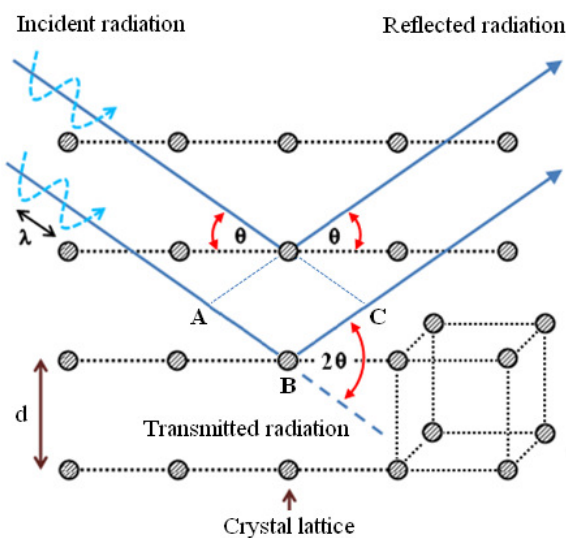
Figure 2.3   Schematic representation of X-rays diffraction by regularly spaced planes of atoms in a crystalline material (modified from Ulery and Drees, 2008).

The relation by which diffraction occurs is known as the Bragg's law

$$n\lambda = 2d \sin\theta \qquad (2.9)$$

where λ is X-ray wavelength, d is distance between lattice planes, θ is angle of incidence with lattice plane, n is integer representing the order of the diffraction peak. Bragg's law will be satisfied when the pathlength difference of the X-rays is AB+BC (see Figure 2.3) equal to $n\lambda$ (Ulery and Drees, 2008).

The d-spacing can be determined in XRD analysis by fixing λ and measuring the θ angle where a peak in X-ray intensity occurs. Such measurements can

be made for a single crystal, for a mineral in powder form, or for a mixture of minerals in powder form. Information gained from diffraction angles and relative peak intensities for pure minerals can be used to establish structural details of those minerals as the patterns for over 80,000 data entries in the International Powder Diffraction File (PDF) database, complied by the Joint Committee for Powder Diffraction Standards (JCPDS). By this method, identification of any crystalline compounds, even in a complex sample, can be made (Ulery and Drees, 2008).

2.5 Hydrogeology survey

Groundwater in the saturated zone is always in motion from higher to lower hydraulic head (Smith and Poehls, 2009). It moves slowly (dm/year to cm/day) (Weight, 2008) and this flow takes place in a three-dimensional space. The three main quantities that govern the flow of groundwater are as follows; hydraulic gradient, which is the driving force, hydraulic conductivity, which describes both the transmissive properties of porous media and the hydraulic properties of the flowing fluid (water), and the cross section area of flow. Their relationship is described by Darcy's law (e.g. Kresic, 2008)

$$Q = KA\frac{\Delta h}{L} \tag{2.10}$$

This linear law states that the rate of fluid flow (Q: m^3/s) through porous medium is directly proportional to the cross-sectional area of flow (A: m) and the loss of hydraulic head between two points of measurement (Δh: m) and it is inversely proportional to the distance between these two points of measurement. K is the proportionally constant of the law called hydraulic conductivity and has units of velocity. This constant is the most important quantitative parameter characterizing the flow of groundwater. Table 2.2 shows the range of hydraulic conductivity for difference geological material.

Table 2.2   Range of hydraulic conductivity for difference geological materials (Hiscock, 2005).

	Hydraulic conductivity, K (m/s)	Porosity (part of 1)
Fluvial deposits (alluvium)	10^{-5}-10^{-2}	0.05-0.35
Glacial deposits		
Basal till	10^{-11}-10^{-6}	0.3-0.35
Lacustrine silt and clay	10^{-13}-10^{-9}	0.35-0.70
Outwash sand and gravel	10^{-7}-10^{-3}	0.25-0.50
Loess	10^{-11}-10^{-5}	0.35-0.50
Sandstone	10^{-10}-10^{-5}	0.05-0.35
Shales		
Unfractured	10^{-13}-10^{-9}	0-0.1
Fractured	10^{-9}-10^{-5}	0.05-0.50
Mudstone	10^{-12}-10^{-10}	0.35-0.45
Dolomite	10^{-9}-10^{-5}	0.001-0.2
Oolitic limestone	10^{-7}-10^{-6}	0.01-0.25
Chalk		
Primary	10^{-8}-10^{-5}	0.15-0.45
Secondary	10^{-5}-10^{-3}	0.005-0.02
Coral limestone	10^{-3}-10^{-1}	0.3-0.5
Karstified limestone	10^{-6}-1	0.05-0.5
Mable, fractured	10^{-8}-10^{-5}	0.001-0.02
Volcanic tuff	10^{-7}-10^{-5}	0.15-0.4
Basaltic lava	10^{-13}-10^{-2}	0-0.25
Igneous and metamorphic rocks:		
Unfractured and fractured	10^{-13}-10^{-5}	0-0.1

Following equation is another common form of the Darcy's equation (Kresic, 2008):

$$v = K \frac{\Delta h}{L} = Ki$$

(2.11)

where v is the so-call Darcy's velocity and i is the hydraulic gradient.
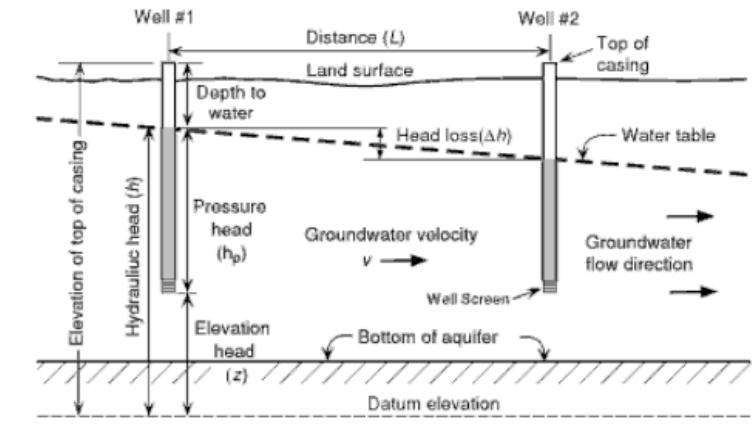
Figure 2.4   Scenario of key elements for determining the hydraulic head and the hydraulic gradient in unconfined aquifer (from Kresic, 2008).

Figure 2.4 shows the key elements for the determination of the hydraulic head. At the bottom of monitoring well #1 where the well screen is open to the saturated zone, the total energy (*H*) or the driving force for water flow at that point in the aquifer is

$$H = z + h_p + \frac{v^2}{2g}$$

(2.11)

where *z* is elevation above datum (datum is usually mean sea level), h_p is pressure head due to the pressure of fluid (groundwater) above that point, *v* is groundwater velocity and *g* is acceleration of gravity.

The groundwater velocity in most cases is very low so the third factor on the right-hand side may be ignored, then (Kresic, 2008)

$$H = h = z + h_p$$

(2.13)

where *h* is hydraulic head also called piezometric level.

In an unconfined aquifer, the water pump from the well is obtained by lowering the water table and draining the volume of rock or sediment just above the water table. Pumping water from the well creates a lower than normal water level surface in vicinity of the well, this is known as the cone of depression (Figure 2.5).

Transmissivity or hydraulic conductivity has an important effect on the cone of depression. In an aquifer with low transmissivity, the cone of depression is deep but of limited extent. In an aquifer with high transmissivity, the cone of depression is much shallower, but its boundaries extend much farther out from the well (Harter, 2008).
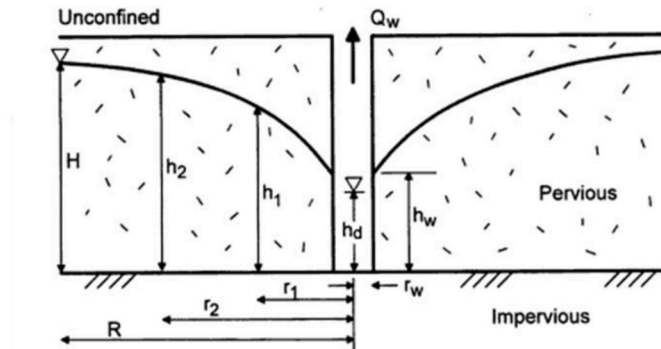
Figure 2.5   Elements of groundwater flow toward penetrating well in unconfined aquifer (Rowe, 2001).

Considering a simple case of steady-state radial groundwater flows toward a fully penetrating pumping well in a homogeneous unconfined aquifer (Figure 2.5), the rate of groundwater flow can be calculated as

$$Q_w = \frac{\pi K(H^2 - h_1^2)}{\ln(R/r_1)}$$

(2.14)

where Q_w is well pumping rate, K is hydraulic conductivity, H is the initial hydraulic head, h_w is hydraulic head in the well, $h_{1,2}$ is hydraulic head at distance $r_{1,2}$ and R, r_w, r_1, r_2 is radius of well influence.

2.6 Geophysical survey plan

Several geophysical methods were employed in this study, from vertical electrical sounding measurements, over a seismic refraction and reflection survey, to a self-potential survey. Figure 2.6 provides a map of the surveys carried out.
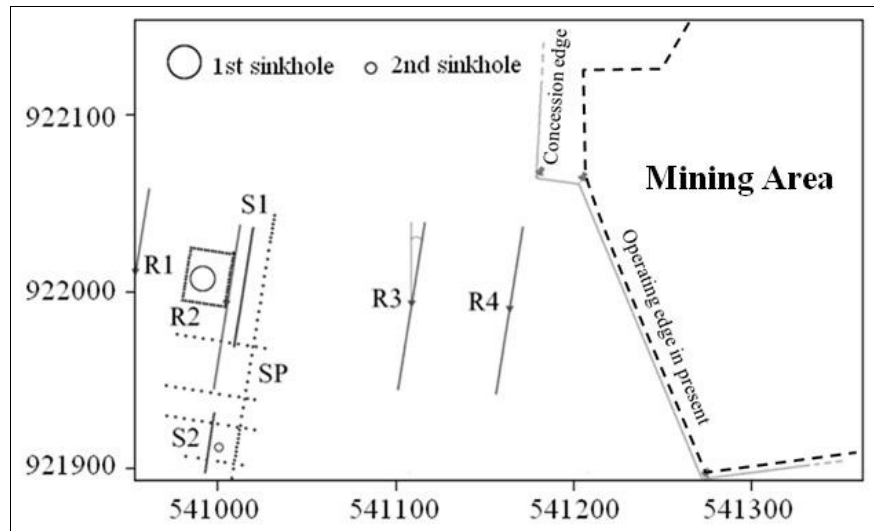
Figure 2.6   Geophysical survey plan of the study area.

2.7 Resistivity method

The electrical resistivity (in unit Ohm-m) of a homogeneous cylindrical solid of length L in meters and cross section area A in square meters, having resistance R in ohms between the end faces, is given by

$$\rho = \frac{RA}{L} \tag{2.15}$$

The resistance R in ohms is given in term of the voltage V in volts applied across the ends of the cylinder and the resultant current I in amperes flowing through it, by Ohm's law:

$$R = \frac{V}{I} \tag{2.16}$$

On the non–homogeneous earth the measured electrical anomalies depend up on the resistivity difference between difference rocks (Table 2.3). The variation in the resistivity of earth materials in the subsurface, especially important in porous sediments and sedimentary rocks, is strongly influenced by the presence of groundwater, which acts as an electrolyte. The minerals that form the matrix of a rock

are generally poorer conductors than groundwater, so the resistivity of sediment decreases with the amount of groundwater it contain and the type of dissolved minerals and it concentration of the groundwater in the interconnected pore(Lowrie, 2007; Telford et al., 1990; Parasnis, 1997). The resistivity of a saturated porous rock can be expressed by Archie's law (Telford et al., 1990) as below

$$\rho = a\phi^{-m} S_w^{-n} \rho_w \qquad (2.17)$$

where ϕ is the fraction pore volume (porosity), S_w is the fraction of pores containing water, ρ_w is the resistivity of water, $n \approx 2$, and a, m are constants, $0.5 \leq a \leq 2.5$, 1.3 (poor, unconsolidated) $\leq m \leq 2.5$ (good, cemented or crystalline).

Table 2.3   Resistivity of common rocks and ore minerals (Milsom, 2003).

	Resistivity (ohm-meters)
Common rocks	
Topsoil	50-100
Loose sand	500-5,000
Gravel	100-600
Clay	1-100
Weathered bedrock	100-1,000
Sandstone	200-8,000
Limestone	500-10,000
Gabbro	100-500,000
Basalt	200-100,000
Graphitic schist	10-500
Slates	500-500,000
Quartzite	500-800,000
Ore mineral	
Pyrite (ores)	0.01-100
Pyrrhotite	0.001-0.01
Chalcopyrite	0.005-0.1
Galena	0.001-100
Magnitite	0.01-1,000
Cassiterite	0.001-10,000
Hematite	0.01-1,000,000

The basics of an electrical resistivity survey is to introduce a known current into the ground through two current electrodes (A, B in Figure 2.7) and measure the potential differences on the surface with two potential electrodes (M, N in Figure 2.7) to estimate the resistivity of the subsurface. Then obtaining the apparent resistivity of current electrode spacing can be calculated from the resistance as equation below

$$\rho_a = k \frac{\Delta V}{I}$$

(2.18)

where ρ_a is the apparent resistivity (Ohm-m), $\Delta V/I$ is resistance, k is geometric factor which depend on the arrangement of four electrodes. For Schlumberger configuration (Figure 2.6) the geometric factor is define as below

$$k = \frac{\pi(L^2 - l^2)}{2l} \approx \frac{\pi L^2}{2l}$$

(2.19)

where L is the half separation between the current electrodes (A, B in Figure 2.7) measured in meters and l is the half separation between the potential electrodes (M, N in Figure 2.7) in meters.
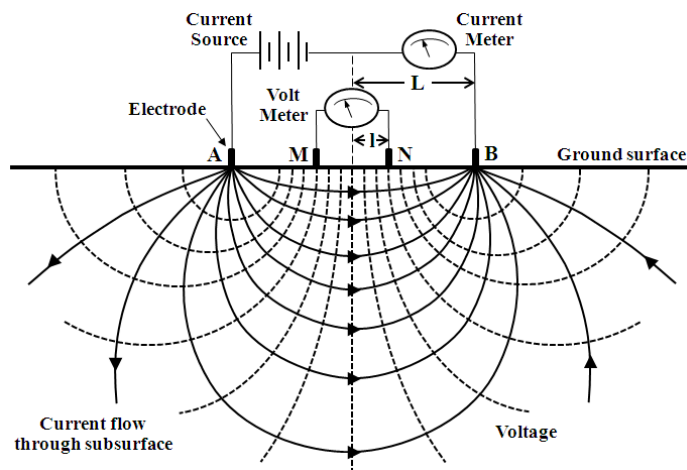
Figure 2.7   Equipotential and current flow lines of Schlumberger configuration on surface of homogeneous ground (Robinson and Thagesen, 2004).

The vertical electrical sounding (VES) procedure is used to determine the variation of electrical conductivity with depth by increasing the distance between the current electrodes, the current will proportionally deeper and apparent resistivity will be influenced by the electrical properties of greater depth.

2.7.1 VES data acquisition and processing

Four vertical electrical sounding points were considered to measure in an E-W line from the mine to the sinkhole area in order to establish the subsurface geoelectric structure. Each measurement line has AB/2 maximum 250 m of R4 point and 350 m of R1-R3 point were applied. The resistance values were measured by ABEM Terrameter SAS1000 with an increased current electrode spacing (see Appendix E, Table E.6) of Schlumberger configurations. The apparent resistivity values were plotted against the current electrode spacing in a log/log scale. These results are sounding curve which is the base of all data inversion to obtain the resistivity and depth of the subsurface structure by using IPI2WIN version 3.0.1a (Bobachev et al., 2003).

2.8 Seismic methods

The seismic methods utilize the propagation of elastic wave through the subsurface in the earth because differences in elastic properties of rocks cause the differences in the propagation in the subsurface. The elastic properties of each substance are characterized by elastic constants, which are specified by the relation between the stress and the strain. The main two elastic constants for studying elastic wave propagation in the earth are the bulk modulus (κ) and the shear modulus (μ).

There are two groups of seismic waves, surface waves and body waves, with the latter ones being utilized in seismic surveys. The velocity of propagation of body waves in any substance can be determined as a function of the density (ρ) and the elastic constants of the earth material. Compressional waves (the longitudinal, primary or P-wave) propagate in the medium in the same direction as the direction of wave propagation, its velocity is given by

$$V_P = \left[\left(k + \tfrac{4}{3}\mu\right)/\rho\right]^{\tfrac{1}{2}} \tag{2.20}$$

Shear waves (transverse, secondary or *S*-wave) propagate in the medium in the direction perpendicular to the direction of wave travel, its velocity is given by

$$V_S = \left(\mu/\rho\right)^{\tfrac{1}{2}} \tag{2.21}$$

Compressional waves always travel faster than shear wave in the same medium and shear waves do not propagate through the liquids and gases because liquids and gases offer no resistance to shear deformation, so $\mu = 0$.

In sedimentary rocks, the range of the density values result mainly from differences in porosity (ϕ) which appears to be the dominant factor after the composition in determining the velocity of a rock. The porosity is determined principally by the existing differential pressure and the maximum depth of the burial. The relationship between velocity (*V*) and porosity (ϕ) (Wyllie et al., 1956) is

$$\frac{1}{V} = \frac{\phi}{V_f} + \frac{(1-\phi)}{V_m} \tag{2.22}$$

where *V* is the wave velocity in the fluid-filled porous rock, which comprises the wave velocity in the fluid (V_f) and in the rock matrix (V_m). This relationship is used extensively in interpretation of seismic well logging measurements (Telford et al., 1990).

For seismic geophysical surveys artificial energy sources are used to generate the seismic waves that are timed as they travel through the subsurface from the energy source to the geophones, the seismic sensors, which measure the incoming seismic wave amplitudes and the timed arrivals. The seismic wave propagation can be described as a ray equivalent to a light wave (Figure 2.8). When a seismic P wave encounters the interface of two rock types that have differences in the acoustic impedance (Z), which is the product of its density (ρ) and it compressional wave

velocity (v) with $Z = \rho v$, the travel directions of the reflected and transmitted seismic waves at this interface can be determined by Snell's law. This law is based only on the incident seismic wave angle and the seismic velocities of the two layers adjacent to the interface. For an incident P-wave, Snell's law gives:

$$\frac{\sin(\theta_I)}{V_1} = \frac{\sin(\theta_R)}{V_1} = \frac{\sin(\theta_T)}{V_2}$$

(2.23)

where θ_I is the incident P-wave travel direction angel, θ_R is the reflected P-wave travel direction angle and θ_T is the transmitted P-wave travel direction angle.
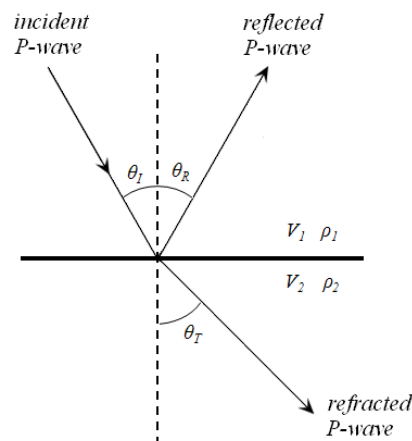
Figure 2.8 The generation of reflected and refracted P-wave from a P-wave incident on a plane interface (Lowrie, 2007).

When the transmitted angle (θ_T) of a seismic wave equals 90°, critical refraction occurs in which the seismic wave travels below the interface in layer 2 with the V_2 velocity. This incident angle that produces a refracted wave (or head wave) is referred to as the critical angle (θ_c), which can occur only where the seismic wave velocity in the layer below the interface (V_2) is greater than the seismic wave velocity in the layer above the interface (V_1). Snell's law was also used to the reflected wave to explain its reflection, following that the angle of reflection equals the angle of incidence. The ratio of the reflected wave amplitude to the incident wave amplitude is called the reflection coefficient. For incident P-waves normal to the interface, the reflection coefficient (R) is expressed as follows

$$R = \frac{Z_2 - Z_1}{Z_2 + Z_1} = \frac{\rho_2 V_2 - \rho_1 V_1}{\rho_2 V_2 + \rho_1 V_1}$$

(2.24)

The transmission coefficient (T) is the ratio of the transmitted wave amplitude to the incident wave amplitude, and it gives an incident seismic wave normal to the interface, which can be quantified using the following relationship:

$$T = 1 - R = \frac{2Z_1}{Z_2 + Z_1}$$

(2.25)

These coefficient values are referred to as the acoustic impedance (Z) for a particular soil and rock material in the subsurface.

Table 2.4   Compressional wave values of various materials (Reynolds, 1997).

Material	V_p (m/s)	Material	V_p (m/s)
Air	330	Anhydrite	3500 – 5500
Water	1450 – 1530	Rock salt	4000 – 5500
Petroleum	1300 – 1400	Gypsum	2000 – 3500
Loess	300 – 600	Shales	2000 – 4100
Soil	100 – 500	Granites	4600 – 6200
Snow	350 – 3000	Basalts	5500 – 6500
Solid glacier ice*	3000 – 4000	Gabbro	6400 – 7000
Sand (loose)	200 – 2000	Peridotite	7800 – 8400
Sand (dry, loose)	200 – 1000	Serpentinite	5500 – 6500
Sand (water saturated, loose)	1500 – 2000	Gneiss	3500 – 7600
Glacial moraine	1500 – 2700	Marbles	3780 – 7000
Sand and gravel (near surface)	400 – 2300		
Sand and gravel (at 2 km depth)	3000 – 3500	Sulphide ores	3950 – 6700
Clay	1000 – 2500		
Estuarine muds/clay	300 – 1800	Made ground (rubble etc.)	160 – 600
Floodplain alluvium	1800 – 2200	Landfill refuse	400 – 750
Sandstone	1400 – 4500	Concrete	3000 – 3500
Limestone (soft)	1700 – 4200	Disturbed soil	180 – 335
Limestone (hard)	2800 – 7000	Clay landfill cap	355 – 380
Dolomites	2500 – 6500	(compacted)	

* Strongly temperature dependent (Kohnen, 1974).

2.8.1 Seismic refraction method

A seismic refraction survey can be illustrated in the case of a flat interface between two horizontal layers (Figure 2.9). The depth to the interface is h_1 and the seismic velocities of the upper and lower layers is V_1 and V_2, respectively, with $V_1 < V_2$. The arrival time of the direct wave that travels from the shot-point S along the upper layer with the velocity V_1 and then is recorded by a geophone G at distance x on the surface is $t = x/V_1$, and it appearance on time-distance (t-x) graph with a straight line through the origin with slope $m_1 = 1/V_1$. When the refracted P-wave incident with critical angle (θ_c) at the interface of the upper and lower layer, the refracted wave (head wave) will travel along the interface in the lower layer with velocity V_2, and returns back to the surface with the time travel given as

$$t = \frac{x}{V_2} + \frac{2h_1 \cos\theta_c}{V_1} \qquad (2.26)$$

Equation 2.26 represents a straight line with slope $m_2 = 1/V_2$. The refracted wave is only recorded at distances greater than the critical distance x_c which is the arrival time recorded both for the refracted wave and the first reflected wave and the refracted travel time line is tangential to the reflection hyperbola. The intersection of the refraction time on the time-axis is known as the intercept time t_i which given by

$$t_i = \frac{2h_1 \cos\theta_c}{V_1} = \frac{2h_1(V_2^2 - V_1^2)^{\frac{1}{2}}}{V_1 V_2} \qquad (2.27)$$

The crossover distance x_{cr} is the distance where the direct and refracted waves arrive at the same time at the geophone on the surface as shown in the t-x graph and where the direct and refracted wave cross each other. It can be calculated as following

$$x_{cr} = \frac{2h_1(V_2 + V_1)^{\frac{1}{2}}}{(V_2 - V_1)^{\frac{1}{2}}} \qquad (2.28)$$

If the velocities of layers have been determined, it is possible to compute the depth h_1 to the interface by using either the intercept time t_i or the crossover distance x_{cr}, which can be read directly from the time distance plot. For the horizontal multilayer case, the crossover distance and interception method are also used and accommodated for solving depth and velocity at each horizontal layer.
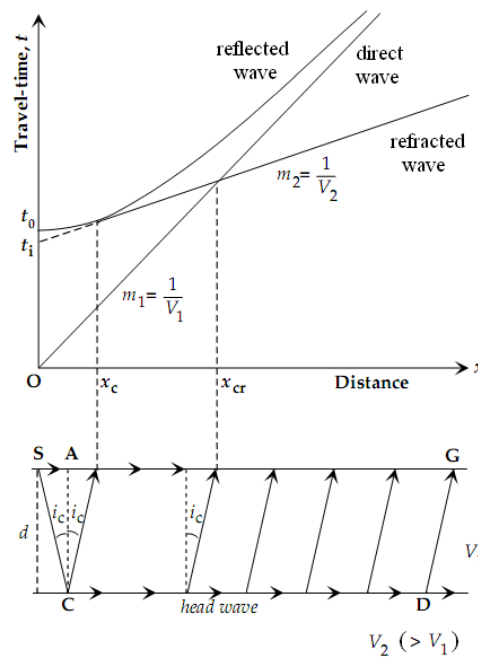
Figure 2.9 Travel time versus distance curves for the direct wave and the reflected and refracted waves at a horizontal interface between two layers with seismic velocities V_1 and V_2 ($V_2 > V_1$) (from Lowrie, 2007).

In the case of a dipping refractor or irregular interface (Figure 2.10), the delay time method is widely used for solving the seismic refraction interpretation (Telford et al., 1990; Parasnis, 1997). Let consider a horizontal refractor case, where the upper layer has a velocity V_1 and the lower one a higher velocity V_2. The travel time (t) of the head wave arrives at an offset distance x given by $t = x/V_2 + t_i$. In case of an irregular refractor, the intercept time (t_i) can be considered to be composed of two delay time, which is shot point delay time (δ_S) and geophone delay time (δ_G), as they are associated with the portion of the path down from the shot and up to the geophone.
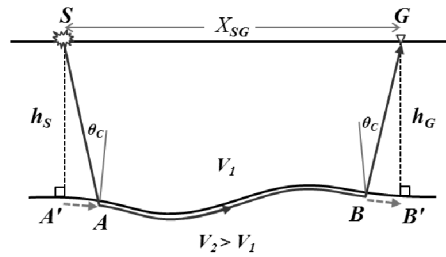
Figure 2.10   Schematic of refraction ray path on irregular plane considering in delay time method (Telford et al., 1990).

The delay time at the shot point (δ_S) is defined as the time difference between the wave that travels in the first layer along an actual path AB with velocity V_1 and the wave that travels in the second layer along the virtual path $A'B$ with velocity V_2, as shown below:

$$\delta_S = \frac{SA}{V_1} - \frac{A'A}{V_2}$$

$$= \frac{h_S}{V_1 \cos\theta_C} - \frac{h_S \tan\theta_C}{V_2}$$

$$= h_S \left(\frac{1}{V_1 \cos\theta_C} - \frac{\sin\theta_C}{V_2 \cos\theta_C} \right) \quad ; \sin\theta_C = \frac{V_1}{V_2}$$

$$= h_S \left(\frac{1 - \sin^2\theta_C}{V_1 \cos\theta_C} \right) \quad ; \sin^2\theta_C + \cos^2\theta_C = 1$$

$$\delta_S = \frac{h_S \cos(\theta_C)}{V_1} \tag{2.29}$$

This equation above also used to determine the delay time at the geophone (δG) with

$$\delta_G = \frac{h_G \cos(\theta_C)}{V_1} \tag{2.30}$$

and the travel time of the refracted wave from shot point A to the to geophone G (t_{AG}) is therefore

$$t_{SG} = \delta_S + \delta_G + \frac{X_{SG}}{V_2} \qquad (2.31)$$

This approximate value of the delay time (δ) is sufficiently accurate when the dip is less than 10 degree (Telford et al., 1990).

2.8.2 Seismic refraction survey and data processing

Two seismic refraction survey lines were performed on flat plain and parallel to the sinkholes in N-S direction (Figure 2.11). A Smartseis^{TM} S-24 seismograph was used for data recording with a sampling rate of 125 ms and a 10 kilograms sledge hammer as energy source. The twenty-four 14-Hz-geophones were placed in north-south direction with one meter geophone spacing. Reverse-spread shooting was performed for each refraction seismic line with seven shot points, one shot point at the center of geophone spread, one shot point at each end of the line, two shot point at 12 meters and two last records at 24 meters from the line end (Figure 2.11).
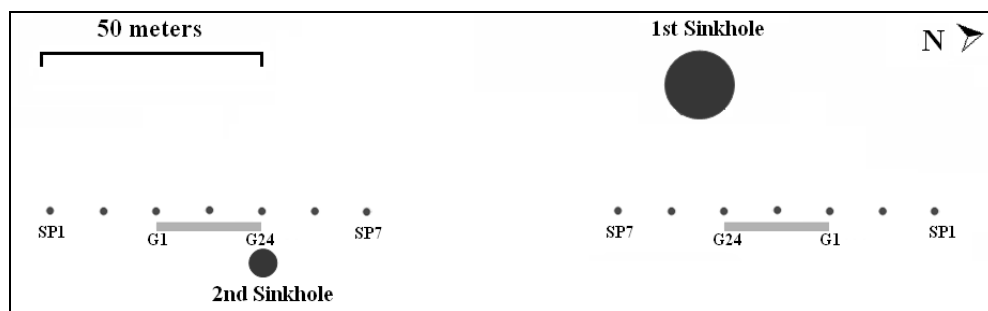
Figure 2.11   Seismic refraction survey plan.

For the seismic refraction interpretation SIP version 1 software from Rimrock Geophysics was used. Data were analyzed with delay-time method to produce a depth section along the survey line with the P-wave velocities and depth for each layer. More details of this program can be found at Scott (1973).

The general processing and interpretation procedure were done in following steps: First, determination of the first arrival time (picking the first break) of the seismic wave at each geophone for every geophone spread. This is the most

important one and will determined reliability of the resulting model. Then, the first arrival time was plotted in time-distance graphs for assigning layer numbers. Then, interpretation of the data using the iterative ray-tracing technique as an inversion program for modeling, and after that, determining the velocity of each layer.

The velocity of the top layer is computed by dividing the distance from each shot point to each geophone by the corresponding the arrival times. These individual velocities are averaged for each shot point, and a weighted average is computed. The refraction velocities of all layers beneath the top layer are computed by two methods. The first one is a regression method, in which a straight line is fit by least squares to the arrival times, representing the velocity of the layer and average velocities are computed by taking the reciprocals of the weighted average of the slopes of the regression line. The second is the Hobson-Overtone method, by which velocities can be computed if there are reciprocal arrivals from two opposing source points at two or more geophones. Final velocities used in the inversion process are computed by taking an average of the two methods. The inversion procedure normally requires only two iterations (Scott, 1973).

2.9 Seismic reflection method

The depth to the interface between two rock formations can be determined by measuring the travel time of seismic wave generated from the source at the surface and reflected back from the interface to be recorded by the geophone at the surface. Figure 2.12 shows a basic geometry of the reflected ray path for a simple case of a single horizontal reflector lying at the depth h below a homogeneous top layer of velocity V. The equation for the travel time t of the reflected wave from the shot point to the geophone at horizontal offset x is given by the ratio of the travel path length to the velocity as

$$t = \frac{\left(x^2 + 4h^2\right)^{\frac{1}{2}}}{V}$$

(2.32)

This equation is referred to as two-way travel time, it shows that graph of travel time of reflected wave plotted against offset distance (the time-distance curve) is a hyperbola (Figure 2.12). The location of reflecting bed is determined by measuring t_0 which is the travel time of the vertically reflected ray. Setting $x=0$, the equation above will be $t_0=2h/V$ which represent the intercept on the time axis of the time distance curve as

$$t^2 = \frac{4h^2}{V^2} + \frac{x^2}{V^2} = t_0^2 + \frac{x^2}{V^2}$$

(2.33)

Normal move out (NMO) at an offset distance x is defined as the difference in travel time ΔT between reflected arrivals at x and at zero offset

$$\Delta T \approx t_x - t_0 \approx \frac{x^2}{2V^2 t_0}$$

(2.34)

When the calculated ΔT, which is provided from a corrected velocity V, was subtracted from a recorded time at each geophone, then it will be a straight line instead of hyperbola. Finally the vertical depth to a reflector at each geophone can be determined.
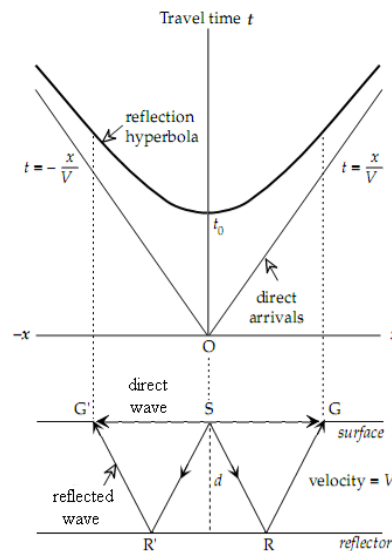
Figure 2.12 Travel-time versus distance curve for reflections from a horizontal boundary is a hyperbola. The vertical reflection time t_0 is the intercept of the hyperbola with the travel-time axis (Lowrie, 2007).

2.9.1 Seismic reflection survey

A Smartseis[TM] S-24 seismograph for data recording was used with a sampling rate of 125 ms and a 10 kilograms sledge hammer as energy source which was 30 meter off-end. Two seismic reflection survey lines were used 12-channel of 14-Hz geophones with 2 and 1 meters spacing of single geophone which located at the first and second sinkhole, respectively. This geometry was fixed and rolled with the sources and receivers along each survey line with 2– and 1-meter increments for 24 shots at each survey line (Figure 2.13).
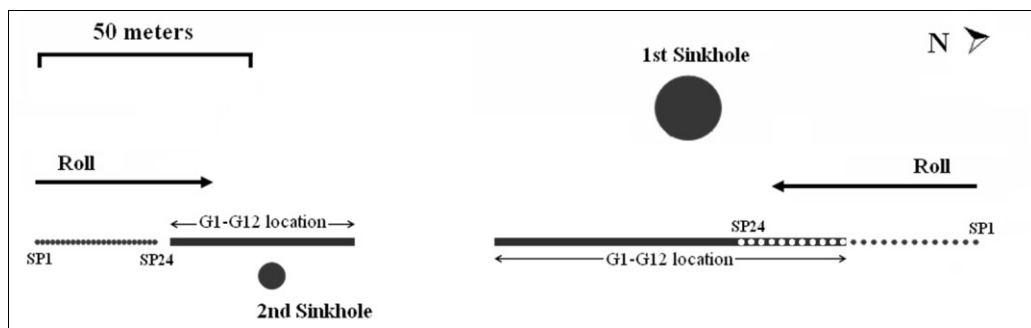
Figure 2.13   Seismic reflection geometry plan.

2.9.2 Optimum offset determination

The first step in seismic reflection survey is to find the optimum offset in order to obtain the reflected wave, which is clearly separated from the refracted wave and the airwave arrival time in the record data (Figure 2.14, top). To distinguish the seismic reflection signal from noise in the field survey and during data processing, following general features of noise can be considered. Air waves usually contain higher frequencies than others and their velocity should be about 330 to 340 m/s. Ground roll is identified by a slow phase velocity (steep slope) and typically has a lower dominant frequency than near surface refractions or reflections. The offset-test distance can be defined as the distance between the source and first geophone; it was test at each site with 0, 10, 20, 25, 30, 35, and 40 meters and at the center of the 24-geophones spread, which was located in N-S direction near the first and second sinkhole. An optimum offset distance of 30 meters was chosen for the two sites, as clearly reflected waves were revealed at arrival times of 60-80, 80-100 and 125-130 ms on the combined offset-test record shown in Figure 2.14 (bottom).
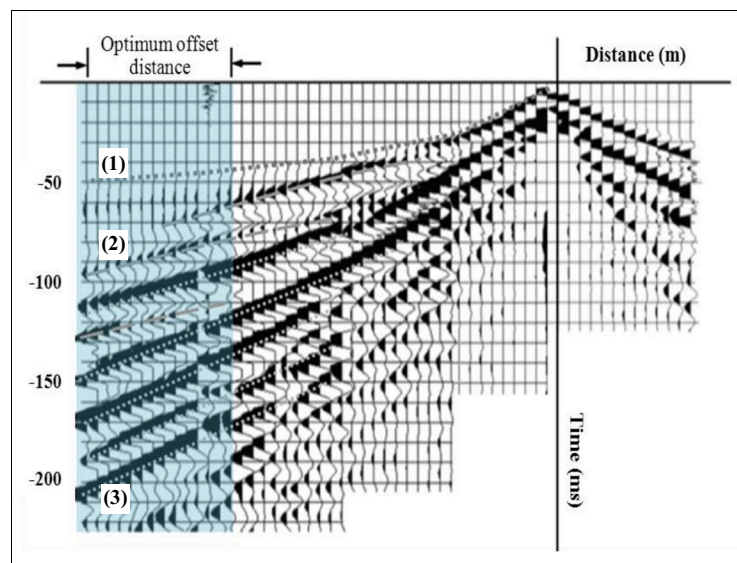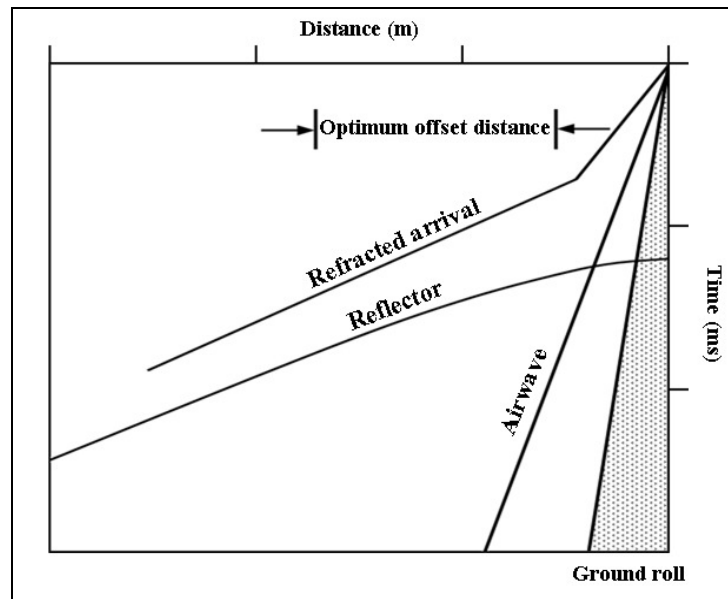
Figure 2.14   Time-distance graph show main phases (top) that need to be considered for choosing the optimum offset in a field survey (from Pullan and Hunter, 1990). The combined offset-test records, along the survey line near the first sinkhole, clearly show continuing reflectors (bottom); straight gray dot line (earlier time) (1) is the time arrival of refracted wave while curve dash lines (2) denote as time arrival of reflected wave and straight white dot lines (3) are airwave arrival.

2.9.3 Seismic reflection data processing and interpretation

        The GLOBE claritas program was used to process and interpret the data with common-depth-point reflection technique. The generalized processing flowchart used in this study is shown in Figure 2.15 and the acquisition details of each processing step are described below.
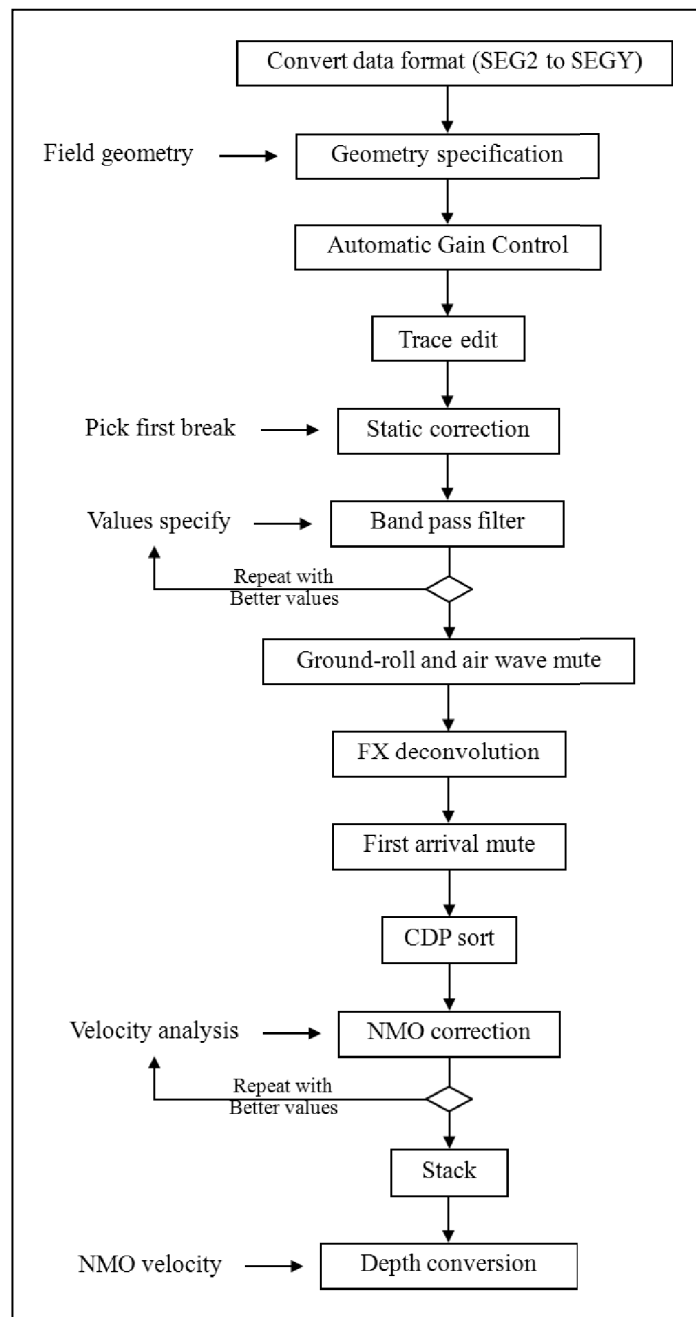
Figure 2.15   General processing flow chart for seismic reflection applied to both survey lines of this study.

The first step in seismic reflection processing is to convert raw data from SEG-2 to SEG-Y format and define correctly the coordinates of shot and receiver locations (Figure 2.15). The next step in the processing is to improve the quality of the shot gather and stack sections. Then apply a 100-ms automatic gain control (AGC) (Figure 2.26b) window in order to increase the amplitudes of the weak signals all shot data. Then remove noisy traces (Figure 2.16c), open channels and bad records. After that apply refraction static corrections (Figure 2.16d), which are time shifts applied to traces to adjust for variations of the near–surface weathering zone. To attenuate noise outside of the reflection frequency band and in order to enhance the reflection signal, the seismic data was filtered using a bandpass filter (Figure 2.16e) with 50 Hz up to 130 Hz up and from 200 Hz to 300 Hz down, which was applied to both seismic lines. The next process is air wave attenuation (Figure 2.16f), which deletes the arrival or decreases the amplitude of the air wave at the region with the air waves specified velocity of about 330 m/s. Then FX-deconvolution (Figure 2.16g) was applied to further attenuate noise and improve the vertical resolution of the seismic traces by predicting continuity in the signal using the nearby traces, while noise is the unpredicted factor. After that first arrival mute (Figure 2.16h) was applied to remove the coherent noise from the refraction events in the near surface; it starts at 0 ms until the refraction arrival time. In CDP sorting (Figure 2.16i) the trace-data are transformed from shot-receiver to midpoint offset coordinates to group them together. Normal move out (NMO) are applied to get the zero-offset travel time of a particular reflector by using constant velocity scan (CVS) technique to define an appropriated velocity of the reflector. After the NMO corrections are applied to a CDP gather the hyperbolic reflection events become flat events. After that all the traces of each CDP location will be stacked, which can attenuate random and much coherent noise. The result of applying this process to all the CDP gathers of the line is the time stack section (Figure 2.16k). To correct the position of the reflector event in vertical section the time stack section will be conversed to depth section (Figure 2.16l) by using previously defined stacking velocities used for the NMO processing step.
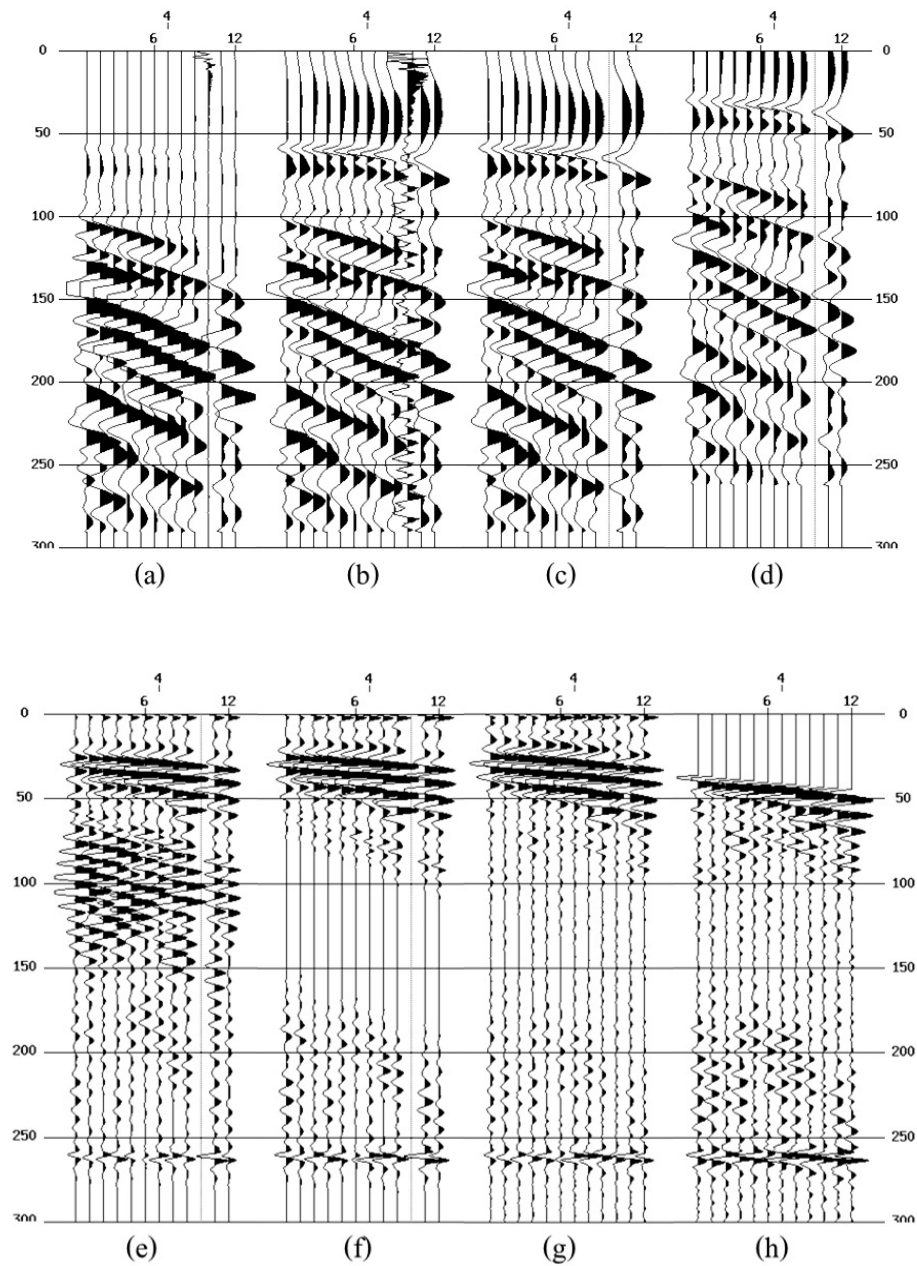
Figure 2.16 An example of shot records for each seismic processing step: (a) raw shot data, (b) AGC, (c) kill bad traces, (d) static correction, (e) filtering, (f) air muting (g) FX-deconvolution, and (h) first arrival mute.
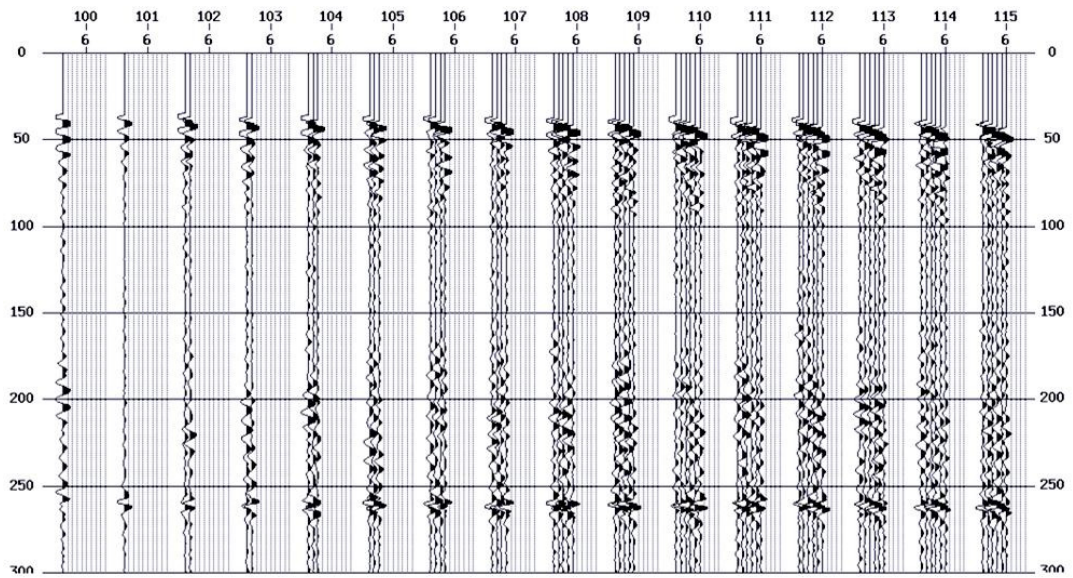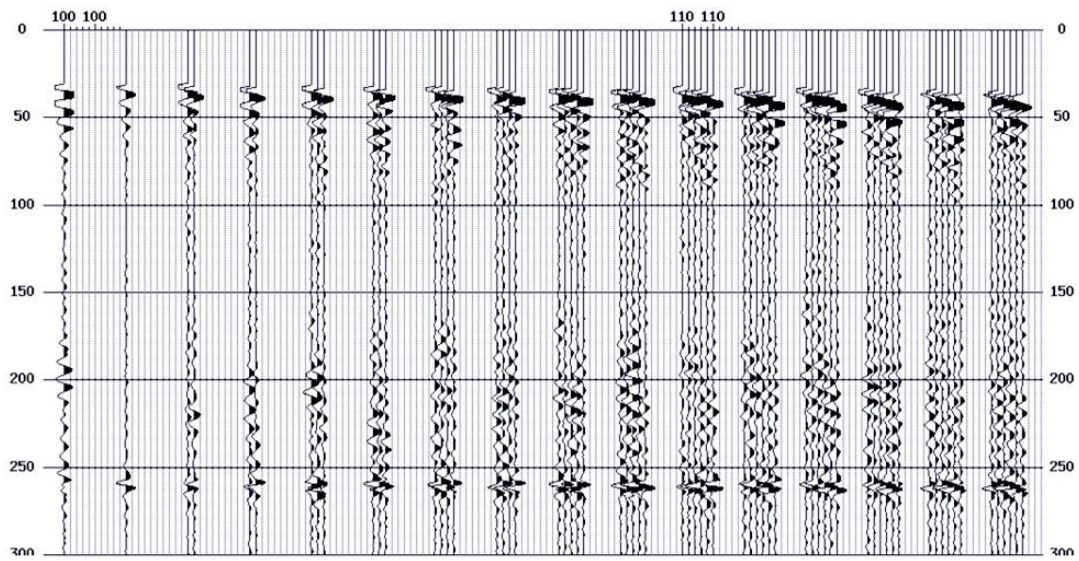
Figure 2.16 (cont.)   An example of shot records for each seismic processing step; (i) CDP sorting shot data and (j) NMO correction.
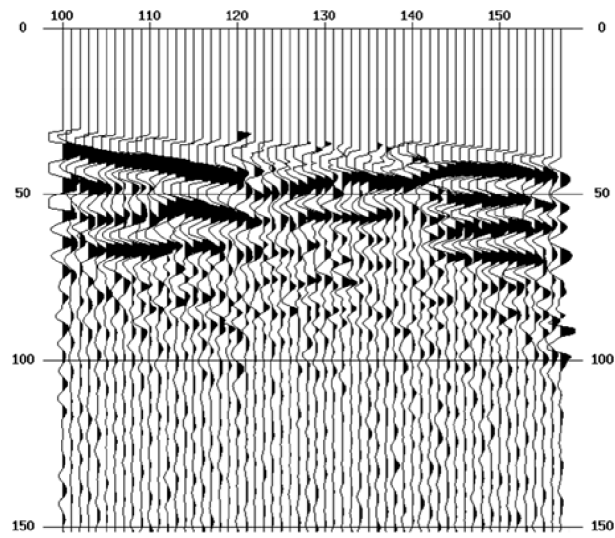
(k)
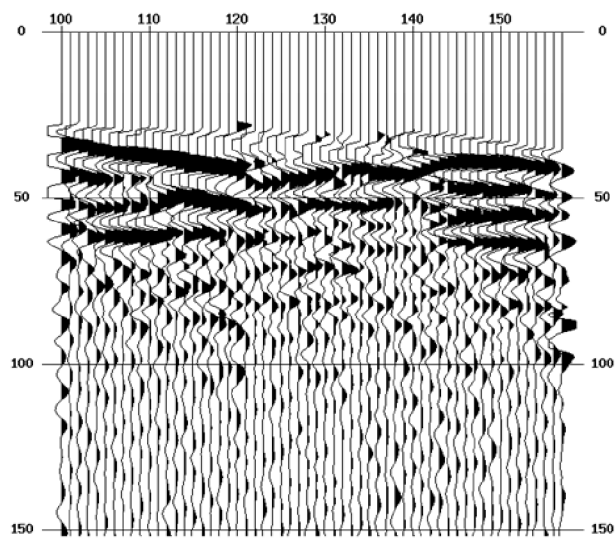
(l)

Figure 2.16 (cont.) An example of shot records for each seismic processing step; (k) stacked section and (l) depth section.

2.9.4 Pitfalls in seismic data processing and interpretation

Problems that sometimes arise during some processing step such as choosing inappropriate range in filtering steps, will result in to the misinterpretation of reflectors and make artifacts occur in the final stack section. To avoid these pitfall, some processing step need a clear understanding.

1. Gibbs effect on filtering processing

When an appropriate band-pass filter was applied on the raw data (Figure 2.17), then in the enhanced section the reflectors clearly appear, but the roll off on either side of the band-pass filter regularly should not more 12 dB/octave (Baker, 1999). On the other hand, an inappropriate design of the filter, e.g. when the slope is more than 12 dB/octave, can generate ringing reflectors, which is the Gibbs effect (Figure 2.19, right). An example of the difference band-pass filters, which was applied on the raw data is shown in Figure 2.18 (top) with the first range from 40 Hz up to 100 Hz and down from 200 Hz to 300 Hz. This slope is about 6.53 dB/octave, which does not generate the Gibbs effect (Figure 2.19, left). While the second range from 70 Hz up to 140 Hz and down from 200 Hz to 300 Hz gives 11.74 dB/octave (Figure 2.18, bottom), which is a steep slop and causes the Gibbs effect in the final time stack section (Figure 2.19, right).

$$slope(dB/octave) = \frac{A_1 - A_2}{\log_2\left(\dfrac{f_1}{f_2}\right)}$$
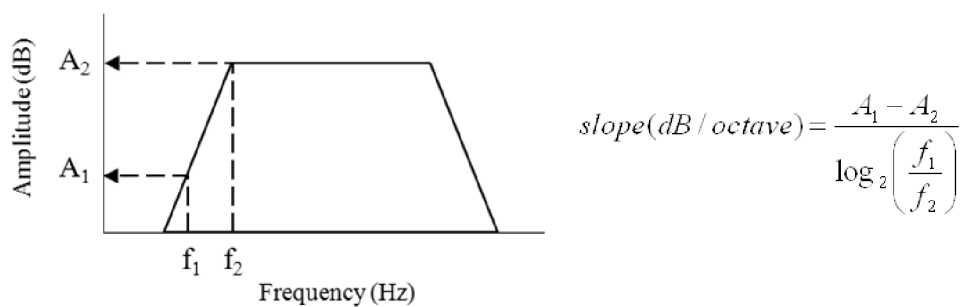
Figure 2.17   Appropriate bandpass filter calculation (modified from Ghosh, 2007).
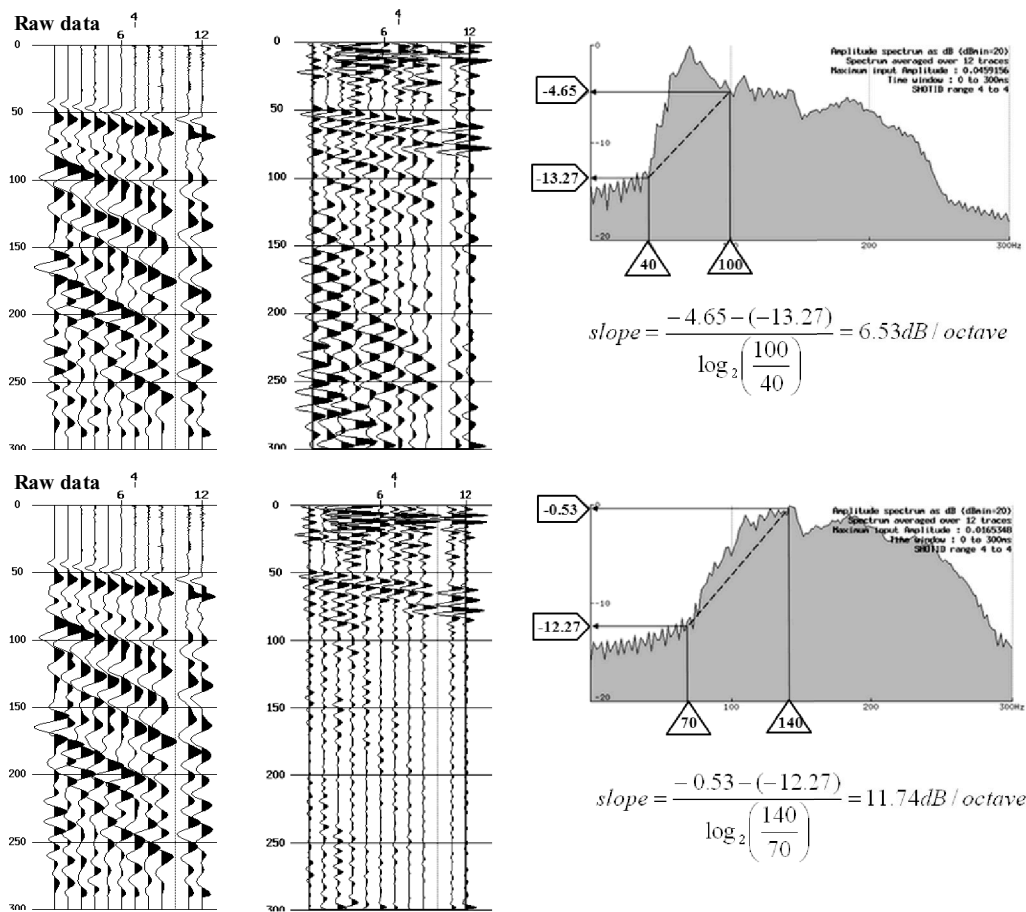
Figure 2.18 Filtering range comparison: an appropriate range with 6.53 dB/octave has obvious reflectors in the data (middle, top), while another inappropriate filter makes a ringing signal with 11.74 dB/octave (middle, bottom).

$$slope = \frac{-4.65 - (-13.27)}{\log_2\left(\dfrac{100}{40}\right)} = 6.53 dB / octave$$

$$slope = \frac{-0.53 - (-12.27)}{\log_2\left(\dfrac{140}{70}\right)} = 11.74 dB / octave$$
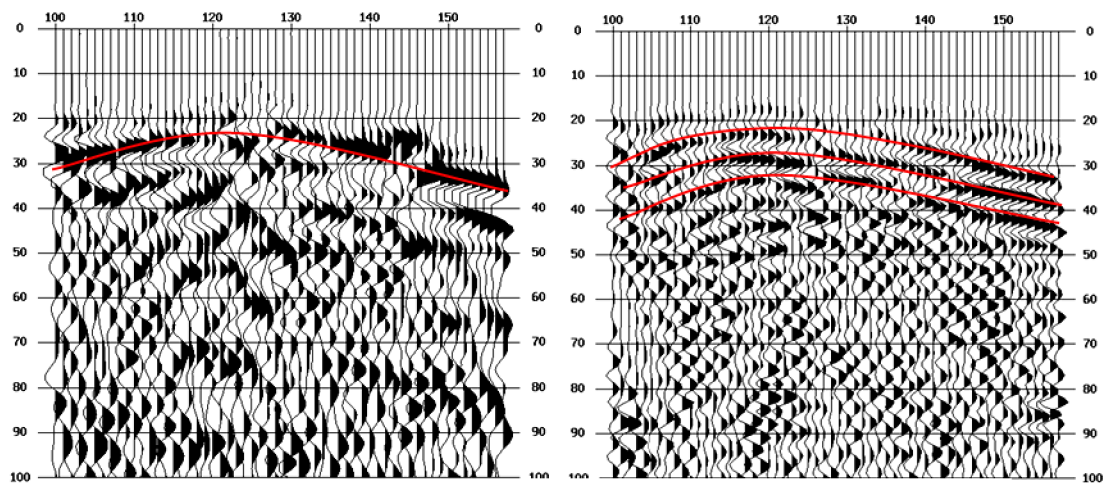
Figure 2.19 Steep slope causes ringing reflectors in the final time stack section (right).

2. Misidentification of refraction as reflection

An inappropriate filter range can cut off the reflection frequencies or attenuate the amplitudes of the reflectors, while remaining the amplitude of refraction signals (Figure 2.20). This can cause a misidentification of the refraction as a reflection and by this allowing it to be in the final stack section (Figure 2.21). If the range of filtering is appropriate, the reflection signal will appear (Figure 2.22) and in the final time section it will appear as a real reflector (Figure 2.23). Another mistake on signal identification is if the top mute is not applied. It will make the refractions stack to form coherent events, which will mask the reflection events on the final time section (Figure 2.24, left). When the top mute was eliminated, the true reflectors were dominant and tend to be obvious on the time stack section (Figure 2.24, right).

$$slope = \frac{-1.3-(-10.94)}{\log_2\left(\frac{100}{70}\right)} = 18.72 dB / octave$$
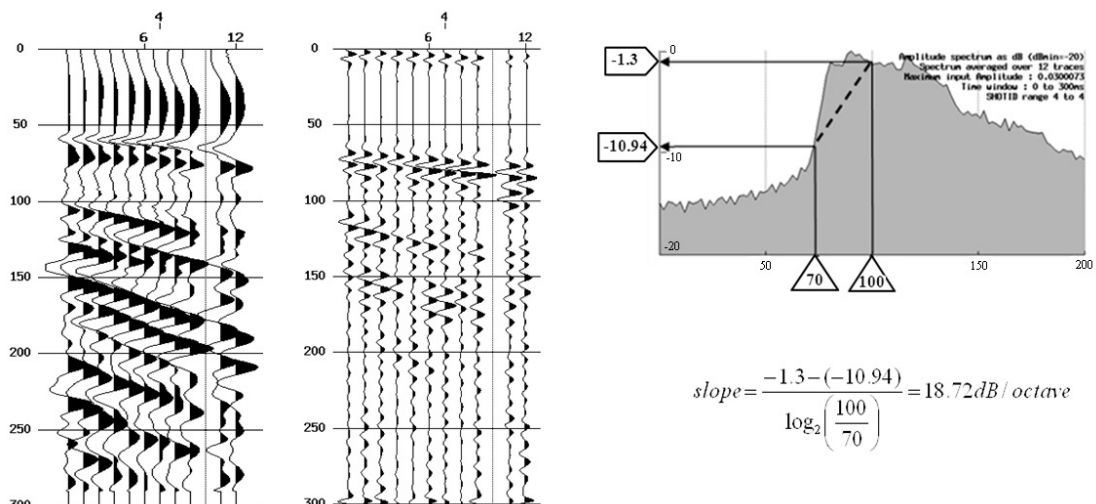
Figure 2.20   Inappropriate filtering that attenuates the true reflector and keep the refractor, which can lead to misinterpretations.
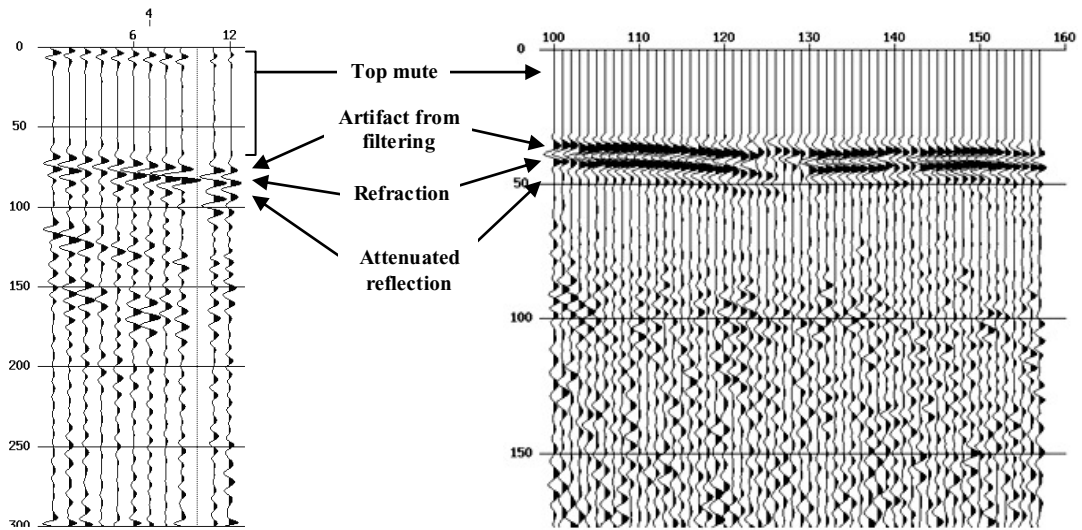
Figure 2.21 In the seismic time section seems to be double reflectors caused by too steep side slopes of the bandpass filter. It can attenuate the real reflection signals.
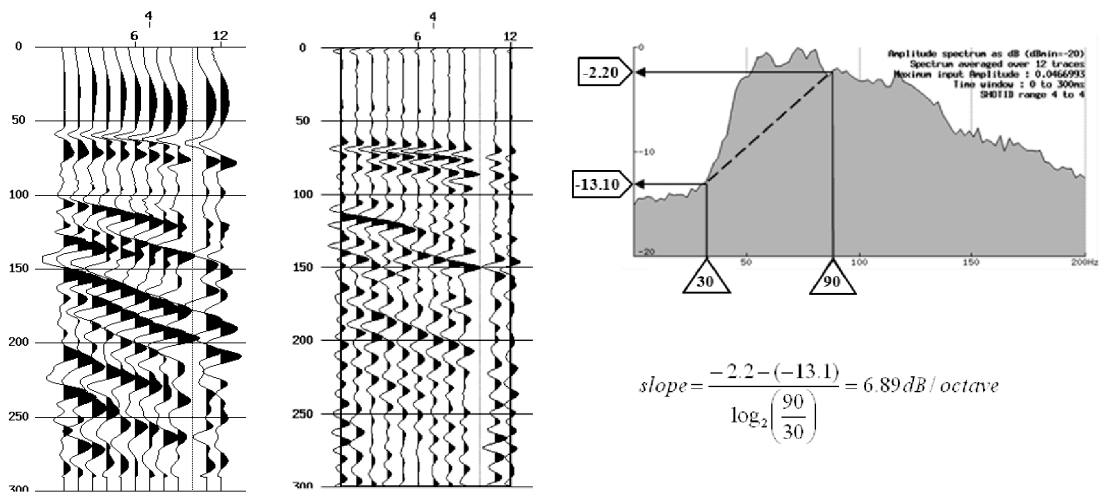
Figure 2.22 Appropriated filter will have the true reflectors appearing in the data.
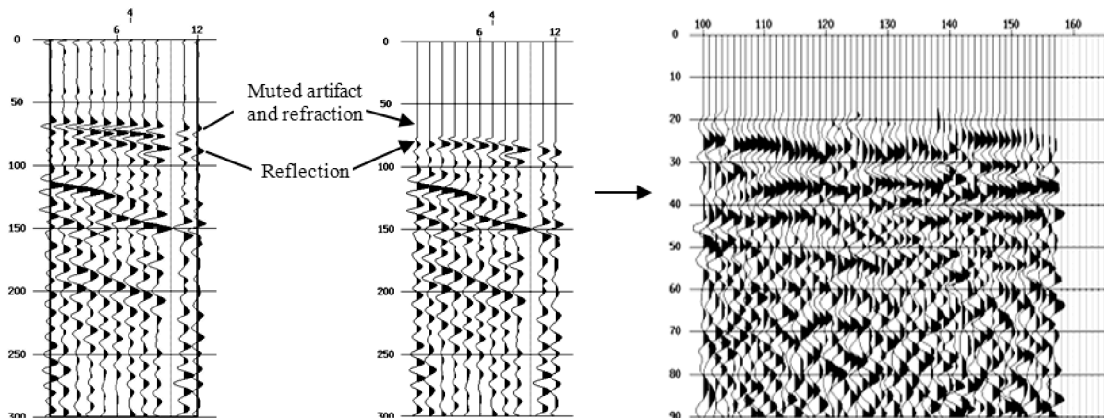
Figure 2.23 The artifact reflectors after filtering step (left) will result in misinterpretation as real reflectors. Check and remind the first arrival time is helpful to indicate actual reflectors for applying the top mute (middle) to eliminate refraction and artifact in the final stack and reveal the true reflectors (right).
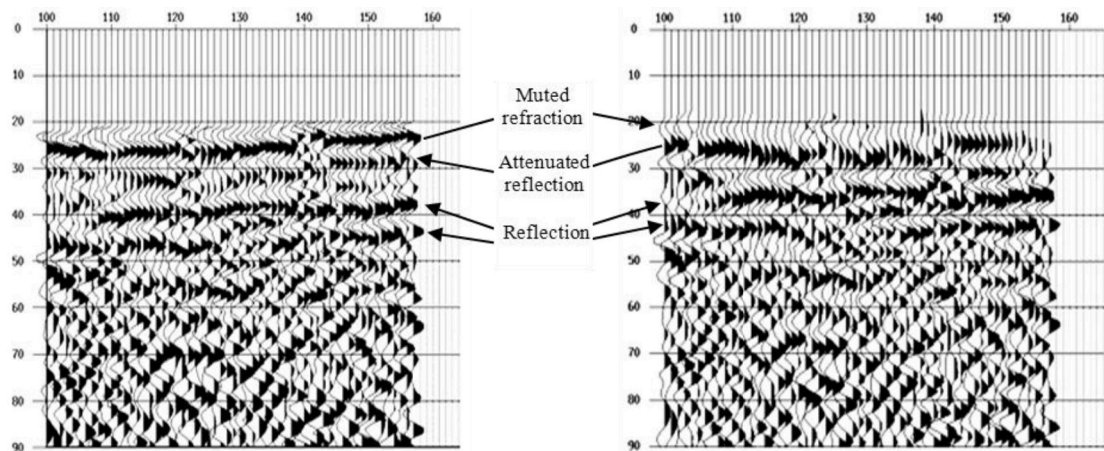
Figure 2.24 Example of allowing the first arrivals to remain in the seismic reflection data (left). Energy arriving at 25 ms is primarily refraction energy. The true reflections become obviously at times between 30 and 45 ms (left) after removing the first arrival (right).

2.10 Self-potential method

Self-potential (SP) is an electrical method to measure a naturally occurring electric potential difference between two locations in the ground surface. The electric potential difference measured is associated with non–artificial electric currents transmitted through the ground. These naturally generated electric potential differences range in magnitude from less than a millivolt (mV) to over one volt (Reynolds, 1997). The magnitude and sign (positive or negative) of a delineated self-potential anomaly can provide indications as to the character of the subsurface feature producing the anomaly. In hydrogeological investigations, self-potential measurements are a very useful technique, which has been used to study groundwater movement and flow path to map sinkholes, and evaluate the risk of potential collapses in karst areas (Wanfang et al., 1997). Certain natural potentials occurring in the subsurface are caused by electrochemical or mechanical activity. The controlling factor in all cases is the groundwater (Telford et al., 1990). There are three principal mechanisms producing the potential (Sharma, 1997).

(a) First, the electrokinetic potential, also called electrofiltration or streaming potential, which is associated with electric currents generated by the movement of dissolved ions containing water through a porous media, such as soil or rock. The underlying mechanism creating current and potential differences is believed to be electrokinetic coupling between pore side walls and dissolved ions (Sharma, 1997). The Helmholtz-Smoluchowski law links the electrofiltration potential (EF in V/m) amplitude with the electrolyte characteristics as following

$$EF = \frac{\rho \varepsilon \zeta}{4\pi\eta} \Delta P \qquad (2.35)$$

where ρ is the electrical resistivity of electrolyte (Ω-m), ε is the dielectric constant of electrolyte (F/m), ζ is the electrical potential of the double layer (zeta potential) (V), η is the dynamic viscosity of the electrolyte (Pa-s), and ΔP is the pressure difference (Pa/m) between the measurement points of EF.

Electrokinetic potentials are in the same direction as the pressure gradient that is opposite to the direction of the electrolyte flow (Parasnis, 1997;

Reynolds, 1997). The parameter $C=(\varepsilon\rho\zeta/\eta)$ is called streaming potential coefficient and for the earth material it ranges from a fraction of a millivolt per kilopascal (0.1 m water head) to about 1.3 mV/Pa. The flow of water due to a pressure gradient is not sufficient for electrofiltration anomalies to arise. It is necessary that the flow takes place across a boundary between two rocks media for which C difference (Parasnis, 1997).

(b) Second, the electrochemical potential is the combined diffusion (liquid-junction) and Nernst (membrane) potential (Telford et al., 1990). Considering the ionic concentration in an electrolyte that varies with locations, the ions tend to diffuse through the electrolyte to equalize the concentration. The diffusion is driven by an electric diffusion potential, which depends on the temperature as well as the difference in ionic concentration. When a metallic electrode is inserted in the ground, the metal reacts electrochemically with the electrolyte (i.e., groundwater), causing a contact potential. If two identical electrodes are inserted in the ground, variations in concentration of the electrolyte cause different electrochemical reactions at each electrode. A potential difference arises, called the Nernst potential. It is temperature sensitive and may be either positive or negative, amounting to at most a few tens of millivolts (Lowrie, 2007). The electrochemical potential is expressed by

$$E_C = -70.7 \frac{(T+273)}{273} \log\left(\frac{C_1}{C_2}\right)$$ (2.36)

where T is the absolute temperature (K), C_1 and C_2 are the solution concentrations.

(c) Third, the mineralization potential, which is still not well understood. The spatial self-potential anomalies are often measured at the ground surface over massive metal ore bodies. The mechanism generating these anomalies is not completely understood. However, the explanation having the greatest acceptance involves natural electric currents originating from chemical oxidation and reduction reactions between a metal ore body straddling the water table and the pore water dissolved ions present in the surrounding rock or soil (Allred, 2008).

Remainder of these self-potential can be classified as background or noise. Background potentials are created by fluid streaming, geochemical reaction and other processes. with either positive or negative amplitudes very greatly but generally are less than 100 mV. The influence of topography is usually negative going up hill, which is probably cause by streaming potential (Telford et al., 1990) and the maximum of it effect is 80 mV per 100 meters difference in elevation (Ernstson et al., 1986). Potential arising from bioelectric activity of plants and trees character as sharp anomaly with negative several hundred millivolts (see Appendix E, Table E.10)

The basic equipment setup (Figure 2.25) needed for self-potential surveying consist of a pair of electrodes connected via a high impedance voltmeter. The electrode must be non-polarizing electrodes as simple metal spikes would generate their own SP effects. Non-polarizing electrodes consist of a metal immersed in a saturated solution of its own salt, such as copper in copper sulfate (Allred, 2008).
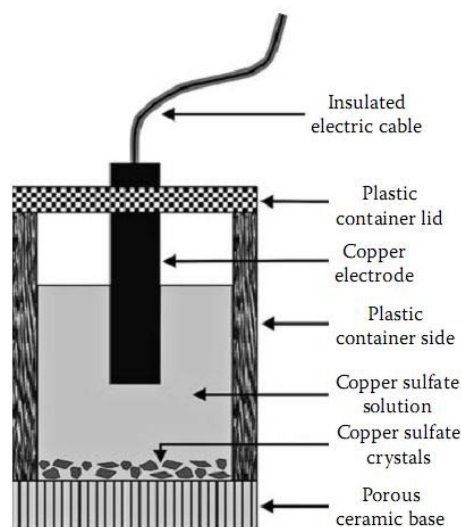
Figure 2.25 Typical components making up a non-polarizing electrode of self potential survey (Allred, 2008).

There are two common techniques in survey field to perform the SP mapping. The first one is the gradient configuration (also called the dipole, leapfrog or fixed-electrode configuration) that utilized two electrodes (P_1 and P_2) consecutively moving together along a line survey or a series of transects with constant-distance

electrodes separation, for each move of the electrode pair, the new position of electrode P_1 corresponds with the previous position electrode P_2 (Figure 2.26a). The self-potential measurement value (in voltage) is assumed to be the midpoint between the two electrodes for each moving (x-position in Figure 2.26a). The second one is the fixed-base (or total field) configuration uses a stationary base electrode P_1 and a measuring electrode P_2 is moved along a line survey or a series of transects (Figure 2.26b). The location referenced for self-potential measurement value is assumed to coincide with the position of the moving electrode P_2 (Figure 2.26b) (Corwin and Hoover, 1979).
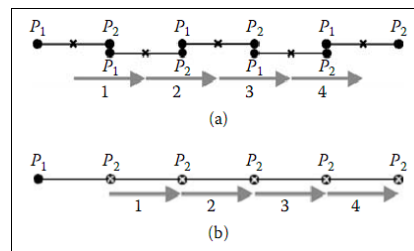
Figure 2.26   Two modes of self-potential data collection: (a) gradient and (b) fixed-base configuration (Allred, 2008).

2.10.1 Self potential survey

All 134 measurement points of the self-potential survey of this study composed of one loop around the first sinkhole, one long line parallel to seismic lines and four cross lines between first and second sinkhole (Figure 2.27). Additionally 62 elevation leveling points were also measured along SP line using the Pentax leveling system and a 4-meter staff rod.

The total-field technique was performed and using two copper-copper sulfate (Cu/CuSO$_4$) non-polarizing electrodes. The analytical reagent of copper sulfate powder is composed of 99% copper sulfate pentahydrate (CuSO$_4$·5H$_2$O) and the copper sulfate electrolyte is saturated (about 40 grams dissolved in 100 ml distill water). The measurements are carried out by using a terrameter SAS 300C, a digital high-input impedance voltmeter ($22 \times 10^6\,\Omega$), with a measuring precision of 0.01 mV.

At the reference station the electrode was buried 20 cm deep in a shaded location to minimize temperature and polarization effects. At each measuring point the vegetation was cleared and the roving electrode was set approximately

20 cm deep into the soil to reduce the SP effect from chemical and moisture variations in the topsoil. The base-station (near the reference electrode) readings was repeated at every hour for drift correction.
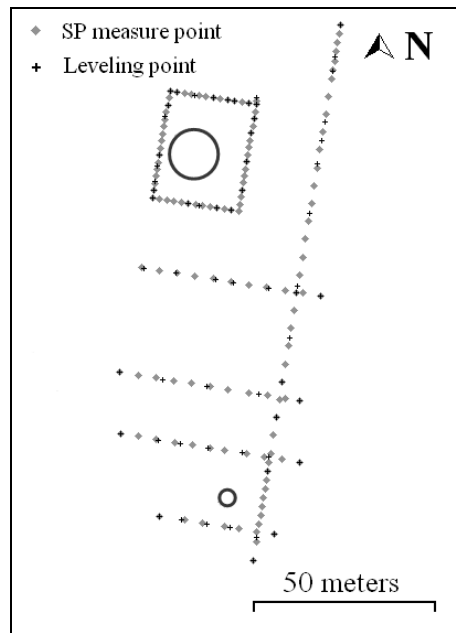
Figure 2.27   Self-potential survey plan with leveling measurement.

The objective of data processing is to get SP anomalies resulting from streaming potential that is associated with groundwater flow in the subsurface. The processing was performed by drift-correction.

2.10.2 Self potential data processing and interpretation

1. Drift correction

As the measurements are made in the shape of a loop, theoretically, the value at the base station of the first and the last measurement must be equal. However, because the measurements are not made at the same time, there is always a drift (Wanfang et al., 1999) as shown by Equation 2.37 below.

$$SP_{Ci} = SP_i + SP_{Drift} \tag{2.37}$$

where SP_{Ci} is the corrected SP value of the drift correction and SP_i is the SP measurement value for point i and SP_{Drift} is the drift correction value. In order to

correct any drift occurring during the measurement period the drift value has been calculated as following (Wanfang et al., 1999):

$$SP_{Drift} = t_i \times C_{Incrementdrift} \qquad (2.38)$$

and
$$C_{Incrementdrift} = \frac{-\left(SP_{last} - SP_{first}\right)}{\Delta t} \qquad (2.39)$$

where SP_{first} and SP_{last} are the SP values at the base station of the first and last measurement, Δt is the absolute time difference at the base station of the first and the last measurement, $C_{Incrementdrift}$ is the value of the gradient of the SP value per unit time and t_i is the absolute time difference of base station and measurement point i. An example of a drift correction calculation is given in Table 2.5.

Table 2.5   Example of drift correction calculation of self-potential data.

Mobile electrode on tape (m)	Elevation (m)	Time (hh:mm:ss)	Average SP (mV)	Δt (min)	SP_{drift} (mV)	SP_C (mV)
(Base) 0	0	14:25:00	-3.035	0	0	-3.035
80	1.375	14:27:30	22.75	2.5	-0.00723	22.75723
85	2.2	14:30:30	20.7	5.5	-0.01591	20.71591
90	2.812	14:34:30	18.995	9.5	-0.02748	19.02248
95	3.289	14:36:30	17.655	11.5	-0.03326	17.68826
100	3.678	14:39:30	26.6	14.5	-0.04194	26.64194
105	4	14:45:00	14.92	20	-0.05785	14.97785
110	4.524	14:46:30	8.36	21.5	-0.06219	8.42219
115	4.5	14:49:30	12.395	24.5	-0.07087	12.46587
120	4.5	14:52:30	8.98	27.5	-0.07955	9.059545
122.5	4.875	14:55:30	12.065	30.5	-0.08822	12.15322
125	5.044	15:01:00	10.54	36	-0.10413	10.64413
127.5	5.122	15:05:00	3.695	40	-0.1157	3.810702
130	5.202	15:07:00	1.203	42	-0.12149	1.324488
132.5	5.272	15:09:30	-2.32	44.5	-0.12872	-2.19128
135	5.351	15:11:30	0.9995	46.5	-0.1345	1.134004
137.5	5.43	15:15:00	11.12	50	-0.14463	11.26463
140	5.5	15:16:30	11.48	51.5	-0.14897	11.62897
145	5.947	15:18:30	7.285	53.5	-0.15475	7.439752
150	6	15:20:00	11.45	55	-0.15909	11.60909
(Base)		15:25:30	-3.21	60.5	-0.175	-3.035

2. Topographic effect

Many previous investigations of SP have measured an electric field characterized by increasing potential in the downhill direction. This phenomenon is known as a topographic effect (Aubert and Atangana 1996). A topographic correction can be calculated follow the equation below

$$C_{TE} = -K\Delta h \qquad (2.40)$$

where C_{TE} is the topographic effect correction value (mV), K is the topographic correction factor (mV/m), and Δh is the absolute elevation difference from base station (m). The topographic correction factor (K) can be determined by the plotting self-potential values versus elevation. The negative slope (-4.4007 in Figure 2.28) of the linear regression line of the SP value change per unit elevation increasing (Wanfang et al., 1999) is defined as the topographic correction factor.

$$y = -4.4007x + 31.208$$
$$R^2 = 0.5423$$
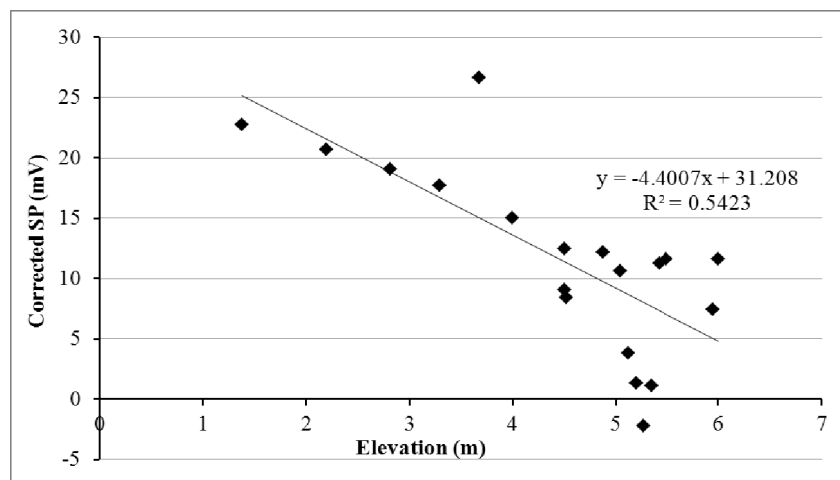
*Figure 2.28*   Correlation of self-potential values related to elevation changes.

Thus, the residual SP (SP_Residual) can be calculated by removing the topographic effect from the drift-corrected SP as following:

$$SP_C = SP_{Re\,sidual} + C_{TE} \qquad (2.41)$$

An example of the topographic correction of self potential data from a survey in this study is given in Table 2.6.

Table 2.6   Example of topographic correction of self-potential data.

Elevation (m)	SP_C (mV)	C_{TE}	$SP_{Residual}$
1.375	22.75723	6.05	16.70723
2.2	20.71591	9.68	11.03591
2.812	19.02248	12.3728	6.649679
3.289	17.68826	14.4716	3.216664
3.678	26.64194	16.1832	10.45874
4	14.97785	17.6	-2.62215
4.524	8.42219	19.9056	-11.4834
4.5	12.46587	19.8	-7.33413
4.5	9.059545	19.8	-10.7405
4.875	12.15322	21.45	-9.29678
5.044	10.64413	22.1936	-11.5495
5.122	3.810702	22.5368	-18.7261
5.202	1.324488	-22.8888	-21.5643
5.272	-2.19128	-23.1968	-25.3881
5.351	1.134004	-23.5444	-22.4104
5.43	11.26463	-23.892	-12.6274
5.5	11.62897	-24.2	-12.571
5.947	7.439752	-26.1668	-18.727
6	11.60909	-26.4	-14.7909

2.11 Groundwater geochemistry

The chemical composition of the groundwater is the result from geochemical process including the dissolution of soluble minerals in the subsurface and it can express characteristic and behavior of the groundwater. Therefore, it can be assumed that the dominant sulfate (SO_4^{2-}) in the groundwater is derived principally from the groundwater flowing and the dissolution of anhydrite and/or gypsum ($CaSO_4$/$CaSO_4 \cdot 2H_2O$) deposits and by this producing calcium and sulfate ions in large quantities in the groundwater. Fundamental to the equilibria in water is the law of mass action. According to that following chemical reaction of gypsum occurs:

$$CaSO_4 \cdot 2H_2O \leftrightarrow Ca^{2+} + SO_4^{2-} + 2H_2O \qquad (2.42)$$
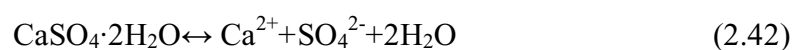
For the dissolution of the gypsum, the distribution of the SO_4^{2-} and Ca^{2+} at equilibrium can be characterized by an equilibrium constant (K_{SP}), which expresses the ratio of the product of the concentrations of the reaction products (right side) to the product of the concentration of the reactants (left side) as shown below:

$$K_{SP} \approx [Ca^{2+}][SO_4^{2-}] = 10^{-4.6} \tag{2.43}$$

The amount of Ca^{2+} and SO_4^{2-} ions, which were associated from gypsum can be used to predict the saturation state of the groundwater by considering the saturation index (*SI*), which is the logarithm of the quotient of the ion activity product (*IAP*) that is derived from water sample analysis and solubility product constant (K_{SP}) of gypsum, with

$$IAP = [Ca^{2+}][SO_4^{2-}] \tag{2.44}$$

$$SI = \log(IAP / K_{SP}) \tag{2.45}$$

When *SI* = 0, it means the solution is at saturation equilibrium, *SI < 0* reflects the solution is undersaturated, which means any solid present will dissolve, and *SI > 0* reflects the solution is supersaturation which means it begin precipitate (Appelo and Postma, 2005).

2.11.1 Geochemical investigations

In this study the geochemical investigations composed of two parts. First is the chemical composition analysis in groundwater samples done by the Scientific Equipment Center, Prince of Songkla University (see Appendix D, Figure D.1 and D.2). Water samples were collected from the second sinkhole, 541001E and 921913N, at a depth of 9 to 10 meters below surface, and from an adjacent well, which was made from concrete rings. The sample was taken at about 6 meters depth below surface at its location 540809E and 922358N (see Figure 2.2). The elevation difference between both locations is about 4.5 meters with the well location lower, so that the water samples refer to a similar depth (see also Section 3.8.1). Two water samples were analyzed for pH, TDS, and major cations and anions. The analysis

results were used to evaluate the saturation state of groundwater sample by calculating the saturation index.

The second part is the experiment of gypsum concentration effects on electrical resistivity. A Mettler AE200 electronic analytical balance was used to weigh the gypsum powder for initial concentration, with 0.86 grams of gypsum dissolved in one liter distilled water and by this assuming a 100%-saturation (Table 2.7). A portable conductivity meter, Thermo Electron Corporation 3-Star, was used to measure the resistivity in relation to different gypsum concentrations. The calculation of amount of gypsum, which was used to dissolve and assumed as 100%-saturation can be considered from the solubility of the gypsum mineral, which is governed by the solubility product. The equilibrium constant for a reaction of gypsum is

$$K_{SP} \approx [Ca^{2+}][SO_4^{2-}] = 10^{-4.6}$$

$$x^2 \quad = 10^{-4.6}$$

$$x \quad = 5 \times 10^{-3} \text{ mol/L}$$

therefore the solubility of gypsum, which has a molecular weight (MW) of 172 g/mol, is

$$(5 \times 10^{-3} \text{mol/L})(172 \text{ g/mol}) = 0.86 \text{g/L}$$

and the saturation of gypsum in 200 ml water is (0.86g/l)(200ml) = 0.172 g at saturation state. Table 2.7 shows the different concentration used in this experiment and the related relevant data.

Table 2.7 Variation of the gypsum concentration used for the electrical resistivity measurements versus concentration of gypsum.

% saturate	[CaSO$_4$.2H$_2$O] M	[CaSO$_4$.2H$_2$O] mg/l	TDS mg/l	[Ca^{2+}] mg/l	[SO$_4^{2-}$] mg/l	[SO$_4^{2-}$] ppm	Amount
100	0.005	860	860	200	480	0.48	0.172 grams in 200 ml
90	0.0045	774	774	180	432	0.432	dilute from 100%
80	0.004	688	688	160	384	0.384	dilute from 100%
70	0.0035	602	602	140	336	0.336	dilute from 100%
60	0.003	516	516	120	288	0.288	dilute from 100%
50	0.0025	430	430	100	240	0.24	dilute from 100%
40	0.002	344	344	80	192	0.192	used 80% to dilute
30	0.0015	258	258	60	144	0.144	used 60% to dilute
20	0.001	172	172	40	96	0.096	used 40% to dilute
15	0.00075	129	129	30	72	0.072	used 60% to dilute
10	0.0005	86	86	20	48	0.048	used 100% to dilute
5	0.00025	43	43	10	24	0.024	used 50% to dilute
4	0.0002	34.4	34.4	8	19.2	0.0192	used 40% to dilute
3	0.00015	25.8	25.8	6	14.4	0.0144	used 30% to dilute
2	0.0001	17.2	17.2	4	9.6	0.0096	used 20% to dilute
1	0.00005	8.6	8.6	2	4.8	0.0048	used 10% to dilute
0.1	0.000005	0.86	0.86	0.2	0.48	0.00048	used 1% to dilute
0.01	0.0000005	0.086	0.09	0.02	0.048	0.000048	used 0.1% to dilute

The gypsum concentration versus electrical resistivity data in the second part of the geochemical study (see Table 2.7) will be used in the interpretation of the results from the geophysical investigations and also for the sinkholes scenario development.

CHAPTER 3

RESULTS AND DISCUSSION

3.1 Regional geology of the study area

The general near–surface geology in the study area comprises mainly unconsolidated sediments. There are hills made of sedimentary rocks in the north and south. The Department of Mineral Resources, Bangkok, classified the rock units in this area as following (DMR, 2011; Figure 3.1a):

Carboniferous-Permian (CPk) can be found as mountain in the north parallel to mountain in Permian age. It is classified in *Kaeng Krachan Group* that composed of shale, with intercalated sandstone and siltstone, shale with interbedded sandstone, chert, feldspathic sandstone, tuffaceous sandstone, quartzose sandstone, pebbly shale, and pebbly mudstone, dark gray, greenish gray and brown. *Permian(Pr)* can be found at mountains along a north-south trend. It was classified in *Ratburi* Group which composes of limestone dolomitic limestone, with nodular and bedded chert, dolomite and abundant fossils (*Fusulinid, Brachiopod, Bryozoa, Coral and Bryozoa*). *Triassic Lampang Group (TRl)* composed of mudstone, limestone, sandstone, silstone, conglomerate, with *Halobia sp.*, *Daonella sp.*, and *Claraia sp..* *Lam Thap Formation (JKl)* and *Phun Phin (Kp)* were classified in *Trang Group* in the vicinities of Thung Yai and Khlong Thom Districts (Teerarungsigul, 1999). The *Lam Thap Formation* is composed of sandstone, Arkosic and lithic, mudstone, siltstone, reddish brown, cross-bedded, conglomerate and sandstone in the upper part; fresh and brackish water bivalves in the lower part. Whereas the *Phun Phin Formation* consists of red siltstone with interbedded trough cross-bedded brownish red Arkosic sandstone (Meesook et al., 2002). *Quaternary* is comprised of unconsolidated sediments, which can be divided in two groups, alluvial deposits composing of gravel, sand, silt and clay, and terrace deposits composed of gravel, sand, silt and lateritic soil.
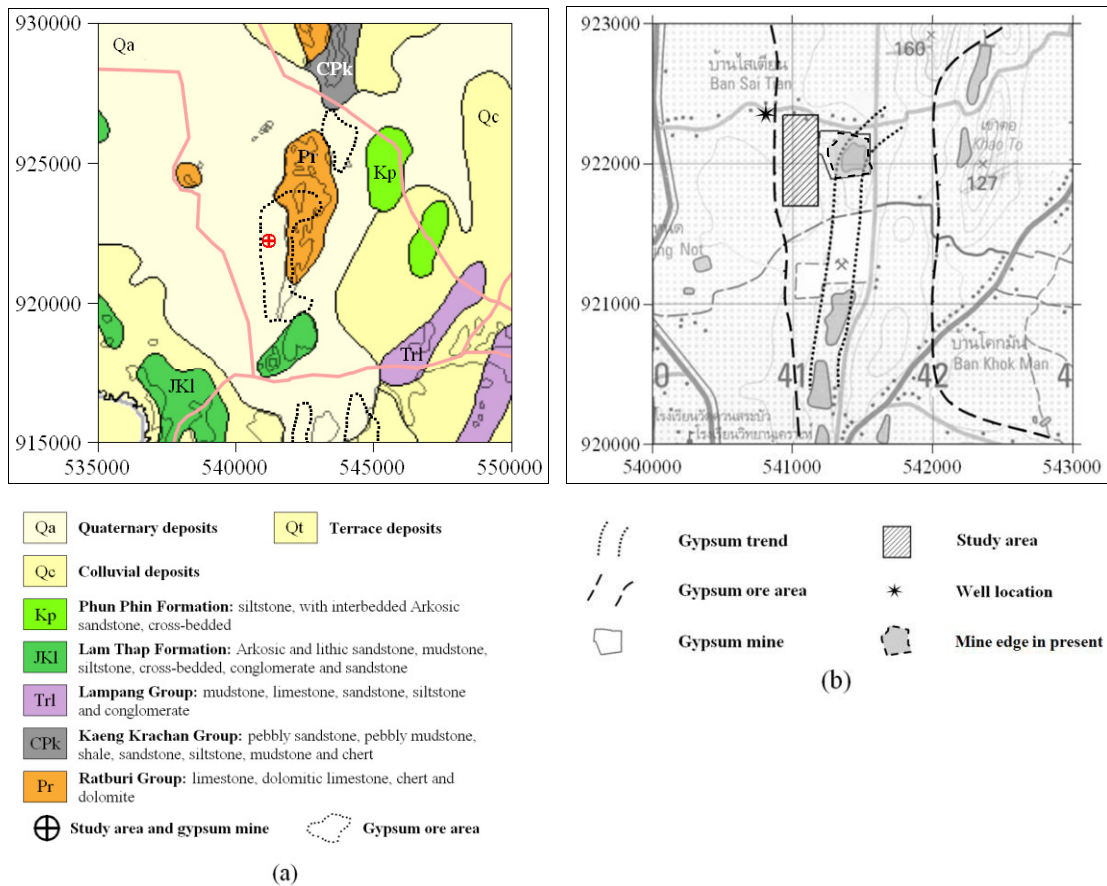
Figure 3.1 General geology of the study area showing the main rocks (a) and the discovered boundaries of a potential gypsum trend area (b), modified from, Rattanajarurak (1994), and Kheunkhong (2001).

The general geology of Ban Tarang-Khao To, where the gypsum mine and study area are located, comprises of sedimentary rocks of the Late Paleozoic, which can be classifies as following. Khao Hun formation is in Lower Permian age composed of sandstone, and reddish brown shale. It was found as Khao To Hill located in the middle of the study area. Ratburi Group in the Permian age composed of gray limestone insert and shuffled with shale layers and a conglomeratic limestone layer. These rocks make the limestone hills. Sediments of Quaternary age composed of unconsolidated gravel and sand.

Gypsum ore in southern Thailand is indicated its deposit in Lower Permian age in a trend in north to south direction west of Khao Luong and Khao Yai

Mountain in Surat Thani to Nakhon Si Tammarat Province with its layering related to Khao Hun Formation and Ratburi Group (Rattanajarurak, 1994).

The gypsum potential source area covers a trend parallel to the Permain outcrops of the mountains along a north-south direction (Figure 3.1a). The general trend (Figure 3.1b) is in average about 50 meters wide and approximately 25 meters thick with a dip of 45-70 degrees. It is suggested that the gypsum layers form an anticline structure (Rattanajarurak, 1994; Figure 3.1b).

3.2 Geology of the gypsum mine

The origin of the gypsum in Thailand was formed by rehydration at the top of the anhydrite and a mineralogy study indicated that there has been many times a change from gypsum to anhydrite and back (Utha-aroon and Ratanajarurak, 1996). Many of the information were revealed during mining in the past, including geological structures of gypsum and anhydrite. The overall mineralogical features of this mine are gypsum under a surface layer of laterite and anhydrite under gypsum. Gypsum is classified in two parts that is high quality gypsum without impurity and one with high impurity such as grayish black shale inserted in gypsum caused by faults crossing across in the mine area (Figure 3.2).

The unconsolidated sediments are 4-7 meters thick, mainly a laterite layer covering the gypsum layer. The uppermost near–surface layer is 1-2 meters thick (Figure 3.3 and 3.4) composed of well sorted silt to fine sand, light gray, light yellow and light brown. The layer below is 3-5 meters thick, lateritic soil, which is a clay–sediment mix with gravel, which has been formed from iron oxide to be rather round concretion. The general feature of this soil texture is yellowish brown, reddish brown and tan, with high iron oxide in soil. There is further concretion gravel with an average diameter of three centimeters with mixed less than 25% in soil.

The thickness of the gypsum layer is in average 19 meters. Most gypsum is alabaster; its feature is aphanitic with soft texture, tiny grain size of about 0.5-1.5 mm, generally white to light gray and some 15 cm wide straight gray bands inserted alternating. The top gypsum surface is undulant and generally has holes

caused by groundwater flow. The strike of the gypsum structure in the mine is around N010E–N020E (Figure 3.1b); its dip is between 70–75 degrees (Figure 3.3). The high impurity gypsum is in a zone where gypsum experienced tectonic forces that caused breakage in the NE part of the ore deposit. The gypsum was broken apart in small to big pieces and generally spread to the carbonaceous shale where a zone of large fault crosses through (Figure 3.2). Carbonaceous shale is dark black, has an aphanitic texture and is mixed with silt. About one mm. pyrite crystals occur together with the broken carbonaceous shale, which is inserted in the fractured gypsum (Figure3.2).

Large faults pass through the gypsum mine causing two gypsum facieses to be found. The main fault is a horizontal plain in direction N050E and N010E (Figure 3.2) with a dip almost vertical (Figure 3.3). Another small one is in direction N060E and N035W (Figure 3.2). These faults caused many fractures inside the gypsum layer.
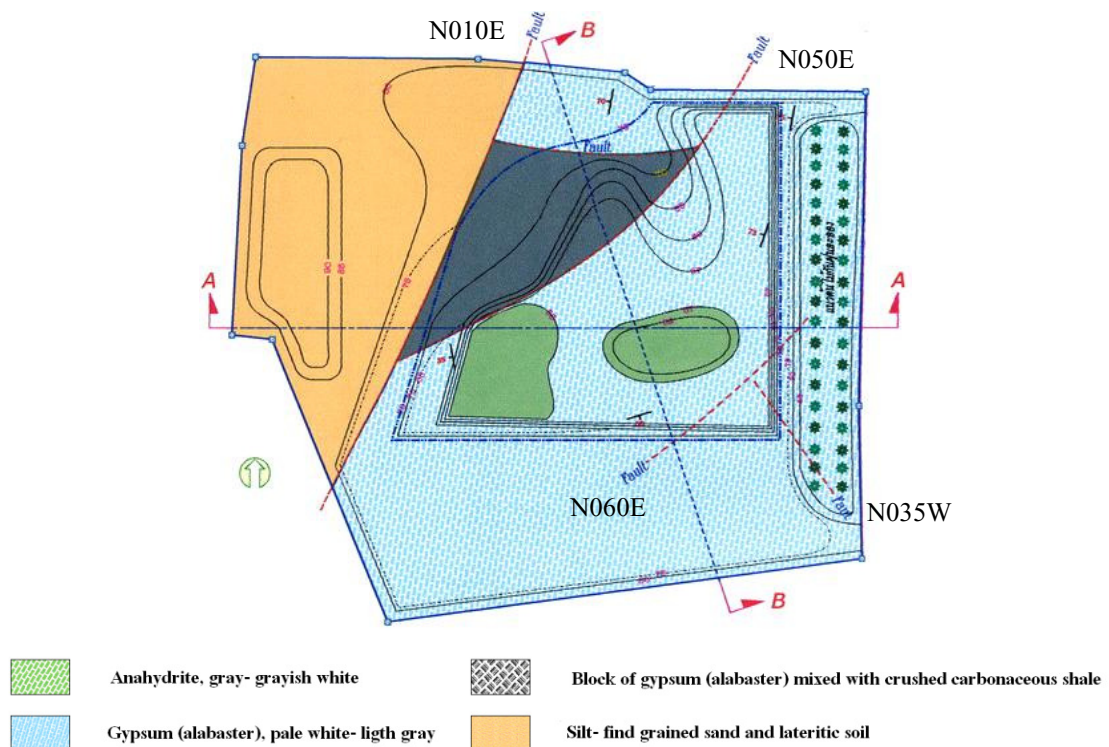
Figure 3.2 Overview of gypsum mine geology (from Saelea, 2004).
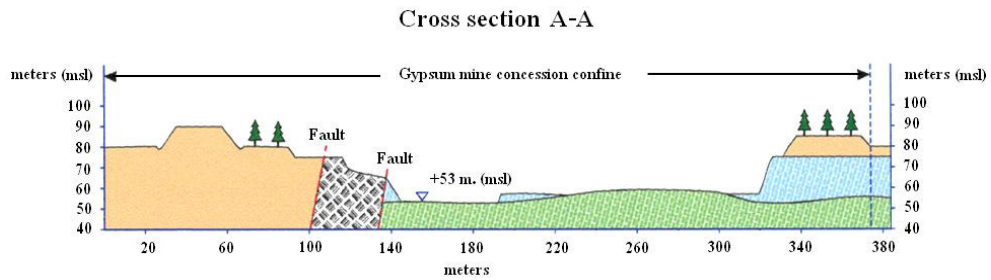
Cross section A-A

Figure 3.3   Geological cross section line AA' (see Figure 3.2) shows gypsum layer overlaying on anhydrite in East-West direction (from Saelea, 2004).
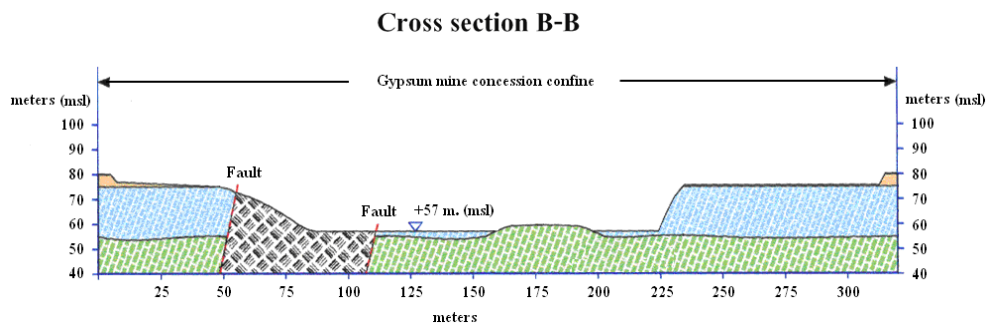
Cross section B-B

Figure 3.4   Geological cross section line BB' (see Figure 3.2) shows gypsum layer overlaying on anhydrite in NW-SW direction (from Saelea, 2004).

From the study the mine geology can be summarized as shown in Figure 3.5. The gypsum layer is about 19 meters thick with about dipping 72˚ overlaying on the anhydrite layer. The anhydrite layers in the mine will be continuing in the west side of the mine, due to the continuity of the undulant anhydrite layer, which is revealed outside the mine in the west (Figure 3.6). It seems to be dipping-continuation in the west because it still in the gypsum potential area (Figure 3.1b).
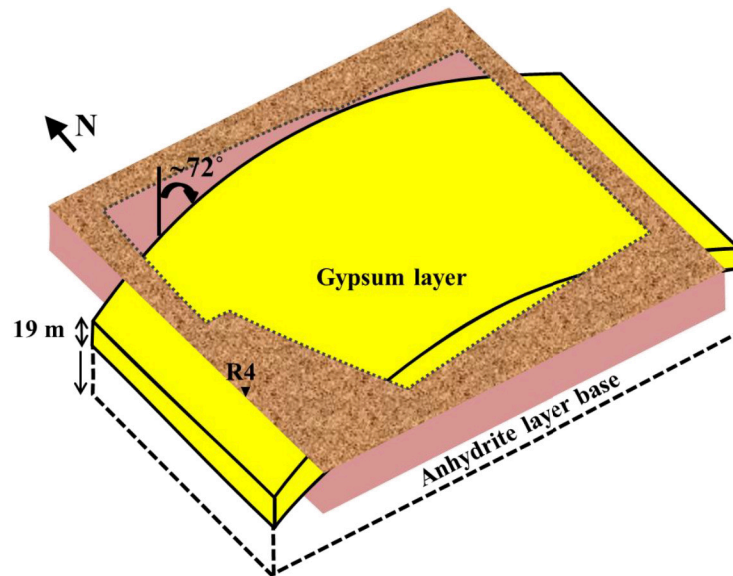
Figure 3.5   Schematic diagram of the structure in the gypsum mine.

Figure 3.6   Continuation of the rough anhydrite outside the active mine (rectangular dash) and it maybe dipping (dash arrow) to the west (arrow).

3.3 Sinkholes

In the Tha Yang Sub-district, Thung Yai District, Nakhon Si Tammarat Province, two larger sinkholes occurred and their subsurface feature was disclosed through their open hole. The first one with 15 meters in diameter and 10 meters depth occurred in January 2005 (Figure 3.7, left). The top surface is unconsolidated crumbly clay and the ground water is at about 5 meters depth from the surface. In June 2009, on another field survey the first sink hole was already partly filled with clay from the

near surface (Figure 3.7, right). The development of the second was observed in this month with ground subsurface of about 0.7 meters (Figure 3.8, left). In August 2009 the second sinkhole had already been formed to be 19 meters deep with 5 meters in diameter (Figure 3.8, right). The top dense clay at the near surface can be directly seen at the inside surface of the hole and the groundwater is at around 9 meters depth from the surface. Both sinkholes were about 100 m apart from each other, and about half a kilometer away from an active gypsum/anhydrite mine (see Figure 2.5 in Section 2.5).

Figure 3.7   First sinkhole occurred in January 2005 (left) and later in June 2009 partly with clay filled in (right).

Figure 3.8   Ground subsidence observed in June 2009 (left) and the development to sinkhole in August 2009 (right).

In 2009, the gypsum in the mine was exhausted with the anhydrite remaining at a depth of about 40 to 45 meters (Figure 3.9, left). The subsurface layers of the nearby study area can be clearly seen at the steep high face of the open pit mine. Figure 3.9 shows the direction where the sinkhole occurred in the west as well as the opposite side in the east, with no visible differences near the resistivity R4 measurement point (see Figure 2.6 in Section 2.6). A 12 to 14 meters thick unconsolidated clay cover was found on top of a 24 to 30 meter thick anhydrite layer (Figure 3.9, left). This correlates with the opposite site that reveals two layers of clay with 12 meters thickness overlaying on the anhydrite (Figure 3.9, right). A closer look at the top of the anhydrite surface at the western side of the mine, in the direction of the sinkhole occurrence, shows that the top of anhydrite is extremely rough (Figure 3.10, right) and have been fragmented due to weathering processes. It can be assumed that this surface was in contact to the groundwater flow for some time before the opening of the mine. At the southern mine side a cross cut through an already filled sinkhole (Figure 3.11, left) can be seen, probably of historical or geological age. The surface diameter must have been around 20–30 m with main parts of the sinkhole are filled with clay (Figure 3.11, Right), so that at the surface the sinkhole can not be identified anymore. However still open holes of a few meters in size in the anhydrite can be seen about 10 meters below the surface.
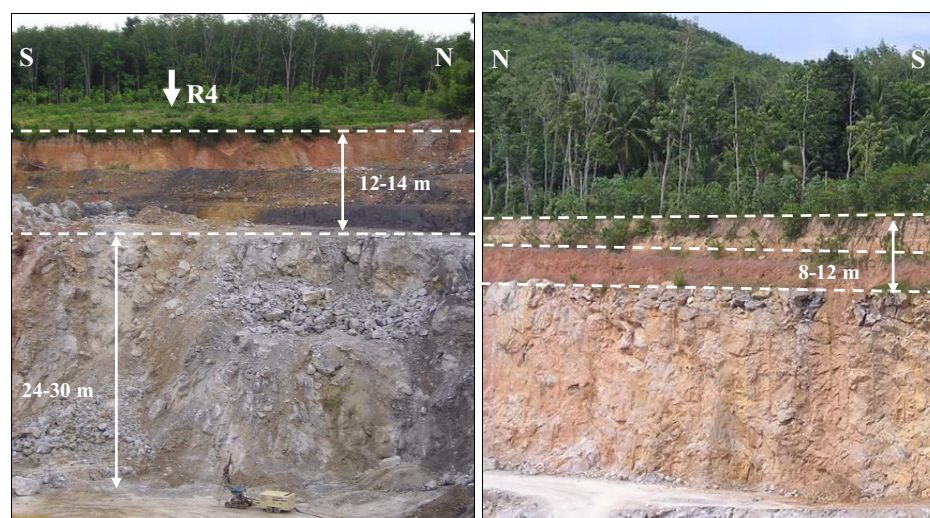
Figure 3.9 Geological cross section at the gypsum mine at the sinkhole side (west, left) that correlated to opposite 12 to 14 clay layering on anhydrite.(right)

Figure 3.10 Rough and fragmented, weathered anhydrite (right) of the top surface at the western side (left).

Figure 3.11 At the southern side of the mine a sinkhole of historical or geological age (left) filled with clay and still open holes in the anhydrite (right).

3.4 Rock sample description

Several rock samples, anhydrite and gypsum, shown in Figure 3.12 were collected from the mine area with permission. They show different features and different state of weathering mainly as a result of their contact with groundwater or water in the mine.

Sample (a): Anhydrite with mainly gray color and clearly seen small white grains. The sample is hard and its edges are rather sharp and the surface cannot be scratched with a fingernail.

Sample (b): Anhydrite with alternation of gray and white colored bands. Clearly seen are the small grains. The sample is hard and the edges are sharp. It cannot be scratched with a fingernail.

Sample (c): Gypsum (see Section 3.6); the sample's colors are mainly gray mixed with white grains together. It is rather hard and it edges are rather round and cannot be scratched with a fingernail.

Sample (d) Anhydrite (?) with light gray to gray color with some white small grains in layers inserted; the grain size of the gray minerals is larger than of the white ones. The sample shows signs of beginning weathering, as small grains easy get off the rock's surface. The sample is not quite hard, its edges are round and the white surface is easier to scratch with a fingernail than the gray one.

Sample (e): Anhydrite (?) sample with very light gray small grains and small white grains. This sample also shows signs of abrasion as a result of weathering; further it is not quite hard and all surfaces can be scratched with a fingernail.

Sample (f): Anhydrite (?) sample with white color. It seems to be weathered but it is not quit soft. The edges are round and it can be scratched with a fingernail.

Sample (g): Gypsum (see Section 3.6) of white color; the small white grains, which look like compacted sugar, can be clearly seen. The whole sample seems to be weathered. It is quite soft by touching it, and some of the small white grains fall out easy. The sample can be scratched with a fingernail. The edges of the sample are quite smooth and round.

Sample (h): Gypsum sample, colorless and transparent. It shows perfect cleavage. The sample is not weathered and it can be easily scratched with a fingernail.

Figure 3.12   Photos of the rock samples from the gypsum mine with anhydrite of various weathering stages and structures, Sample (a) and (b); gypsum, Sample (c), (g) and (h), others might be anhydrite or gypsum or mixture of both.

3.5 Density of rock samples

For the density determination Sample (b), (c), (g), and (h) were chosen. The different density values of the samples with and without silicone glue covering for waterproof are shown in Table 3.1. Further details are given in Appendix E., Table E.12 and E.13. Differences in the values between the measurements with and without glue cover are related to accessible pore space. Without glue cover some water can enter the pores and by this increases the weight and subsequently the bulk density. Therefore, the data with glue cover likely to be closer to the real bulk density.

Table 3.1   Bulk density of anhydrite (a) and gypsum samples (c), (g), (h) with and without glue-cover and calculated porosity.

Sample	Bulk density (without glue cover) (g/cm^3)	Bulk density (with glue cover) (g/cm^3)	Porosity (calculated)* (%)
(b)	2.93	2.94	0.8
(c)	2.26	2.21	4.1
(g)	2.09	1.96	15
(h)	2.29	2.29	0.7

* based on single crystal density values with 2.963 g/cm^3 for anhydrite and 2.305 g/cm^3 for gypsum (Schön, 1996), and related to bulk density values with glue cover.

The bulk density values measured here are in good agreement with data from other studies, with mean density values of anhydrite 2.963 g/cm^3 and gypsum 2.305 g/cm^3 (Schön, 1996). Sample (b) is a fresh anhydrite and Sample (h) is a non–weathered gypsum sample. Sample (c) and (g) are both weathered gypsum samples (see Section 3.6), with the latter sample more weathered than Sample (c). The weathering comes with the dissolution of the sulfate minerals and by this increase the porosity of the samples (Table 3.1). This results in a lower bulk density as shown in Table. 3.1. The weathering also results in lesser grain–grain contacts that make the samples more susceptible to abrasion. The density reduction and porosity increase due to weathering is significant with up to 15% porosity for Sample (g), which is still an intact rock.

3.6 X-ray diffraction identification of the weathered anhydrite

Although Sample (c) and (g) were initially indicated that they are weathered to high weathered anhydrite from considering the rock features and their bulk density values which are ambiguous of anhydrite state while comparing to the bulk density of Sample (h), gypsum, there seem to be deformation (rehydration by contacting to groundwater) to gypsum as shown by their lower bulk density value than that of gypsum.

Therefore powder X-ray diffraction technique was used to identify the composition of two assumed weathered anhydrite samples (see Figure 3.13 and 3.14) by comparing them with the reference peak pattern of gypsum JCPDF no.01-074-1433 (see Appendix E, Figure E.). All expected peak positions and relative intensities of both weathered anhydrite sample on the diffractogram (see Figure 3.13 and 3.14) were considered to be excellent matches with the reference diffracted pattern of gypsum and there are no peaks that are unaccounted for in either the experimental or the reference data. Therefore the state of the weathered anhydrite using XRD technique indicated that both of them deformed already to gypsum by rehydration.
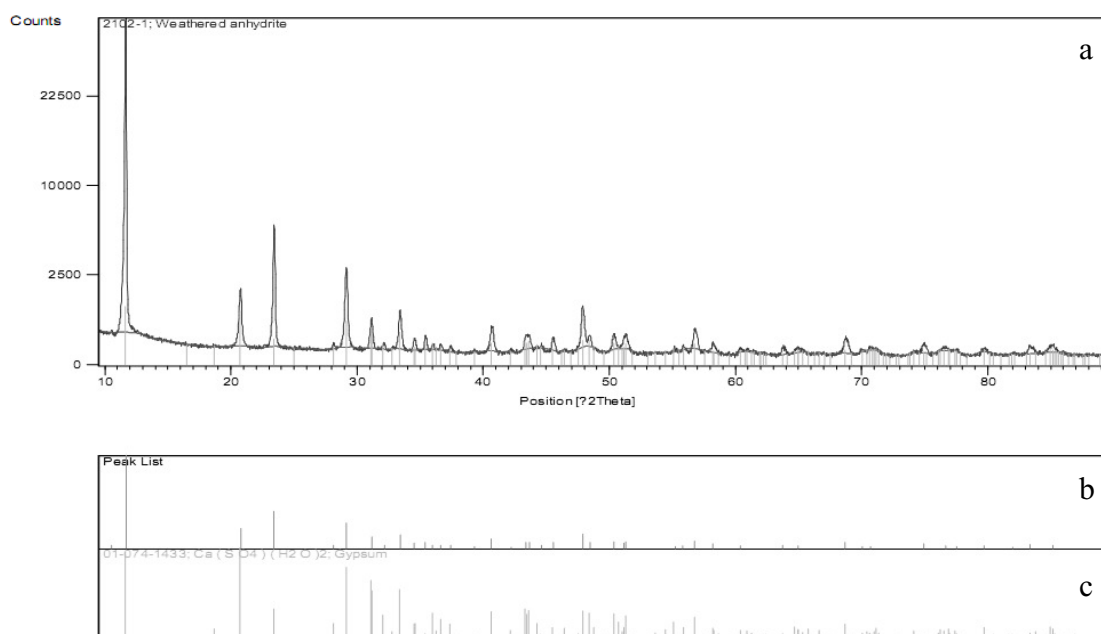
Figure 3.13 Powder diffractogram (a) and its identified peak pattern (b) of anhydrite sample (g) matching with the reference pattern (c) of gypsum.
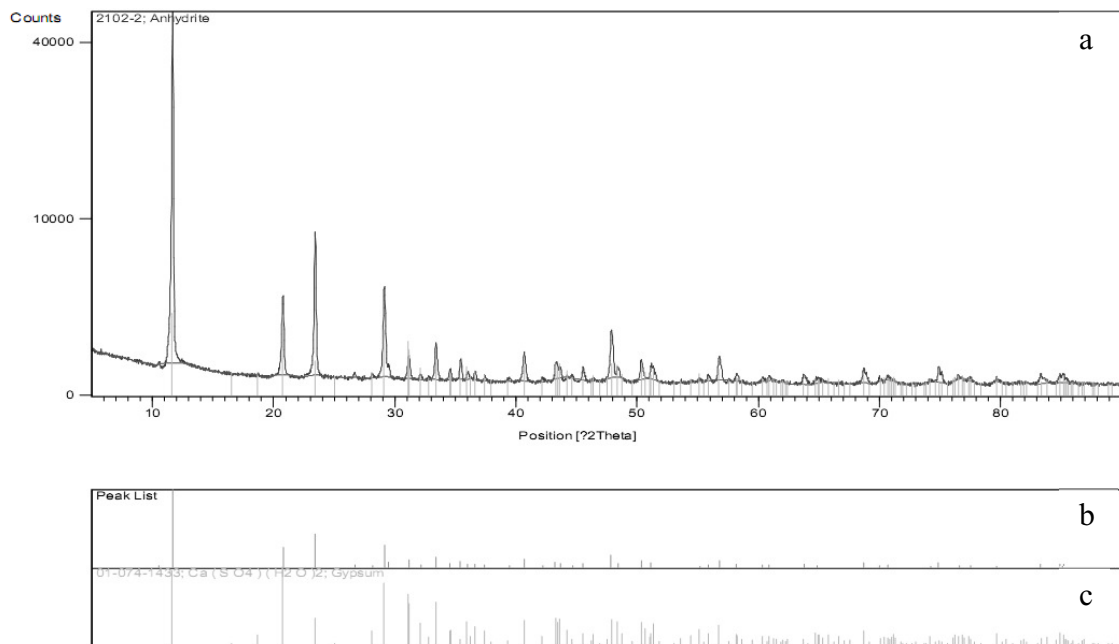
Figure 3.14   Powder diffractogram (a) and its identified peak pattern (b) of anhydrite sample (c) matching with the reference pattern (c) of gypsum.

3.7 Assumptions on hydrogeology

From water level information in the mine and the study area and the relative horizontal and vertical distances between the sinkhole and the mine the flow direction of the groundwater at the study area has been considered. The water level in the second sinkhole was found at about 9 meters (Figure 3.15, top left) from the surface. Also a private well a few hundred meters further NNW provided such depth about 6 meters below surface at its location 540809E and 922358N. At 40-45 meters at the base in the mine there was no groundwater (Figure 3.15, top right). From these data a gradient can be assumed of the groundwater flow down from the sinkhole to the base of the mine relative below in west to east direction (Figure 3.15, bottom).
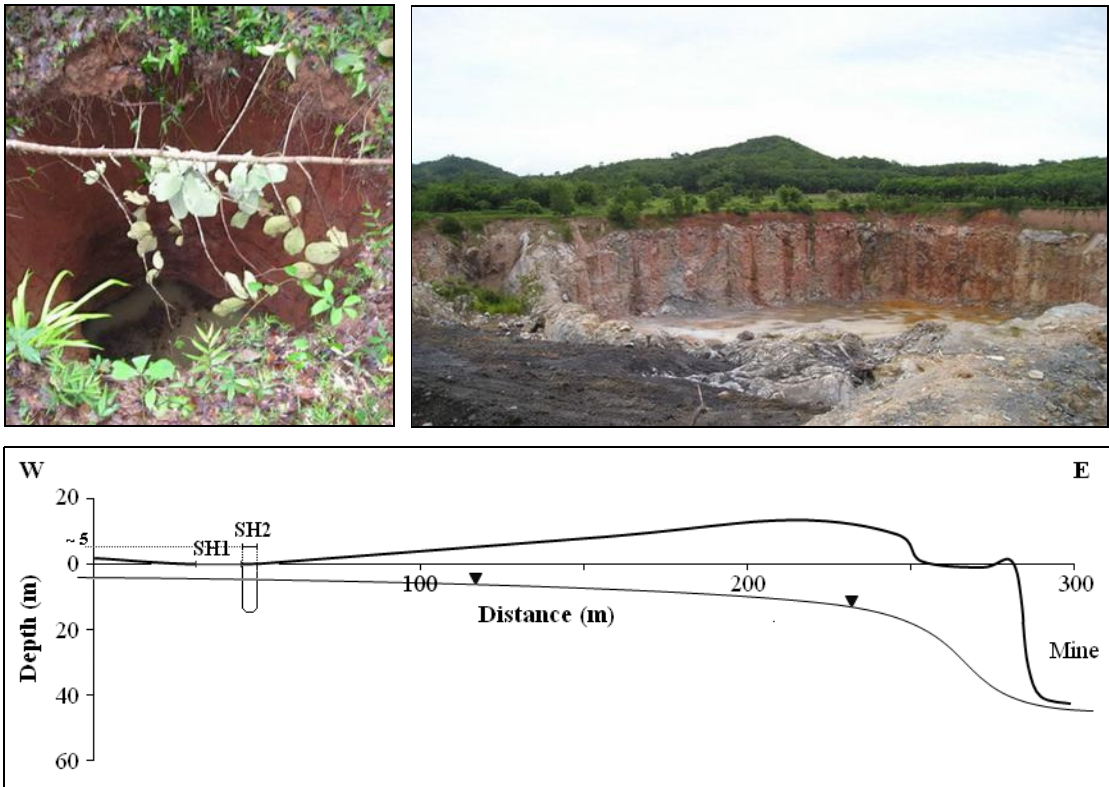
Figure 3.15   Proposed groundwater level (▼) in a cross section (bottom) from the second sinkhole in the west (top right) to the gypsum mine in the east (top left). The second (SH2) sinkhole is higher than first (SH1) around 5 meters.

3.8 Geophysical investigations

3.8.1 Resistivity imaging subsurface characterization

The resistivity data interpretation resulted (Table 3.2) in five layers at each of the four measurement points (Table, 3.2, Figure 3.16).
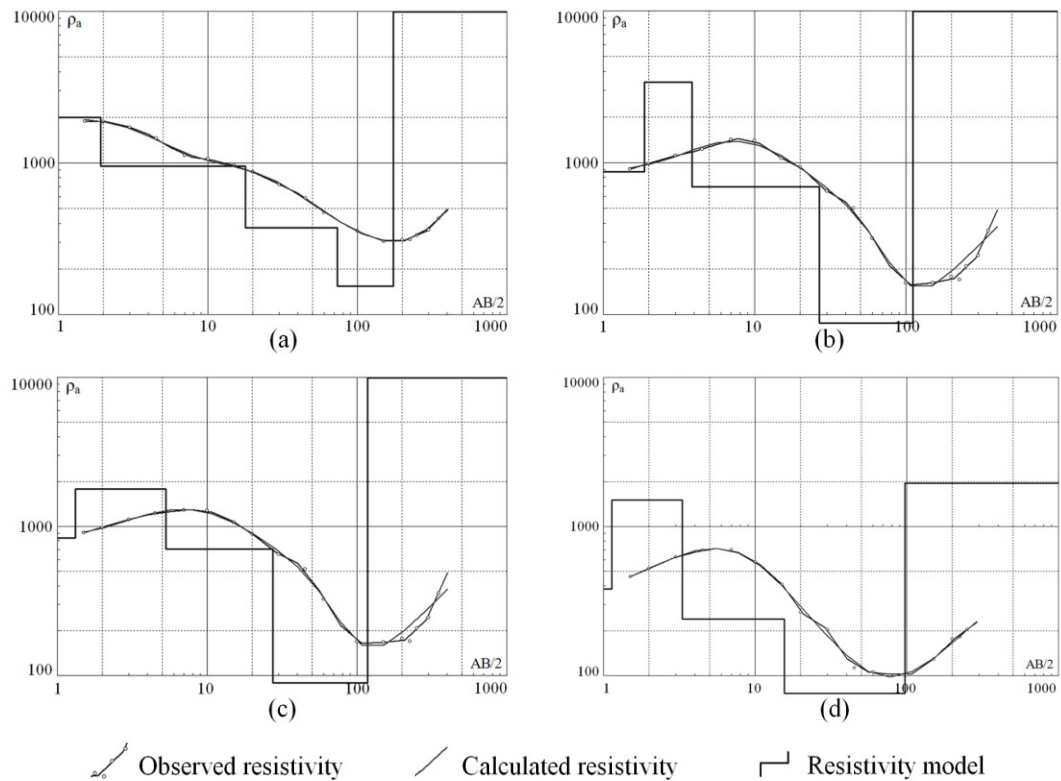
Figure 3.16   VES sounding curves of point R1 to R4.

The two upper most layers have a resistivity of about 1,000 and 1,900 ohm-m with 1-2 and 1-16 meters thickness. For all VES points they are likely to be clay and sandy clay layer, respectively. Inside the first sinkhole the sediments can be seen but without to be able to separate a layer 1 from layer 2 (Figure 3.7). The third layer has a resistivity of about 240-700 ohm-m with 10-39 meters thickness; it may be sand and/or lateritic soil (Figure 3.9). The fourth layer has about 76-154 ohm-m with 45-70 meters thickness; this layer likely to be weathered anhydrite/gypsum (Figure 3.10, right) because the weathered layer will have more interconnected pore containing water, which will result in low resistivity values following Archie's law (Equation 2.16). Beck and Herring (2001) gave resistivity values of 100 to 150 ohm-m for a highly weathered gypsum layer. The last layer has a very high resistivity about 31,000 ohm-m and it is likely to be massive anhydrite or carbonate with no or almost no water content. After Guinea et al. (2010), a non-weathered gypsum layer with 100% purity would have a resistivity value about 1,000 ohm–m.

Table 3.2   Interpretation results of the resistivity measurements with resistivity (ohm–m) and bottom depth values (m) of each layer.

Layer	R1 point Resistivity (ohm-m)	Depth (m)	R2 point Resistivity (ohm-m)	Depth (m)	R3 point Resistivity (ohm-m)	Depth (m)	R4 point Resistivity (ohm-m)	Depth (m)
1	1998	2	868	2	838	1	382	1
2	956	168	3381	4	1785	5	1509	3
3	373	73	692	27	702	27	239	15
4	154	173	83	110	89	117	76	97
5	32644		46492		45699		1959	

The layers from the resistivity results (Figure 3.17, top) show an increase in the depth from east to west and especially steep increase depth between measurement point R1 and R2, the area where the first and second sinkhole occurred. There is a continuity of the geology structures from the mine to the sinkhole area, which can be seen from the resistivity good correlation of the resistivity values at point 4 (R4) and the geology from the wall at the west side of the mine (Figure 3.17, bottom).

The first upper three layers comprise top soil, possibly laterite and sandy clay with a combined thickness of 12 meters. Below that depth, the mine face reveals solid anhydrite, probably with some gypsum. The boundary is the exposed rough surface in the mine (Figure 3.10). As mentioned earlier, this is likely due to interaction with groundwater and subsequent weathering and erosion. Therefore it can be assumed that the anhydrite layer (layer 4) is also weathered indicated by lower resistivity values (76–154 ohm–m). In the mine itself water can be seen seeping out from the faces at several locations and depth levels. From the resistivity depth data it has to be assumed that the lowest layer, the high resistive layer 5, is not exposed in the mine, which might be solid anhydrite rather than carbonates due to the high to very high resistivity values (about 2,000–45,000 ohm–m). However, the depth value of the interface between layer 4 and 5 might be found somehow up due to the high resistivity contrast between both layers, almost hundred to thousand times. The electrical current would preferable follow layer 4 rather than layer 5 and by this distorting the depth value in the interpretation (see also Ernston and Kirsch, 2006).

At R4 the resistivity values for layer 5 are much lower than for the other resistivity points. This might be related to an increased weathering due to the

proximity of the excavated mine, or changes in lithology, like more gypsum in the anhydrite.
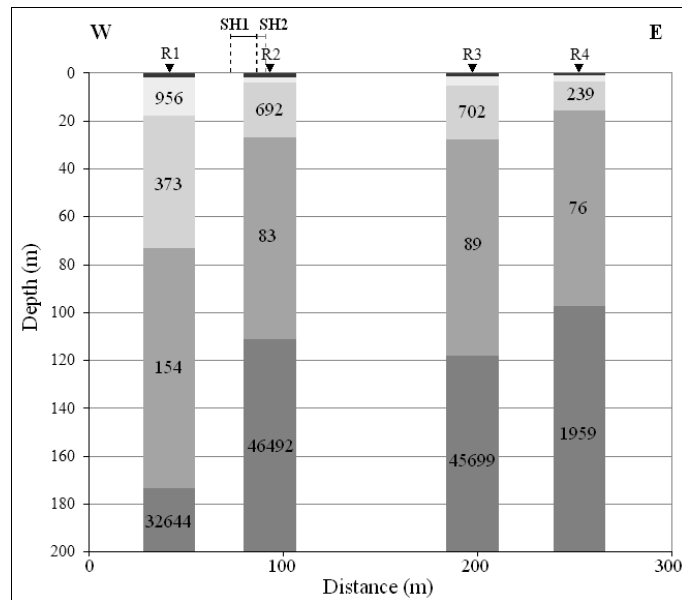
Figure 3.17   Subsurface structure from resistivity interpretation (top), which can be correlated to the geology survey around and inside the mine, a sandy clay layer overlay on the anhydrite. R4–resistivity survey point no. 4.

3.8.2 Seismic refraction interpretation

The results of two seismic refraction lines along a small pathway parallel to the first and second sinkhole in north to south direction provided information down to a depth of about 8 m. The survey line parallel to the 1st sinkhole revealed two layers, which can be seen inside the first sinkhole (Figure 3.9) that are clay and sandy clay with a P–wave velocity of 384 m/s and 699 m/s. The third layer below 8 m depth shows a velocity increases to 1,665 m/s; this layer might be a clayey,

a clayey sand, or a sandy layer, or a groundwater in a sandy clay or sand layer, or a lateritic soil layer (Figure 3.18).
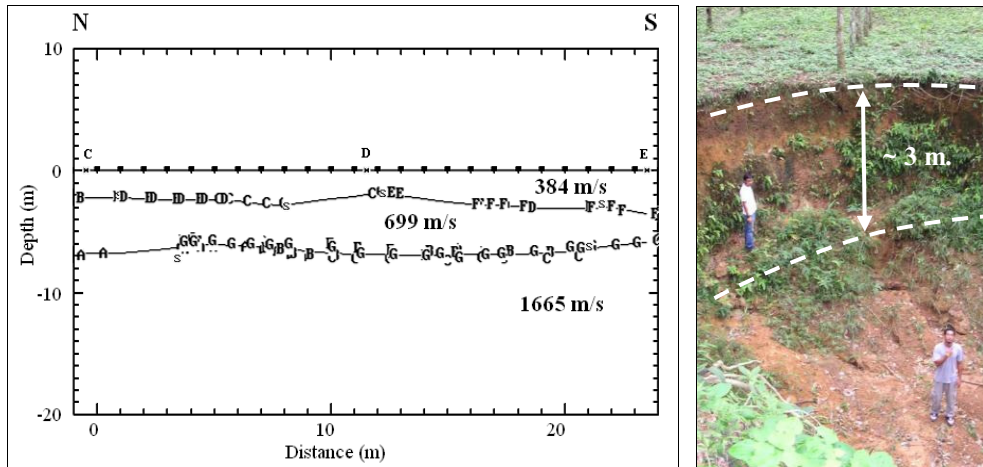
Figure 3.18   Subsurface structures from refraction interpretation parallel to the first sinkhole with three layers.

An overall similar picture is provides by the second line parallel to the second sinkhole. At the top there are two layers of clay or sandy clay with velocity 360 m/s down to 9 meters depth and below is a layer with 1,493 m/s velocity (Figure 3.19). At 9 m depth is also the water level in the second sinkhole (Figure 3.15, top left). Interestingly, the resistivity survey is not indicating an interface with related resistivity change (decrease) at this depth.
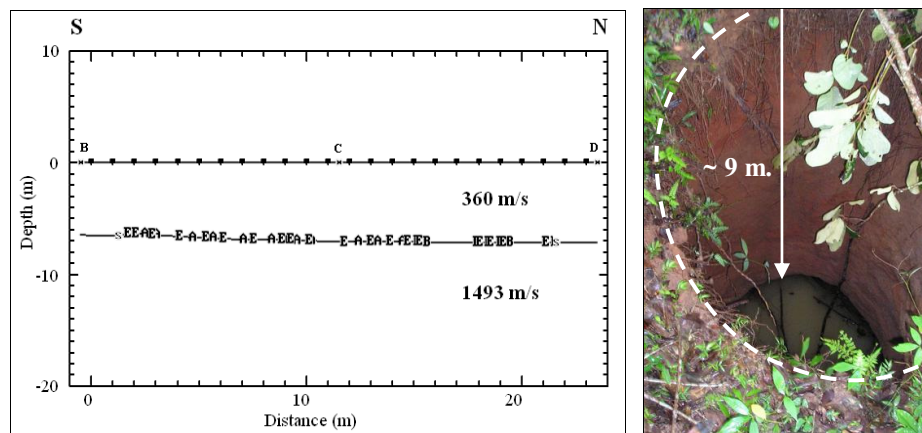
Figure 3.19   Subsurface structures from refraction interpretation parallel to the second sinkhole with two layers.

During the first refraction survey near the first sinkhole, the offset was extended up to 96.5 meters (see Appendix E, Table E.9) showing no change in the third layer velocity (Figure 3.20) and indicating that the layer is not relatively thin. Therefore, it might be more likely to have a more lateritic sand/clay layer (maybe also more compacted) with some groundwater, not an aquifer, resulting in overall higher seismic P–wave velocities and higher resistivity values of about 700 ohm–m.
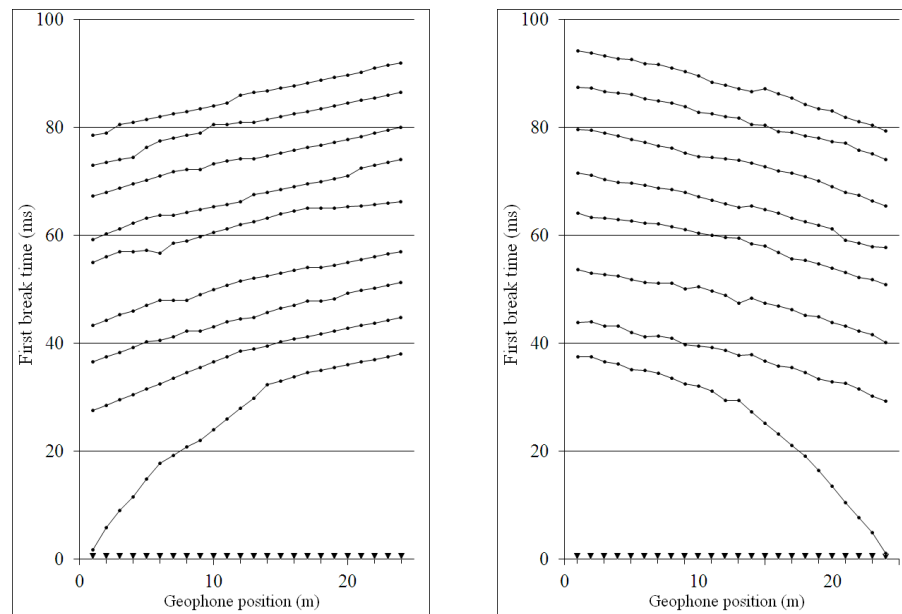
Figure 3.20   17-shots with 96 meters extended offset of seismic refraction survey for considering the thick and its velocity of the 3rd layer.

3.8.3 Seismic reflection interpretation

Two seismic reflection sections parallel to the refraction survey lines near the first and second sinkhole can be correlated with each other and reveal the interface between the lateritic layer and the weathered anhydrite/gypsum layer. At the first sinkhole the reflection section disclosed three main reflectors at depths of 25, 35, and 42 meters with an interval velocity of 1,800 m/s (Figure 3.21) and a thickness of 15 to 25 meters. The seismic reflection section at the second sinkhole also shows three reflectors with an interval velocity of 1,850 m/s at depths of 32, 50, and 60 meters (Figure 3.22) and a thickness of 25 to 30 meter. The reflector depths at the first sinkhole correlate with the depth of the interface from the resistivity survey at about

23 m, which was interpreted as weathered gypsum/anhydrite. The interval velocities of about 1,800 m/s are in agreement with the seismic refraction data, as below 8–9 m the seismic P–wave velocities are already at 1,500–1,600 m/s (see Section 3.7.2).
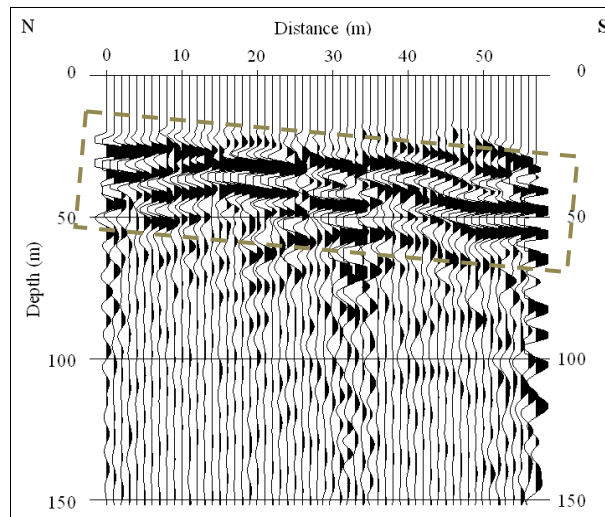
Figure 3.21 Three main reflectors (in dash box) of the seismic reflection section at the first sinkhole, interpreted as weathered gypsum/anhydrite layer at a depth of 25 meters.
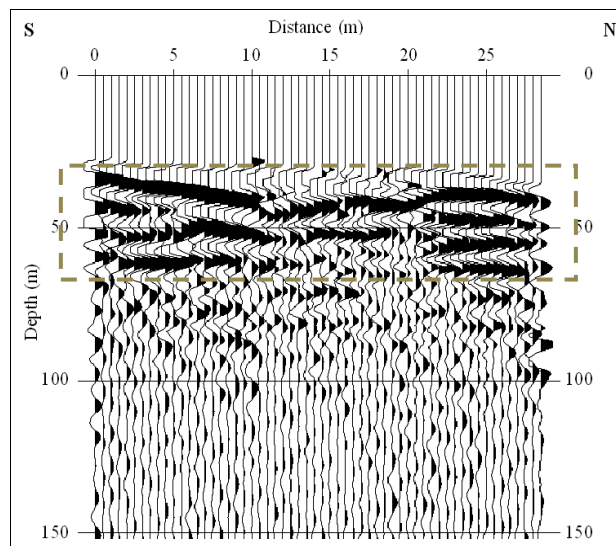
Figure 3.22 Three main reflectors (in dash box) of the seismic reflection section at the second sinkhole, interpreted as weathered gypsum/anhydrite layer with their velocity close to the reflector at the first sinkhole.

Both seismic sections reveal that the reflectors are not continuing over the length of the survey. For the reflector at the top of the anhydrite/gypsum layer it can be related to the surface roughness as revealed in Figure 3.10. The deeper reflectors might be explained by differential weathering both in horizontal and vertical direction. The velocity of a dense anhydrite/gypsum layer with less or no porosity is very high (~3,500 m/s, Table 2.4). Weathering through groundwater contact will increase the porosity resulting in a decrease of the bulk density (see Section 3.5) and by this decreasing the seismic velocities. As the groundwater might mainly comes from the top of the anhydrite/gypsum layer a decrease in the weathering with depth can be expected. However, the weathering front is not a clear boundary due to spatial differences resulting in non–continuous reflectors.

3.8.4 Self-potential interpretation

After drift correction the SP values were considered for a correlation between elevation and the self-potential values as shown in Figure 3.21. A linear regression analysis shows a poor correlation between both values with R^2=0.1268, which is not significant. A closer look and considering especially the SP values of the long survey line with its elevation (Figure 3.24), there seems to be a significant correlation beginning at 1.5 meters height. The SP values show an inverse trend compare to the elevation with a relatively good correlation of R^2=0.5423. Therefore, a topographic correction was applied to the SP values measured along the long line (see Table 2.6 in subhead 2 of Section 2.9.2). The resulting topography corrected SP values are in general lower than without the correction (see Figure 3.25), however, the main differences between different SP measuring points remain. Further, this correction results in clear negative SP values around the second sinkhole (see Figure 3.25 and 3.26).
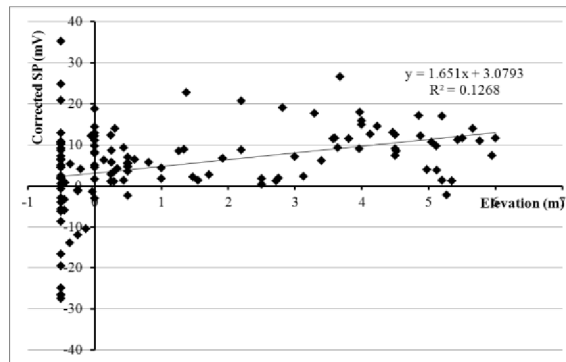
Figure 3.23   Correlation with linear regression analysis between all self-potential values (in mV) and related elevation (in m).
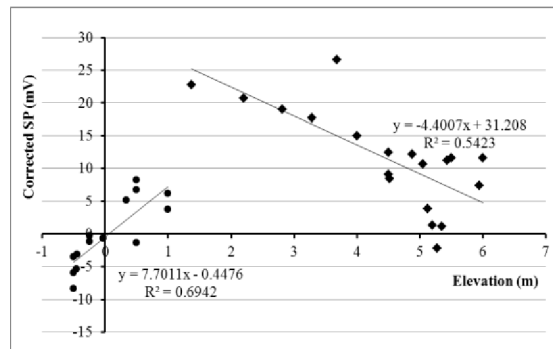
Figure 3.24   Correlation between self-potential values (in mV) and the related elevation (in m) beginning at 1.5 meters height on the long line, which is in north–south direction.
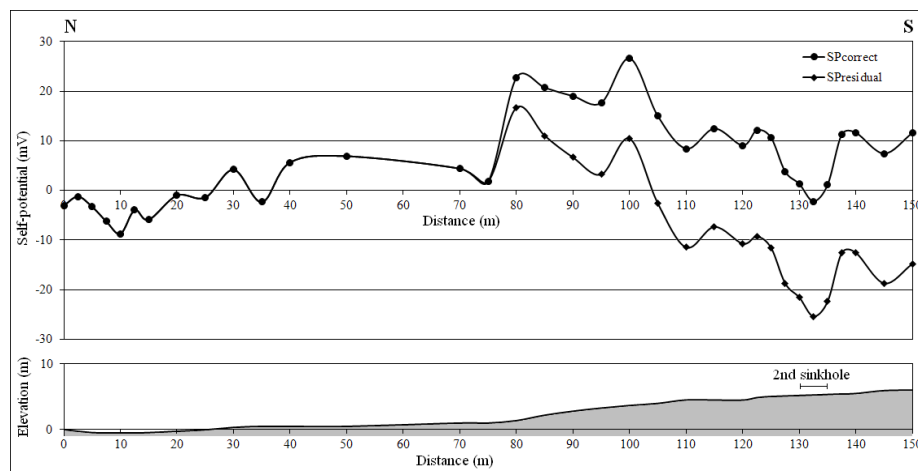
Figure 3.25   SP values after corrected topographic effect ($SP_{residual}$) and SP values with no topographic correction applied ($SP_{correct}$) on the long line parallel to the mine in north-south direction.

A contour map of all SP data without any topographic correction and with topographic correction is shown in Figure 3.24 left and right, respectively. For further interpretation the topographic corrected SP contour map is used. The SP contour data indicate different zones with positive and negative SP values. This result from differences in the streaming potential coefficient where water flow takes place across boundaries between different geological media (Figure 3.26, right; see also Section 2.9). The negative SP values are the result of the water flowing down from the surrounding area into subsurface holes. In general, the lower and negative values of self-potential survey were observed with a N–S trend parallel to the dip of weathered sulfate layer (see Figure 3.5 and Figure 3.17, top).
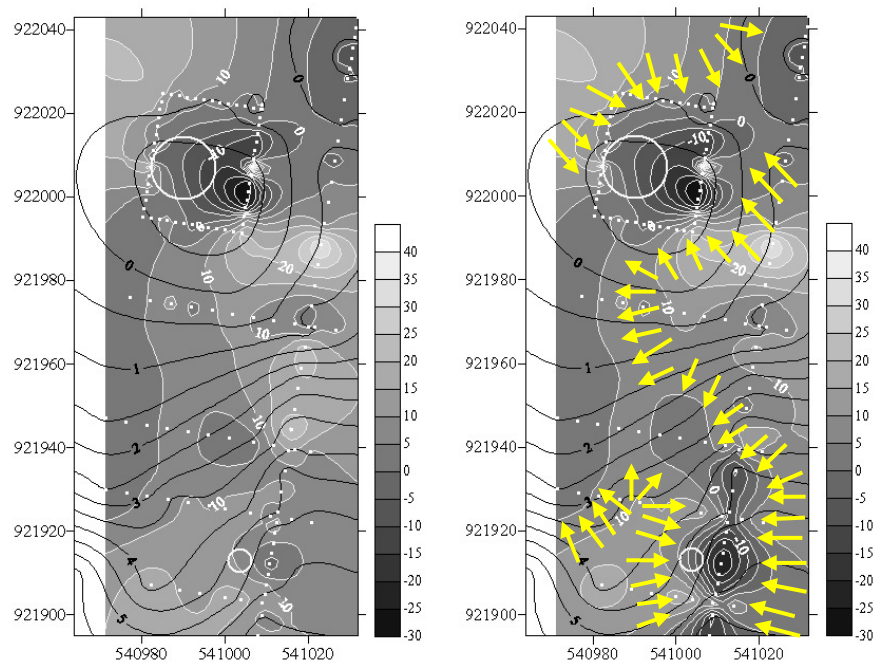
Figure 3.26   SP values with SP measure point on elevation contour (left) with none topographic correction and (right) with topographic correction only provide on long line survey of SP. Arrow indicate the zone of the dipping layer, a sinkhole risk area. Location grid in UTM (WGS–84, Zone 47).

Figure 3.26 (right) shows the groundwater flow direction towards the first and second sinkhole site with negative SP values of down to about -25 mV. The SP value distribution reveals that the subsurface holes and open pathways for the

water flow downwards are ESE of the sinkhole locations at the surface, for both the first and second sinkhole. This might relate to the structural west–dip of the sulfate layer (see Figure 3.5). In the NE part of the survey at 541020-541050E 922020-922040N the SP contour map outlines an area with around -5 mV (Figure 3.26, right). This might an area where a potential new hole in the subsurface is under development with the potential to become a sinkhole in the future.

3.9 Geochemical analysis

3.9.1 Water chemistry

Chemical analysis (Appendix D, Figure D.1 and D.2) of the groundwater samples collected in the study area reveal that the TDS of the water from the second sinkhole, located at elevation about 26 m above sea level (asl), is 44.67 ppm and the pH 4.81. Water from a well nearby (see Section 2.10.1), at the lower elevation of about 21.5 m asl, is 1674.33 ppm and the pH is 5.51. The major ion of the groundwater samples collected at these two sources is sulfate. The amount of sulfate in the groundwater sample from the second sinkhole is 23 ppm and calcium ion is 0.59 ppm, while the adjacent well contains 1,035 ppm sulfate ion and 114 ppm calcium ion. These results indicate that both major ions come from the sulfate dissolution of the subsurface anhydrite/gypsum layer.

The origin of the water from the well is clear as it is coming from the first unconfined aquifer; however the aquifer properties are not known. The water from the second sinkhole was between 9 and 19 m below surface above the collapsed roof of the (sink)hole. This level correlates to the seismic refraction result (see Figure 3.19), showing a refractor at this depth with the layer below having a P–wave velocity of almost 1,500 m/s. The sampled water in the sinkhole might be a mix of original water in the shallow subsurface and deeper water pushed up by the collapse of the sinkhole. Before the collapse of the sinkhole happened the shallow groundwater in the area might have similar water chemistry as the water in the well nearby, with higher calcium and sulfate content due to water flow from the nearby shallow gypsum and anhydrite layers (near the mine) due to higher topography there (see Figure 3.15). The

amount of water in the shallow subsurface might not be much (not an aquifer) as it is mainly clay so that the effect on the resistivity data is not significant.

At depth the continuing dissolution of the anhydrite/gypsum causes the actual hole in the subsurface (Figure 3.27, left), which is filled with water of higher sulfate and calcium content. The resistivity value of the layer there is much lower than above and similar to the weathered anhydrite/gypsum layer (at R2 measurement) with around 80 ohm-meter. During the collapse of the sinkhole the deeper water might have been pushed up into the actual near surface sinkhole where it mixed with the water there (Figure 3.27, right); however with the main part of the water coming from the area of the subsurface void dissolution. Further, seismic reflection and electrical resistivity interpretation put the top of the weathered anhydrite/gypsum layer at about 25–28 m, which are a few meters below the current bottom of the second sinkhole. Therefore, it is more likely that the collected water at the second sinkhole represent mainly water from or close to the area of the actual dissolution that resulted in the subsurface hole before becoming a sinkhole.
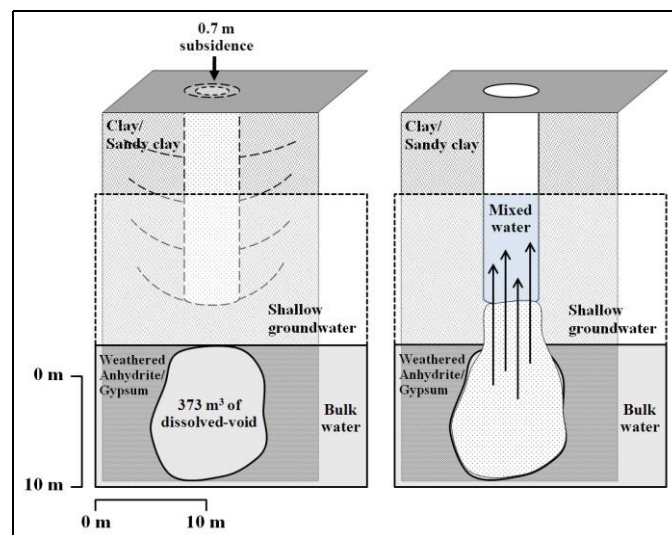
Figure 3.27 Schematic diagrams showing the locations of the different waters before and after the sinkhole development. Left: showing the near surface water with higher sulfate content, and the dissolved sulfate causes the void filled with water of lower sulfate concentration. Right: The ground collapse causes the mass falling down into the void and the deeper water in the void was push up and mixed with the shallow water.

For both water samples the saturation index for calcium sulfate was calculated as described in Section 2.10.1. A value for the sample from the 2nd sinkhole shows a negative saturation index with -3.84, which indicates an undersaturated groundwater with further dissolution possible. The saturation index calculation for the groundwater in the well revealed a positive value with 0.09, which means it is in a supersaturated state.

An explanation for this difference might relate to the locations where the samples were taken. The water from the second sinkhole is undersaturated for calcium sulfate because dissolved ions where somehow already transported from the location through active groundwater flow, likely through a fracture network in the weathered anhydrite/gypsum layer. Therefore, due to the negative saturation index, further dissolution will occur as originally, before the sinkhole collapse, the water was located at about 20–40 m depth in or close to the sulfate formation. The well, however, is likely to be located in an area with very low groundwater flow. Therefore, the existing groundwater was contaminated through the dissolution of the deeper sulfate formation directly or indirectly through diffusion processes over possibly geological times.

From the sulfate ions content in the 2nd sinkhole an approximation was made about the solution rate of gypsum, which is about 10 mm/year. This is in the order of magnitude of the dissolution of limestone (Klimchouk and Aksem, 2005).

3.9.2 Resistivity of gypsum solution

Figure 3.28 shows the correlation between electrical resistivity and the amount of sulfate from the dissolved gypsum (see Section 2.10.1). In general, the resistivity decreases with increasing gypsum content. However, the curve can be divided in to three main parts. First, the resistivity rapidly decreases from 10^{4} down to 10^{2} ohm-m with the amount of sulfate from the dissolved gypsum increasing from zero to 48 mg (10% of saturation, Table 2.7). Second, the resistivity moderately decreases from 100 down to 20 ohm-m with the amount of sulfate increasing from 48 to 240 mg (10-50% of saturation, Table 2.7). Third, the resistivity slowly decreases from 20 to about 10 ohm–m after 240 mg sulfate content. These results display that

the resistivity is sensitive and changes rapidly at low sulfate contents (first group) and less sensitive at higher sulfate contents (second and third group).
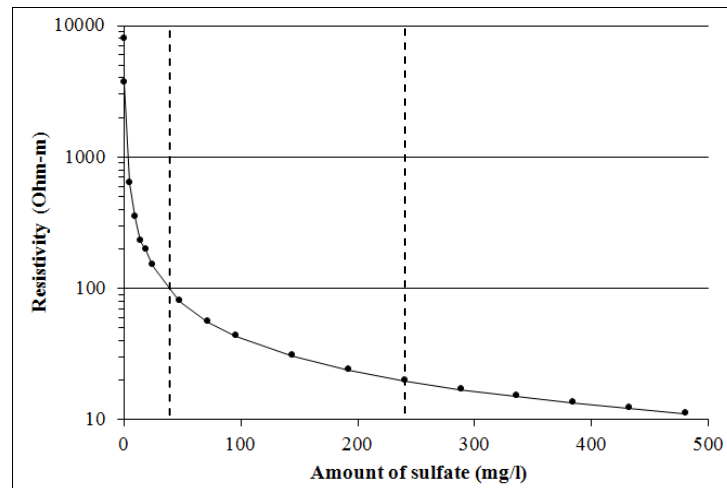
Figure 3.28   Correlation between amounts of sulfate (mg/l) and resistivity (ohm–m) of the solution.

The amount of dissolved sulfate in the groundwater sample from the second sinkhole is 23 mg/l (Appendix D, Figure D.2), which corresponds to a resistivity value about 151.3 ohm-m using the relationship in Figure 3.28. This resistivity values are for a fluid only. In order to compare it with data from the resistivity survey a solid with fluid has to be assumed, which likely will increase the overall resistivity due to the lower resistivity of the solid part. However, as no data are available it can be stated that using the values from the resistivity survey (from 76 ohm–m at R4 to 154 ohm–m at R1) the amount of dissolved sulfate in the weathered anhydrite/gypsum layer is around 50 mg/l or less, as higher resistivity values would be related to lower sulfate concentrations. In general, it would show undersaturated conditions with the potential of further dissolution and continues development of subsurface holes and cavities.

3.10. Scenario of sinkhole development

The geophysical interpretation, geochemical study and hydrological and geological survey were integrated to draw a scenario of the development of the sinkholes in the study area. The main subsurface structures were considered from the electrical resistivity results, which identified five layers (Figure 3.29), but summarized into three layers: (1) near–surface the sedimentary layers with sandy clay to clayey sand (Qa), which also correlate to the seismic refraction results, (2) the weathered anhydrite/gypsum layer (A/G) and (3) the bedrock layer (B), likely solid anhydrite due to the very high resistivity values. At about 25 to 30 meters depth is differential weathered gypsum/anhydrite zone (Wz) with 15 to 25 meters thickness, following the results of the seismic reflection interpretation (Figure 3.29). In general, the layers show an increase in depth from the east (mine edge) to the west (study area) and a steep slope appears in the area of the sinkhole locations (Figure 3.29).
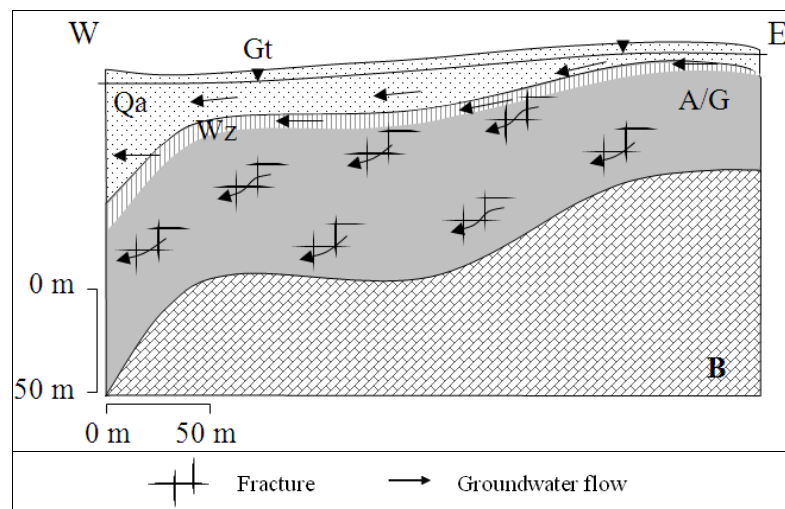
Figure 3.29   E–W cross section schematically illustrating the situation before the mine opened and started to operate; before1983. Qa is Quaternary alluvial, Wz is weathered zone of the anhydrite top surface, A/G is Anhydrite or gypsum layer and B is the dense and low porosity bedrock.

The beginning of the development of the sinkholes has been seen from the second sinkhole with its subsidence at the surface in June 2009. Later in August of

the same year the sinkhole occurred, only about 2–3 months later. To understand its development the second sinkhole will be used as a case study.

First, considering the situation before the mine began to open and operate as shown in Figure 3.29. The groundwater generally flew from the higher to lower hydraulic head in east to west direction. The difference in the hydraulic head of the groundwater level is small so its flow is sluggish. It can flow through the anhydrite/gypsum layer due to the existence of fractures and the contact of groundwater to the top surface of the gypsum/anhydrite layer increased the weathering in this zone over time. Continuous dissolution leads to the development of sinkholes that can be seen today at the top of the mine (see Figure 3.11).
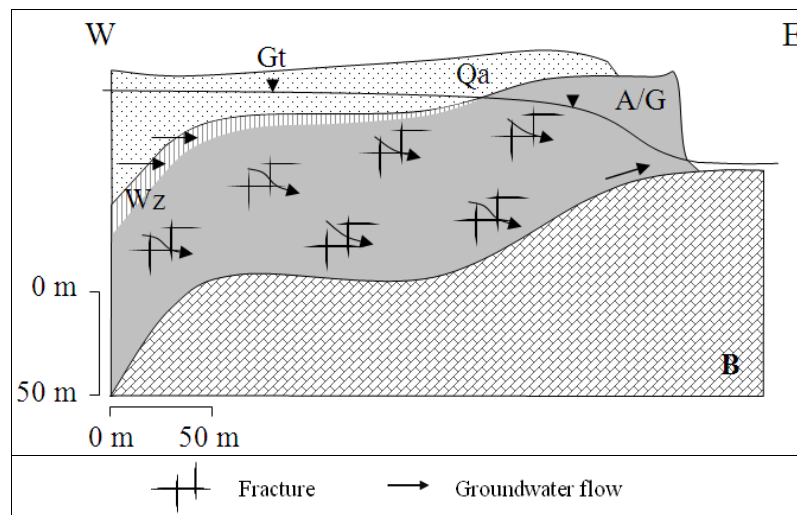
Figure 3.30   E–W cross section schematically illustrating the situation after the mine opened. Groundwater drawdown occurred below the base of the mine and by this changing the flow from west to east direction.

Then the mine opening and the subsequent excavation of the mine resulted in a drawdown of the groundwater table (Gt) affecting the area around the mine and changed the general groundwater flow direction from west to the east (see Figure 3.30). By this the groundwater came in direct vertical contact with the steeper slope zone of the gypsum/anhydrite layer. This drawdown of the groundwater caused a larger difference in the hydraulic head so that the groundwater flows faster than

before. By this the groundwater can transport much faster away any dissolved solids, mainly calcium and sulfate.
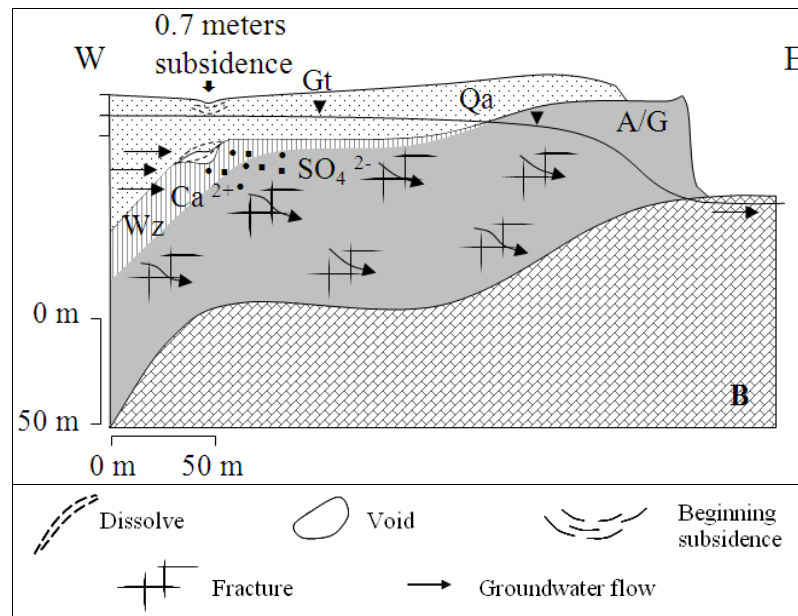
Figure 3.31   E–W cross section schematically illustrating the situation ground subsidence as a sign of the sinkhole development in June 2009.

The groundwater flow and dissolution continued at the steeper slope zone leading to a thicker and larger highly weathered zone, which accelerates the dissolution due to an increasing contact area (Figure 3.31). Subsequently over time these processes resulted in void development in the subsurface with increasing size over time. Due to the shallow depth of the void development in the weathered anhydrite/gypsum layer the overburden sandy clay to clayey sand layers move slowly downwards resulting in a ground subsidence at the area of the second sinkhole occur. The dissolved ions in the groundwater flow down with the groundwater resulting in a low amount of anhydrite related ions (sulfate and calcium). Due to this geochemical undersaturation the dissolution continues over time.
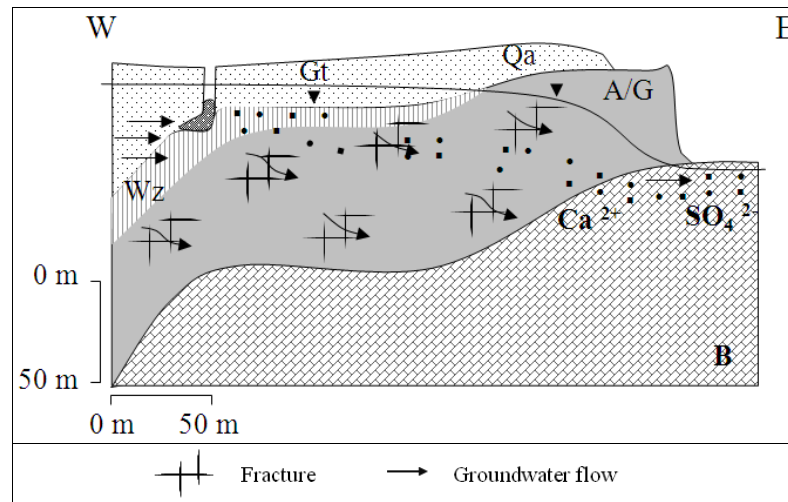
Figure 3.32   E–W cross section schematically illustrating the situation of the second sinkhole development in August 2009.

Finally, the continued dissolution resulted in larger voids in the subsurface. The actual collapse of the sinkhole in the study area can be related to two big earthquakes in the Andaman Sea (see Figure 3.32). For the first sinkhole the Mw 9.3 Andaman Sumatra Earthquake on the 26 December 2004 can be seen as the trigger (USGS, 2011a). The larger sinkhole was then observed some days after. The earthquake shaking and/or the passing of the seismic waves through the subsurface of the area lead to the mechanical instability of the roof of the subsurface hole or void. The actual sinkhole developed likely in less than a day, probably within a few hours. For the second sinkhole the Mw 7.6 earthquake near the Andaman Islands on 10 August 2009 can be related to the final sinkhole development (USGS, 2011b) with the same mechanism described above.

3.11 Discussion of the sinkhole development scenario

3.11.1 Different groundwater flow directions

From the topography and water sample chemistry it is possible that the groundwater in the shallow subsurface flows from E to W, however due to the clayey composition it is not considered an aquifer so the permeability or hydraulic conductivity is considered very low (see Figure 3.33). This flow regime gets dissolved

calcium and sulfate at higher topography and distributes it downwards further W. The higher sulfate content in the water sample at the well indicates this. At depth, the groundwater is flowing from W to E following the seepage drawdown due to the open pit mining. The water flow velocity might be higher than above as the water can flow through the open fractures of the anhydrite gypsum. This flow regime is in contact to the weathered zone of the anhydrite layer due to the dipping structure. These results in the further dissolution until becoming voids in the subsurface, which then cause the sinkhole occurrence (see Figure 3.33).
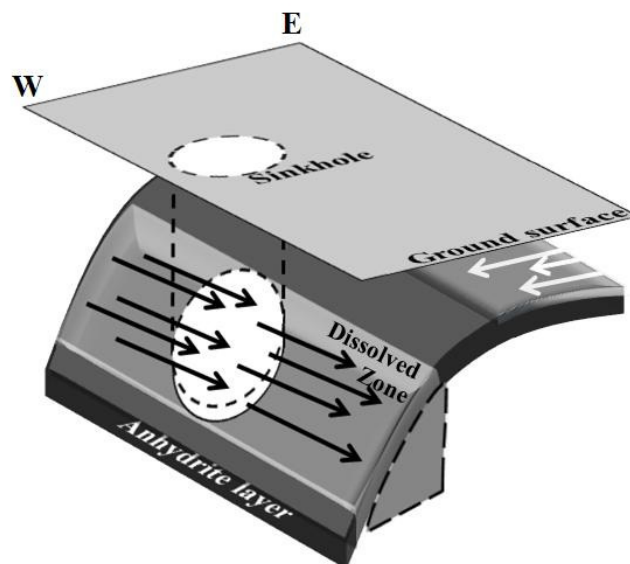
Figure 3.33 Different groundwater flow in the shallow subsurface (white arrows) and in the depth (black arrows). The first one is not in contact with the anhydrite layer, whereas the latter one is in contact due to the structural dipping resulting in void development and subsequent sinkhole occurrence.

3.11.2 Different distribution of subsurface formations

The observations in the mine open another possibility for the geological model. From Figure 3.34, which shows the mine wall with the anhydrite, can be seen that only at some locations water is flowing out, but at the time of the survey not in large amounts. This might indicate that the anhydrite layer there is dense and has relatively low porosity (A in Figure 3.35). However, it seems that relatively more water is coming out into the mine from the south rather than from the west (see

Figure 3.34). From this it might be possible that the anhydrite is in the western part is denser with less porosity or fractures like a bedrock (B in Figure 3.35), which makes its resistivity higher. Therefore, it might not be possible to separate the interface between A and B by resistivity (dashed line in Figure 3.35).
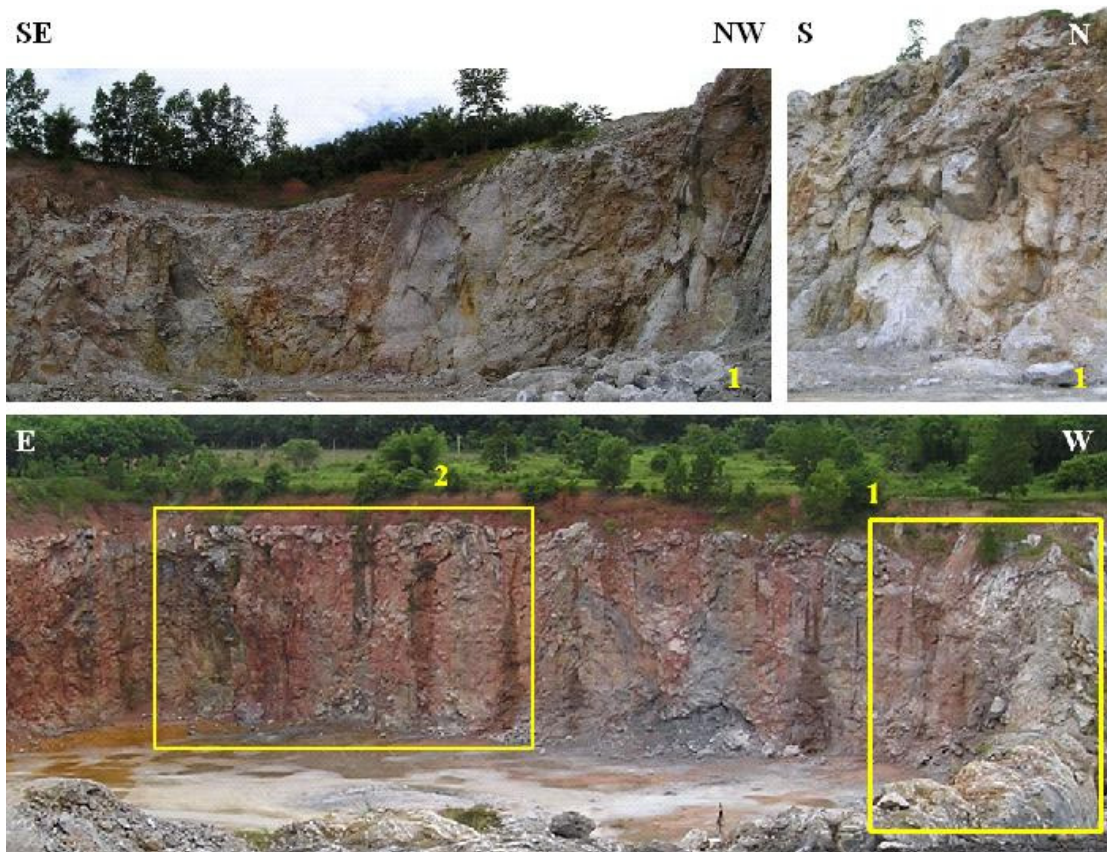
Figure 3.34   Photos of the vertical rock faces in the mine showing water outflow. In the south (bottom, box 2) there seems to be less water outflow than in the west (box 1, top, left and right).

Based on this consideration the geological model can be modified as shown in Figure 3.35. The mine exposes the anhydrite layer (A); however the interface to the bedrock (B) probably not. Both units are dense with very high resistivity values. The weathered anhydrite layer (Wz) starting further west from the mine and then dipping in the same direction. Above is clay layers and younger formations (Qa). The data resistivity points R1 to R4 would be still consistent with this model, as well as the seismic interpretation.
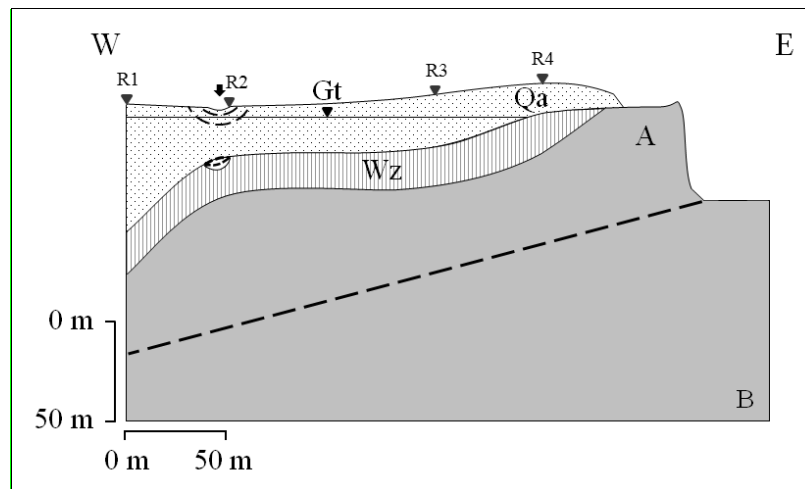
Figure 3.35 Modified geological model showing the anhydrite (A) wall at the mine with high resistivity (least fracture) like bedrock (B), and the weathered zone (Wz) on top of anhydrite layer, however starting further west.
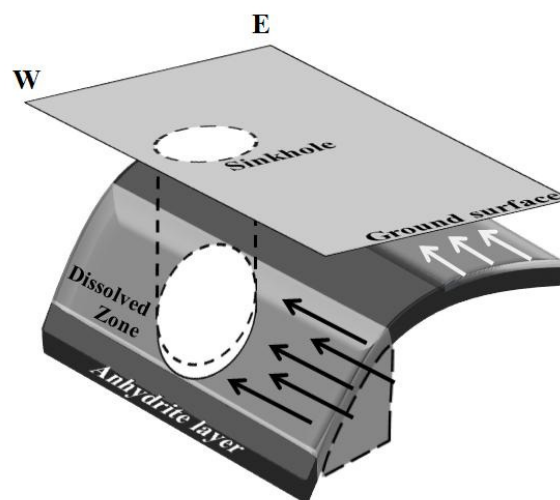
Figure 3.36 Groundwater flow regime related to the modified geological model shown in Figure 3.35. Groundwater comes in contact to the top of the anhydrite layer (white arrow) resulting in the undulated weathered surface, while the deeper groundwater flow (black arrows) is in contact to the dipping structure of the anhydrite layer, leading to weathering and voids in the subsurface, finally leading to sinkholes.

Due to the modified geology it is possible that the groundwater flow in south to north direction due to higher elevation in the south. The groundwater might flow on the top of anhydrite surface (Figure 3.36, white arrow), which results in the

top of the anhydrite to be weathered resulting in an undulated interface as seen in Figure 3.10 (right). Further, while the groundwater flows from south to north it also comes in contact to the dipping zone of the anhydrite layer (Figure 3.36, black arrow), which results in weathering and dissolution of the anhydrite, then forming voids in the subsurface, which finally causes the sinkholes.

3.11.3 Fault occurrence instead of dipping structure

The initial scenario stated a dipping structure to the west based on the resistivity data. However, it is also possible to have a fault there as the dipping structure requires a quite steep slope. At a fault the gypsum and anhydrite are likely to be broken and fractured with possible insertion of shale from the layer on top (see Figure 3.). Especially the vertical face of the fault would be fractured and by this weathering with dissolution would be easier and thereby faster (Figure 3.37). These would finally result in subsurface voids and subsequent sinkholes.
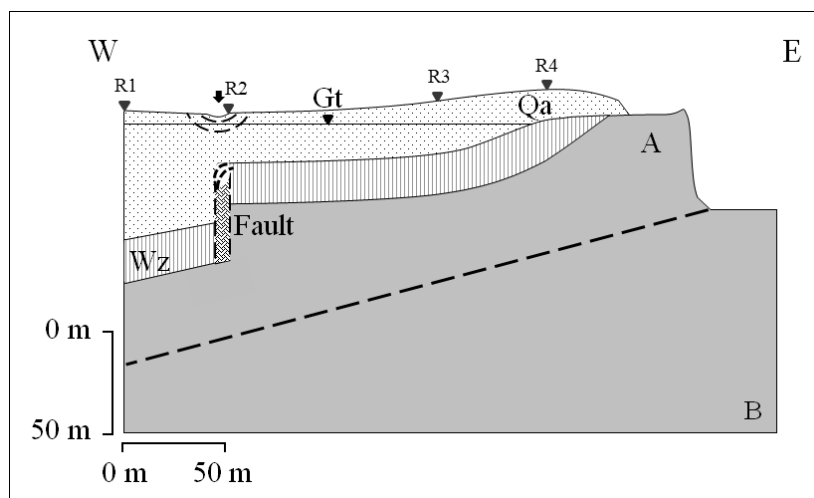
Figure 3.37   Instead of a dipping anhydrite structure a fault zone is introduced in the geological model that resulted in a fractured anhydrite and gypsum zone, probably with clay from the layers on top. The fractured zone is subject to easier and faster weathering.
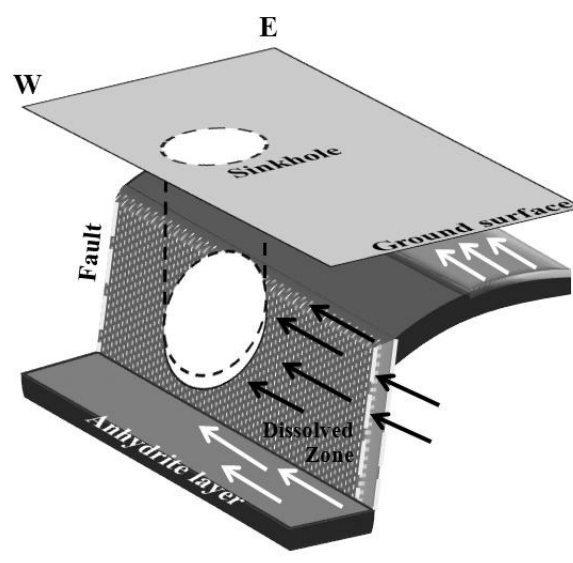
Figure 3.38   Groundwater flow regime in a geological model with a vertical fault. Flow on top of the horizontal anhydrite layer (white arrow) results in undulated weathered surface, while the flow contact to the fault with broken anhydrite (black arrow) can result in voids in the subsurface that cause the collapse of the ground.

The groundwater flow for this scenario is shown in Figure 3.38, with the main flow direction from south to north due to the difference in groundwater level. On top of the anhydrite layer the groundwater flow results in weathering and undulated surface (Figure 3.38, white arrow). However, the groundwater can flow along the fault easier due to the broken rock mass and by this dissolve the anhydrite and gypsum (Figure 3.38, black arrow), and so causing the voids and the subsequent sinkholes.

However, all the modified cases indicate that anhydrite layer at either the dipping structure or at the vertical fault can be easier dissolved by the flowing groundwater than at the horizontal interface to the top layer.

3.12. Sinkhole scenario considering regional lithology and hydrogeology

From the gypsum geology in the mine (see Section 3.1) it was found that there are faults crossing through both gypsum and anhydrite (see Figure 3.3 and 3.4). If the faults are only caused by shrinking and extension due to rehydration at the top of the anhydrite to form gypsum, the faults will only cross through the gypsum layer. Considering the regional geology with the geological cross section AA′ shown in Figure 3.39 and 3.40, the Permian mountains (i.e. at the study area) form a syncline structure with a relative uplift of the limestone mountains, likely the related anticline structures. As mentioned above the faults cross through the gypsum and anhydrite layer it can be assumed that the anhydrite and gypsum layers were also uplifted and this caused the faulting observed in the layers.
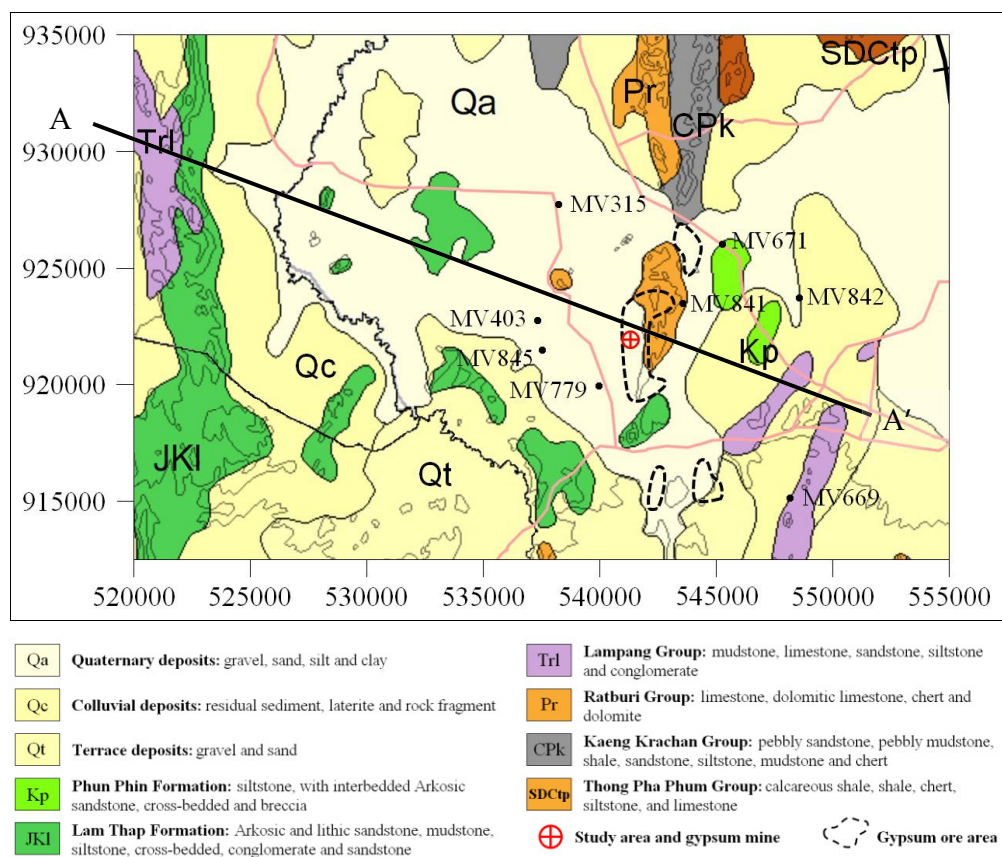
Figure 3.39   Groundwater well log positions on the regional geological map. AA′ cross section in Figure 3.40.
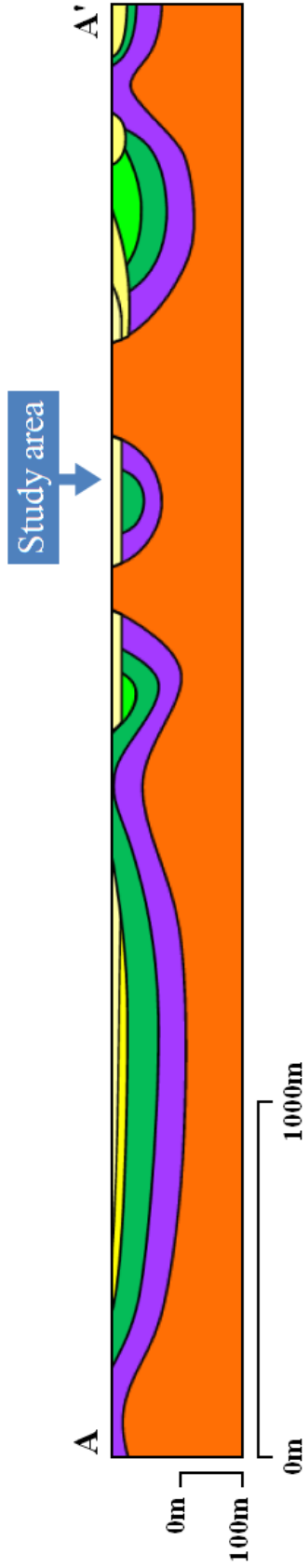
Figure 3.40   Schematic geological cross section showing the principle geological structures based on the geological map. For geological map legend see Figure 3.39.
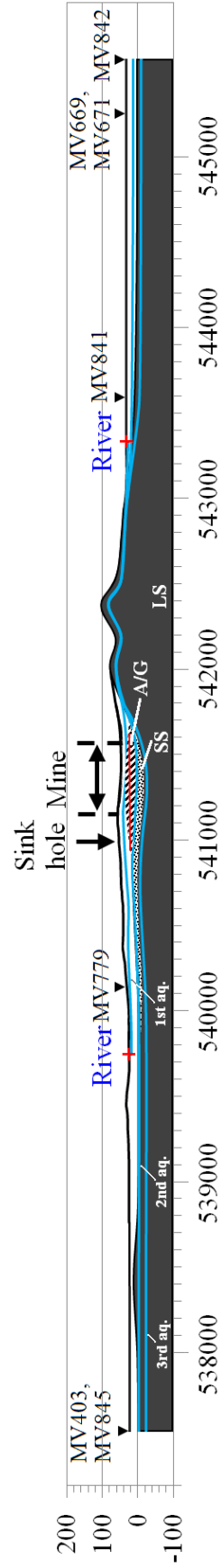
Figure 3.41   Regional lithology and hydrology from well log information. 3rd aquifer is in the sandstone, limestone and mudstone in the east. For well locations see map in Figure 3.39.

The geology cross section shown in Figure 3.40 was prepared from the continuity of the rock units and their age and the horizontal distribution shown on the geological mal (Figure 3.39). The information from eight groundwater well logs, namely MV315, MV403, MV669, MV671, MV779, MV841, MV842, MV845 with their locations shown on the geological map in Figure 3.39 (see Appendix F, Table F.1) were used to correlate the lithology around the sinkhole area

Well logs which are oriented along north-south direction disclose the continuity of rock layers in the subsurface; these are well log MV403 and MV845. They reveal the depth of the limestone layer in the west at around 21-27 meters, which correlates with the well log MV671 and MV669 in the east indicating a depth of the limestone layer at 30 meters (Figure 3.39). In the west of the study area rock fragments were found in well log MV779 (see Appendix F, Table F.1) indicating it can be arkose sandstone (SS) (Selley, 2000) at a depth of 14 to 26 meters that overlay the limestone (LS) layer similar to the well log MV845 nearby. The gypsum/anhydrite (A/G) layer, which related to Khao Hun Formation and Ratburi Group (Rattanajarurak, 1994) are assumed to overlay on the sandstone. All the well log information are used for a correlation of the layers as shown in Figure 3.41

The perforation intervals of well logs were used to distinguish aquifer types and their depths (see Appendix F, Table F.1) for understanding subsurface water flow that relates to the main geological structures and the development of sinkholes. The perforation interval of well MV779, which is near the study area, indicates that the second aquifer (2nd aq.) is about 18-24 meters in the sandstone and this aquifer depth conforms with data from well log MV403 and MV845 with about 22-28 meters depth in the limestone. In the east the depth of the second aquifer is around 20-25 meters in the claystone using well log MV841 and MV842 data (see Figure 3.41). Therefore, the second aquifer (2nd aq.) has a general depth of around 20-26 meters and it seems to be in the interface between clay and other rock types as see in the well log data.

The third aquifer (3rd aq.) is at about 36-40 meters depth in the limestone indicated by data from well log MV671 (see Figure 3.41). The first aquifer (1st aq.) was found in the wells nearby the study area (see it location as Appendix G,

Table G.1) at about 6 meters depth with high sulfate content and not really fresh water (see Appendix D, Table D.1).

According to the water analysis (see Section 3.9 and Appendix D, Table D.1, D.2), the first aquifer was found with higher sulfate content than the water in the sinkhole at the same 6-meter groundwater level. This difference in sulfate content is an important factor indicating that the analyzed waters, which were taking from nearby locations and almost the same level, do not come from the same aquifer. These effects can be explained with the faults that crossing through the gypsum, anhydrite and sandstone layers (see Figure 3.42) during the mountain building period. The faults likely do not pass through the limestone (LS) layer because the water in the upper aquifer has low concentration of calcium ions as known from the water analysis of the second sinkhole.
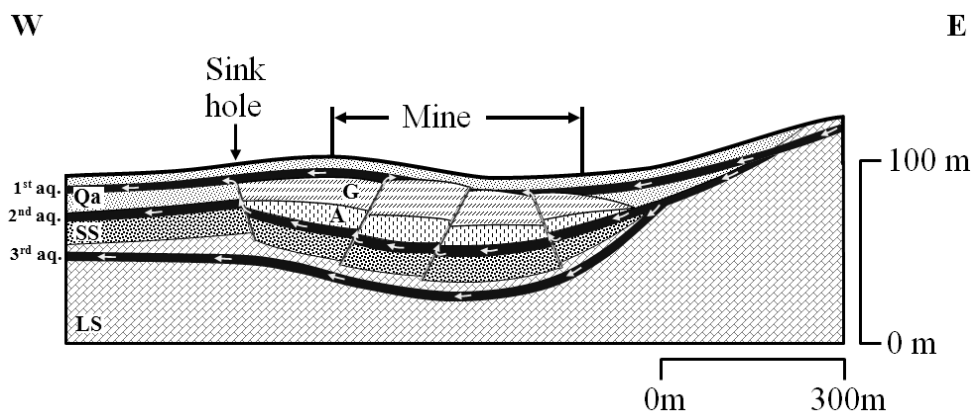
Figure 3.42   Geological and hydrological cross section from W to E at the study area based on well log data.

After the main aquifers could be distinguished it can be seen that the second aquifer is parallel to the top of sandstone along the interface with dense anhydrite layer (see Figure 3.42). The faults that cross through the layers can be also another water pathway where the water can flow up and mix up into the first aquifer (see Figure 3.42). During flowing up into the first aquifer through the pathway, water flow from the second aquifer passes the gypsum layer and by this dissolving it. This makes the water from the second aquifer containing the actual sulfate ion only from the gypsum layer (as the well perforation is only at fresh water aquifers) as was found

in the analyzed water of the second sinkhole. This is conform to gypsum solution measurements (see Section 3.9.2) and the resistivity interpretation (see section 3.8.1).

During the flow up of the sulfate containing water it also can pass through the faults. Therefore, if the faults are the pathways connecting to the first aquifer sulfate containing water in the second aquifer will be distributed and mixed with the first aquifer. This makes the first aquifer having a much higher sulfate content as the analyzed water from well in the study area. The water from the sinkhole and its 6 meters water level are equal to the water in the well assuming to be the first aquifer. This can be explained by the potentiometric level. Another reason confirming that the first aquifer has been dispersed sulfate content from the second aquifer through the faults is its low pH value as shown in the analyzed water from the well nearby and from the second sinkhole (see Appendix D, Table D.1 and D2). Because the faults that crossing through rock layers of gypsum mixed with crushed carbonaceous shale (see Figure 3.3) that generally composing with pyrite. When it was in contact with groundwater, the oxidization process produces sulfuric acid that causing the low pH value in the first aquifer (Hoover, 2008).

From the geological structures and hydrology studies it can assume that the important factors causing the sinkhole development are the fault structures that are crossing through the gypsum layer as shown in Figure 3.13 and the water from second aquifer can flow upwards through the faults.

CHAPTER 4

CONCLUSION AND RECOMMENDATION

In the Tayang Sub-district, Tungyai District, Nakhon Si Tammarat Province large sinkholes occurred in January 2005 and August 2009. A detailed geo–scientific study was carried out in order to understand the sinkhole development.

From the results and interpretations it can be concluded that the main factors that control the dissolution process of sulfate layer are, first, the saturation state of the groundwater. Naturally, groundwater hardly reaches the saturate state because it always flows. The amounts of chemical compounds in the groundwater indicate whether the groundwater is in dissolution or precipitation state. The chemical composition analysis of groundwater in the second sinkhole indicated that the groundwater is not in the saturation state, it means that it is continuing to dissolve the gypsum/anhydrite layer in the subsurface.

The second main factor is the structure of the sulfate layer and the related groundwater flow direction. The geophysical data interpretation displays that an important condition of the sinkhole formation are the dissolved-cavities forming either at dipping area of the anticline structure with 70-75° to the west or at the fault structure. Third, the study of the regional geology and hydrogeology indicate different aquifers with depth that might be connected through faults and fractures and by this allowing water flow through the sulfate layers resulting in the dissolution that leads to the formation of sinkholes.

Considering the general situation that groundwater flow and normally sluggish, however, it always is in contact and dissolves the top of the horizontal sulfate layer. This can cause ground collapse or only undulant of the top sulfate surface that have been seen in the mining area. The difference to the situation in the study area is either at the dipping zone of the anticline structure where the groundwater dissolves to a large amount at the inclined to vertical surface of the sulfate layer or more likely at the vertical fault structure, which is assumed a possible groundwater pathway to the upper aquifer. Both scenarios can easily result in the

formation of a hole in the subsurface. Finally, it might be possible that some subsurface cavities of the later sinkholes were induced and/or accelerated by human activities, e.g. mining; but the data of this study are insufficient to give a clear answer to that question. However, the final sinkhole collapse can be related to greater magnitude earthquakes in the Andaman Sea area. As these earthquakes are still frequent sinkhole development is still possible. Anyhow, a non–earthquake induced collapse might be just a matter of time.

The mechanism of sinkhole development is always different depending on the area and the conditions there, geological structures and hydrogeology features. A plausible mechanism of the sinkhole development in this study area was presented with the sinkholes occurring at either dipping part of weathered sulfate formation in the subsurface or the vertical fault structure, which creates a larger contact to the groundwater as the dissolving agent.

The understanding of these mechanisms and conditions can be used in a hazard assessment involving the identification and characterization of the existing sinkholes and the prediction of future subsidence phenomena. The sinkhole occurrence in the same area in the future will have a similar behavior than that of the past. In order to create any probability maps geophysical techniques can be applied in a larger area, for example electrical resistivity sounding.

As a recommendation, further studies applying geophysical techniques, for example seismic reflection along the west to east direction, to confirm either the dipping of the sulfate formation following the anticline structure or the vertical fault. Additional hydrogeological surveys are also recommended; with more water samples taken around the sinkhole area for further understanding the distribution of the chemical composition in the groundwater that correlates to the occurrence of the sinkholes. Finally, local villagers should be made aware of the situation so that they can identify and observe any subsidence development as a possible precursor of a potentially hazardous sinkhole development.

BIBLIOGRAPHY

Allred, B.J., Rogers, M., Ehsani, M.R. and Daniels, J.J. 2008. Handbook of agricultural geophysics. CRC Press, Taylor & Francis Group. 147-164.

Appelo, C.A.J. and Postma, D. 2005. Geochemistry, groundwater and pollution. 2nd Ed. A.A. Balkema Publishers, Amsterdam, The Netherlands. 131 pp.

Aubert, M. and Atangana, Q.Y. 1996. Self-potential method in hydrogeological exploration of volcanic areas. Groundwater. 34, 1010-1016.

Bachrach, R. and Mukerji, T. 2004. The effect of texture and porosity on seismic reflection amplitude in granular sediments: Theory and examples from a high-resolution shallow seismic experiment. Geophysics. 69(6), 1513-1520.

Baker, G.S. 1999. Processing near-surface seismic-reflection data. Society of Exploration Geophysicists. p. 41.

Batayneh, A.T., Abueladas, A.A., and Moumani, K.A. 2002. Use of ground-penetrating radar for assessment of potential sinkhole conditions: an example from Ghor al Haditha area, Jordan. Environmental Geology. 41, 977-983.

Beck, B.F. and Herring, J.G. 2001. Geotechnical and environmental applications of karst geology and hydrology: proceeding of the Eighth Multidisciplinary Conference on Sinkholes and the Engineering and Environmental impacts of Karsts, Louisville, Kentucky, 1-4 April 2001. Taylor & Francis. 107 pp.

Bell, F.G. 1998. Environmental geology: principle and practice, Wiley-Blackwell. Oxford University. London, UK. 368 pp.

Birk, S., Liedl, R., Sauter, M. and Teutsch, G. 2005. Simulation of the development of gypsum maze caves. Environmental Geology. 48, 296-306.

Bobachev, A., Modin, I. and Shevnin, V. 2003. IPI2Win software version 3.0.1a. Geoscan-M Ltd., Moscow State University, Geological Faculty, Department of Geophysics. Moscow, Russia.

Cooper, A.H. and Calow, R.C. 1998. Avoiding gypsum geohazards: guidance for planning and construction. British Geological Survey Technical Report. WC/98/5.

Corwin, R.F. and Hoover, D.B. 1979. The self-potential method in geothermal exploration. Geophysics. 44, 226-245.

Crespo, T.M. and Ortiz, D.G. 2007. Collapse hazard assessment in evaporitic materials from ground penetrating radar: a case study. Environmental Geology. 53, 57-66.

DMR, 2011. Geological map of Nakhon Si Thammarat province [online]. Available from http://www.dmr.go.th/download/pdf/South/nakorn.pdf

Elorza, M.G. and Santolalla, F.G. 1998. Geomorphology of the Tertiary gypsum formations in the Ebro Depression (Spain). Geoderma. 87, 1-29.

Ernstson, K and Scherer, H.U. 1986. Self-potential variations time and their relation to hydrogeologic and meteorological parameter Geophysics 51. (10), 1967-1977.

Ezersky, M. 2006. The seismic velocities of Dead Sea salt applied to the sinkhole problem. Journal of Applied Geophysics. 58, 45-58.

Ezersky, M. 2008. Geoelectric structure of the Ein Gedi sinkhole occurrence site at the Dead Sea shore in Israel. Journal of Applied Geophysics, 164. 56-69.

Ezersky, M., Legchenko, A., Camerlynck, C. and Al-Zoubi, A. 2009. Identification of sinkhole development mechanism based on a combined geophysical study in Nahal Hever South area (Dead Sea coast of Israel). Environmental Geology. 58, 1123-1141.

Fell, R., MacGregor, P., Stapledon, D. and Bell, G. 2005. Geotechnical engineering of dams. A.A. Balkema, Rotterdam, The Netherlands. 119 pp.

Filin, S., Baruch, A., Avni, Y. and Marco, S. 2011. Sinkhole characterization in the Dead Sea area using airborne laser scanning. Natural Hazards, Springer.

Ford, D.C. and Williams, P.W. 2007. Karst hydrology and geomorphology, John Wiley and Sons. p. 26.

Fournier, C. 1989. Spontaneous potentials and resistivity surveys applied to hydrogeology in a volcanic area: case history of the Chaîne des Puys (Puy-de-Dôme, France). Geophysics Prospecting. 37(6), 647-668.

Ghosh, S. 2005. Control system: Theory and Application. Pearson Education Pte. Ltd, Singapore. pp. 388-389.

Guinea, A., Playá, E, Rivero, L., Himi, M. and Bosch, R. 2010. Geoelectrical classification of gypsum rocks. Survey Geophysics, 31, 557-580.

Gutiérrez, M. and Gutiérrez, F. 1998. Geomorphology of the Tertiary gypsum formations in the Ebro depression (Spain). Geoderma. 87, 1-29.

Gutiérrez, F, Cooper, A.H. and Johnson, K.S. 2008. Identification, prediction, mitigation of sinkhole hazards in evaporite karst areas. Environmental Geology. 53, 1007-1022.

Harter, T. 2008. Watersheds, groundwater and drinking water: a practical guide, ANR Publication. p. 25-29

He, B.B. 2011. Two-dimensional X-Ray Diffraction. John Wiley and Sons. 1-10.

Hiscock, K.M. 2005. Hydrology: principle and practice. John Wiley and Sons. p.19.

Hoover, S.E. 2008. The expansive effects of concentrated pyritic zones in shales of the Marcellus formation. ProQuest Pennsylvania, USA. p. 15-20.

James, A.N. and Lupton, R.R. 1978. Gypsum and anhydrite in foundations of hydraulic structures. Geotechnique. 28, 249-272.

Jeschke, A.A., Vosbeck, K. and Dreybrodt, W. 2001. Surface controlled dissolution rates of gypsum in aqueous solutions exhibit nonlinear dissolution kinetics. Geochima Cosmichima Acta. 65, 27-34.

Kresic, N. 2008. Groundwater resource: sustainability, management and restoration. Mc Graw Hill Professional. p. 109-111.

Kheunkhong, P. 2001. Mineralogy map of Nakhon Si Thammarat Province 1:250,000, Economic Geology Division, Department of Mineral Resource

Klimchouk, A. 1996. The dissolution and conversion of gypsum and anhydrite. International Journal of Speleology. 25(3-4), 21-36.

Klimchouk, A. 2000. Dissolution and conversions of gypsum and anhydrite. In: Klimchouk A., Ford, D.C., Palmer, A.N., Dreybrodt, W., (eds) Spelogenesis. Evolution of karst aquifers. National Speleological Society, Hunstville, pp 160–168.

Klimchouk, A. and Andrejchuk, V. 1996. Sulfate rocks as an Arena for karst development. International Journal of Speleology. 25(3-4), 9-20.

Klimchouk, A. B. and Aksem, S. D. 2005. Hydrochemistry and solution rates in gypsum karst: case study from the Western Ukraine. Environmental Geology. 48, 307-319.

Klimchouk, A., Cucchi, F., Calaforra, J.M., Aksem, S., Finocchiaro, F. and Forti, P. 1996. Dissolution of gypsum from field observations. International Journal of Speleology. 25(3-4), 37-48.

Lowrie, W. 2007. Fundamentals of geophysics, 2nd Ed. Cambridge University Press. Cambridge, UK. 381 pp.

Mares, S. 1984. Introduction to applied geophysics. Springer. p. 19-22.

McCormick, W.W. 1969. Fundamentals of University Physics. The Macmillan Company, New York, U.S.A. p. 236-239.

Miller, R.D., Xia, J. and Steeples, D.W. 2009. Seismic reflection characteristics of naturally-induced subsidence affecting transportation. Journal of Earth Science. 20(3), 496-512.

Meesook, A., Suteethorn, V., Chaodumrong, P., Teerarungsigul, N., Sardsud, A., and Wongprayoon, T. 2002. Mesozoic Rocks of Thailand: A Summary, proceedings of the Symposium on Geology of Thailand 26-31 August 2002, Bangkok, Thailand. Geological Survey Division, Department of Mineral Resources, Bangkok, Thailand.

Milsom, J. 2003. Field Geophysics, 3rd Ed. John Wiley & Sons. UK. 88 pp.

Mochales, T., Casas, A.M., Pueyo, E. L., Pueyo, O., Román, M.T., Pocoví, A., Soriano, M.A. and Ansón, D. 2008. Detection of underground cavities by combining gravity, magnetic and ground penetrating radar surveys: a case study from the Zaragoza area, NE Spain. Environmental Geology. 53,1067–1077.

Parasnis, D.S. 1986. Principles of Applied Geophysics. Chapman & Hall. London, UK. 429 pp.

Pecharsky, V. K. and Zavalij, P. Y. 2009. Fundamentals of powder diffraction and structural characterization of materials, 2Ed. Volume 69 of Recent Results in Cancer Research. p 142-165.

Poehls, D.J. and Smith, G.J. 2009. Encyclopedic dictionary of hydrogeology. Academic Press Burlington, MA, U.S.A. p. 154.

Pullan, S.E. and Hunter, J.A. 1990. Delineation of buried bedrock valleys using the optimum offset shallow seismic reflection technique. In: Ward, S.H. (editor), Geotechnical and Environmental Geophysics; Vol. 3: Geotechnical: Society of Exploration Geophysicists Investigations in Geophysics. 5, 75-87.

Rattanajarurak, P. 1994. Amount of reserving gypsum ore in Surat and Nakhonsri Tammarat province. Economic geology report NO.13/1994. Economic geology division, Department of Mineral Resources. p. 29.

Reynolds, J.M. 1997. An introduction to applied and environmental geophysics. John Wiley & Sons, London, UK. p. 221.

Robinson, R. and Thagesen, B. 2004. Road engineering for development, 2nd Ed. Taylor & Francis, London, UK. p.145.

Rowe, R.K. 2001. Geotechnical and geoenvironmental engineering handbook. Springer. p. 199.

Scott, J. 1973. Seismic refraction modeling by computer. Geophysics. 38(2), 271-284.

Schön, J.H. 1996. Physical properties of rocks: Fundamentals and principles of petrophysics. Vol. 18, Handbook of Geophysical Exploration, Seismic Exploration, Series editors, K. Helbig and S. Treitel, Pergamon Press, Elsevier, U.K..

Sharma, P.V. 1997. Environmental and engineering geophysics. Cambridge University Press, Cambridge, UK. 475 pp.

Saelea, P. 2004. Mineral geology report for demand to add anhydrite for operating in a mining concession no. 26200/15465 in Tayang Subdistrict, Tungyai District, Nakhon Si Tammarat Province. Department of Primary Industries and Mines, Songkhla Province.

Selley, R. C. 2000. Applied sedimentology. 2nd Ed. Academic Press, San Diego, California, USA. p. 354.

Sprynskyy, M., Lebedynets, M. and Sadurski, A. 2009. Gypsum karst intensification as a consequence of sulphur mining activity (Jaziv field, Western Ukraine). Environmental Geology. 57, 173-181.

Sumanovac, F. and Weisser, M. 2001. Evaluation of resistivity and seismic methods for hydrogeological mapping in karst terrains. Journal of Applied Geophysics. l47, 13-28.

Tallini, M., Gasbarri, D., Ranalli, D. and Scozzafava, M. 2006. Investigating epikarst using low-frequency GPR: example from the Gran Sasso range (Central Italy). Engineering Geological Environment. 65, 435-443.

Teerarungsigul, N., 1999. Lithostratigraphy of non-marine Mesozoic rocks: Thung Yai-Khlong Thom areas in southern part of Thailand. unpublished M.Sc. thesis, Department of Geology, Faculty of Sciences, Chulalongkorn University, p. 190.

Telford, W. M., Geldart, L. P.and Sheriff, R. E. 1990. Applied Geophysics, 2nd Ed. Cambridge University Press. Cambridge, UK. 770 pp.

Ulery, A. L. and Drees, L. R. 2008. Methods of soil analysis: Mineralogical methods. Issue 5 of Soil Science Society of America book series, SSSA, Madison, Wisconsin, USA. 81-85.

USGS, 2011a. NEIC Earthquake Catalog [online]. Available from http://earthquake.usgs.gov/earthquakes/eqinthenews/2004/us2004slav/

USGS, 2011b. NEIC Earthquake Catalog [online]. Available from http://earthquake.usgs.gov/earthquakes/eqinthenews/2009/us2009kdb2/

Utha-aroon, C and Ratanajarurak, P, 1996. A new concept in gypsum geology of Thailand, Annual Technical Meeting of the Economic Geology Division, Department of Mineral Resources. p. 1-11.

Wanfang, Z., Beck, B. F. and Stephenson, J. B. 1999. Investigation of groundwater flow in karst areas using component separation of natural potential measurements. Environmental Geology. 37(1-2), 19-25.

Warren, J.K. 2006. Evaporites: sediments, resources and hydrocarbons. Springer, Berlin, Heidelberg, Germany, 1035 pp.

Weight, W.D. 2008. Hydrogeology field manual, 2nd Ed. McGraw-Hill Professional, New York, U.S.A. p. 173.

White, W.B. 1988. Geomorphology and hydrology of karst terrains. Oxford University Press. Oxford, UK, 464 pp.

Wikipedia, 2011. Nakhon Si Thammarat Province [online]. Available from http://en.wikipedia.org/wiki/Nakhon_Si_Thammarat [24 April 2011].

Wyllie, M.R.J., Gregory, A.R., Gardner, L.W. 1956. Elastic wave velocities in heterogeneous and porous media. Geophysics. 21(1), 41-70.

Wyllie, M.R.J., Gregory, A.R., Gardner, L.W., Gardner, G.H.F. 1958. An experimental investigation of factors affecting elastic wave velocities in porous media. Geophysics. 23(3), 459-493.

Yilmaz, I. 2007. GIS based susceptibility mapping of karst depression in gypsum: A case study from Sivas basin (Turkey). Engineering Geology. 90, 89-103.

APPENDIX

APPENDIX A

SEISMIC REFRACTION SHOT DATA
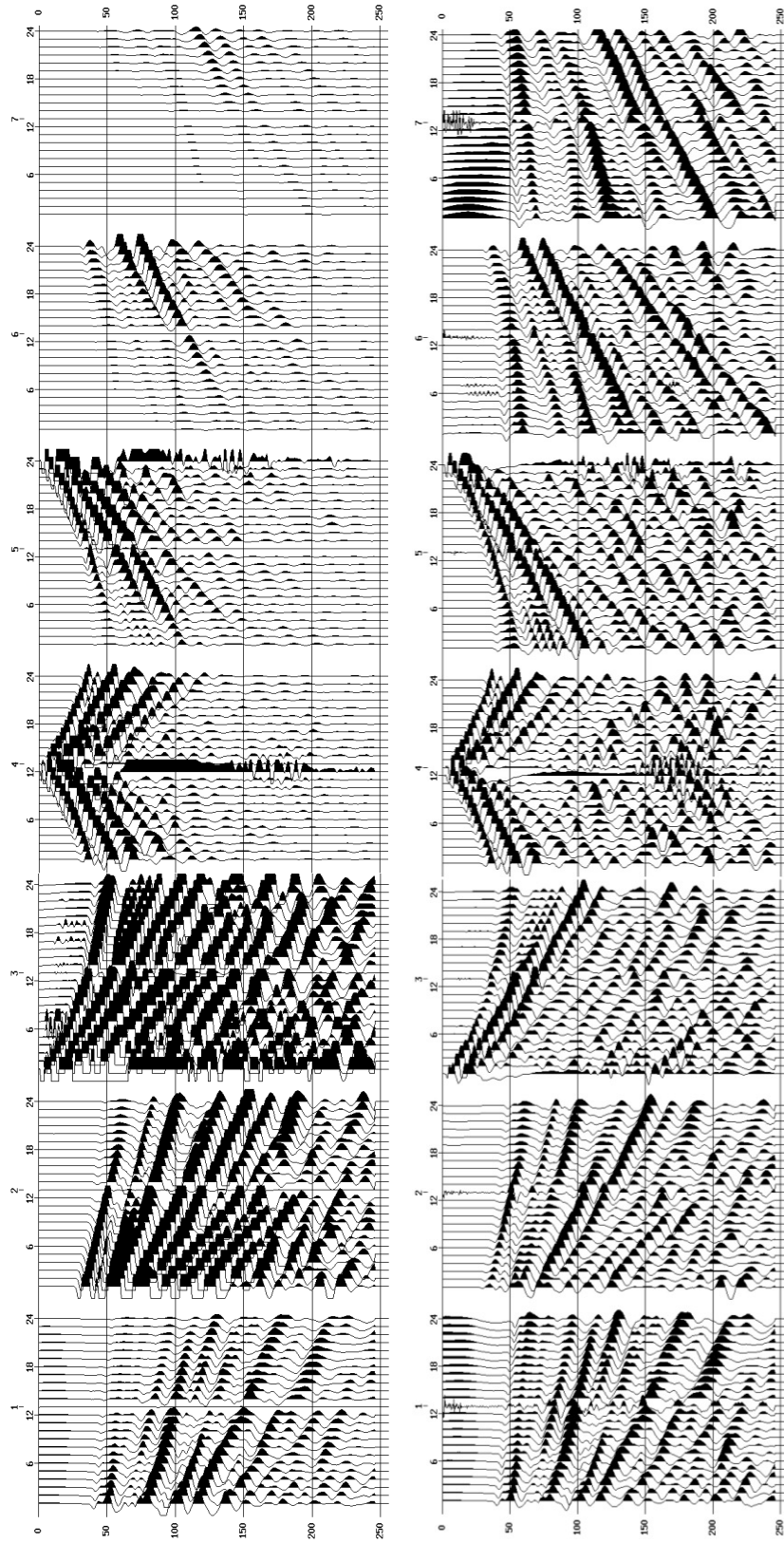
Figure A.1   Refraction raw data at first sinkhole site on 200609, raw shot data (top) and with 100 AGC window (bottom).
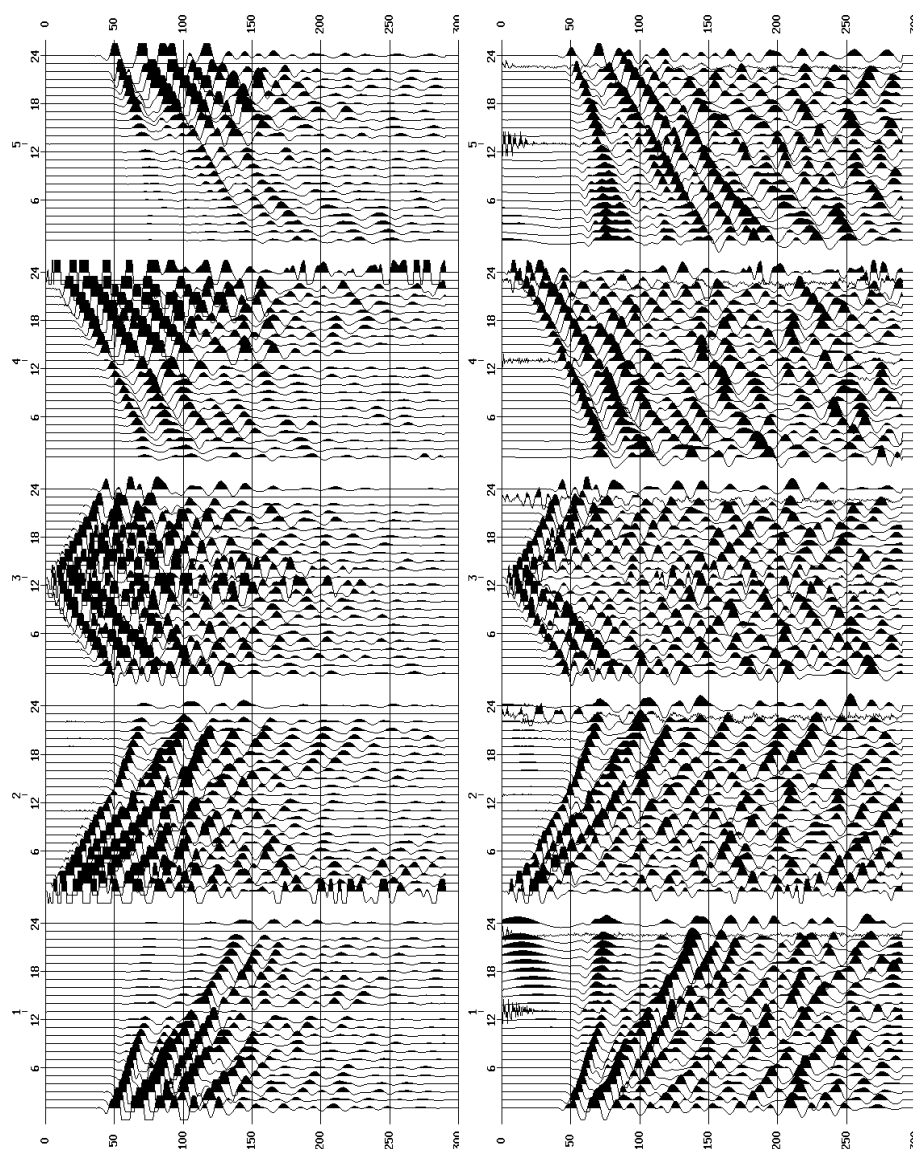
Figure A.2   Refraction raw data at the second sinkhole site on 070909, raw shot data (top) and with 100 AGC window (bottom).

APPENDIX B

OFFSET CONSIDERATION FOR SEISMIC REFLECTION SURVEY
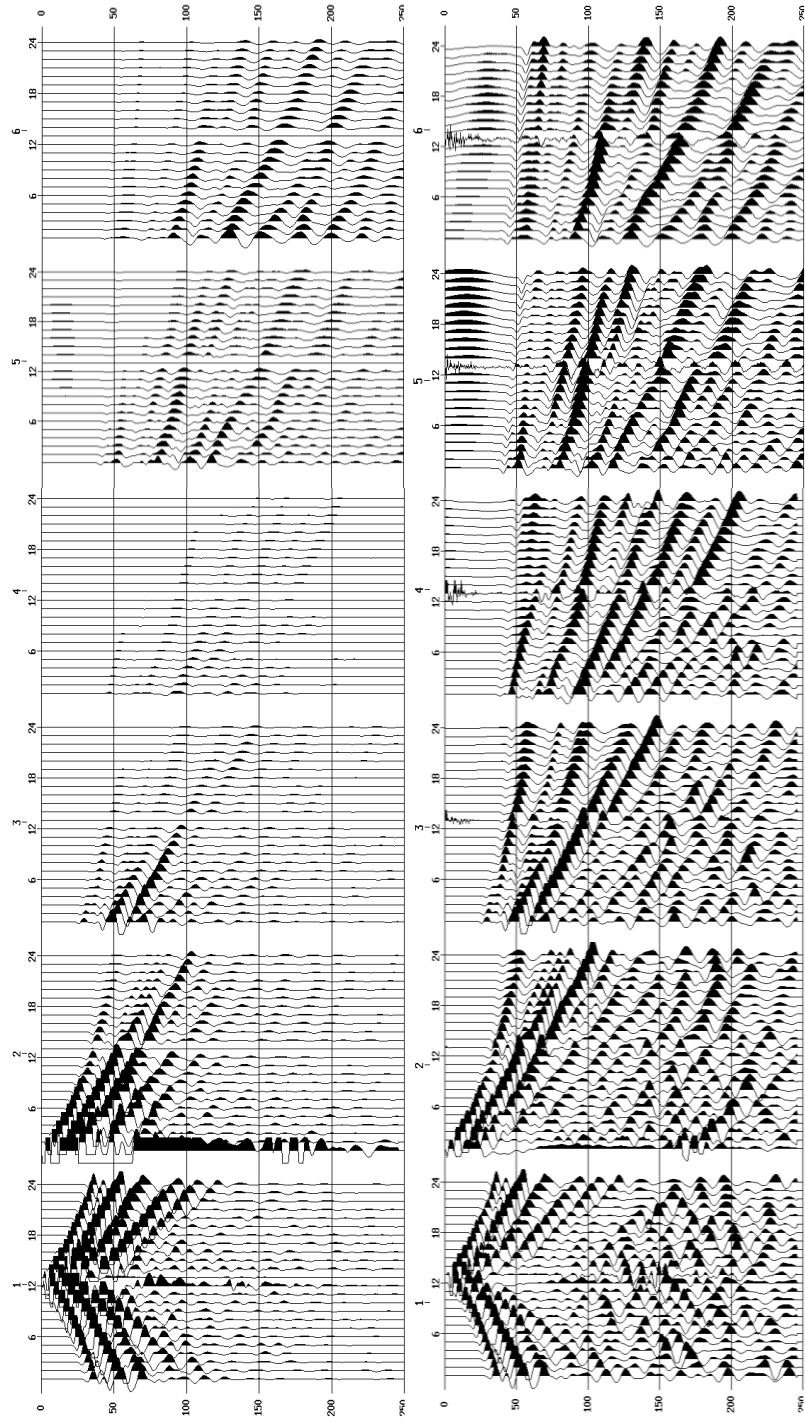
Figure B.1   Offset determination at first sinkhole site on 200609, raw shot data (top) and with 100 AGC window (bottom).
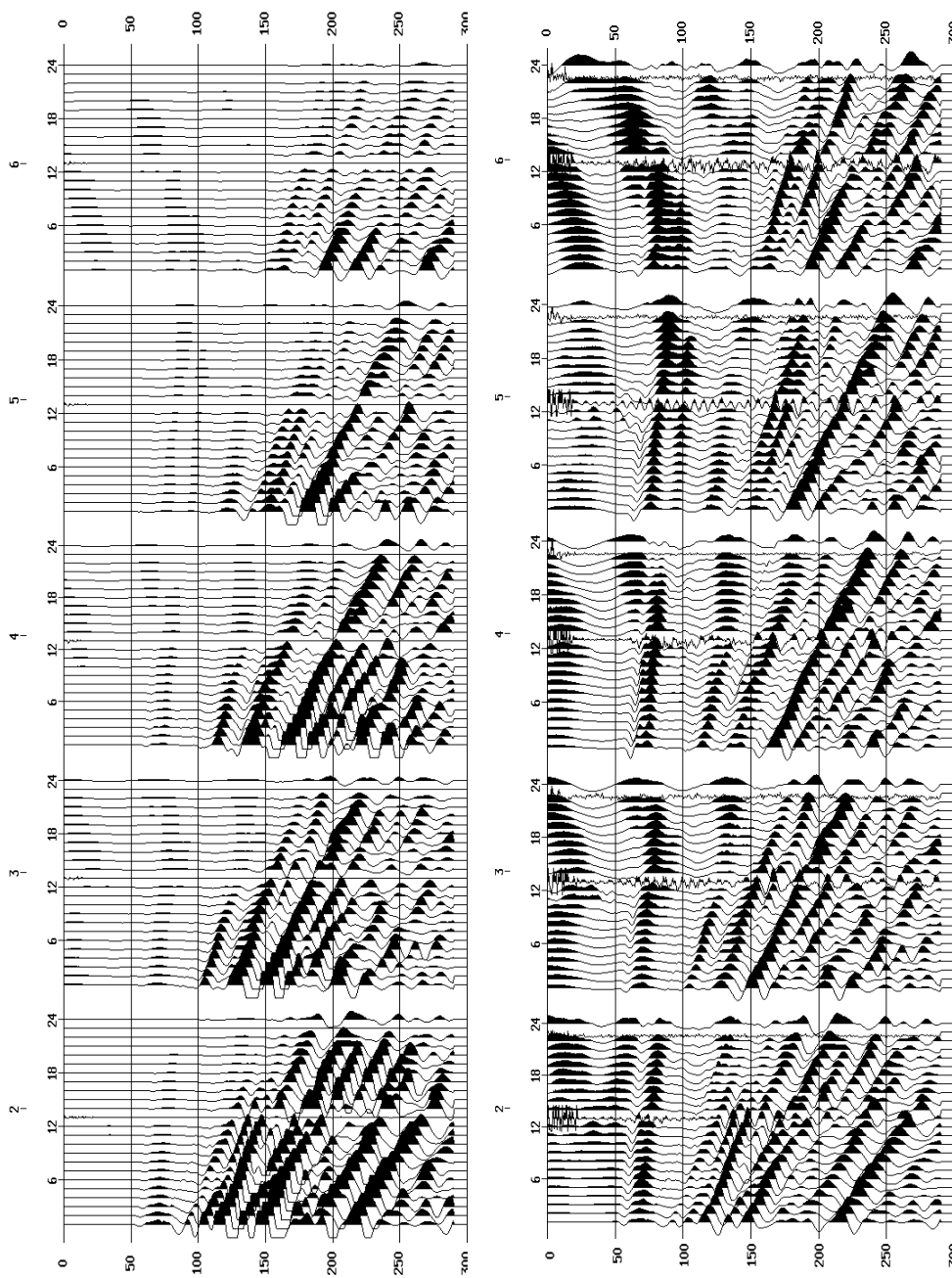
Figure B.2   Offset determination at the second sinkhole on 070909, raw shot data (top) and with 100 AGC window (bottom).

APPENDIX C

SEISMIC REFLECTION PROCESSING STEPS

First sinkhole site
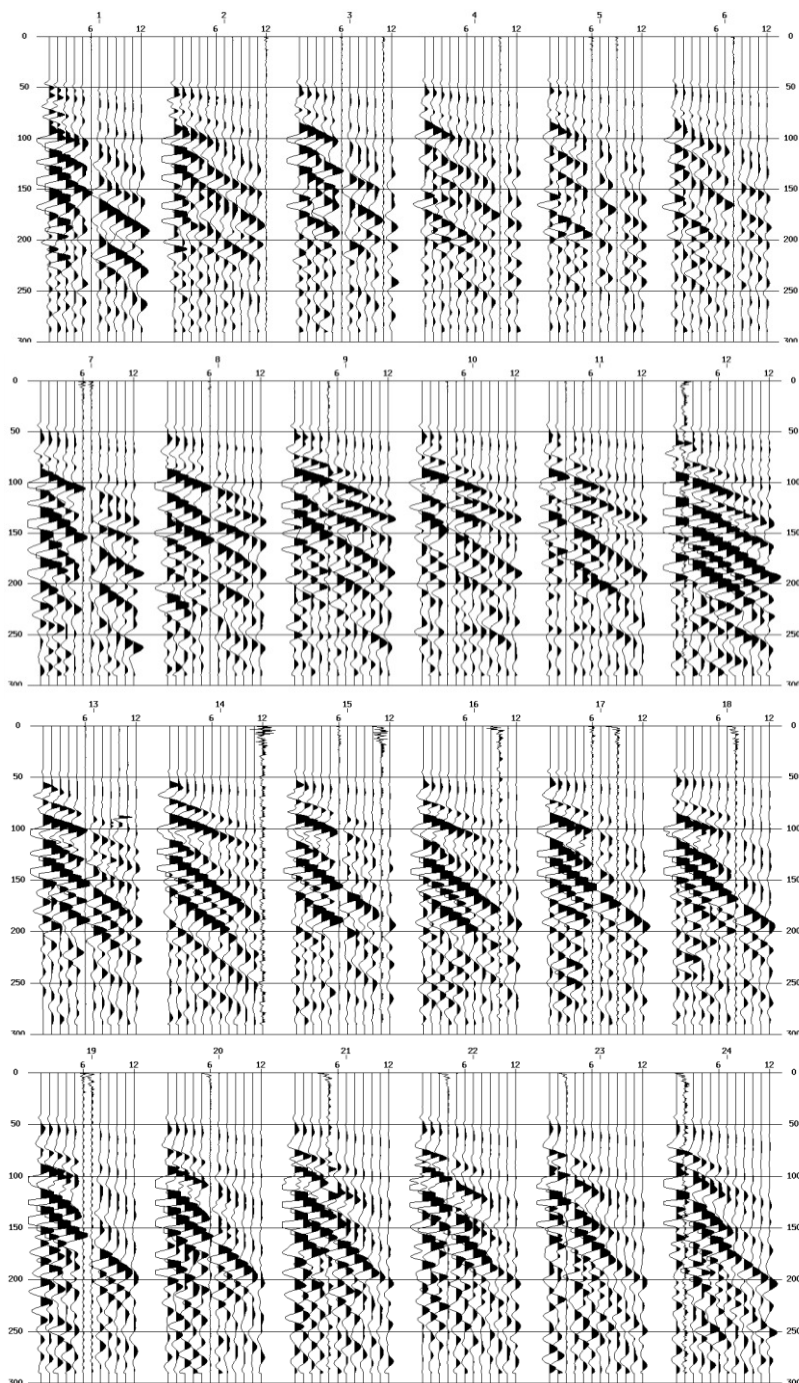
Figure C.1   24-shots of seismic reflection raw data.
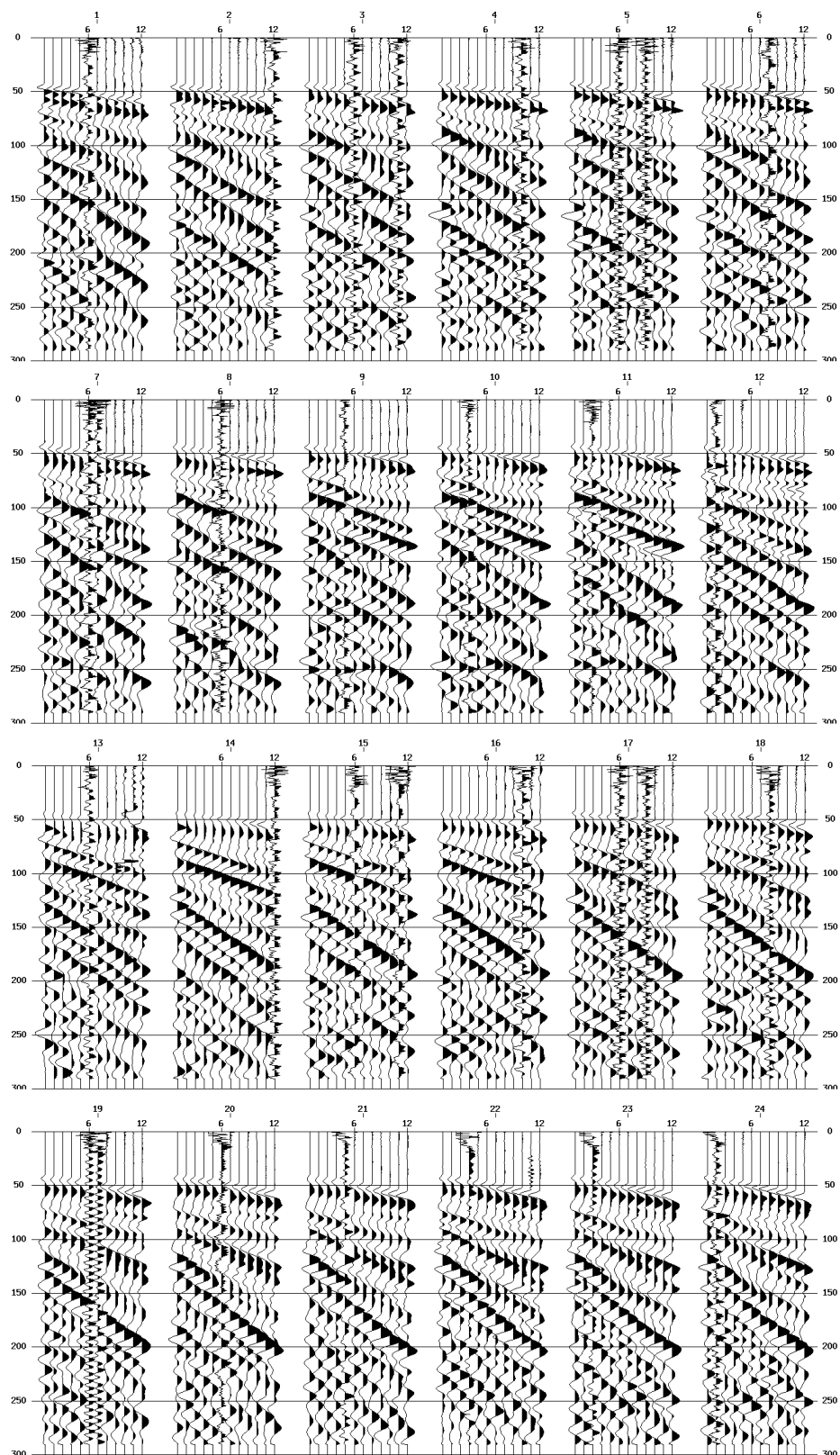
Figure C.2   Reflection raw data with applied 100 AGC window.
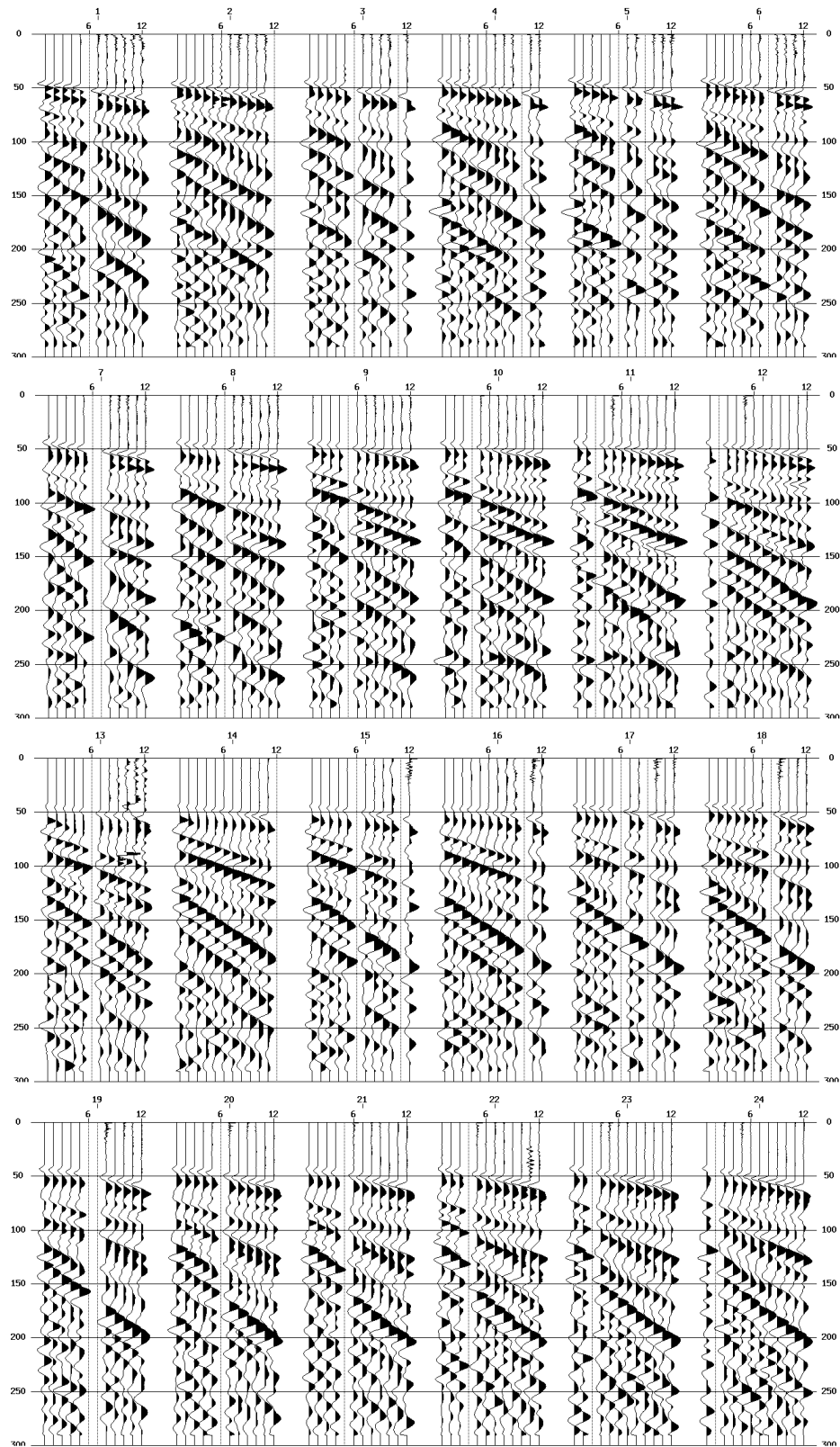
Figure C.3   Seismic reflection raw data with noisy traces edited.
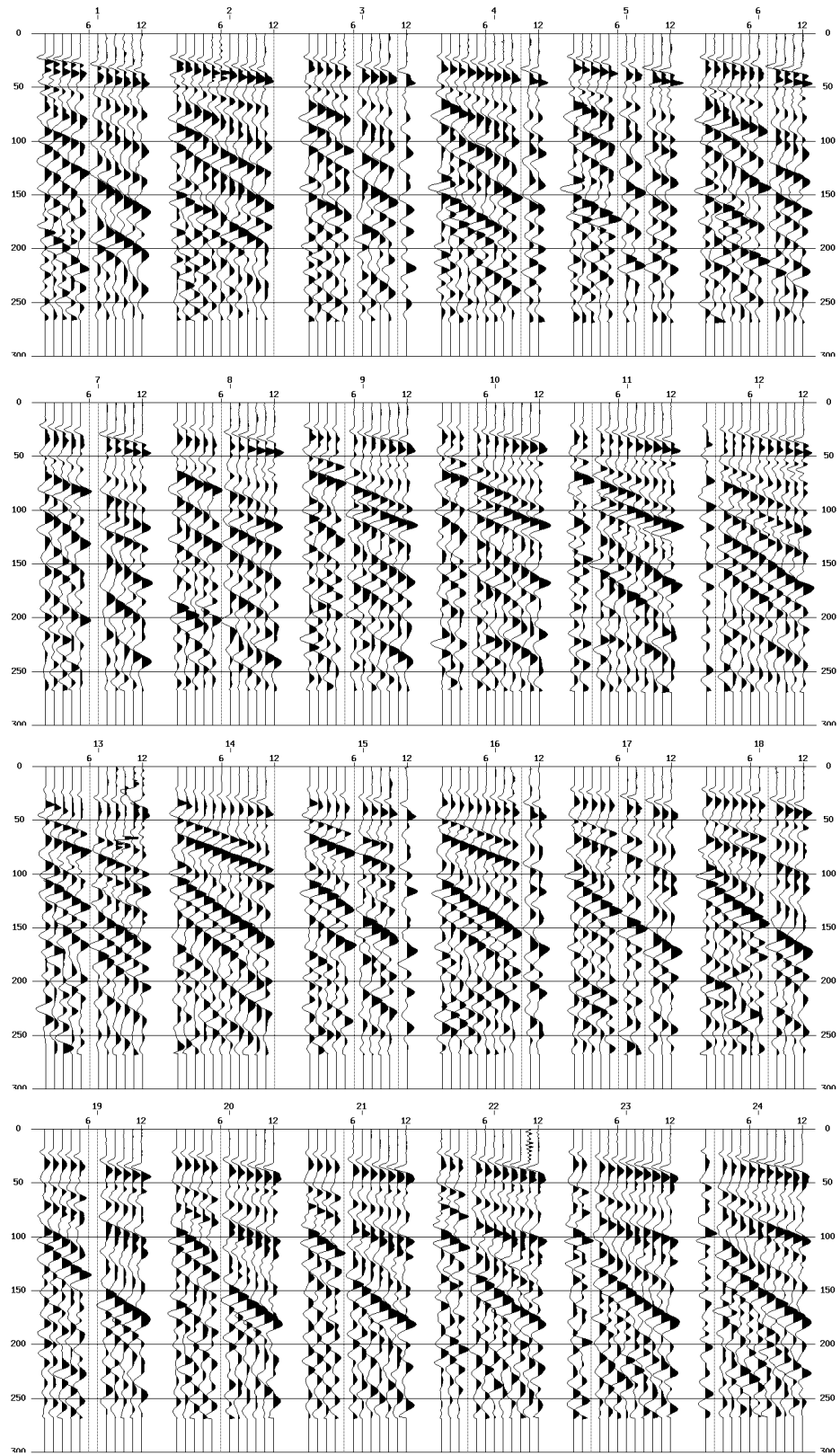
Figure C.4   Seismic reflection data with applied static correction.
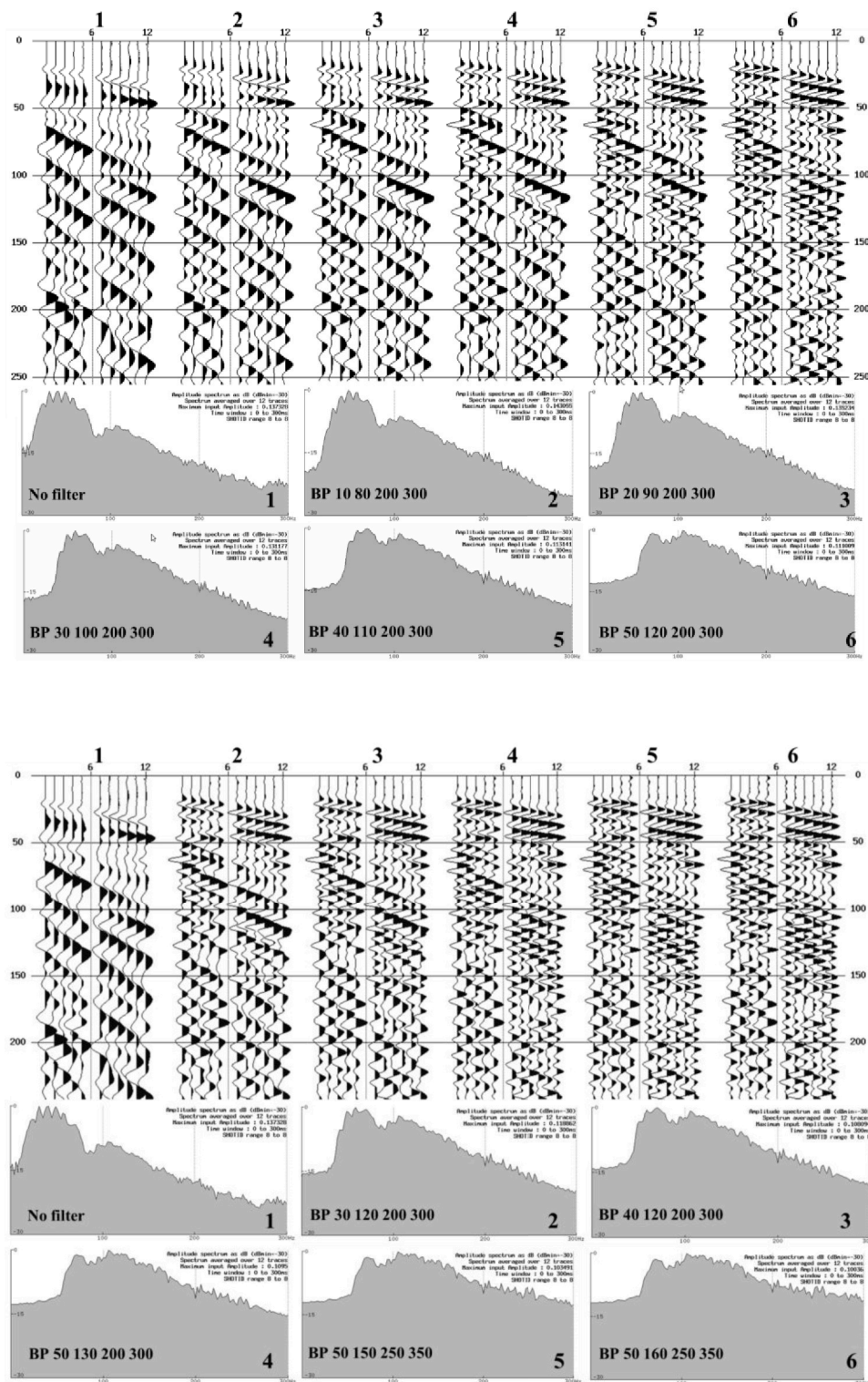
Figure C.5   A shot of seismic reflection raw data with varied applied filter ranges for the consideration of the appropriated filter range.
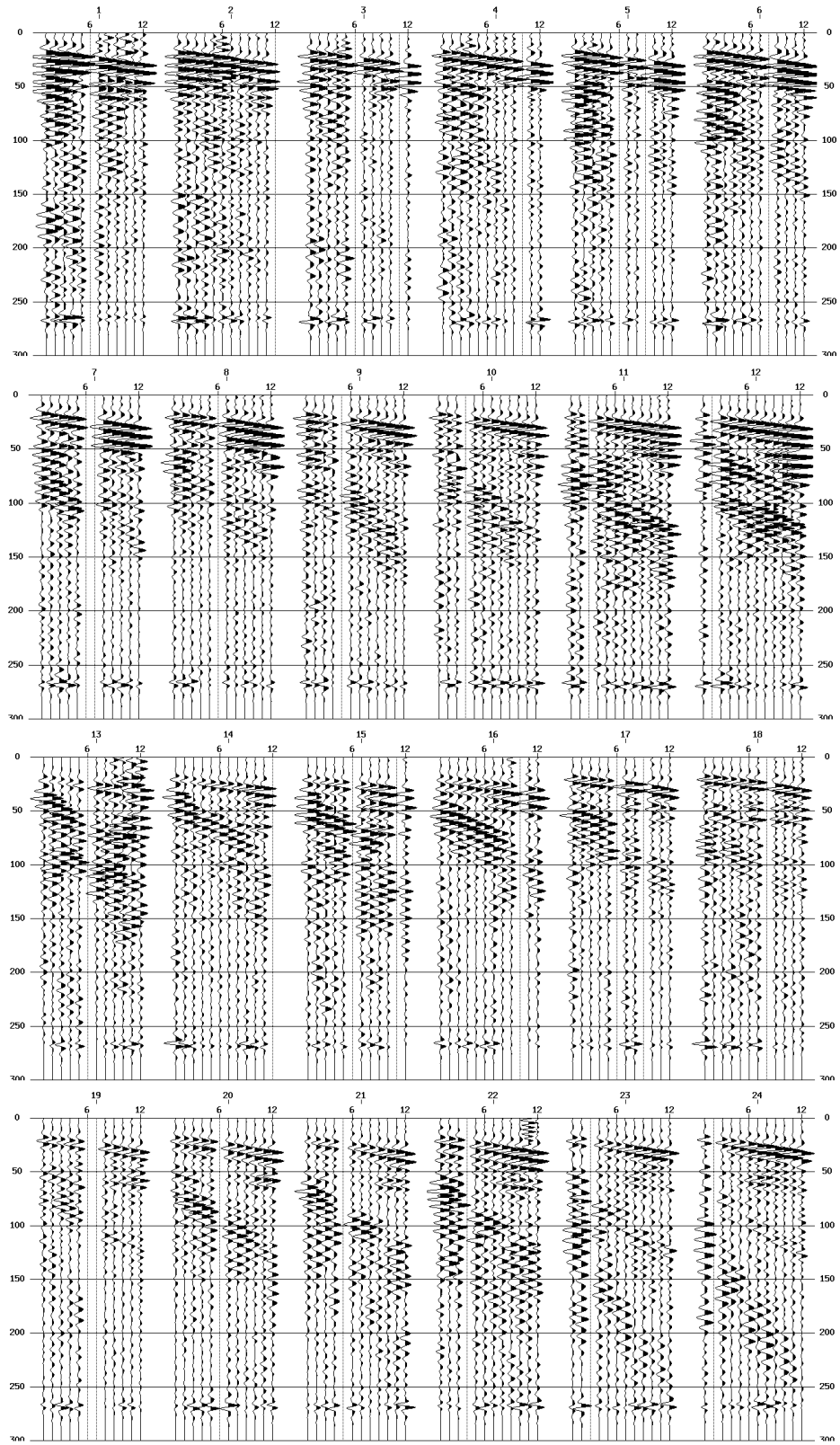
Figure C.6 Seismic reflection shots data with applied bandpass filter in the range of 50-130-250-350.
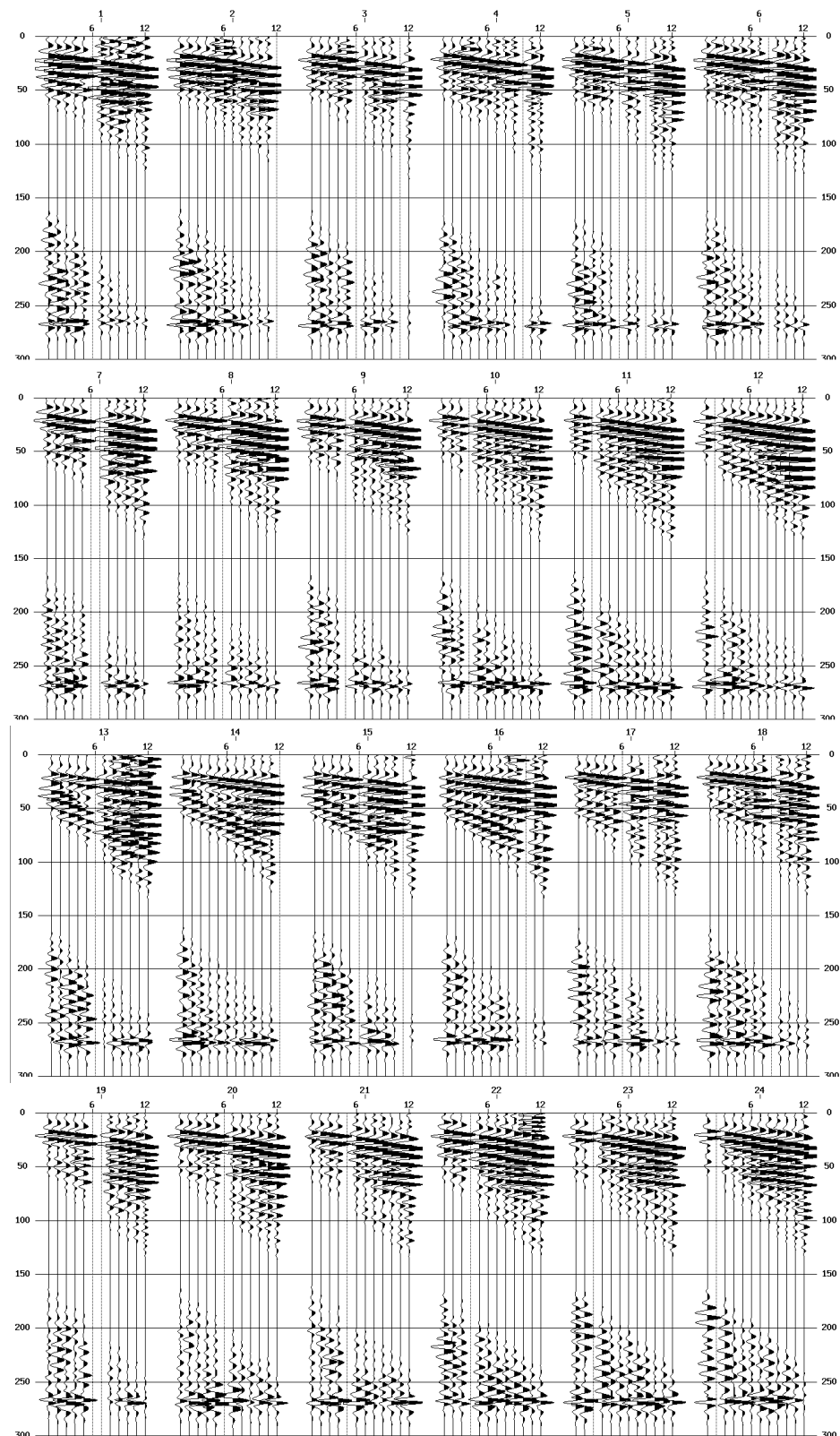
Figure C.7   Seismic reflection shots data with applied airwave mute with a velocity of 330 m/s.
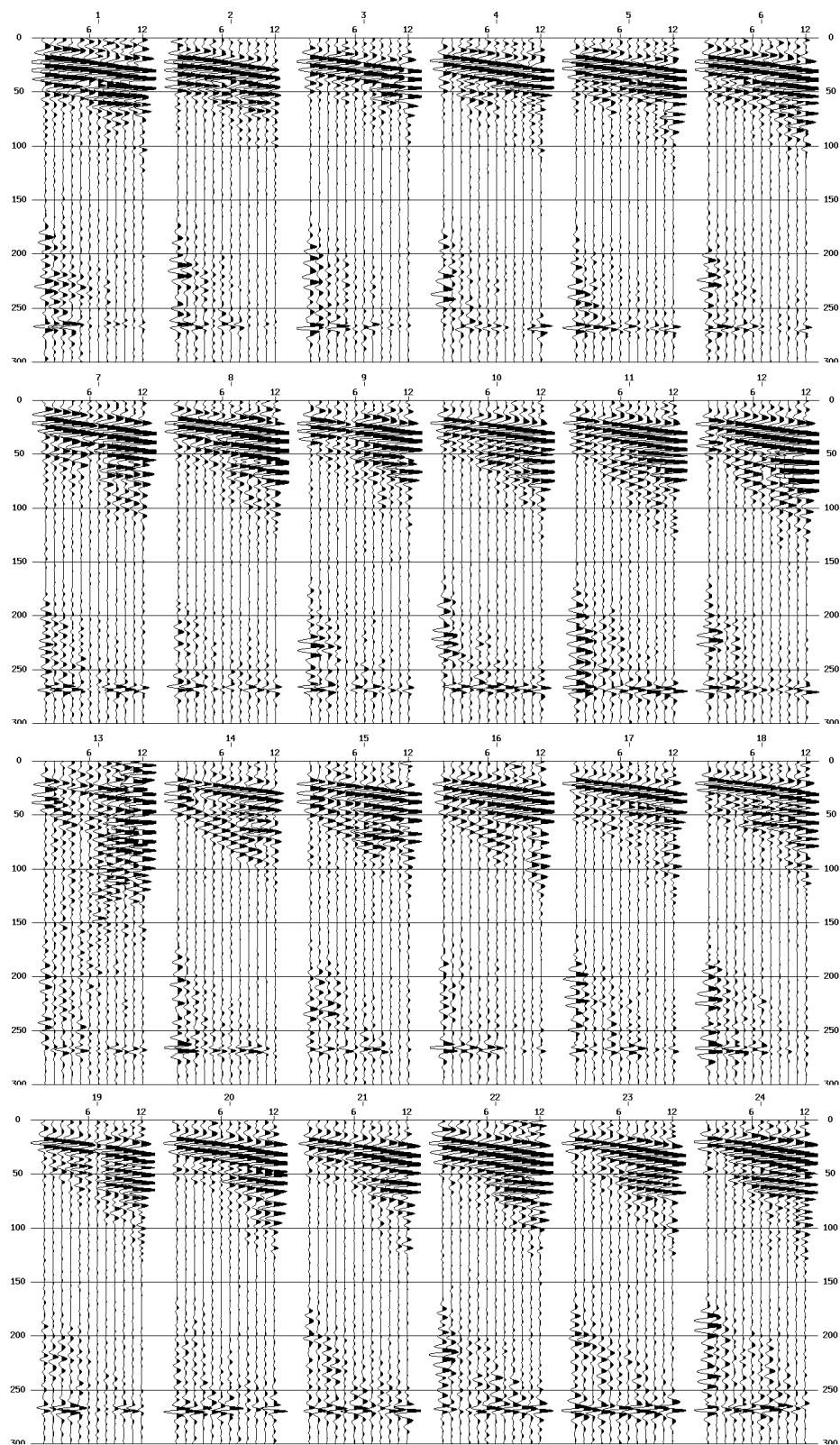
Figure C.8   Seismic reflection shots data with applied f-x deconvolution.
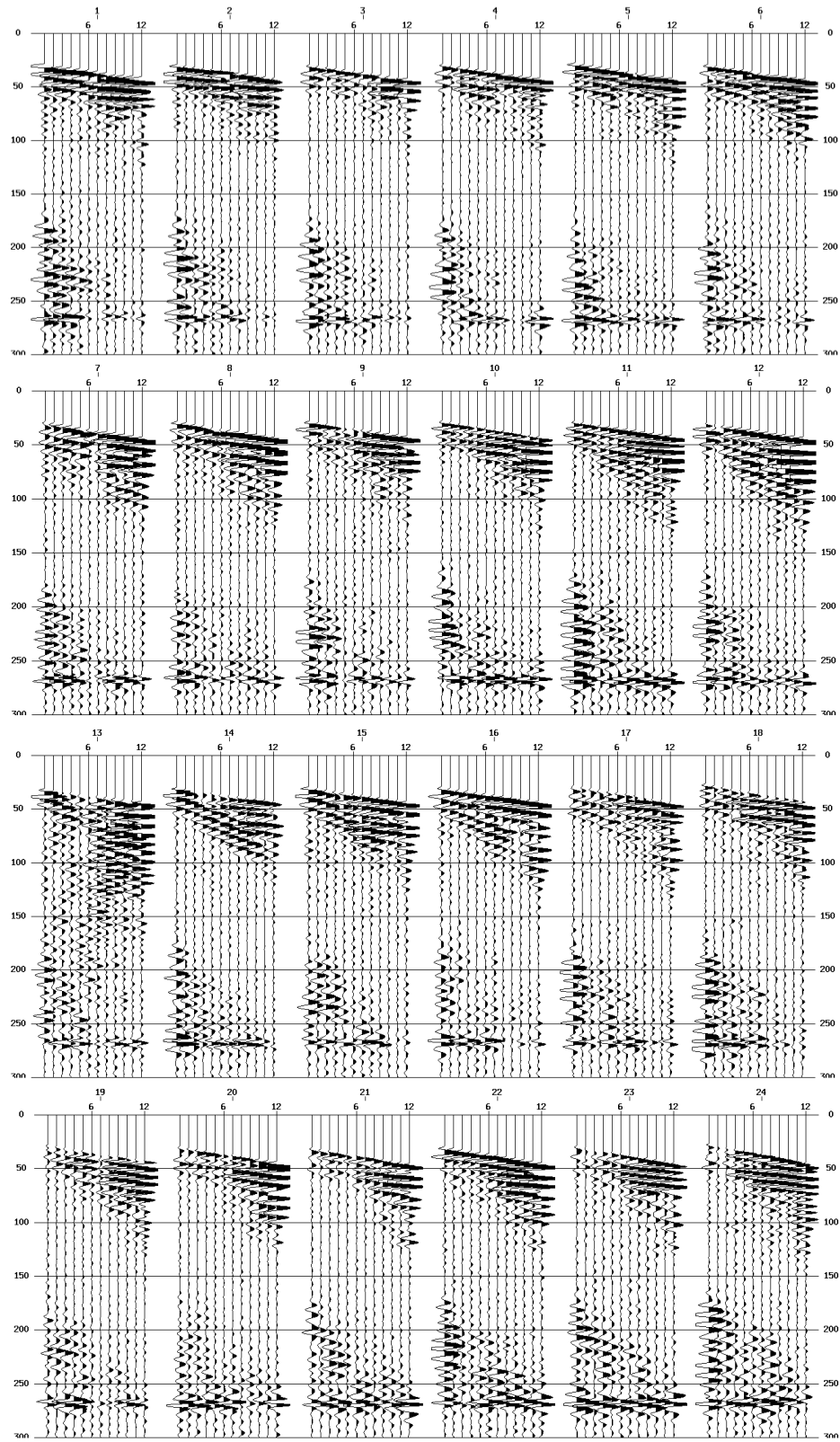
Figure C.9   Seismic reflection shots data with muted refracted wave and artifact.
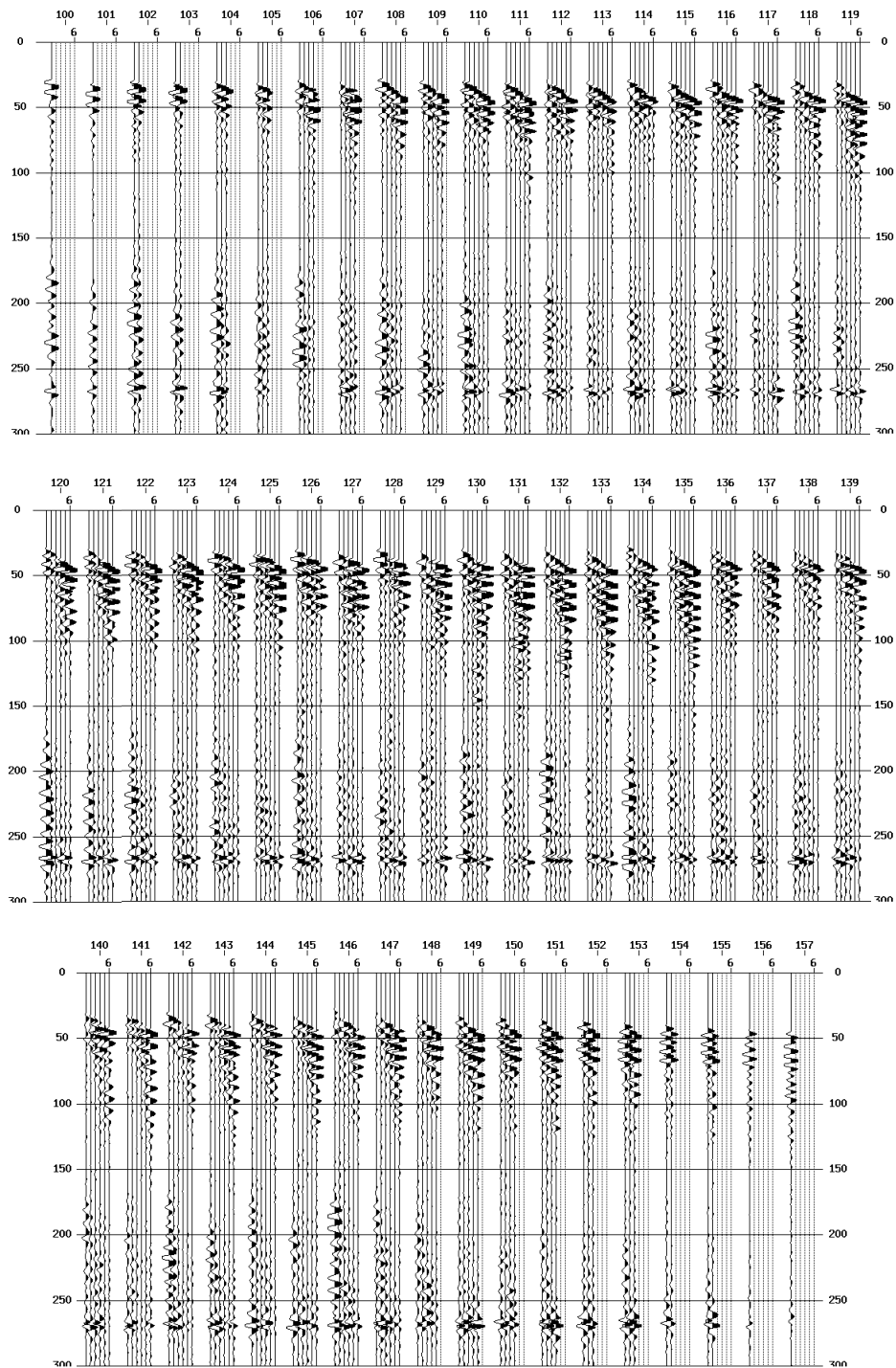
Figure C.10 Seismic reflection traces were sort at common depth point (CDP).
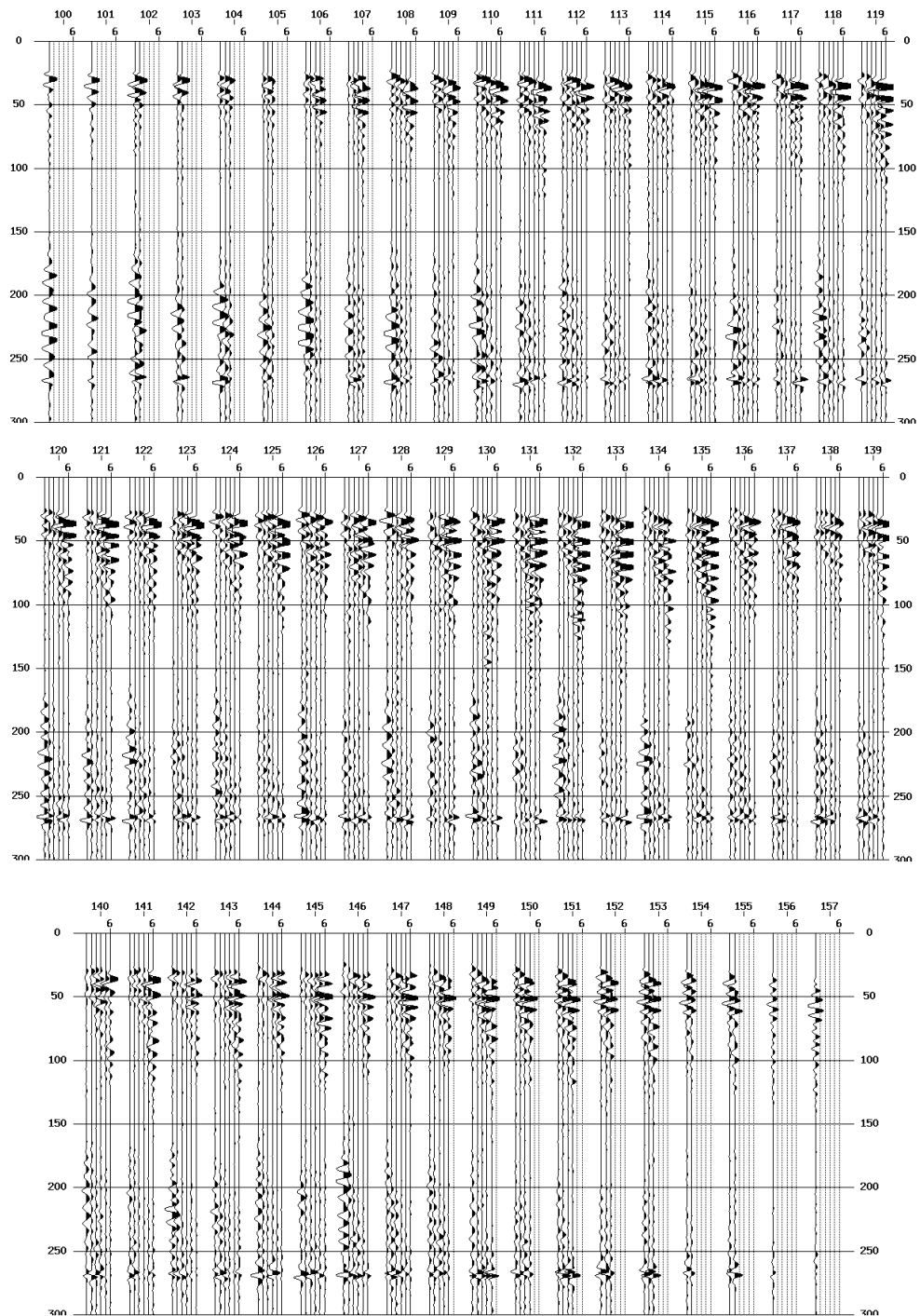
Figure C.11   Application of NMO to each CPD with a velocity of 1,800 m/s.
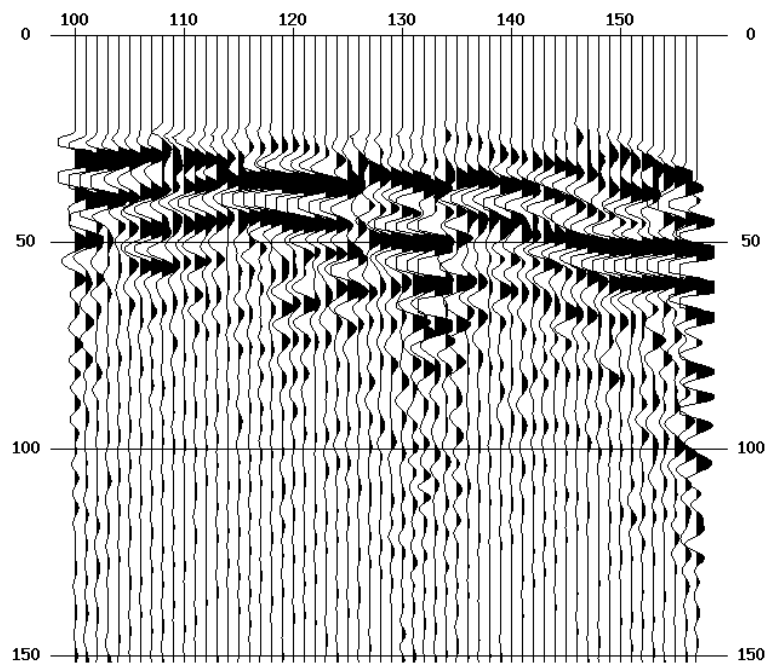
Figure C.12   Each CDP after applied NMO velocity were stacked to time section.
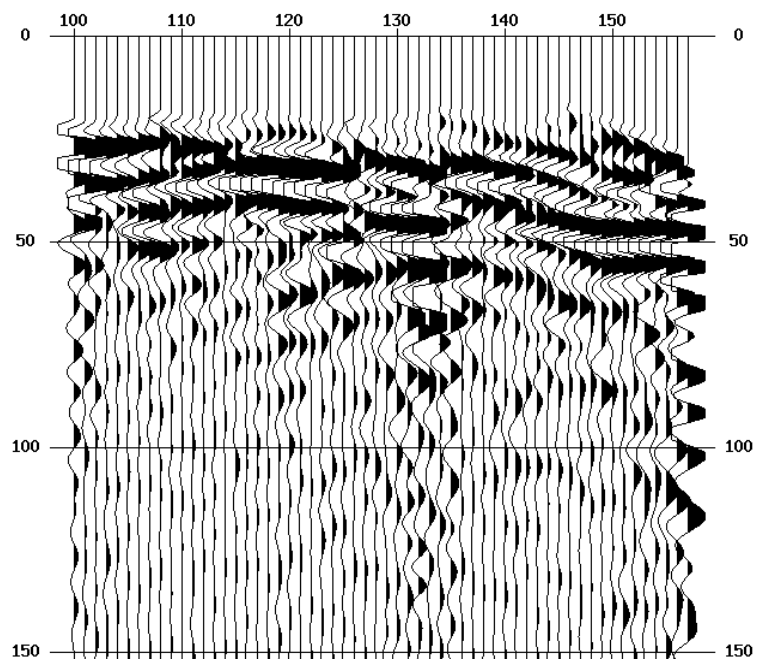
Figure C.13   Seismic reflection time section converted to depth section.

Second sinkhole site
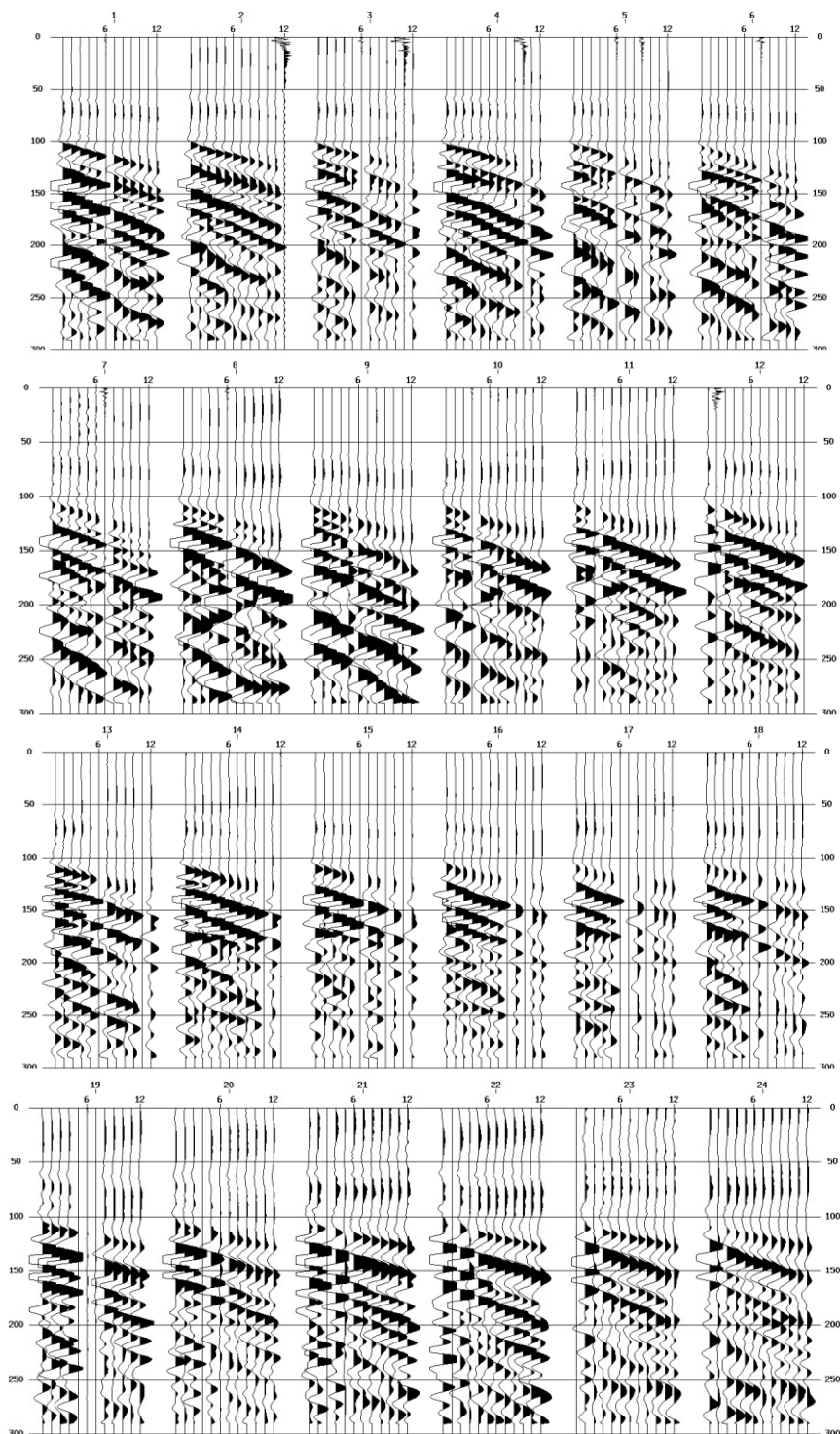
Figure C.14   24-shots of seismic reflection raw data.
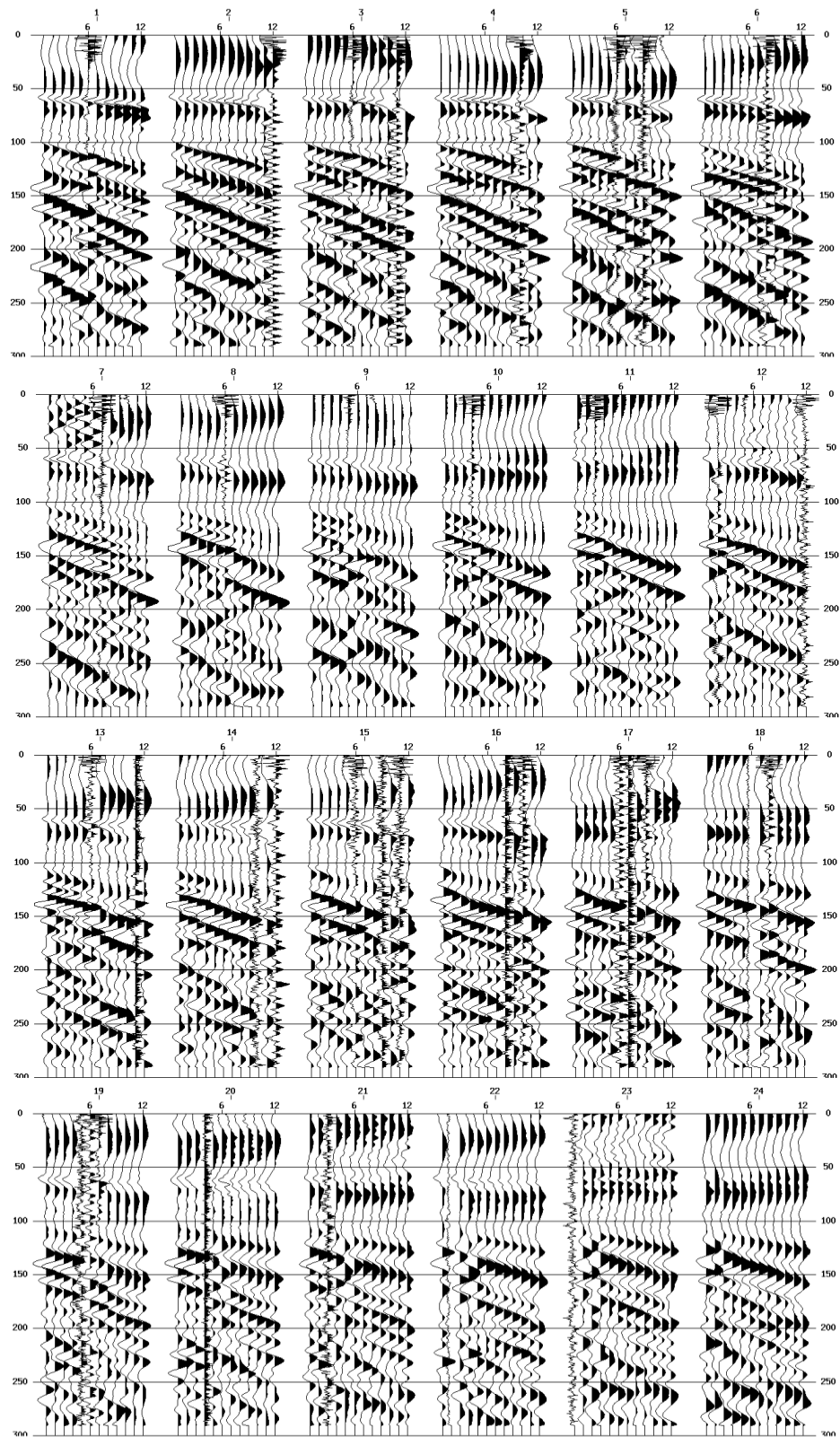
Figure C.15   Seismic reflection shots data with applied 100 AGC window.
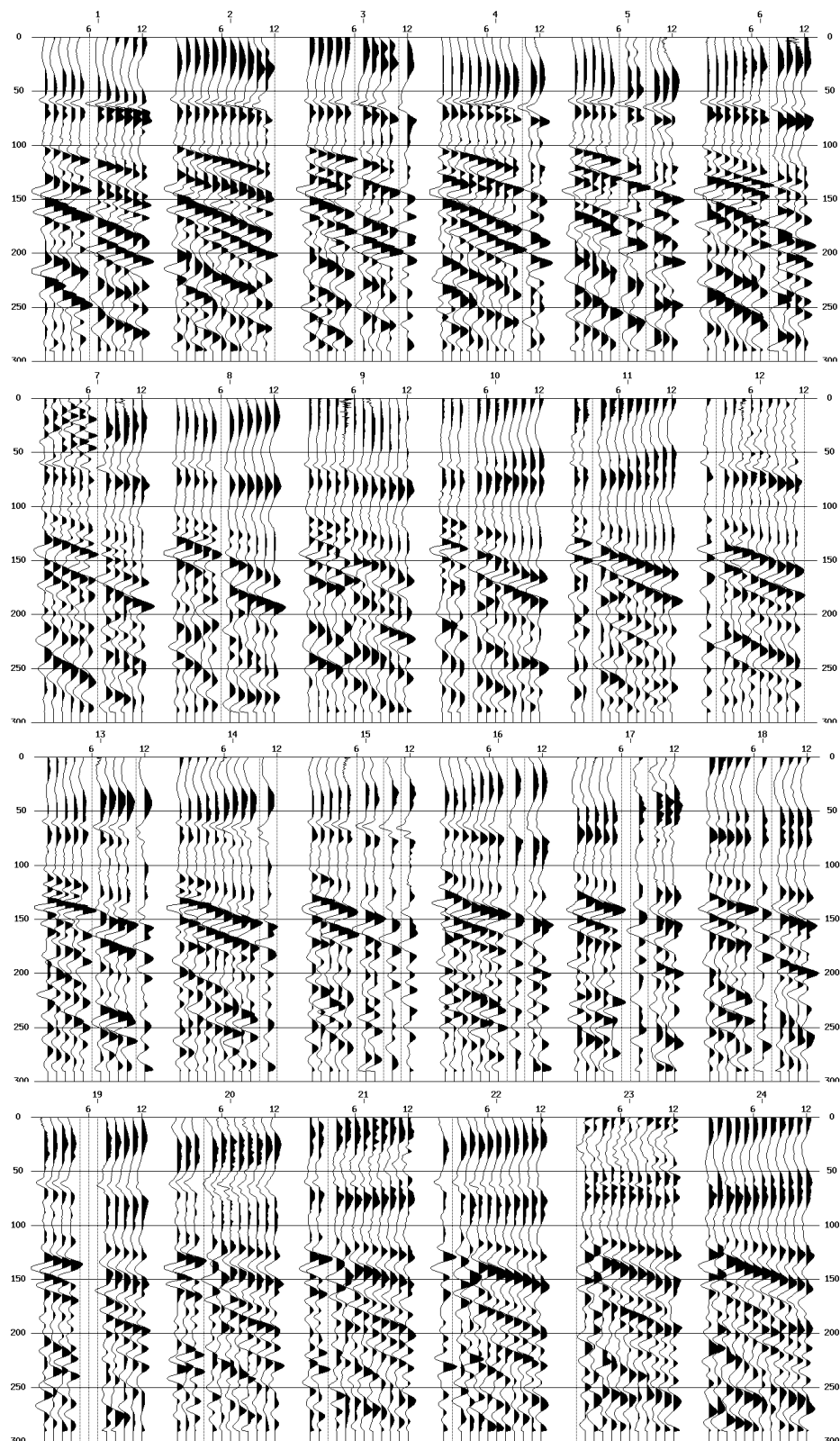
Figure C.16   Seismic reflection shots data with edited noisy traces.
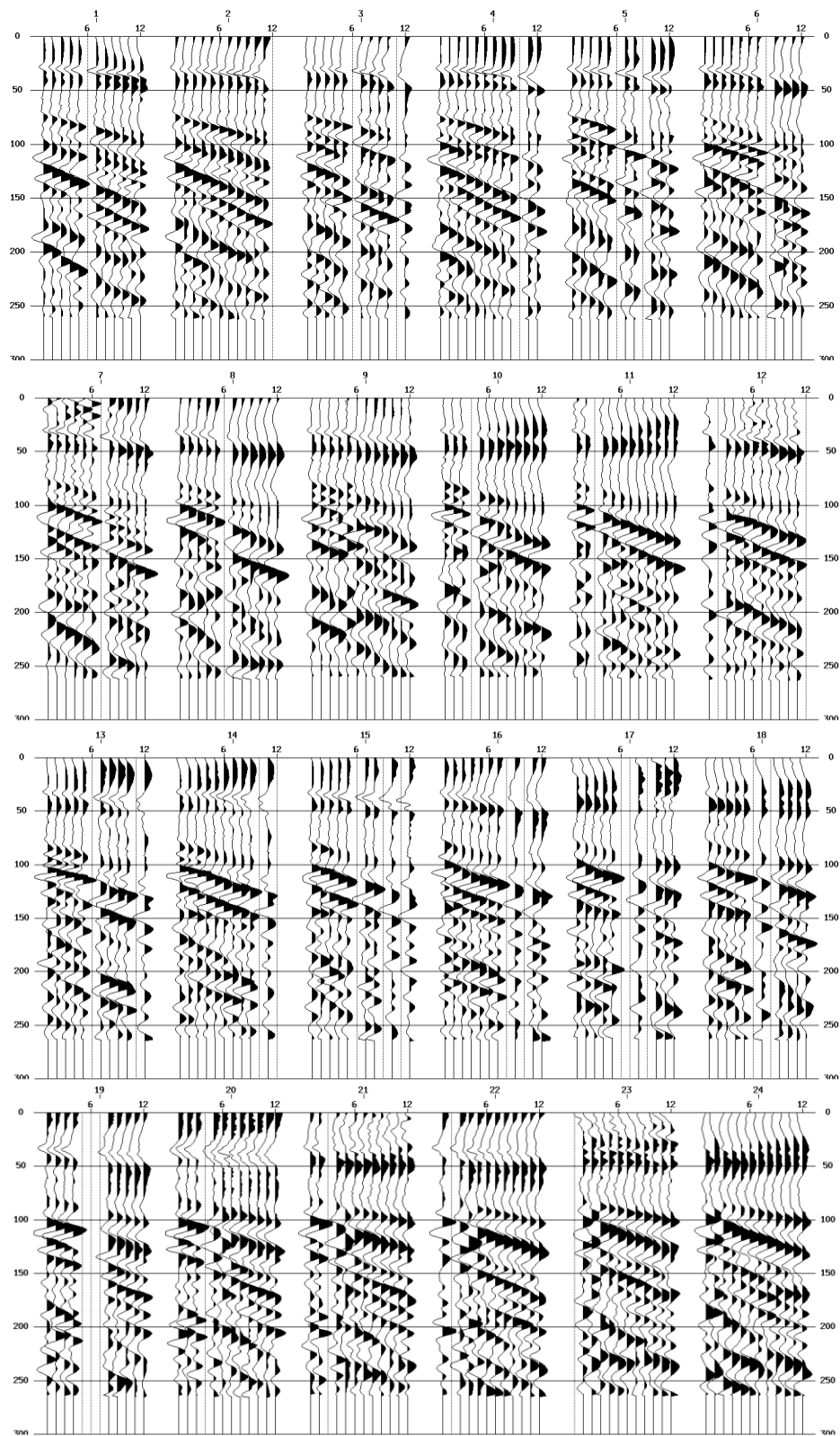
Figure C.17   Seismic reflection shots data with applied static correction.
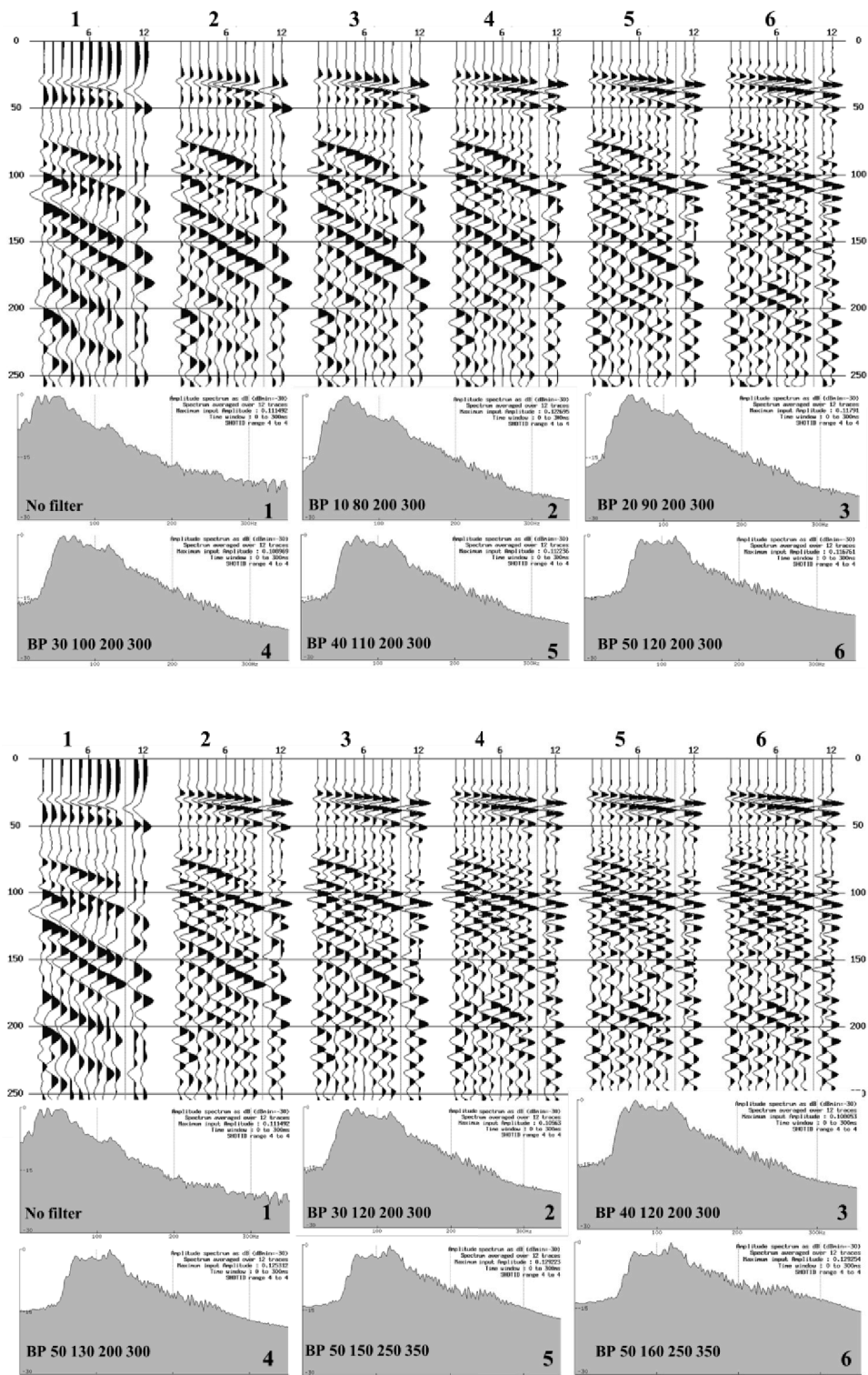
Figure C.18   A shot of seismic reflection raw data with varied applied filter ranges for consideration of an appropriate range.
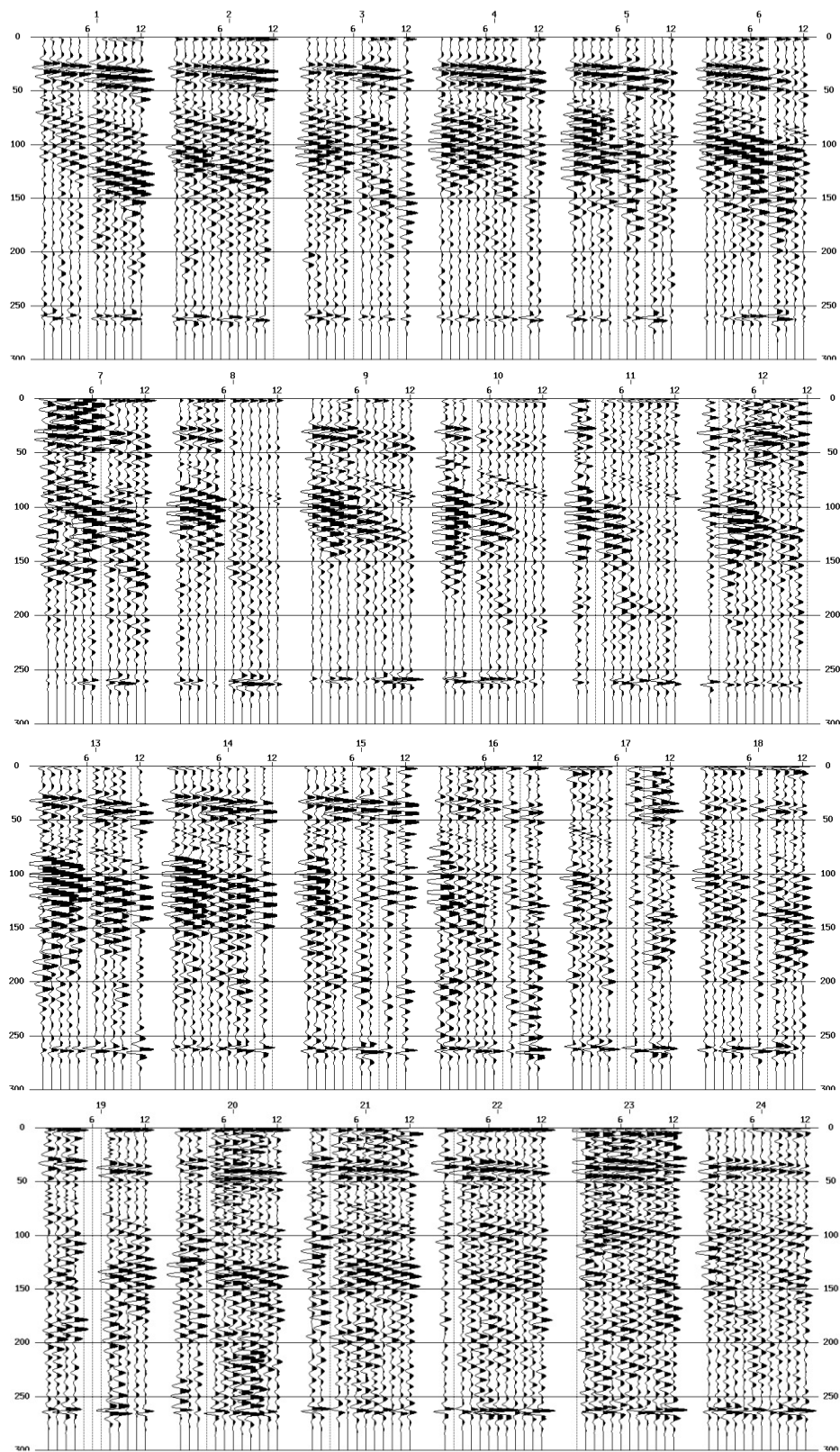
Figure C.19   Seismic reflection shots data with applied bandpass filter in the range
50-130-250-350.
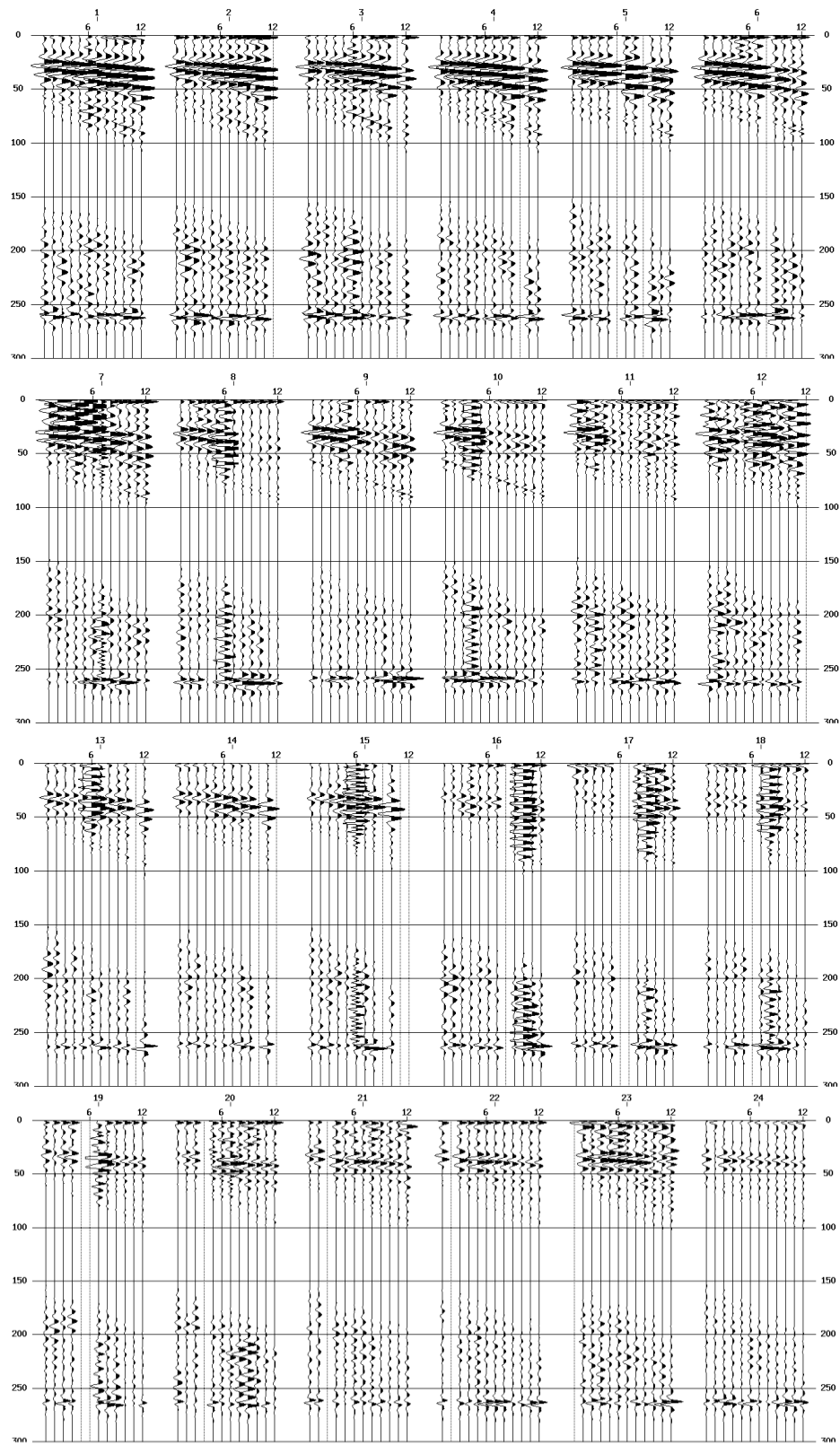
FigureC.20 Seismic reflection shots data with applied airwave mute using a velocity of 330 m/s.
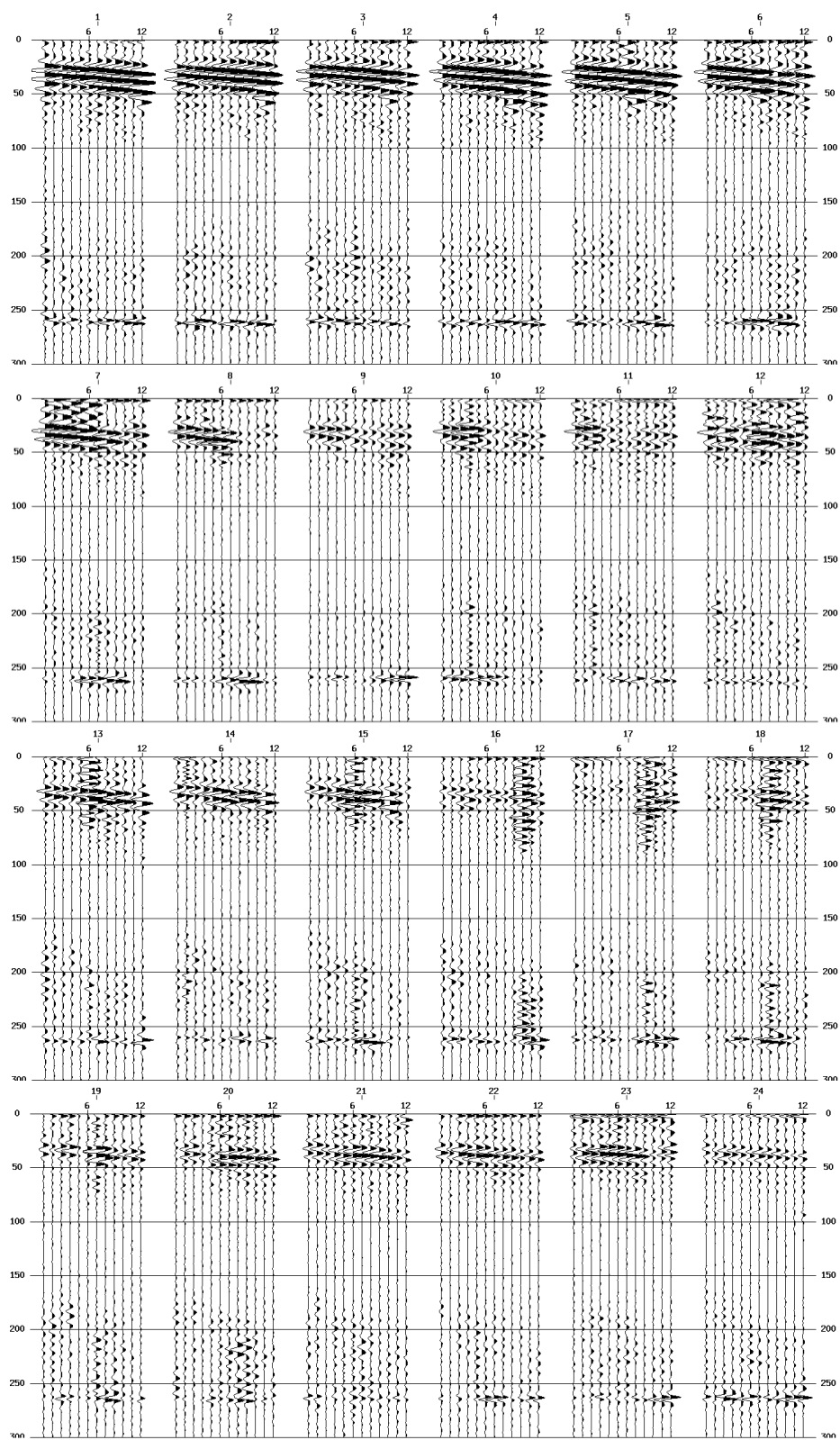
Figure C.21   Seismic reflection shots data with applied f-x deconvolution.
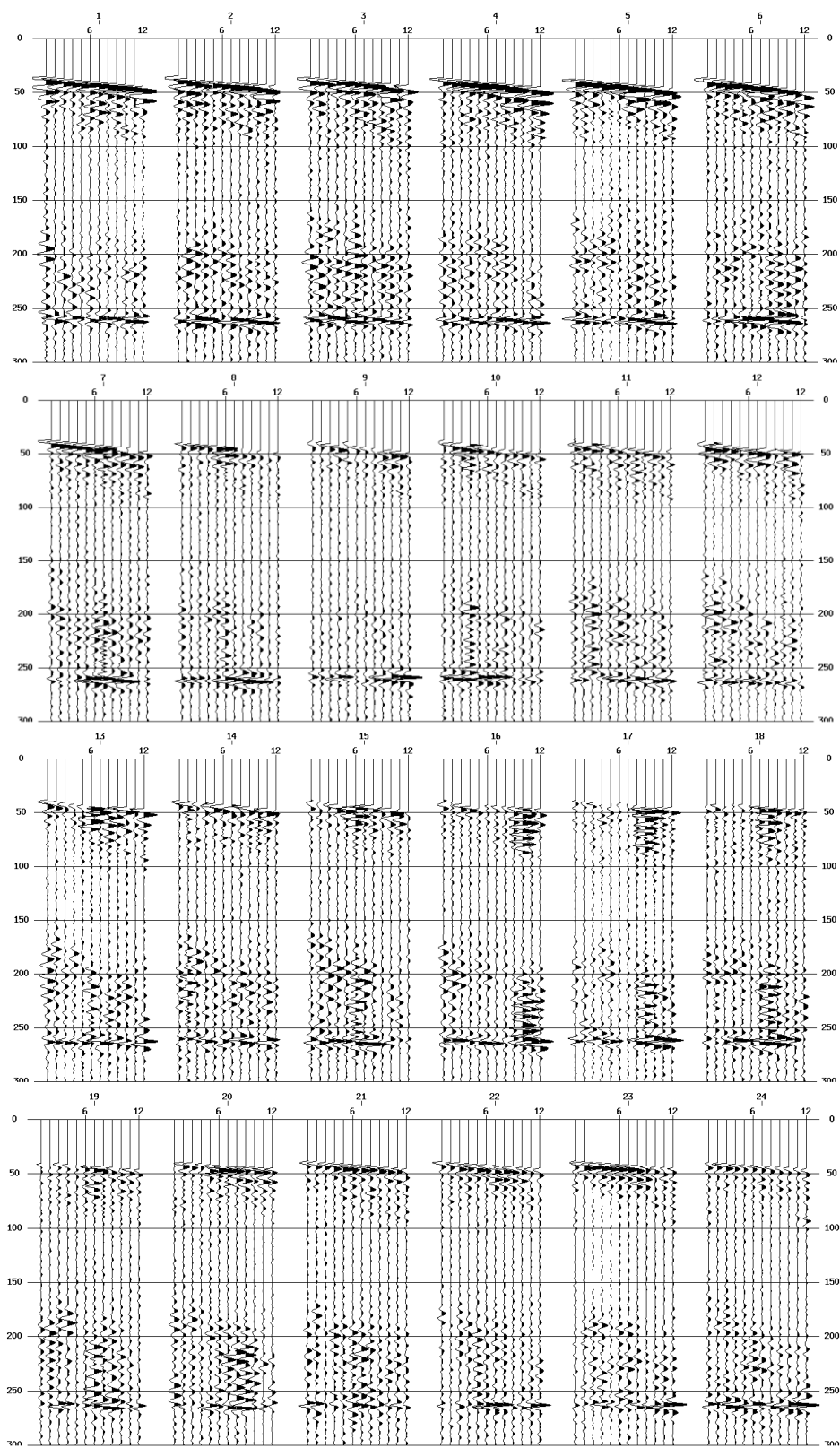
Figure C.22   Seismic reflection shots data with muted refracted waves and artifacts.
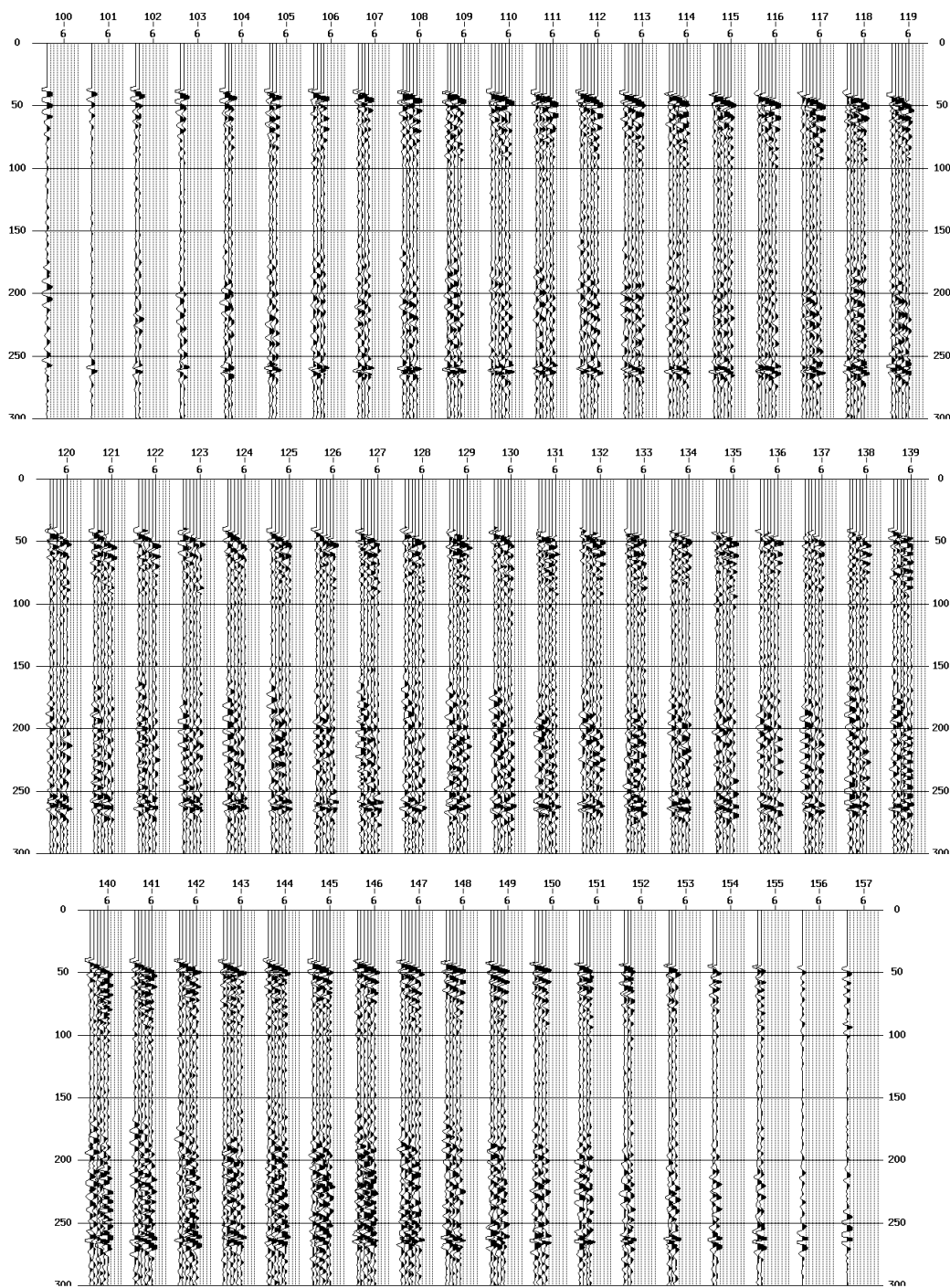
Figure C.23 Seismic reflection traces were sort at common depth point (CDP).
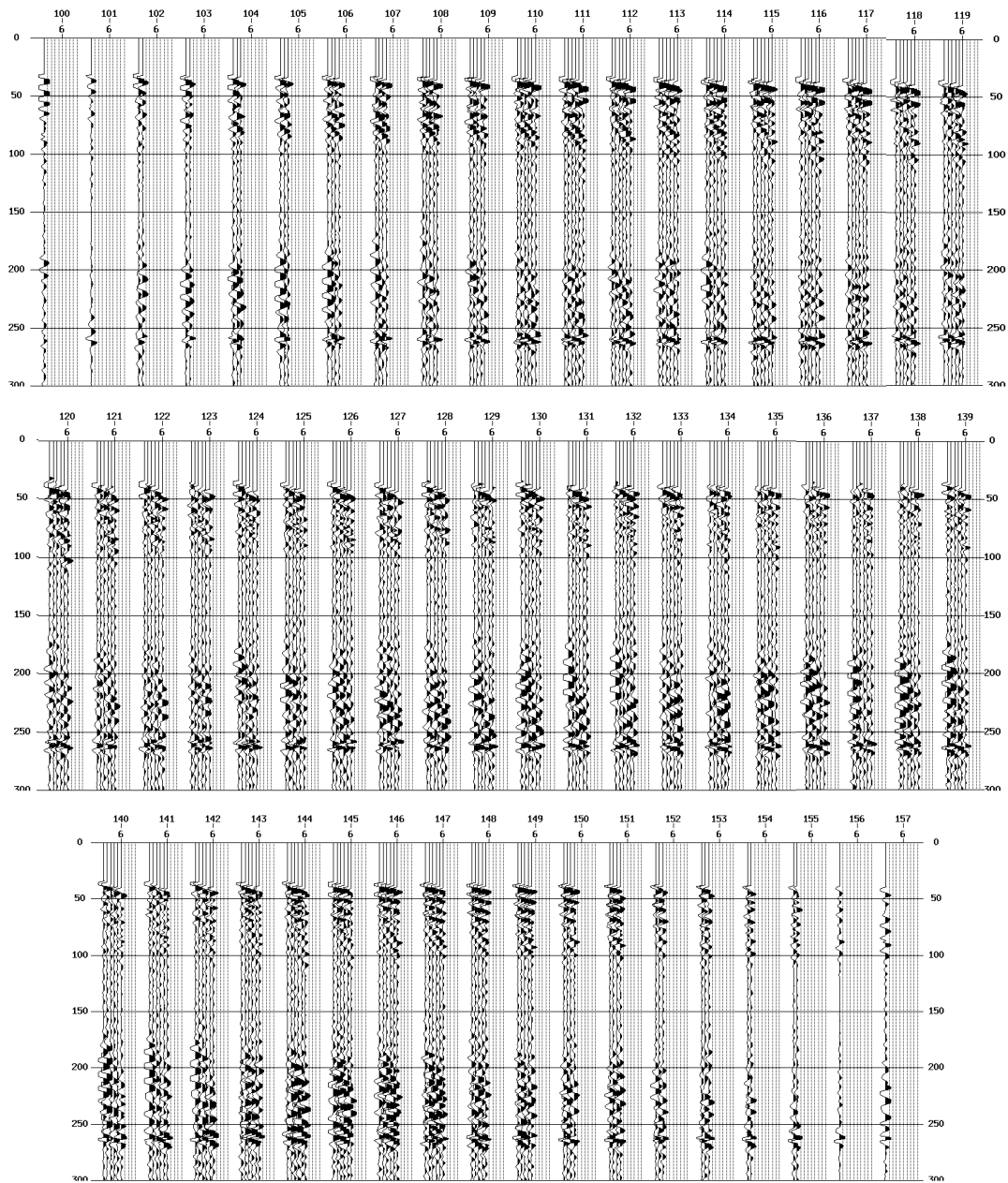
FigureC.24   Applied of NMO to each CPD with a velocity of 1,850 m/s.
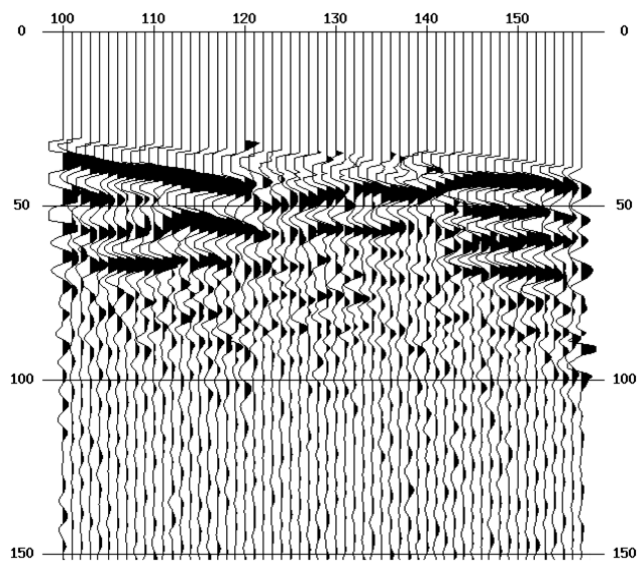
Figure C.25   Each CDP after applied NMO velocity were stacked to time section.
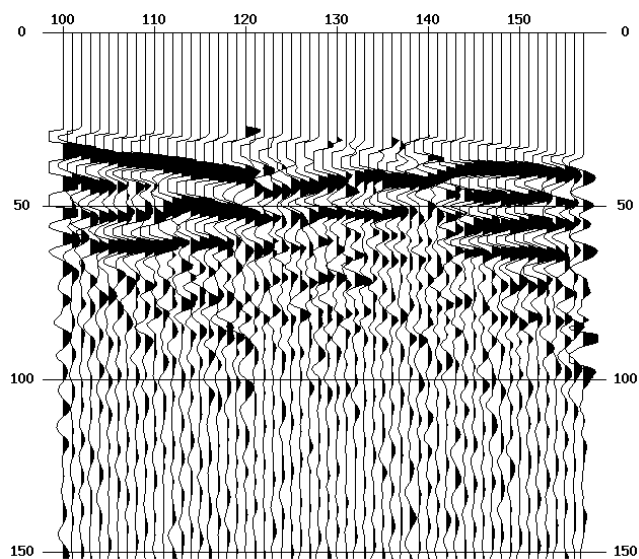
Figure C.26   Seismic reflection time section converted to depth section.

APPENDIX D

CHEMICAL ANALYSIS OF GROUNDWATER IN STUDY AREA

ศูนย์เครื่องมือวิทยาศาสตร์ มหาวิทยาลัยสงขลานครินทร์

ชั้น I อาคารบริหารวิชาการรวม มหาวิทยาลัยสงขลานครินทร์ วิทยาเขตหาดใหญ่ อำเภอหาดใหญ่ จังหวัดสงขลา 90110

Scientific Equipment Center, Prince of Songkla University

Central Academic Administrator Bld. Hat-Yai Campus, Songkhla 90110 Tel.0 7428 6904-7 Fax.0 7421 2813

F-RES-003I/E Rev. 5 29/05/52

No. 1631/52 Page 1/1

TEST REPORT

Customer Name and Address : Ms. Aksara Mayamae

Department of Physics, Faculty of Science, Prince of Songkla University

Test Request Form No. : 1758/52

Test Item(s) Received Date : July 2, 2009

Test Request Date : July 2, 2009

Analyst : Ms. Nitchanan Nantakakul and Mr. Wiangchai Chongsrirattanakun

Test Performed Date : July 2, 2009 – July 10, 2009

Test Method Used : Wet Lab refer to WI-RES-NOVA-001rev_1 REF-RES-Wet Lab-001 Rev.4

ICP-OES refer to REF-RES-ICP/Si – 006 Rev.0

Test Equipment : pH meter (cyberscan 500^{pH}), Optical Emission Spectrometer (Optima 4300 DV)

Perkin Elmer Instruments and Spectroquant$^®$ NOVA 60

Test Technique: Inductively Coupled Plasma Optical Emission Spectrometry, Spectrometry and Gravimetric method

Test Condition : Wavelength : Ca = 317.933 nm, TDS at 180°C

Test Item(s) Description : Water in well   **Quantity** : 1 sample

Test Result(s):

Parameter	Well in Tambon Tayang	
	Results	%RSD
Total Dissolved Solids (TDS)	1,674.33 mg/L	0.18
Calcium (Ca)	114 mg/L	4.49
pH	5.51	0.002
Sulfate	1,035 mg/L	0.00

* Limit of Quantitation (LOQ); Ca = 0.002 mg/L

* Refer raw data at 1555-52

(Ms. Patchara Sukonrat)

Inspector

Remark This Test report is valid only for the tested sample.

This Test report shall not be reproduced except in full, without written approval of the Scientific Equipment Center.

Figure D.1   Chemical analysis result of the groundwater in the adjacent well.

ศูนย์เครื่องมือวิทยาศาสตร์ มหาวิทยาลัยสงขลานครินทร์
ชั้น I อาคารบริหารวิชาการรวม มหาวิทยาลัยสงขลานครินทร์ วิทยาเขตหาดใหญ่ อำเภอหาดใหญ่ จังหวัดสงขลา 90110
Scientific Equipment Center, Prince of Songkla University
Central Academic Administrator Bld. Hat-Yai Campus, Songkhla 90110 Tel.0 7428 6904-7 Fax.0 7421 2813

F-RES-003I/E Rev. 5 29/05/52

No. 3185/52 Page 1/1

TEST REPORT

Customer Name and Address :   Ms. Aksara Mayamae

        Department of Physics, Faculty of Science, Prince of Songkla University

Test Request Form No. :   3447/52

Test Item(s) Received Date :   December 16, 2009

Test Request Date :   December 16, 2009

Analyst :   Ms. Nitchanan Nantakakul and Ms. Sowaluk Aubpatham

Test Performed Date :   December 17, 2009 - December 18, 2009

Test Method Used :   Wet Lab refer to WI-RES-NOVA-001rev_1 , WI-RES-Wet Lab-001 Rev.5

        ICP-OES refer to REF-RES-ICP/Si – 006 Rev.0

Test Equipment :   pH meter (cyberscan 500^{pH}), Optical Emission Spectrometer (Optima 4300 DV)

        Perkin Elmer Instruments and Spectroquant® NOVA 60

Test Technique :   Inductively Coupled Plasma Optical Emission Spectrometry, Spectrometry and

        Gravimetric method
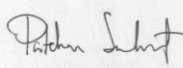
Test Condition :   Wavelength Mg = 279.077 nm, Ca = 317.933 nm

        TDS Dry at 180°C

Test Item(s) Description : in   water in second sinkhole   **Quantity :**   1 sample

Test Result(s) :

Parameter	water in second sinkhole	
	Results	%RSD
Total Dissolved Solids (TDS)	44.67 mg/L	2.59
Sulfate	23 mg/L	2.55
pH	4.81	0.24
Magnesium (Mg)	0.43 mg/L	0.63
Calcium (Ca)	0.59 mg/L	2.37

* Limit of Quantitation (LOQ); Mg = 0.011 mg/L, Ca = 0.028 mg/L,

* Refer raw data at 3368-52

(Ms. Patchara Sukonrat)

Inspector

<u>Remark</u> This Test report is valid only for the tested sample.

This Test report shall not be reproduced except in full, without written approval of the Scientific Equipment Center.

Figure D.2   Chemical analysis result of the groundwater in the second sinkhole.

APPENDIX E

X-RAY DIFFRACTION IDENTIFICATION RESULTS

ศูนย์เครื่องมือวิทยาศาสตร์ มหาวิทยาลัยสงขลานครินทร์
ชั้น 1 อาคารบริหารวิชาการรวม มหาวิทยาลัยสงขลานครินทร์ วิทยาเขตหาดใหญ่ อำเภอหาดใหญ่ จังหวัดสงขลา 90110
Scientific Equipment Center, Prince of Songkla University
Central Academic Administrator Bld. Hat-Yai Campus, Songkhla 90110 Tel.0 7428 6904-7 Fax.0 7421 2813

F-RES-003E Rev. 6 20/10/53

No. 2115/54 Page 1/1

TEST REPORT

Customer Name and Address:	MissAksara Mayamae
	Department of Physics, Faculty of Science, Prince of Songkla University
Test Request Form No.:	2102/54
Test Item(s) Received Date:	July 22, 2011
Test Request Date:	July 22, 2011
Analyst:	Miss Sunaree Bordeepong
Test Performed Date:	July 25, 2011
Test Method Used:	Refer to WI-RES-XRD-001
Test Equipment:	X-ray Diffractometer, X'Pert MPD, PHILIPS, Netherlands
Test Technique:	X-ray Diffraction

Test Condition: X-ray tube : Cu tube   Sample preparation : Pressed Powder

Objective : Phase Identify   Scan Program : clay & rock-0.4

Test Item(s) Description: Anhydrite   **Quantity:** 2 samples

Test Result(s):

No.	Sample	JCPDF No.	Chemical Name	Chemical Formula
2102-1	Weathered anhydrite	01-074-1433	Gypsum	$Ca(SO_4)(H_2O)_2$
2102-2	Anhydrite	01-074-1433	Gypsum	$Ca(SO_4)(H_2O)_2$

As shown in attached diffractogram and refer to /2102

(Mrs. Roosanee Kulvijitra)

Head of Research Equipment Service

August 4, 2011

Remark This test report is valid only for the tested sample.

This test report shall not be reproduced except in full, without written approval of the Scientific Equipment Center.

Figure E.1   Sample G, test No. 2102-1, and Sample C, test No 2102-2, were identified as gypsum.

	Date: 3/8/2011 Time: 14:22:43			File: 2102-1			User: SEC
No.	Pos. [°2Th.]	d-spacing [?]	Rel. Int. [%]	FWHM [°2Th.]	Matched by	Area [cts...	Backgr.[cts]	Height [cts]
1	10.5318	8.40001	0.16	0.1181		6.87	315.91	58.96
2	11.6737	7.58079	100.00	0.1181	01-074-1433	4321.70	323.00	37102.50
3	20.7639	4.27800	4.57	0.1378	01-074-1433	230.64	110.00	1697.20
4	23.4330	3.79642	16.01	0.1574	01-074-1433	922.34	106.00	5938.85
5	28.1420	3.17096	0.14	0.1968	01-074-1433	10.36	80.00	53.39
6	29.1311	3.06550	7.60	0.1574	01-074-1433	437.94	95.00	2819.86
7	31.1674	2.86971	1.64	0.1574	01-074-1433	94.67	84.00	609.56
8	32.1653	2.78293	0.17	0.1968	01-074-1433	12.23	74.00	62.98
9	33.4029	2.68259	2.31	0.1771	01-074-1433	149.49	77.35	855.57
10	34.5487	2.59621	0.38	0.1968	01-074-1433	27.57	66.00	142.03
11	35.4019	2.53557	0.48	0.0787	01-074-1433	13.86	72.00	178.54
12	35.9843	2.49586	0.16	0.1574	01-074-1433	9.12	69.00	58.72
13	36.6398	2.45270	0.15	0.2362	01-074-1433	12.69	64.00	54.48
14	37.4303	2.40270	0.15	0.1968	01-074-1433	11.01	50.00	56.70
15	39.3447	2.29009	0.05	0.2362	01-074-1433	3.94	48.00	16.92
16	40.6576	2.21912	1.10	0.1181	01-074-1433	47.57	59.00	408.42
17	42.2564	2.13878	0.04	0.2362	01-074-1433	3.85	49.00	16.53
18	43.3697	2.08643	0.52	0.1771	01-074-1433	33.96	75.98	194.36
19	43.6643	2.07303	0.48	0.1968	01-074-1433	34.90	82.00	179.77
20	44.6217	2.03075	0.13	0.1574	01-074-1433	7.48	87.42	48.19
21	45.5334	1.99219	0.47	0.1968	01-074-1433	33.80	62.83	174.13
22	47.8570	1.90075	2.45	0.1181	01-074-1433	105.75	94.35	907.84
23	48.4400	1.87923	0.45	0.1968	01-074-1433	32.36	103.00	166.67
24	50.3892	1.81101	0.59	0.1378	01-074-1433	29.92	76.00	220.20
25	51.1484	1.78442	0.43	0.1920	01-074-1433	40.87	76.00	159.67
26	51.3385	1.77973	0.56	0.1574	01-074-1433	32.08	76.00	206.57
27	55.2265	1.66329	0.05	0.2362	01-074-1433	4.63	53.00	19.89
28	55.8389	1.64649	0.11	0.1574	01-074-1433	6.32	68.45	40.70
29	56.7649	1.62182	0.76	0.1378	01-074-1433	38.27	81.00	281.65
30	58.2080	1.58500	0.27	0.1574	01-074-1433	15.51	46.00	99.88
31	60.3842	1.53298	0.10	0.3149	01-074-1433	11.33	50.71	36.47
32	63.7561	1.45980	0.14	0.1968	01-074-1433	10.29	31.00	53.03
33	64.9345	1.43613	0.11	0.3936	01-074-1433	15.79	45.22	40.67
34	68.6984	1.36634	0.49	0.2362	01-074-1433	42.42	41.00	182.11
35	70.0418	1.34339	0.06	0.3149	01-074-1433	6.61	52.59	21.28
36	70.7176	1.33220	0.08	0.2362	01-074-1433	6.83	68.00	29.31
37	74.9047	1.26778	0.26	0.2362	01-074-1433	22.60	42.00	97.03
38	76.6454	1.24327	0.09	0.7085	01-074-1433	22.98	60.00	32.89
39	77.5533	1.23097	0.05	0.2362	01-074-1433	4.75	52.83	20.39
40	79.7444	1.20256	0.09	0.3542	01-074-1433	12.04	52.00	34.47
41	82.0029	1.17507	0.03	0.4723	01-074-1433	4.58	32.00	9.83
42	83.3324	1.15967	0.21	0.1574	01-074-1433	12.28	36.00	79.05
43	85.1728	1.13832	0.19	0.5760	01-074-1433	52.95	49.00	68.94

Figure E.2   Fitting precise peak parameters (position, intensity, FWHM, shape) to the corresponding d–spacings lattice values of test No. 2102-1 of sample G.

No.	Pos. [°2Th.]	d-spacing [Å]	Rel. Int. [%]	FWHM [°2Th.]	Matched by	Area [cts...]	Backgr. [cts]	Height [cts]
					Date: 3/8/2011 Time: 14:26:49	File: 2102-2		User: SEC
1	10.5393	8.39404	0.09	0.1181		4.88	309.93	41.88
2	11.6847	7.57368	100.00	0.0984	01-074-1433	4484.02	341.00	46195.29
3	20.7737	4.27602	6.62	0.1181	01-074-1433	356.35	131.00	3059.31
4	23.4367	3.79584	18.17	0.1378	01-074-1433	1140.85	135.00	8395.16
5	26.7252	3.33575	0.16	0.1378		9.93	110.00	73.09
6	28.1750	3.16732	0.08	0.2362	01-074-1433	8.40	98.00	36.07
7	29.1508	3.06348	7.98	0.1574	01-074-1433	572.43	115.00	3685.84
8	29.5039	3.02762	0.48	0.0787		17.07	109.31	219.83
9	31.1698	2.86950	0.91	0.1771	01-074-1433	73.15	89.00	418.67
10	32.1331	2.78564	0.13	0.1574	01-074-1433	9.03	79.00	58.16
11	33.3874	2.68381	1.75	0.1771	01-074-1433	141.20	81.00	808.15
12	34.5583	2.59551	0.32	0.1574	01-074-1433	22.70	79.00	146.18
13	35.4101	2.53500	0.63	0.1771	01-074-1433	51.20	85.00	293.06
14	36.0391	2.49219	0.18	0.1574	01-074-1433	13.26	81.00	85.41
15	36.6555	2.45168	0.20	0.1574	01-074-1433	14.11	80.00	90.86
16	37.4131	2.40376	0.11	0.1574	01-074-1433	8.00	68.00	51.54
17	39.4453	2.28448	0.07	0.2362	01-074-1433	7.94	61.76	34.09
18	40.6655	2.21870	1.15	0.1378	01-074-1433	72.13	66.00	530.80
19	42.2483	2.13917	0.07	0.2362	01-074-1433	7.63	59.00	32.76
20	43.2452	2.09215	0.46	0.0590	01-074-1433	12.33	86.76	211.66
21	43.6747	2.07256	0.31	0.1574	01-074-1433	22.30	99.23	143.57
22	44.6485	2.02960	0.09	0.1574	01-074-1433	6.23	95.08	40.10
23	45.5282	1.99241	0.33	0.1181	01-074-1433	18.00	74.09	154.49
24	47.8463	1.90115	2.56	0.1181	01-074-1433	137.68	99.81	1181.99
25	48.4081	1.88039	0.33	0.1378	01-074-1433	20.74	107.00	152.63
26	50.3368	1.81277	0.74	0.0984	01-074-1433	33.28	80.34	342.84
27	51.1573	1.78561	0.44	0.1181	01-074-1433	23.77	85.64	204.07
28	55.2152	1.66360	0.05	0.2362	01-074-1433	4.87	65.00	20.88
29	55.8487	1.64623	0.13	0.1968	01-074-1433	12.03	70.00	61.97
30	56.7799	1.62142	0.88	0.1378	01-074-1433	55.03	78.00	404.92
31	58.2130	1.58487	0.18	0.1574	01-074-1433	12.85	66.00	82.75
32	60.3692	1.53333	0.10	0.1574	01-074-1433	7.52	61.96	48.43
33	60.8917	1.52141	0.11	0.1574	01-074-1433	7.93	73.00	51.06
34	63.7821	1.45926	0.21	0.1378	01-074-1433	13.40	39.00	98.59
35	64.8543	1.43771	0.09	0.3149	01-074-1433	12.77	48.00	41.11
36	68.7268	1.36585	0.40	0.1378	01-074-1433	25.23	51.16	185.65
37	69.9932	1.34420	0.09	0.1181	01-074-1433	5.05	62.16	43.37
38	70.6819	1.33278	0.13	0.1574	01-074-1433	9.60	76.00	61.79
39	74.1909	1.27820	0.04	0.2362	01-074-1433	4.68	56.00	20.07
40	74.8800	1.26813	0.44	0.1378	01-074-1433	27.93	55.00	205.55
41	76.5801	1.24416	0.06	0.3936	01-074-1433	11.35	86.50	29.24
42	77.5050	1.23161	0.09	0.1181	01-074-1433	4.89	66.25	42.02
43	79.6960	1.20317	0.05	0.4723	01-074-1433	10.11	61.00	21.71
44	83.3197	1.15981	0.23	0.1181	01-074-1433	12.11	44.00	103.95
45	84.9039	1.14123	0.20	0.1440	01-074-1433	17.48	51.00	91.03
46	85.1808	1.13823	0.20	0.1440	01-074-1433	18.17	51.00	94.65

Figure E.3   Fitting precise peak parameters (position, intensity, FWHM, shape) to the corresponding d–spacings lattice values of test No. 2102-2 of sample C.

APPENDIX F

GEOLOGY FROM GROUNDWATER WELL CUTTINGS

Table F.1: Geological information from groundwater wells in the greater study area in Tayang Sub-district.

Well no.	UTM_E	UTM_N	Perforation interval (m.)	Aquifer type	Depth (m.)	Lithology Description
MV403	537336.0	922751.6	21 - 27	limestone	0 - 21.34	clay: pinkish purple and pink, plastic to high plastic, silty, compacted.
					21.34 - 30.49	limestone: light gray and pinkish gray, limonitic, dense, slightly weathered, hard.
MV845	537525.9	921501.6	24 - 30	limestone	0 - 27	clay: reddish brown, plastic, moderately compacted.
					27 - 33	limestone: grayish red, slightly clayey, highly weathered.
MV669	548175.0	915150.0	42 - 48	limestone	0 - 30.49	clay
					30.49 - 50.3	limestone
MV671	545262.5	926015.4	30 - 36	limestone	0 - 6.1	laterite
					6.1 - 27.44	clay
					27.44 - 30.49	clay
					30.49 - 36.59	limestone
MV841	543567.1	923497.9	21 - 27	claystone	0 - 9.15	clay: orangish brown, clayey, very fine sand, well rounded, very well sorted, composed of clay, moderately hard.
					9.15 - 27	claystone: reddish brown, clayey, very fine sand, well rounded, very well sorted, composed of clay, hard.
MV842	548565.9	923701.6	18 - 24	claystone	0 - 3.05	clay: dark brownish yellow, highly clayey, composed of clay, clay minerals, moderately compacted.
					3.05 - 27	claystone: dark brownish red, highly dense, composed of clay, clay minerals, hard to compacted.
MV779	539980.5	919958.3	18 - 24	igneous / granite	0 - 14	clay: orangish red and dark yellowish brown, plastic.
					14 - 26	igneous & granite: light brownish gray, composed of rock fragments, quartz, feldspars, slightly weathered to highly weathered, stiff to very hard and highly weathered at the upper parts.
MV315	538245.9	927731.6	12 - 18	igneous / rock	0 - 7.62	clay: reddish brown, limonite stained, non-plastic, compacted
					7.62 - 18.29	igneous/rock: dark grey, high weathered, very hard, dense

APPENDIX G

OBSERVED AND CALULATED DATA

Table G.1: Location coordinates of field surveys (WGS–84, Zone 47).

		UTM_E	UTM_N
SP reference position		541023	922070
First SP-measure point of loop		541009	922022
First SP-measure point of parallel-way line		541032	922043
End SP-measure point of parallel-way line		541008	921899
First geophone position parallel 2nd SH		540993	921897
2nd sinkhole		541001	921913
1st sinkhole		540982	922014
VES measurement point	Line1	541005	921993
	Line2	541109	921993
	Line3	541164	921990
	Line4	540954	922011
First geophone position parallel 1st sinkhole		541020	922036
Well position (taken water sample)		540809	922358

Table G.2: Raw data and calculated of the topographic-elevation survey.

Station	UTM_E	UTM_N	Backward (m)	Forward (m)	different	Absolute elevation (m)
Base	541037	922028	1.19	0	0	0
B1	541045	922029	3.198	0.635	0.555	0.555
B2	541090	922014	3.802	0.381	2.817	3.372
B3	541114	922012	3.296	0.365	3.437	6.809
B4	541140	922014	2.749	0.158	3.138	9.947
B5	541150	922009	1.971	0.348	2.401	12.348
B6	541148	921989	1.688	0.595	1.376	13.724
B7	541171	921929	0.783	2.645	-0.957	12.767
B8	541182	921896	2.858	1.93	-1.147	11.62
B9	541145	921883	1.545	0.196	2.662	14.282
B10	541081	921857	0.3	3.722	-2.177	12.105
B11	541038	921842	0.23	2.8	-2.5	9.605
B12	541008	921875	0.347	3.318	-3.088	6.517
B13	540999	921917	0.565	2.45	-2.103	4.414
B14	541013	921965	0.487	3.612	-3.047	1.367
B15	541011	922001	1.765	2.068	-1.581	-0.214
B16	541016	922030	1.765	1.374	0.391	0.177

Table G.3: Raw data and calculated elevation data of SP survey loop.

	Position on tape	different	UTM_E	UTM_N	forward	Absolute elevation
	Base				1.348	0
Tape1	31.7	0	541009.11	922021.89	0.83	0.518
	26	5.7	541008.2	922017.06	1.43	-0.082
	21.55	10.15	541007.49	922012.67	1.638	-0.29
	14	17.7	541006.28	922005.22	2.072	-0.724
	6	25.7	541005	921997.32	2.061	-0.713
Tape2	2	2	541002.07	921991.72	2.068	-0.72
	6	6	540998.12	921992.36	2.11	-0.762
	11	11	540993.19	921993.16	2.19	-0.842
	14	14	540990.22	921993.64	2.13	-0.782
	24	24	540980.35	921995.24	1.77	-0.422
Tape3	2	28	540980.67	921997.21	1.85	-0.502
	4.5	25.5	540981.07	921999.68	1.89	-0.542
	9	21	540981.79	922004.12	1.962	-0.614
	12	18	540982.27	922007.08	2.018	-0.67
	17	13	540983.07	922012.02	1.905	-0.557
	23	7	540984.03	922017.94	1.569	-0.221
	26	4	540984.51	922020.9	1.15	0.198
	30	0	540985.15	922024.85	0.905	0.443
Tape4	2	22	540987.12	922024.53	1.15	0.198
	7	17	540992.06	922023.73	1.21	0.138
	12	12	540996.99	922022.93	1.375	-0.027
	16	8	541000.94	922022.29	1.305	0.043
	18	6	541002.92	922021.97	1.31	0.038
	22	2	541006.87	922021.33	0.568	0.78
	24	0	541008.84	922021.01	0.765	0.583

Table G.4: Raw data and calculated elevation of SP survey of parallel-way line.

	Position on tape	UTM_E	UTM_N	Backward	Forward	difference	Absolute elevation (m)
Base					1.555	0	0
	0	541032	922043		1.556	-0.001	-0.001
	9	541030.6	922034.1		2.397	-0.842	-0.842
	13	541029.9	922030.2		2.105	-0.55	-0.55
	27	541027.7	922016.4		1.534	0.021	0.021
	33	541026.7	922010.4		0.89	0.665	0.665
	39	541025.8	922004.5	3.381	1.491	0.064	0.729
	53	541023.5	921990.7		3.512	-0.131	0.534
	74	541020.2	921970		2.735	0.646	1.311
transect point 1	75.3						
	88	541017.9	921956.1		1.328	2.053	2.718
	100	541016	921944.3	2.579	0.227	3.154	3.819
transect point 2	104						
	110	541014.4	921934.4		1.765	0.814	4.633
transect point 3	121						
	125	541012	921919.6		1.065	1.514	5.333
transect point 4	142						
	144	541009	921900.9		0.441	2.138	5.957
	150	541008	921894.9		0.125	2.454	6.273

Table G.5: Raw data and calculated elevation of SP survey of cross line.

	Position on tape	UTM_E	UTM_N	Backward	forward	difference	absolute elevation (m)
Base				1.86		0	0
crossline1	0	541026.55	921967.65		0.725	1.135	1.135
	6.55	541020	921968.7		1.095	0.765	0.765
	15	541011.55	921970.05		1.307	0.553	0.553
	25	541001.55	921971.65		1.609	0.251	0.251
	30	540996.55	921972.45		1.519	0.341	0.341
	43	540983.55	921974.53		1.555	0.305	0.305
	50	540976.55	921975.65		1.526	0.334	0.334
transect point 2				2.761	0.222	1.638	1.638
crossline2	0	541020.73	921939.44		0.55	2.211	3.849
	11	541009.87	921941.2		1.217	1.544	3.182
	26	540995.06	921943.59		1.998	0.763	2.401
	38	540983.22	921945.51		2.665	0.096	1.734
	50	540971.37	921947.43		2.965	-0.204	1.434
transect point 3				2.102	1.089	1.672	3.31
crossline3	0	541020.89	921922.27		0.242	1.86	5.17
	8.3	541012.7	921923.6		0.908	1.194	4.504
	16	541005.1	921924.83		1.412	0.69	4
	25.5	540995.72	921926.35		1.825	0.277	3.587
	33	540988.32	921927.55		1.81	0.292	3.602
	39	540982.39	921928.51		2.419	-0.317	2.993
	50	540971.54	921930.27		2.975	-0.873	2.437
transect point 4				1.974	1.301	0.801	4.111
crossline4	0	541013.8	921902.08		0.511	1.463	5.574
	12	541001.8	921904		1.225	0.749	4.86
	18	540995.8	921904.96		1.565	0.409	4.52
	26	540987.8	921906.24		1.965	0.009	4.12
	32	540981.8	921907.2		2.242	-0.268	3.843
end of long line	50	540963.8	921910.07		0.381	1.593	5.704

Table G.6: Measured resistance and calculated apparent resistivity data.

AB/2	MN/2	K	R1 point		R2 point		R3 point		R4 point	
			R_1	ρ_1	R_2	ρ_2	R_3	ρ_3	R_4	ρ_4
1.5	0.5	6.283	271.11	1703.43	125.12	786.15	144.09	905.34	73.307	460.60
2	0.5	11.781	143.92	1695.52	80.448	947.76	83.793	987.16	44.441	523.56
3	0.5	27.489	56.413	1550.73	41.495	1140.65	40.509	1113.55	22.663	622.98
4.5	0.5	62.832	20.863	1310.86	20.147	1265.87	19.428	1220.70	11.006	691.53
7	0.5	153.153	6.5849	1008.49	9.1823	1406.29	9.2304	1413.66	4.9938	764.81
7	2	35.343	29.805	1053.40	31.744	1121.93	33.211	1173.77	18.016	636.74
10	0.5	313.374	3.0576	958.17	4.2838	1342.43	4.4615	1398.12	2.0121	630.54
10	2	75.398	13.02	981.68	14.018	1056.93	15.407	1161.66	7.0238	529.58
15	2	173.573	5.1818	899.42	5.943	1031.54	6.1707	1071.07	2.3599	409.61
20	2	311.018	2.6222	815.55	3.2812	1020.51	3.0164	938.15	0.9146	284.46
20	6	95.295	9.1893	875.69	10.333	984.68	8.9192	849.95	2.6257	250.22
30	6	226.195	3.2112	726.36	3.6498	825.57	2.8652	648.09	0.8961	202.69
45	6	520.719	1.1409	594.09	1.3475	701.67	0.96	499.89	0.2134	111.12
45	10	302.378	1.9228	581.41	2.2583	682.86	1.768	534.60	0.3831	115.84
60	10	549.779	0.871	478.86	0.992	545.38	0.5786	318.10	0.1838	101.05
60	20	251.327	1.88	472.50	2.1656	544.27	1.3241	332.78	0.4447	111.77
100	20	753.982	0.47273	356.43	0.40388	304.52	0.21506	162.15	0.1402	105.71
100	30	476.475	0.74214	353.61	0.69265	330.03	0.36951	176.06	0.2042	97.30
150	30	1130.973	0.26703	302.00	0.24448	276.50	0.14324	162.00	0.1091	123.39
150	50	628.319	0.49504	311.04	0.4435	278.66	0.27458	172.52	0.2156	135.47
200	50	1178.097	0.26312	309.98	0.23457	276.35	0.14956	176.20	0.1495	176.13
225	50	1511.891	0.20663	312.40	0.22966	347.22	0.112	169.33	0.1205	182.18
250	50	1884.956	0.17669	333.05	0.18045	340.14	0.11013	207.59	0.1081	203.76
300	50	2748.894	0.13188	362.52	-	-	0.089351	245.62		
350	50	3769.911	0.11393	429.51	0.115	433.54	0.094662	356.87		

Table G.7: First break picking of refraction data of line parallel first sinkhole.

Geophone	First break picking time (ms)						
	1st shot	2nd shot	3rd shot	4th shot	5th shot	6th shot	7th shot
1	36.750	25.750	2.000	26.625	36.625	43.500	52.875
2	37.000	27.250	3.750	25.000	36.375	42.875	51.750
3	38.250	28.000	6.750	23.875	35.500	42.000	51.750
4	38.500	29.000	9.500	22.250	35.125	41.625	51.000
5	39.500	30.500	12.500	20.500	35.625	41.750	51.000
6	40.250	31.500	16.750	18.625	35.000	41.125	50.500
7	40.750	32.750	19.750	15.250	33.375	40.125	50.125
8	41.000	33.750	20.750	12.375	33.750	40.000	49.375
9	41.750	35.500	22.000	9.625	33.000	38.625	49.000
10	42.250	36.750	24.000	6.750	32.250	38.500	49.375
11	42.750	36.750	26.000	3.875	31.625	38.500	48.375
12	43.500	37.250	28.000	0.625	30.500	38.125	47.875
13	44.250	38.250	29.500	1.125	29.000	37.375	46.750
14	45.000	39.000	31.750	3.750	26.500	36.750	47.250
15	45.750	39.750	32.500	6.750	24.500	34.500	46.250
16	46.000	40.500	33.500	9.750	22.625	33.500	45.750
17	46.750	40.750	34.250	12.500	19.875	34.375	45.125
18	47.000	41.250	34.500	15.375	18.000	33.125	44.125
19	47.250	42.250	36.250	18.250	15.250	32.250	43.750
20	48.500	43.000	36.250	20.625	12.375	31.750	42.750
21	49.000	43.500	37.250	23.125	9.375	31.375	42.125
22	50.250	44.500	38.250	24.750	6.500	30.750	41.125
23	50.250	44.500	38.500	26.750	3.750	29.500	40.250
24	50.250	45.500	39.250	29.125	1.000	28.250	39.500

Table G8: First break picking of refraction data of line parallel second sinkhole.

Geophone	First break picking time (ms)				
	1st shot	2nd shot	3rd shot	4th shot	5th shot
1	35.75	1.25	31.75	52.00	59.00
2	38.75	3.75	30.00	52.50	57.50
3	41.50	6.50	27.00	51.75	58.75
4	44.25	9.25	24.25	51.25	58.00
5	46.75	12.00	21.50	50.50	57.25
6	47.50	15.25	18.25	50.25	56.25
7	48.00	18.25	15.75	48.50	55.75
8	49.00	21.25	12.25	47.00	54.75
9	49.75	24.50	9.75	44.50	54.00
10	50.25	27.25	7.25	41.25	53.75
11	50.75	29.25	6.25	38.25	53.25
12	51.50	31.75	0.75	35.75	53.25
13	52.25	36.00	1.25	32.75	52.25
14	54.00	37.25	3.25	30.00	51.50
15	54.25	41.25	6.75	27.25	49.50
16	54.00	44.00	9.75	24.50	49.25
17	55.25	47.00	12.25	21.75	49.00
18	55.25	49.00	15.00	19.75	47.75
19	56.75	49.75	17.25	17.25	47.00
20	57.75	51.25	21.00	14.75	47.00
21	57.25	52.25	23.75	11.00	44.50
22	58.00	53.00	26.75	7.00	41.50
23	58.50	53.75	28.50	4.25	39.25
24	58.50	53.75	32.00	1.50	35.75

Table G.9: First break picking of extended-offset of first refraction survey at the first sinkhole site.

Shot position (m) Geophone	-96.5	-84.5	-72.5	-60.5	-48.5	-36.5	-24.5	-12.5	-0.5	23.5	35.5	47.5	59.5	71.5	83.5	95.5	107.5
1	78.5	73	67.25	59.25	55	43.25	36.5	27.5	1.75	37.5	43.875	53.625	64.125	71.5	79.625	87.5	94.25
2	79	73.5	68	60.25	56	44.25	37.5	28.5	5.75	37.5	44	53	63.375	71.125	79.5	87.25	93.75
3	80.5	74	68.75	61.25	57	45.25	38.25	29.5	9	36.625	43.125	52.75	63.25	70.375	79	86.625	93.25
4	81	74.5	69.5	62.25	57	46	39.25	30.5	11.5	36.125	43.125	52.5	62.875	69.875	78.375	86.375	92.75
5	81.5	76.25	70.25	63.25	57.25	47	40.25	31.5	14.75	35.125	42	51.75	62.625	69.75	77.75	86.125	92.625
6	82	77.5	71	63.75	56.75	48	40.5	32.5	17.75	35	41.25	51.25	62.25	69.25	77.25	85.375	91.875
7	82.5	78	71.75	63.75	58.5	48	41.25	33.5	19.25	34.5	41.375	51.125	62.125	68.75	76.625	84.875	91.675
8	83	78.5	72.25	64.25	59	48	42.25	34.5	20.75	33.5	40.875	51.125	61.625	68.5	76.125	84.5	91
9	83.5	79	72.25	64.75	59.75	49	42.25	35.5	22	32.5	39.75	50.125	61.125	68	75.25	83.875	90.375
10	84	80.5	73.25	65.25	60.5	50	43	36.5	24	32	39.5	50.5	60.375	67.125	74.625	82.75	89.625
11	84.5	80.5	73.75	65.75	61.25	50.75	44	37.5	26	31.125	39.25	49.625	60	66.5	74.5	82.5	88.375
12	86	81	74.25	66.25	62	51.5	44.5	38.5	28	29.375	38.625	48.875	59.625	65.875	74.25	82	87.875
13	86.5	81	74.25	67.5	62.5	52	44.75	39	29.75	29.375	37.75	47.375	59.5	65.125	73.875	81.75	87.125
14	86.75	81.5	74.75	68	63.25	52.5	45.75	39.5	32.25	27.25	37.875	48.375	58.375	65.5	73.375	80.5	86.625
15	87.25	82	75.25	68.5	64	53	46.5	40.25	33	25.125	36.75	47.375	58	64.75	72.75	80.375	87.125
16	87.75	82.5	75.75	69	64.5	53.5	47	40.75	33.75	23.125	35.75	46.875	56.875	64.125	72	79.25	86.25
17	88.25	83	76.25	69.5	65	54	47.75	41.25	34.5	21	35.5	46.25	55.625	63.25	71.5	79.125	85.5
18	88.75	83.5	76.75	70	65	54	47.75	41.75	35	19.125	34.625	45.125	55.375	62.5	70.875	78.5	84.25
19	89.25	84	77.25	70.5	65	54.5	48.25	42.25	35.5	16.375	33.375	44.875	54.75	61.875	70.125	78	83.5
20	89.75	84.5	77.75	71	65.25	55	49.25	42.75	36	13.5	32.875	43.875	53.875	61.25	69	77.375	83.125
21	90.25	85	78.25	72.5	65.5	55.5	49.75	43.25	36.5	10.5	32.625	43.25	53.125	59.125	68	77.125	81.875
22	91	85.5	79	73	65.75	56	50.25	43.75	37	7.625	31.5	42.25	52.25	58.625	67.375	75.75	81.125
23	91.5	86	79.5	73.5	66	56.5	50.75	44.25	37.5	4.875	30.25	41.625	51.75	57.875	66.375	75.125	80.375
24	92	86.5	80	74	66.25	57	51.25	44.75	38	1	29.25	40.125	50.875	57.75	65.5	74.125	79.375

First break picking time (ms)

Table G.10: Measured and corrected of self-potential data of loop-line.

Mobile electrode point	Distance on tape (m)	UTM_E	UTM_N	Average time	Average SP (mV)	Δt1 (min)	SPdrift1	Corrected SP1 (mV)	Δt2 (min)	SPdrift2	Corrected SP2 (mV)
1 (Base)	0	541009	922022	9:07:00	5.41	0.00	0.00	5.41			
2	1	541009	922021	9:12:30	6.29	5.50	2.79	3.50			
3	3	541009	922019	9:16:30	5.90	9.50	4.82	1.08			
4	5	541008	922017	9:21:30	9.00	14.50	7.35	1.65			
5	7	541008	922015	9:31:30	1.93	24.50	12.42	-10.49			
6	9	541008	922013	9:36:30	3.03	29.50	14.95	-11.92			
7	11	541007	922011	9:44:00	4.88	37.00	18.75	-13.87			
8	13	541007	922009	9:47:30	3.91	40.50	20.53	-16.62			
9	15	541007	922007	9:52:30	58.25	45.50	23.06	35.19			
10	17	541006	922005	9:57:00	5.75	50.00	25.34	-19.59			
11	19	541006	922003	10:02:30	1.46	55.50	28.13	-26.67			
12	21	541006	922001	10:06:00	3.42	59.00	29.90	-26.48			
13	23	541005	921999	10:09:00	3.99	62.00	31.42	-27.44			
14	25	541005	921997	10:11:30	7.86	64.50	32.69	-24.83			
1 (Base)				10:18:30	41.65	71.50	36.24	5.41	0.00	0.00	5.41
15	27	541005	921995	10:22:30	10.47	75.50		10.47	4.00	-0.02	10.48
16	29	541004	921993	10:24:30	10.84	77.50		10.84	6.00	-0.02	10.86
17	31	541004	921991	10:27:30	20.77	80.50		20.77	9.00	-0.04	20.81
18	33	541002	921992	10:32:00	10.00	85.00		10.00	13.50	-0.05	10.05
19	35	541000	921992	10:35:30	8.55	88.50		8.55	17.00	-0.07	8.61
20	37	540998	921992	10:39:00	6.17	92.00		6.17	20.50	-0.08	6.25
21	39	540996	921993	10:42:30	1.66	95.50		1.66	24.00	-0.10	1.75
22	41	540994	921993	10:44:30	0.42	97.50		0.42	26.00	-0.10	0.53
23	43	540992	921993	10:47:30	-2.99	100.50		-2.99	29.00	-0.12	-2.87
24	45	540990	921994	10:49:30	1.89	102.50		1.89	31.00	-0.12	2.01
25	47	540988	921994	10:52:00	4.40	105.00		4.40	33.50	-0.13	4.53
26	49	540986	921994	10:54:30	6.37	107.50		6.37	36.00	-0.14	6.51
27	51	540984	921995	10:57:00	4.36	110.00		4.36	38.50	-0.15	4.51
1 (Base)				11:00:00	5.25	113.00		5.25	41.50	-0.17	5.41

Table G.10 (continued): Measured and corrected of self-potential data of loop-line.

Mobile electrode point	Distance on tape (m)	UTM_E	UTM_N	Average time	Average SP (mV)	Corrected SP2 (mV)	Δt3 (min)	SPdrift3	Corrected SP3 (mV)	Δt4 (min)	SPdrift4	Corrected SP4 (mV)
1 (Base)				11:00:00	5.25	5.41	0.00	0.00	5.41			
28	55	540980	921995	11:07:30	1.63	1.63	7.50	0.82	0.81			
29	57	540981	921997	11:10:00	3.03	3.03	10.00	1.10	1.93			
30	59	540981	921999	11:22:00	1.68	1.68	22.00	2.41	-0.73			
31	61	540981	922001	11:23:30	9.85	9.85	23.50	2.58	7.27			
32	63	540982	922003	11:25:30	15.72	15.72	25.50	2.80	12.92			
33	65	540982	922005	11:29:00	8.16	8.16	29.00	3.18	4.98			
34	67	540982	922007	11:33:30	28.55	28.55	33.50	3.68	24.87			
35	69	540983	922009	11:36:30	-1.63	-1.63	36.50	4.01	-5.64			
36	71	540983	922011	11:40:30	8.95	8.95	40.50	4.45	4.50			
37	73	540983	922013	11:42:30	13.87	13.87	42.50	4.66	9.20			
38	75	540983	922015	11:44:30	10.23	10.23	44.50	4.88	5.35			
39	77	540984	922017	11:46:30	9.25	9.25	46.50	5.10	4.15			
40	79	540984	922019	11:49:30	17.63	17.63	49.50	5.43	12.20			
41	81	540984	922021	11:53:00	20.21	20.21	53.00	5.82	14.39			
42	83	540985	922023	11:58:00	18.49	18.49	58.00	6.37	12.12			
1 (Base)				12:03:00	12.33	12.33	63.00	6.92	5.41	0.00	0.00	5.41
43	85	540985	922025	12:07:00	18.58				18.58	4.00	-0.25	18.82
44	87	540987	922024	12:12:30	9.11				9.11	9.50	-0.59	9.70
45	89	540989	922024	12:14:30	4.29				4.29	11.50	-0.71	5.00
46	91	540991	922024	12:16:00	12.03				12.03	13.00	-0.80	12.83
47	93	540993	922024	12:18:00	10.22				10.22	15.00	-0.92	11.14
48	95	540995	922023	12:20:30	3.35				3.35	17.50	-1.08	4.43
49	97	540997	922023	12:23:30	6.62				6.62	20.50	-1.26	7.88
50	99	540999	922023	12:25:00	6.86				6.86	22.00	-1.36	8.21
51	101	541001	922022	12:27:00	4.84				4.84	24.00	-1.48	6.31
52	103	541003	922022	12:29:30	1.80				1.80	26.50	-1.63	3.44
53	105	541005	922022	12:32:30	-0.50				-0.50	29.50	-1.82	1.32
54	107	541007	922021	12:35:00	2.74				2.74	32.00	-1.97	4.71
55	109	541009	922021	12:37:00	2.59				2.59	34.00	-2.10	4.68
1 (Base)				12:39:30	3.16				3.16	36.50	-2.25	5.41

Table G.10: Measured and corrected of self-potential data of parallel-way and cross lines.

Line	Mobile electrode point	Distance on tape (m)	UTM_E	UTM_N	Average time	Average SP (mV)	Δt1 (min)	SP drift1	Corrected SP1 (mV)	Δt2 (min)	SPdrift2	Corrected SP2 (mV)
Parallel way	57 (base)	0	541032	922043	13:22:30	-3.04	0.00	0.00	-3.04			
	58	2.5	541031.6	922040.5	13:27:00	-1.22	4.50	0.02	-1.24			
	59	5	541031.2	922038.1	13:29:30	-3.26	7.00	0.03	-3.29			
	60	7.5	541030.8	922035.6	13:32:30	-6.19	10.00	0.04	-6.23			
	61	10	541030.4	922033.1	13:34:00	-8.69	11.50	0.05	-8.74			
	62	12.5	541030	922030.7	13:37:30	-3.90	15.00	0.07	-3.97			
	63	15	541029.6	922028.2	13:40:30	-5.83	18.00	0.08	-5.91			
	64	20	541028.8	922023.3	13:44:00	-0.91	21.50	0.09	-1.01			
	65	25	541028	922018.3	13:46:00	-1.33	23.50	0.10	-1.43			
	66	30	541027.2	922013.4	13:50:00	4.32	27.50	0.12	4.19			
	67	35	541026.4	922008.5	13:53:00	-2.21	30.50	0.13	-2.34			
	68	40	541025.6	922003.5	13:55:00	5.80	32.50	0.14	5.65			
	69	45	541024.8	921998.6	13:59:00	159.65	36.50	0.16	159.49		causes by bioelectric roots-tree activity	
	70	50	541024	921993.6	14:02:00	7.08	39.50	0.17	6.90			
	71	55	541023.2	921988.7	14:05:30	37.45	43.00	0.19	37.26			
	72	60	541022.4	921983.8	14:09:00	88.55	46.50	0.20	88.35		causes by bioelectric roots-tree activity	
	73	65	541021.6	921978.8	14:12:30	209.00	50.00	0.22	208.78		causes by bioelectric roots-tree activity	
	74	70	541020.8	921973.9	14:16:30	4.64	54.00	0.24	4.40			
	75	75	541020	921969	14:21:00	2.07	58.50	0.26	1.81			
	57 (base)				14:25:00	-2.76	62.50	0.28	-3.04	0.00	0.00	-3.04
	76	80	541019.2	921964	14:27:30	22.75	65.00		22.75	2.50	-0.01	22.76
	77	85	541018.4	921959.1	14:30:30	20.70	68.00		20.70	5.50	-0.02	20.72
	78	90	541017.6	921954.2	14:34:30	19.00	72.00		19.00	9.50	-0.03	19.02
	79	95	541016.8	921949.2	14:36:30	17.66	74.00		17.66	11.50	-0.03	17.69
	80	100	541016	921944.3	14:39:30	26.60	77.00		26.60	14.50	-0.04	26.64
	81	105	541015.2	921939.4	14:45:00	14.92	82.50		14.92	20.00	-0.06	14.98
	82	110	541014.4	921934.4	14:46:30	8.36	84.00		8.36	21.50	-0.06	8.42
	83	115	541013.6	921929.5	14:49:30	12.40	87.00		12.40	24.50	-0.07	12.47
	84	120	541012.8	921924.5	14:52:30	8.98	90.00		8.98	27.50	-0.08	9.06
	85	122.5	541012.4	921922.1	14:55:30	12.07	93.00		12.07	30.50	-0.09	12.15
	86	125	541012	921919.6	15:01:00	10.54	98.50		10.54	36.00	-0.10	10.64
	87	127.5	541011.6	921917.1	15:05:00	3.70	102.50		3.70	40.00	-0.12	3.81
	88	130	541011.2	921914.7	15:07:00	1.20	104.50		1.20	42.00	-0.12	1.32
	89	132.5	541010.8	921912.2	15:09:30	-2.32	107.00		-2.32	44.50	-0.13	-2.19
	90	135	541010.4	921909.7	15:11:30	1.00	109.00		1.00	46.50	-0.13	1.13
	91	137.5	541010	921907.3	15:15:00	11.12	112.50		11.12	50.00	-0.14	11.26
	92	140	541009.6	921904.8	15:16:30	11.48	114.00		11.48	51.50	-0.15	11.63
	93	145	541008.8	921899.9	15:18:30	7.29	116.00		7.29	53.50	-0.15	7.44
	94	150	541008	921894.9	15:20:00	11.45	117.50		11.45	55.00	-0.16	11.61
	57 (base)				15:25:30	-3.21	123.00		-3.21	60.50	-0.18	-3.04

Table G.10 (continued): Measured and corrected of self-potential data of parallel-way and cross lines.

Line	Mobile electrode point	Distance on tape (m)	UTM_E	UTM_N	Average time	Average SP (mV)	Corrected SP2 (mV)	Δt3 (min)	SPdrift3	Corrected SP3 (mV)	Δt4 (min)	SPdrift4	Corrected SP4 (mV)
Cross L1	57 (base)				15:25:30	-3.21	-3.04	0.00	0.00	-3.04			
	95	0	541026.6	921968	15:35:30	9.33	9.33	10.00	0.40	8.93			
	96	5	541021.7	921968.8	15:39:00	8.98	8.98	13.50	0.54	8.44			
	97	10	541016.7	921969.6	15:40:30	6.26	6.26	15.00	0.59	5.67			
	98	15	541011.8	921970.4	15:43:00	7.16	7.16	17.50	0.69	6.46			
	99	20	541006.9	921971.2	15:46:00	10.11	10.11	20.50	0.81	9.30			
	100	25	541001.9	921972	15:47:30	14.86	14.86	22.00	0.87	13.99			
	101	30	540997	921972.8	15:49:30	9.50	9.50	24.00	0.95	8.54			
	102	35	540992.1	921973.6	15:52:00	3.93	3.93	26.50	1.05	2.88			
	103	40	540987.1	921974.4	15:53:30	13.37	13.37	28.00	1.11	12.25			
	104	45	540982.2	921975.2	15:55:30	6.97	6.97	30.00	1.19	5.78			
	105	50	540977.2	921976	16:00:30	2.45	2.45	35.00	1.39	1.06			
Cross L2	106	0	541020.7	921939	16:06:30	10.65	10.65	41.00	1.63	9.02			
	107	4	541016.8	921939.6	16:11:00	17.67	17.67	45.50	1.80	15.87			
	108	9	541011.8	921940.4	16:13:30	13.54	13.54	48.00	1.90	11.63			
	109	14	541006.9	921941.2	16:17:00	4.33	4.33	51.50	2.04	2.28			
	110	20	541001	921942.2	16:20:30	4.12	4.12	55.00	2.18	1.93			
	111	25	540996	921943	16:22:30	4.07	4.07	57.00	2.26	1.81			
	112	30	540991.1	921943.8	16:25:00	11.05	11.05	59.50	2.36	8.69			
	113	35	540986.2	921944.6	16:27:00	9.14	9.14	61.50	2.44	6.70			
	114	40	540981.2	921945.4	16:31:00	5.36	5.36	65.50	2.60	2.76			
	115	45	540976.3	921946.2	16:32:30	3.97	3.97	67.00	2.66	1.31			
	116	50	540971.3	921947	16:34:00	4.83	4.83	68.50	2.72	2.11			
	57 (base)				16:41:30	-0.02	-0.02	76.00	3.01	-3.04	0.00	0.00	-3.04
Cross L3	117	0	541020.9	921922	16:45:30	9.95	9.95			9.95	4.00	0.23	9.72
	118	5	541016	921922.8	16:47:30	4.25	4.25			4.25	6.00	0.34	3.91
	119	10	541011	921923.6	16:49:30	7.79	7.79			7.79	8.00	0.46	7.33
	120	15	541006.1	921924.4	16:51:30	13.16	13.16			13.16	10.00	0.57	12.59
	121	21	541000.2	921925.4	16:53:30	12.21	12.21			12.21	12.00	0.68	11.52
	122	25	540996.2	921926	16:55:30	10.12	10.12			10.12	14.00	0.80	9.32
	123	30	540991.3	921926.8	16:57:30	12.45	12.45			12.45	16.00	0.91	11.54
	124	35	540986.4	921927.6	17:00:00	7.19	7.19			7.19	18.50	1.05	6.14
	125	40	540981.4	921928.4	17:02:30	8.31	8.31			8.31	21.00	1.20	7.11
	126	45	540976.5	921929.2	17:05:30	2.50	2.50			2.50	24.00	1.37	1.13
	127	50	540971.5	921930	17:07:30	1.92	1.92			1.92	26.00	1.48	0.44
Cross L4	128	0	541013.8	921902	17:13:30	12.78	12.78			12.78	32.00	1.82	10.96
	129	5	541008.9	921902.8	17:15:00	15.92	15.92			15.92	33.50	1.91	14.01
	130	10	541003.9	921903.6	17:17:30	19.05	19.05			19.05	36.00	2.05	17.00
	131	14	541000	921904.2	17:20:30	19.32	19.32			19.32	39.00	2.22	17.09
	132	20	540994.1	921905.2	17:22:00	15.25	15.25			15.25	40.50	2.31	12.94
	133	25	540989.1	921906	17:24:30	17.03	17.03			17.03	43.00	2.45	14.57
	134	32	540982.2	921907.1	17:26:30	20.45	20.45			20.45	45.00	2.57	17.88
	57 (base)				17:34:00	-0.04	-0.02		2.99	-0.04	52.50	2.99	-3.04

Table G.11: Measured resistivity data of gypsum solution.

% saturate	[CaSO4·2H2O] (mg/L)	TDS	[SO42-] (mg/L)	conductivity (μs/cm)	conductivity (s/m)	resistivity (ohm-m)
100	860	860	480	897	0.0897	11.15
90	774	774	432	818	0.0818	12.22
80	688	688	384	744	0.0744	13.44
70	602	602	336	668	0.0668	14.97
60	516	516	288	588	0.0588	17.01
50	430	430	240	506	0.0506	19.76
40	344	344	192	418	0.0418	23.92
30	258	258	144	325	0.0325	30.77
20	172	172	96	230.9	0.02309	43.31
15	129	129	72	181.1	0.01811	55.22
10	86	86	48	124.8	0.01248	80.13
5	43	43	24	66.1	0.00661	151.29
4	34.4	34.4	19.2	51.3	0.00513	194.93
3	25.8	25.8	14.4	43.5	0.00435	229.89
2	17.2	17.2	9.6	28.91	0.002891	345.90
1	8.6	8.6	4.8	15.75	0.001575	634.92
0.1	0.86	0.86	0.48	2.73	0.000273	3663.00
0.01	0.086	0.09	0.048	1.28	0.000128	7812.50

Table G.12: Rock density measurement with silicone glue cover.

Sample	m_a	m_a+m_a of glue (dry)	m_f+m_f of glue (dry)	m_f of glue	m_f of sample without glue	density of sample
(b)	1421.2	1458.3	946.4	7.8	938.6	2.94
(c)	968.6	1025.3	545	13.8	531.2	2.21
(g)	903.1	972.9	460.8	17.6	443.2	1.96
(h)	331.5	357.8	193.2	6.6	186.6	2.29

Table G.13: Rock density measurement without silicone glue cover.

Sample	mg before put in the water (dry)	m_a	m_f	mg after put in the water (wet)	density of sample
(b)	1421.4	1421.2	935.9	1420.8	2.93
(c)	967.9	965.3	538.5	979.6	2.26
(g)	773.5	772.2	402.8	976.8	2.09
(h)	330.7	330.4	186.4	331.4	2.29

VITAE

Name	Miss Aksara Mayamae
Student ID	5010220167

Education

Degree	Name of Institution	Year of Graduation
B.Sc. (Physics)	Prince of Songkla University	2006

List of Publication and Proceedings

Mayamae, A. and Dürrast, H. 2010-2011. Understanding of Sulfate-Formation Related Sinkhole Occurrence from an Integrated Geoscientific Study. Journal of The Geological Society of Thailand. 1, 7-14.

Mayamae, A. and Dürrast, H. 2010. An Integrated Geophysical and Geochemical Study of Sulfate Dissolution Related Sinkhole Occurrence. In Proceedings of the 5th International Conference on Applied Geophysics (Geophysics Phuket Thailand 2010): Geological Resources-Natural Hazards Climate Change, 11-13 November 2010, Phuket, Thailand.

Mayamae, A. and Dürrast, H. 2010. Understanding of Sulfate-formation Related Sinkhole Occurrence from an Integrated Geophysical Study. In Proceedings of the 5th Siam Physics Congress (SPC 2010), Thai Journal of Physics Series 6: Thai Physics Society, 25-27 March 2010, Kanchanaburi, Thailand.